Doctoral Dissertation

High-throughput experimentation and automatic feature engineering for catalyst discovery in dry reforming of methane

DU Wentao

Supervisor: Toshiaki Taniike

Graduate School of Advanced Science and Technology

Japan Advanced Institute of Science and Technology

Materials Science

September 2025

Referee-In-Chief: Professor Toshiaki Taniike
Japan Advanced Institute of Science and Technology

Referees: Professor Yuki Nagao
Japan Advanced Institute of Science and Technology

Associate Professor Shun Nishimura
Japan Advanced Institute of Science and Technology

Associate Professor Kenta Hongo
Japan Advanced Institute of Science and Technology

Professor Keisuke Nagato
The University of Tokyo

Abstract

DU Wentao (2220433)

Conventional catalyst development has largely relied on trial-and-error experiments, which are time-consuming and costly. To tackle this challenge, data-driven approaches, particularly machine learning (ML), have gained prominence in accelerating catalyst discovery and optimization. However, two key challenges must be overcome for the practical application of ML in catalyst development. First, complex materials like solid catalysts often lack sufficient experimental data for effective ML training. Second, designing comprehensive descriptors for materials typically requires deep domain knowledge. The advent of high-throughput experimentation (HTE) offers a powerful solution to the data scarcity issue in catalysis research. Additionally, a recently developed automatic feature engineering (AFE) technique effectively mitigates the need for prior system knowledge, addressing the challenge of descriptor design. Dry reforming of methane (DRM) is an important catalytic process, typically requiring temperatures above 700 °C for high reactant conversion. However, such conditions cause catalyst sintering and deactivation. Operating at 500 °C or lower presents a promising alternative, as it can mitigate catalyst degradation and reduce environmental impact. Nevertheless, under these milder conditions, undesirable side reactions tend to occur, resulting in carbon deposition. To overcome these challenges, the development of active, stable, and selective catalysts demands a multi-element design strategy. Therefore, this thesis aims to present an approach for developing multi-element DRM catalysts without prior knowledge, leveraging a combination of HTE, ML, and AFE within an adaptive experimental design framework.

The presence of a high-quality, large-scale, and consistent catalyst dataset is essential for effectively applying ML to explore the extensive materials space and achieve efficient catalyst design. Therefore, in **Chapter 2**, I present the acquisition of an unbiased training dataset for DRM at 500 °C, comprising 256 γ-Al_2O_3-supported multi-element catalysts. These catalysts were prepared through HTE by randomly combining 17 elements selected from the periodic table without preconceptions. The resulting data were analyzed from multiple perspectives to extract meaningful insights into catalyst design and catalysis. Overall, this chapter highlights the effectiveness of unbiased exploration in establishing a robust dataset for ML and identifying valuable catalyst design guidelines.

Catalysis research is often hindered by the limited size of available datasets. This poses challenges for training expressive ML models, which typically require numerous tunable parameters to capture complex trends. Additionally, the diversity and complexity of catalysts make it difficult to design comprehensive descriptors based on physicochemical intuition. To overcome this, in **Chapter 3**, a two-step ML approach with AFE was introduced to generate effective descriptors directly from composition, enabling simple models to accurately capture performance trends without prior knowledge. Using the unbiased DRM dataset constructed in Chapter 2, an active learning loop was implemented by integrating AFE, farthest point sampling (FPS), and HTE. This iterative framework expanded the compositional space from 17 to 45 elements and guided efficient exploration of the catalyst landscape. Finally, this approach enabled the construction of a robust predictive model for identifying superior catalysts across vast material space.

Low-temperature DRM is explored as a promising route due to its lower energy demands and improved economic feasibility. However, it remains susceptible to carbon deposition mainly via CO disproportionation. Carbon accumulation deactivates catalysts by blocking active sites and hindering reactant flow, increasing pressure drop and safety risks. To address this, in **Chapter 4**, I investigated high-performance catalysts identified through the active learning loop in Chapter 3. Thermogravimetric–differential thermal analysis (TG-DTA) was conducted after 6 hours of reaction at 500 °C to assess carbon deposition. The analysis reveals key relationships among catalytic activity, carbon formation behavior, and composition, offering essential guidance for designing highly active and carbon-resistant catalysts.

In summary, catalyst discovery has long been constrained by human preconceptions and domain knowledge, which limit exploration to narrow, well-understood regions of design space. This dissertation establishes a transformative strategy that promises to remove these constraints. Through a fully data-driven framework that integrates HTE, ML, and AFE, this study opens access to previously inaccessible areas of the materials landscape and accelerates the identification of high-performing catalysts. Furthermore, by leveraging predictive models and addressing key challenges such as carbon deposition, this study not only deepens our understanding of catalyst behavior but also provides actionable design guidelines for the development of highly active and durable catalysts.

Keywords: High-throughput experimentation, automatic feature engineering, dry reforming of methane, multi-element catalyst design, carbon deposition

Preface

The present thesis is submitted for the Degree of Doctor of Philosophy at Japan Advanced Institute of Science and Technology. The thesis is consolidation of results of the research work on the topic “High-throughput experimentation and automatic feature engineering for catalyst discovery in dry reforming of methane” under the supervision of Prof. Toshiaki Taniike during October 2022–September 2025 at Graduate School of Advanced Science and Technology, Japan Advanced Institute of Science and Technology.

Chapter 1 provides a general introduction and outlines the purpose of this study. **Chapter 2** details the construction of a large-scale, unbiased dataset generated via HTE, providing a foundation for machine learning-driven catalyst discovery. **Chapter 3** builds upon the unbiased dataset established in Chapter 2 as a training foundation and introduces an active learning framework that integrates HTE and AFE. This framework accelerates the identification of high-performance catalysts and enables systematic exploration of unknown material spaces, thereby overcoming conventional bottlenecks in catalyst discovery. **Chapter 4** systematically investigates carbon deposition in low-temperature DRM. TG-DTA analysis of high-performance catalysts reveals key relationships among catalytic activity, carbon formation behavior, and composition, providing valuable guidance for the design of carbon-resistant multi-element catalysts. **Chapter 5** presents the overall conclusions and key findings of this thesis.

DU Wentao

Graduate School of Advanced Science and Technology

Japan Advanced Institute of Science and Technology

September 2025

Acknowledgements

First and foremost, I would like to express my sincere and heartfelt gratitude to my advisor, Professor Toshiaki Taniike of Graduate School of Advanced Science and Technology at Japan Advanced Institute of Science and Technology. His exceptional mentorship, insightful guidance, and continuous support have been the cornerstone of my doctoral journey. Professor Taniike's scientific rigor, patience, and encouragement have profoundly shaped my approach to research and personal development, for which I am deeply indebted.

I would also like to thank Dr. Patchanee Chammingkwan and Assistant Professor Toru Wada for their valuable feedback and kind support, as well as all members of the Taniike Laboratory for fostering an engaging and collaborative research environment.

My sincere appreciation goes to my second supervisor, Professor Masayuki Yamaguchi, for his consistent support and thoughtful advice. I am also grateful to Professor Yoshifumi Oshima, my minor research supervisor, for his guidance and contributions to my sub-theme research.

I gratefully acknowledge the financial support from the JST Mirai Program (Grant Number JPMJMI22G4) and the China Scholarship Council (CSC) (No. 202208050010), which made this work possible.

Finally, I would like to thank my parents, friends, and especially my wife, Dr. Liu Zhaohan, for their unwavering love, encouragement, and support throughout this journey.

Table of Contents

Chapter 1 General introduction

1.1. Role and significance of catalysts

Catalysts—often referred to as the "matchmakers" of the chemical world—are substances that accelerate the rate of chemical reactions without undergoing permanent changes themselves [1]. Their fundamental role lies in lowering the activation energy required for a reaction by offering an alternative reaction pathway with a reduced energy barrier. This not only significantly enhances reaction rates but also improves selectivity and efficiency, making catalysts indispensable in both fundamental chemical research and large-scale industrial applications [2].

Although catalytic phenomena have been utilized since ancient times, as seen in early practices such as fermentation and soap making, the scientific concept of catalysis was not formally articulated until the late 18th century [3]. In 1794, British chemist Elizabeth Fulhame systematically proposed the idea of catalysis while investigating redox reactions, emphasizing the ability of certain substances to promote chemical transformations without being consumed in the process. This early conceptual framework laid the foundation for the development of modern catalysis. Throughout the 19th and 20th centuries, catalysts were systematically incorporated into industrial processes, such as the contact process for sulfuric acid production and the Haber-Bosch process for ammonia synthesis, marking a pivotal turning point as catalysis emerged as a modern scientific discipline with transformative industrial impact [4].

Today, catalysts are ubiquitous across nearly every sector of the chemical industry, serving as the foundational enablers of chemical transformations. It is estimated that

approximately 85% of all industrial chemical processes rely on catalysis to achieve efficient and economically viable production [5]. For instance, in the petrochemical industry, catalysts are indispensable for processes such as catalytic cracking, hydrocracking, and isomerization. These catalytic steps facilitate the conversion of heavy hydrocarbons into high-value fuels, while simultaneously improving product performance and energy efficiency [6]. In the pharmaceutical sector, catalysts play a critical role in the selective synthesis of complex organic molecules, enabling the high-yield and high-specificity production of active pharmaceutical ingredients [7]. In materials science, catalysts are essential to polymerization reactions, the fabrication of functional materials, and the development of advanced coating technologies, thus driving innovation in high-performance materials [8]. Moreover, in response to the growing global emphasis on sustainability and environmental protection, catalysts have assumed a strategically important role in the implementation of green technologies [9,10]. Notable examples include three-way catalytic converters for controlling vehicular exhaust emissions, catalytic oxidation systems for the abatement of industrial pollutants, and advanced catalytic filtration techniques for wastewater treatment. In parallel, a new generation of catalytic technologies is emerging to address future sustainability challenges. These include CO_2 conversion and fixation for the production of fuels and high-value chemicals, photocatalytic and electrocatalytic water splitting for hydrogen generation, and photoelectrochemical systems that utilize solar energy to drive chemical transformations. Catalysts are also integral to advanced oxidation processes for

wastewater treatment, selective catalytic reduction of NO_x emissions, biomass valorization, and clean energy production (**Figure 1.1**). These applications underscore the pivotal role of catalysis in promoting cleaner, more sustainable industrial practices.

Therefore, catalysts enable us to achieve more with fewer resources, facilitating the precise construction of complex molecules while minimizing environmental impact. As global demands for sustainable and energy-efficient chemical processes continue to intensify, the rational design and optimization of catalysts remain central to scientific and technological innovation. The development of novel catalytic systems is imperative for enhancing reaction efficiency, reducing energy consumption, and mitigating ecological consequences.

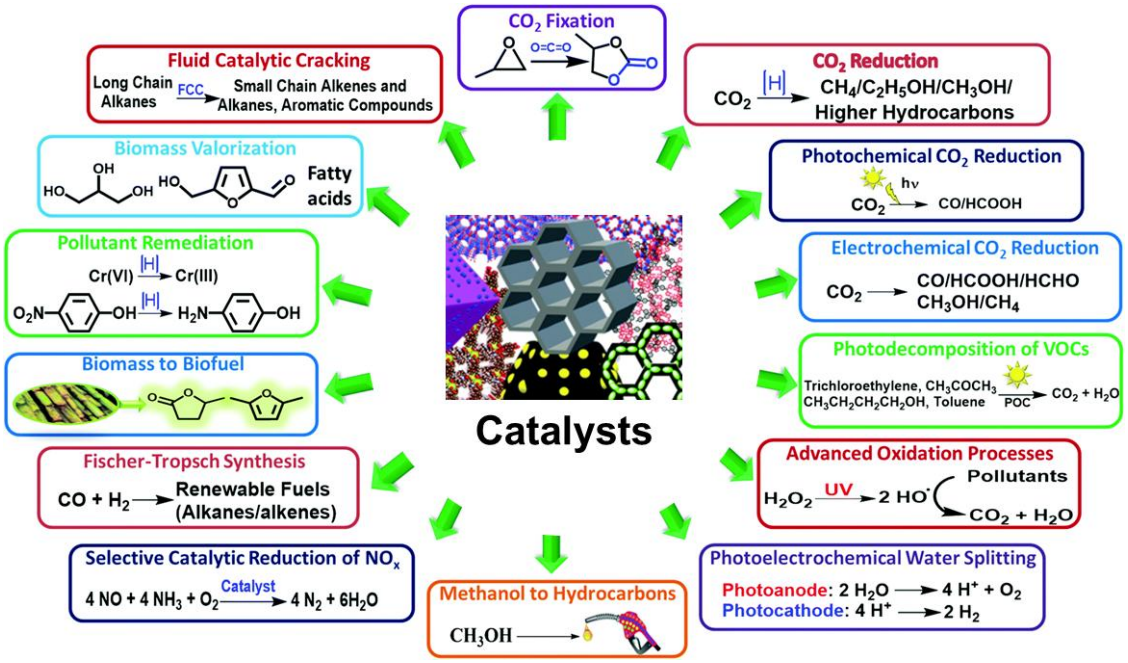

Figure 1.1. Schematic illustration of catalyst applications across various industrial reactions. Reproduced from Ref.[5].

1.2. Development of solid catalysts

Solid catalysts occupy an irreplaceable position in modern chemical industries, not only for their robustness and recyclability, but also for their exceptional adaptability, which enables the integration of diverse functional components to meet complex process demands. This multifunctionality, reflected in the incorporation of active sites, promoters, and hierarchical morphologies on a single solid surface, allows for simultaneous control of activity, selectivity, and stability. Nevertheless, the intricate interplay between chemical composition and surface architecture continues to impede the rational design of high-performance solid catalysts [11,12].

A major obstacle in catalyst design lies in understanding and harnessing the synergistic effects among multiple components [13]. Most catalysts are multicomponent systems comprising active metals, promoters, and supports, whose interactions can lead to emergent behaviors that are difficult to predict [14]. For instance, in multistep reactions, different components may catalyze distinct steps in a cooperative manner; promoters may stabilize active sites or modify their electronic properties; specific elemental combinations may induce the formation of unique surface structures or interfacial configurations. Although such synergistic interactions can dramatically enhance catalytic performance, their underlying mechanisms are highly complex and often influenced by a combination of structural, electronic, and kinetic factors [15]. Consequently, traditional theoretical frameworks and empirical intuition often fall short in accurately predicting

these effects, posing a substantial barrier to the rational design of next-generation catalysts.

Another critical challenge is the structural complexity of catalysts themselves. Catalytic activity and selectivity are governed by a myriad of structural parameters, including surface area, pore architecture, morphology, electronic properties, exposed crystal facets, and defect density [16]. Moreover, these characteristics are further shaped by preparation methods, calcination temperatures, support types, and pretreatment conditions [17]. Importantly, catalyst structures are not static during operation—they may undergo dynamic transformations due to sintering, coking, poisoning, or thermal cycling. Such structural evolution can lead to deactivation or altered catalytic behavior, thereby complicating the mechanistic understanding of the reaction and making long-term performance prediction particularly challenging [18].

Given the aforementioned difficulties and challenges, conventional catalyst development has long relied on an empirical trial-and-error approach [19]. Guided primarily by chemical intuition and accumulated experience, researchers typically synthesize and evaluate catalysts in a sequential manner to identify improved formulations. Representative examples include the Ziegler–Natta catalyst, which continues to be optimized through iterative trial-and-error methods despite its long history [20], and Alwin Mittasch's extensive screening of over 2,500 catalyst compositions to identify an effective system for ammonia synthesis [21]. While these cases demonstrate the critical role of serendipity in early materials discovery, they also underscore the

inherent limitations of the trial-and-error approach, particularly its substantial time requirements and intensive resource consumption. Therefore, there is an urgent need to shift away from the traditional paradigm.

1.3. Catalysts informatics

The evolution of materials science reflects the broader progression of scientific inquiry through four paradigms: empirical, theoretical, computational, and data-driven (**Figure 1.2**). The earliest stage was based on empirical observation, where knowledge was accumulated through experience and trial. The second paradigm introduced theoretical models grounded in physical laws such as thermodynamics and kinetics, providing mathematical formulations to explain material behavior. As systems became increasingly complex, analytical solutions often became intractable. The third paradigm, computational science, emerged with the rise of modern computing. This allowed for the simulation of complex materials and processes using methods such as density functional theory and molecular dynamics. These tools have provided atomistic-level insights into structure–property relationships but often require substantial computational resources and remain limited in scale and accuracy when applied to complex materials like solid catalysts. Recently, the growing volume of data generated from experiments and simulations has enabled a new scientific approach known as data-driven science [23]. This fourth paradigm integrates and extends the earlier ones by applying machine learning (ML) and artificial intelligence to extract patterns and correlations from high-dimensional

datasets. In materials science, this shift has given rise to the field of materials informatics, which is now being increasingly extended to catalysis research in the form of catalyst informatics [24]. It provides a data-centric alternative to traditional hypothesis-driven design by enabling systematic prediction and analysis of catalytic performance based on existing data.

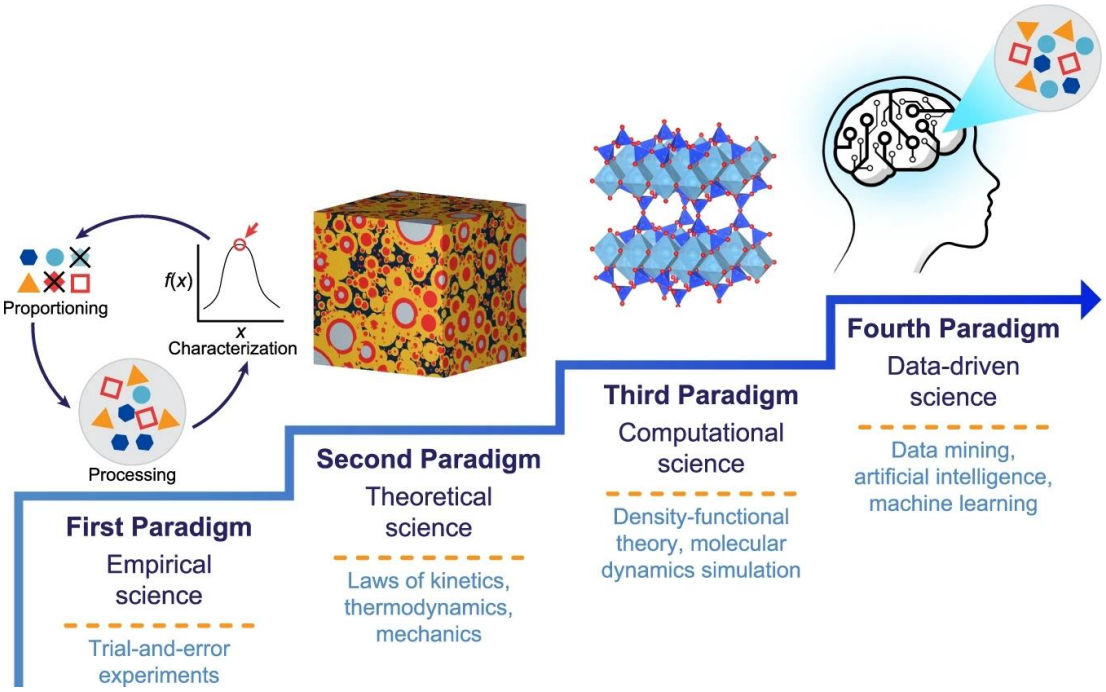

Figure 1.2. Four foundational paradigms of science: empirical investigation, theoretical analysis, computational modeling, and data-driven discovery. Reproduced from Ref.[22].

However, the practical application of ML in catalyst development remains hindered by two fundamental challenges, which are particularly pronounced in the case of solid catalysts [25]. First, the development of solid catalysts often involves multi-element compositions, hierarchical structures, and complex interactions between active phases

and supports. This inherent complexity results in an expansive design space, making it highly resource-intensive to generate sufficient high-quality experimental data. As a consequence, ML models trained on limited datasets frequently lack robustness and generalizability [26]. Second, the construction of universal and informative descriptors, which serve as quantitative inputs for ML algorithms, is especially difficult for solid catalysts. Unlike molecular systems with well-defined structures, solid materials frequently exhibit poorly resolved features such as surface heterogeneity, defect sites, or mixed-phase morphologies. Capturing these characteristics in a meaningful way often requires deep domain expertise and system-specific assumptions, which limit the scalability and objectivity of data-driven discovery efforts [27]. Recent advances in high-throughput experimentation (HTE) offer a compelling solution to the data scarcity problem. By enabling the rapid synthesis and evaluation of large libraries of catalysts under parallel conditions, HTE can generate extensive and consistent datasets that are well-suited for training robust ML models [28]. To further address the challenge of descriptor design, Taniike et al. has developed an automatic feature engineering (AFE) strategy that significantly reduces dependence on prior domain knowledge [27,29]. This approach systematically generates and selects informative features derived from fundamental physicochemical features. Consequently, the AFE method improves model interpretability and facilitates the rapid construction of predictive frameworks for catalyst discovery and optimization.

1.4. High-throughput experimentation

In the development of catalytic materials and processes, it is often essential to evaluate a large number of solid inorganic or soluble organometallic formulations using one or more laboratory-scale reactor systems [30]. As early as the 1980s, such efforts relied on conventional bench-scale reactor setups designed to assess single or a limited number of catalyst candidates under a predefined set of reaction conditions (Schlatter, 1987; Richardson, 1989) [31]. However, these traditional approaches were inherently time-consuming and inefficient, posing a significant bottleneck in catalyst discovery and optimization. Over the past decade, the field has witnessed a paradigm shift driven by the development of HTE technologies, which integrate catalysts performance evaluation into a unified, automated workflow [32,33]. These systems enable the rapid generation of large volumes of high-quality experimental data, thus accelerating the screening and optimization of catalyst formulations.

To meet the increasing demand for speed, flexibility, and scalability in catalyst testing, Taniike et al. developed a simplified yet robust high-throughput screening system (HTS), as shown in **Figure 1.3**. This custom-designed platform offers several distinct advantages: (i) it integrates parallelization with automated high-speed data acquisition, enabling truly high-throughput experimentation; (ii) it is adaptable to a variety of gas-phase catalytic reactions, such as oxidative coupling of methane (OCM), dry reforming of methane (DRM), and three-way catalysis (TWC) [35]; (iii) the catalyst loading and unloading processes are streamlined; (iv) it is equipped with a reliable, easy-to-operate analytical

module for precise performance assessment; (v) and it supports unattended operation with built-in safety protocols, ensuring both efficiency and operational security

This HTS system comprises a gas mixing unit, a flow distributor, 20 individual quartz reaction tubes, an autosampler, and a quadrupole mass spectrometer (QMS). The gas mixing unit (MU-3504, HORIBA STEC) delivers precise mixtures of gas by adjusting the flow rates of individual components. The mixed gases are evenly distributed through a flow manifold into 20 quartz tubes, each with an inlet and outlet inner diameter of 4 mm and 2 mm, respectively. The homogeneously ground catalyst powder is fixed at the center of each tube using quartz wool. The reactor tubes are symmetrically arranged within a three-zone hollow furnace, where temperature zones T_1 and T_3 serve as thermal buffers to stabilize the central zone (T_2), where the catalyst resides. The outlet stream from each reactor is continuously analyzed by the QMS (Transpector CPM, INFICON), which converts the gas-phase mass signal into corresponding partial pressure data, allowing for real-time and precise quantification of reaction products. Altogether, this HTS platform enables rapid, reliable, and parallelized evaluation of catalyst libraries under controlled conditions, significantly enhancing the efficiency and reproducibility of catalytic screening efforts.

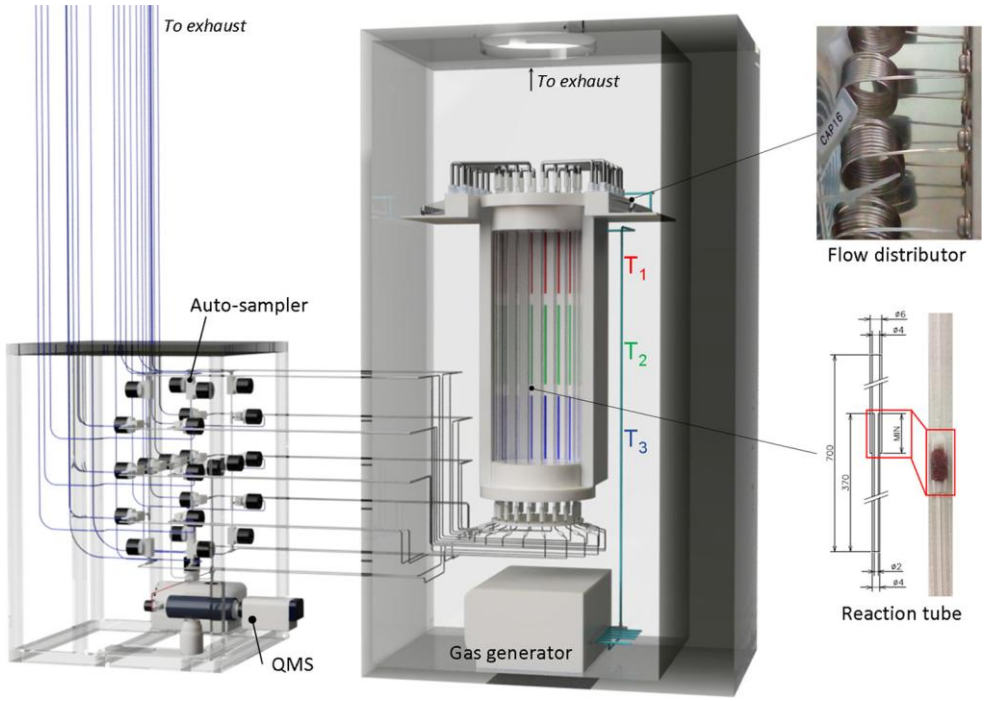

Figure 1.3. Illustration of the HTS system used for catalyst performance evaluation. Reproduced from Ref.[34].

1.5. Automatic feature engineering

AFE is an emerging and powerful strategy in data-driven catalysis research, particularly suited for exploring complex, high-dimensional material spaces with limited prior knowledge [36]. Unlike traditional approaches that rely heavily on descriptors manually crafted based on domain-specific intuition, AFE enables the automated generation of descriptors directly from general physicochemical properties, thereby realizing the discovery of novel catalysts under minimal human bias or assumption. In some previous studies, AFE has yielded reliable predictive models across diverse catalytic systems, including OCM [29], ethanol-to-butadiene conversion (ETB), and TWC [27].

The typical AFE workflow involves four core steps (**Figure 1.4**). First, a broad range of elemental descriptors—such as electronegativity, atomic radius, and bond energy—are collected from comprehensive databases like XenonPy [37]. These descriptors are then assigned to multi-element materials through a series of commutative operations. In the next step, nonlinear mathematical functions are applied to synthesize higher-order features. Finally, supervised machine learning algorithms are employed to identify the most relevant feature combinations for predictive modeling. To further enhance robustness and generalizability, a genetic algorithm is used during feature selection to optimize feature subsets by minimizing cross-validation errors [38].

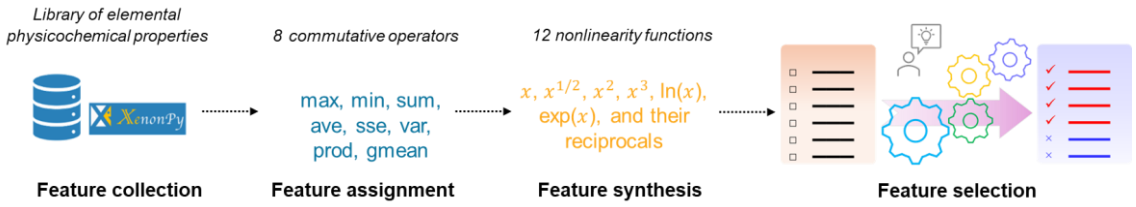

Figure 1.4. Schematic of the AFE workflow. Reproduced from Ref.[27].

Building on the aforementioned successes, in this study, AFE serves as a central component of the catalyst discovery framework. By combining AFE with HTE in an active learning loop (**Figure 1.5**), it enables efficient model training and iterative, autonomous catalyst discovery [27]. Leveraging farthest point sampling (FPS) within the descriptor space defined by AFE, the system strategically selected compositionally diverse candidates that were maximally dissimilar from those in the existing training set [39]. This approach actively expanded the design space beyond local regions of

exploration. Iterative model retraining using newly acquired experimental data progressively refined the system's understanding of catalytic behavior, thereby accelerating the identification of high-performance catalysts.

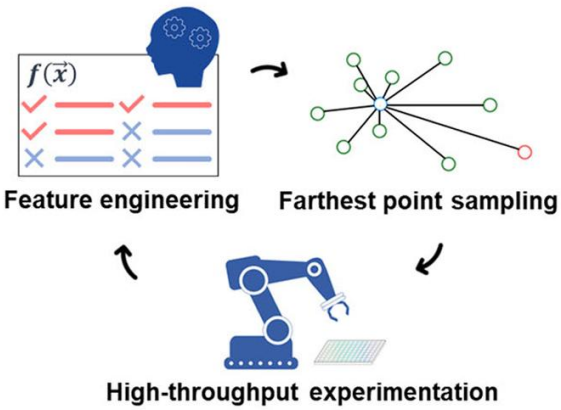

Figure 1.5. Schematic of the active learning loop. Reproduced from Ref.[27].

1.6. Dry reforming of methane (DRM)

With the world's energy demand continuing to rise and fossil fuel reserves being finite, the need for alternative and sustainable energy sources has become urgent rather than optional. In this context, DRM has attracted increasing attention over the past few decades as a promising route to simultaneously address energy production and greenhouse gas mitigation [40]. DRM is a highly endothermic catalytic reaction, typically conducted at temperatures between 700 and 800 °C, in which methane (CH_4) reacts with carbon dioxide (CO_2) to produce syngas, a mixture of carbon monoxide (CO) and hydrogen (H_2) [41]. The reaction can be represented as Eq.1.1:

$$CH_4 + CO_2 \rightarrow 2CO + 2H_2,\ \triangle H_{298}^0 = 248\ KJ \cdot mol^{-1} \quad (1.1).$$

This process not only produces syngas suitable for downstream applications such as Fischer-Tropsch synthesis and oxygenate production (e.g., acetic acid, dimethyl ether), but also offers several environmental and practical advantages [42]. Firstly, both CH_4 and CO_2 are the two major greenhouse gases; their conversion into value-added chemicals contributes to climate change mitigation. Secondly, CH_4 and CO_2 are major components in biomass pyrolysis gases and biogas from anaerobic digestion. Thus, DRM provides a means to valorize these carbon-rich streams, making renewable carbon cycles more economically and environmentally viable [43].

Compared to steam reforming of methane (SRM, Eq.1.2), which is also an endothermic process, DRM requires higher energy input due to its stronger thermodynamic demands. As a result, the sustainable implementation of DRM will likely depend on the integration of renewable energy sources to supply the required heat input.

$$CH_4 + H_2O \rightarrow CO + 3H_2,\ \triangle H_{298}^0 = 206\ KJ \cdot mol^{-1} \quad (1.2).$$

In addition to the main reforming reaction, the reverse water-gas shift (RWGS, Eq.1.3) reaction also occurs under DRM conditions. Although only mildly endothermic, this reaction plays a crucial role in determining the overall product distribution. The consumption of hydrogen during the RWGS reaction lowers the H_2/CO ratio in the resulting syngas to below unity, which is generally undesirable for downstream processes such as Fischer-Tropsch synthesis and methanol production. These applications typically require hydrogen-rich syngas, and a substoichiometric H_2/CO ratio can hinder carbon

chain growth, reduce product yields, and necessitate additional hydrogen supplementation, thereby increasing process complexity and cost. In addition, the water formed as a byproduct can further react with methane through the steam reforming pathway.

$$CO_2 + H_2 \rightarrow CO + H_2O,\ \triangle H_{298}^0 = 41\ KJ \cdot mol^{-1} \quad (1.3).$$

Apart from RWGS, carbon deposition represents one of the most critical challenges in DRM. Coke accumulation on the catalyst surface is widely recognized as one of the main causes of catalyst deactivation, significantly limiting the long-term stability and industrial viability of DRM processes [44]. Carbon formation during DRM occurs mainly through two competing side reactions: CH_4 decomposition (Eq.1.4) and the Boudouard reaction (Eq.1.5).

$$CH_4 \rightarrow C + 2H_2,\ \triangle H_{298}^0 = 75\ KJ \cdot mol^{-1} \quad (1.4).$$

$$2CO \rightarrow C + CO_2,\ \triangle H_{298}^0 = -172\ KJ \cdot mol^{-1} \quad (1.5).$$

$$CO + H_2 \rightarrow C + H_2O,\ \triangle H_{298}^0 = -131\ KJ \cdot mol^{-1} \quad (1.6).$$

The Boudouard reaction is exothermic and tends to favor carbon formation at lower temperatures. However, it has been reported that at temperatures above approximately 973 K, this reaction is thermodynamically shifted toward the formation of carbon monoxide, thereby suppressing carbon deposition. In contrast, CH_4 decomposition is an endothermic reaction and is thermodynamically favored at high temperatures, particularly above 830 K. Hence, this is a more dominant carbon-forming route under typical DRM conditions [45]. Moreover, the reverse carbon gasification reaction (Eq.1.6), may also

contribute to carbon formation; however, its influence is generally considered less significant compared to the CH_4 decomposition and Boudouard reaction.

1.6.1. Reaction mechanism

The reaction mechanism of DRM is inherently complex, involving multiple surface-mediated steps and parallel side reactions that occur simultaneously on the catalyst surface. A schematic overview of these processes is illustrated in **Figure 1.6**. It is widely accepted that the DRM reaction proceeds through the dissociative adsorption of both CH_4 and CO_2 on different active sites of the catalyst. CH_4 activation primarily occurs on metallic sites, where CH_4 undergoes stepwise dissociation into CH_x intermediates (CH_3*, CH_2*, CH*, and C*) and hydrogen atoms. The dissociated hydrogen migrates across the surface or the metal–support interface, eventually recombining to form molecular H_2. The extent of CH_4 dissociation and the fate of CH_x species are highly surface-dependent and play a pivotal role in determining the selectivity and coke formation tendency of the catalyst.

Meanwhile, CO_2 is adsorbed and activated either on the metal surface or, more commonly, on the metal-support interface. This activation may occur via intermediate carbonate (CO_3^{2-}) or bicarbonate (HCO_3^-) species. The surface oxygen generated through CO_2 dissociation can react with hydrogen to form OH groups, which in turn participate in RWGS reaction. Alternatively, these OH groups or directly dissociated O* species can

oxidize CH_x intermediates, leading to the formation of CH_xO, which further decompose into CO and H_2 [47].

Indeed, the availability and mobility of surface oxygen are crucial in suppressing the accumulation and oligomerization of CH_x fragments. When the oxidation of CH_x is delayed or insufficient, these intermediates may undergo polymerization, leading to coke formation. If carbon accumulates to the extent of encapsulating active metal sites, it severely impairs catalytic activity. However, if the rate of carbon formation is balanced by the rate of carbon diffusion or gasification, or if active sites remain exposed above carbon layers, catalyst deactivation may be minimized.

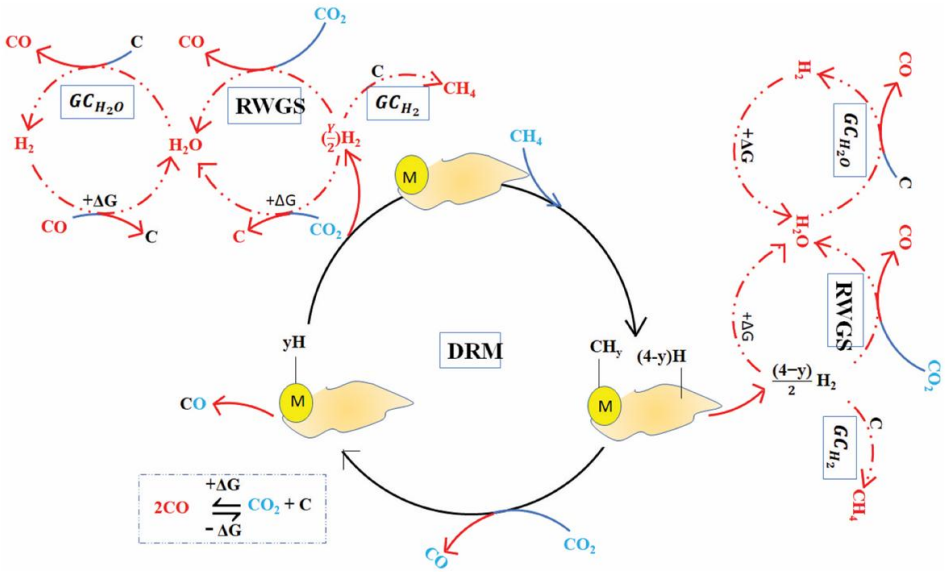

Figure 1.6. Schematic illustration of the reaction mechanism of the DRM. Reproduced from Ref. [46].

1.6.2. Catalysts for DRM

The development of highly active, stable, and economically viable catalysts is essential for the practical implementation and industrialization of the DRM process. A typical DRM catalyst consists of an active metal component, a support, and often one or more promoters [48]. In designing an effective catalyst, multiple factors must be considered, including the choice of active phase, the structural and physicochemical properties of the support, the type and function of promoters.

1.6.2.1. Active metals

Both noble and non-noble metals have been extensively studied as active phases for DRM. Noble metals such as Rh, Ru, Pd, Pt, and Ir exhibit excellent catalytic activity and strong resistance to carbon deposition [49]. However, their high cost and limited availability constrain their large-scale industrial application. Non-noble metals, particularly Ni and Co, are considered more economically feasible alternatives. Among them, Ni is the most widely used active metal due to its favorable balance between catalytic activity and cost, and is the industry standard for commercial steam reforming processes. Nevertheless, Ni- and Co-based catalysts are prone to deactivation through sintering and coke formation under high-temperature DRM conditions [50]. To address these limitations, noble metals are sometimes employed as promoters in Ni-based formulations to enhance performance.

1.6.2.2. Supports

Catalyst supports play a dual role in DRM catalysis. Traditionally, they provide high surface area for dispersing active metal species. However, beyond this physical function, the support can actively influence catalytic behavior through properties such as basicity, redox capability, and oxygen storage capacity. These attributes help regulate the adsorption and activation of CO_2 and play an important role in mitigating carbon formation [51].

γ-Al_2O_3 is the most frequently employed support, followed by ZrO_2, CeO_2, MgO, TiO_2, and SiO_2. While individual binary metal oxides are commonly used, mixed oxides have also shown great promise as a support. For example, Ni/ZrO_2–MgO catalysts with varying MgO contents revealed that 0.4 wt% MgO led to optimal CH_4 conversion and sustained catalytic activity, attributed to stronger metal–support interactions and improved resistance to deactivation [52]. Similarly, Ni catalysts supported on $Ce_xZr_{1-x}O_2$ exhibited enhanced DRM activity, with the optimal performance observed at a Ce:Zr molar ratio of 1:1 [53].

1.6.2.3. Promoters

Promoters are often introduced to improve catalyst performance and stability. They can be broadly categorized into textural and chemical promoters. Textural promoters improve the structural integrity of the catalyst by enhancing thermal stability and inhibiting sintering. Chemical promoters, on the other hand, modulate electronic properties such as basicity and redox behavior, thereby creating additional active sites or facilitating the oxidation of carbonaceous species [54].

Among the most studied promoters, MgO, paired with the Al_2O_3 support, is particularly effective in forming solid solutions such as $MgAl_2O_4$, which prevents the formation of inactive $NiAl_2O_4$, improves Ni dispersion, and enhances thermal stability. CeO_2, as redox-active rare earth oxide, facilitates oxygen mobility and contributes to the continuous removal of carbon deposits through lattice oxygen [55]. ZrO_2, whether used as a support or promoter, enhances CO_2 dissociation and inhibits the formation of inactive phases like $NiAl_2O_4$. Alkaline earth metals (e.g., CaO, BaO) improve surface basicity and thereby CO_2 adsorption when moderately loaded, though excessive amounts may lead to particle agglomeration and activity loss [56]. Alkali metals, especially K, assist in coke suppression by enhancing carbon gasification, although they can reduce catalytic activity depending on loading and catalyst structure. Yttrium-based promoters improve metal dispersion and resistance to sintering, while transition metals such as Mo and W can regulate carbon solubility and electronic properties of the active phase [57]. These studies collectively reveal several commonly observed promotion mechanisms:

(i) improving the dispersion of the main active element,

(ii) preventing the formation of catalytically inactive phases such as $NiAl_2O_4$,

(iii) enhancing CO_2 adsorption through increased surface basicity,

(iv) suppressing coke deposition.

Overall, the selection and optimization of promoter type, amount, and dispersion are therefore critical for maximizing catalyst performance in DRM applications.

1.7. Objective

The development of solid catalysts is inherently challenging due to their multicomponent nature and the vast combinatorial space of possible compositions. Traditionally, catalyst discovery has relied on empirical trial-and-error methods, which are often time-consuming and resource-intensive. In recent years, data-driven approaches have demonstrated considerable potential to accelerate catalyst development. However, their practical application remains limited by the scarcity of high-quality experimental data and the difficulty of constructing effective, generalizable descriptors without deep domain knowledge.

This thesis addresses these challenges by establishing an adaptive catalyst design framework that integrates HTE, AFE, and ML. DRM is chosen as the target reaction for its relevance to greenhouse gas conversion and the challenge it poses in achieving active, stable, and carbon-resistant catalysts, especially under low temperatures. Hence, the main objective is to develop high-performance multi-element DRM catalysts without prior system knowledge, through iterative, data-efficient exploration of the catalyst space.

In Chapter 2, a large-scale, unbiased catalyst dataset was constructed through HTE by randomly combining 17 elements on γ-Al_2O_3. A total of 256 catalysts were synthesized and evaluated at 500 °C. This initial dataset served as a foundation for extracting early design heuristics and enabled the development of a predictive ML framework.

Chapter 3 introduces an adaptive learning loop combining AFE, FPS, and HTE to address both descriptor design and data acquisition challenges. Through iterative model

retraining and continuous experimental validation, the elemental design space was ultimately expanded to 45 elements, along with steady improvements in model accuracy.

In Chapter 4, the carbon deposition behavior of high-performance multi-element catalysts under low-temperature DRM conditions was systematically examined. The results revealed compositional trends linked to high activity and low carbon deposition, providing guidance for designing stable low-temperature DRM catalysts.

In conclusion, I believe this dissertation achieves two closely related objectives. First, it presents a robust and data-driven strategy for the discovery of high-performance, carbon-resistant multi-element catalysts for low-temperature DRM. Second, it offers practical and generalizable guidelines for the rational design of catalysts in other complex catalytic systems, particularly those involving high-dimensional compositional spaces.

Reference

[1] W.N.R.W. Isahak, A. Al-Amiery, Catalysts driving efficiency and innovation in thermal reactions: A comprehensive review, Green Techn. Sustain. 2 (2024) 100078. https://doi.org/10.1016/j.grets.2024.100078.

[2] C. Song, Global challenges and strategies for control, conversion and utilization of CO_2 for sustainable development involving energy, catalysis, adsorption and chemical processing, Catal. today 115 (2006) 2–32. https://doi.org/10.1016/j.cattod.2006.02.029.

[3] J. Moulijn, P. Van Leeuwen, R. Van Santen, History of catalysis, Elsevier, 1993, pp. 3–21. https://doi.org/10.1016/S0167-2991(08)63805-7.

[4] H. Liu, Ammonia synthesis catalyst 100 years: Practice, enlightenment and challenge, Chin. J. Catal. 35 (2014) 1619–1640. https://doi.org/10.1016/S1872-2067(14)60118-2.

[5] R. Chatterjee, P. Bhanja, A. Bhaumik, The design and synthesis of heterogeneous catalysts for environmental applications, Dalton Trans. 50 (2021) 4765–4771. https://doi.org/10.1039/D1DT00544H.

[6] J. Wei, R. Yao, Y. Han, Q. Ge, J. Sun, Towards the development of the emerging process of CO_2 heterogenous hydrogenation into high-value unsaturated heavy hydrocarbons, Chem. Soc. Rev. 50 (2021) 10764–10805. https://doi.org/10.1039/D1CS00260K.

[7] A.I. Osman, A. Ayati, P. Krivoshapkin, B. Tanhaei, M. Farghali, P.-S. Yap, A. Abdelhaleem, Coordination-driven innovations in low-energy catalytic processes: Advancing sustainability in chemical production, Coordin. Chem. Rev. 514 (2024) 215900. https://doi.org/10.1016/j.ccr.2024.215900.

[8] W.F. Maier, K. Stoewe, S. Sieg, Combinatorial and high-throughput materials science, Angew. Chem. Int. Ed. 46 (2007) 6016–6067. https://doi.org/10.1002/anie.200603675.

[9] U. Jafar, U. Nuhu, W.U. Khan, M.M. Hossain, A review on green ammonia as a potential CO_2 free fuel, Int. J. Hydrogen Energ. 71 (2024) 857–876. https://doi.org/10.1016/j.ijhydene.2024.05.128.

[10] X. Li, W. Chen, L. Ma, H. Wang, J. Fan, Industrial wastewater advanced treatment via catalytic ozonation with an Fe-based catalyst, Chemosphere 195 (2018) 336–343. https://doi.org/10.1016/j.chemosphere.2017.12.080.

[11] S. Ahn, M. Hong, M. Sundararajan, D.H. Ess, M.-H. Baik, Design and optimization of catalysts based on mechanistic insights derived from quantum chemical reaction modeling, Chem. Rev. 119 (2019) 6509–6560. https://doi.org/10.1021/acs.chemrev.9b00073.

[12] Z. Huang, Z. Chen, J. Cheng, J. Zhang, S. Wang, T. Chen, X. Zhang, H. Pang, Recent progress in high-throughput on-chip synthesis, screening, and data-driven optimization: toward an electrocatalyst chip for catalysis universe exploration, Adv. Funct. Mater. 35 (2025) 2416117. https://doi.org/10.1002/adfm.202416117.

[13] J. Shi, On the synergetic catalytic effect in heterogeneous nanocomposite catalysts, Chem. Rev. 113 (2013) 2139–2181. https://doi.org/10.1021/cr3002752.

[14] M. Stamatakis, Kinetic modelling of heterogeneous catalytic systems, J. Phys. Condens. Mat. 27 (2014) 013001. https://doi.org/10.1088/0953-8984/27/1/013001.

[15] A. Wang, X.Y. Liu, C.-Y. Mou, T. Zhang, Understanding the synergistic effects of gold bimetallic catalysts, J. Catal. 308 (2013) 258–271.

https://doi.org/10.1016/j.jcat.2013.08.023.
[16] M.-H. Sun, S.-Z. Huang, L.-H. Chen, Y. Li, X.-Y. Yang, Z.-Y. Yuan, B.-L. Su, Applications of hierarchically structured porous materials from energy storage and conversion, catalysis, photocatalysis, adsorption, separation, and sensing to biomedicine, Chem. Soc. Rev. 45 (2016) 3479–3563. https://doi.org/10.1039/C6CS00135A.
[17] F. Kleitz, W. Schmidt, F. Schüth, Evolution of mesoporous materials during the calcination process: structural and chemical behavior, Micropor. Mesopor. Mat. 44 (2001) 95–109. https://doi.org/10.1016/S1387-1811(01)00173-1.
[18] C. Spöri, J.T.H. Kwan, A. Bonakdarpour, D.P. Wilkinson, P. Strasser, The stability challenges of oxygen evolving catalysts: towards a common fundamental understanding and mitigation of catalyst degradation, Angew. Chem. Int. Ed. 56 (2017) 5994–6021. https://doi.org/10.1002/anie.201608601.
[19] E.S. Isbrandt, R.J. Sullivan, S.G. Newman, High throughput strategies for the discovery and optimization of catalytic reactions, Angew. Chem. Int. Ed. 58 (2019) 7180–7191. https://doi.org/10.1002/anie.201812534.
[20] V. Busico, R. Cipullo, A. Mingione, L. Rongo, Accelerating the research approach to Ziegler–Natta catalysts, Ind. Eng. Chem. Res. 55 (2016) 2686–2695. https://doi.org/10.1021/acs.iecr.6b00092.
[21] A. Trunschke, Prospects and challenges for autonomous catalyst discovery viewed from an experimental perspective, Catal. Sci. Technol. 12 (2022) 3650–3669. https://doi.org/10.1039/D2CY00275B.
[22] Z. Li, J. Yoon, R. Zhang, F. Rajabipour, W.V. Srubar III, I. Dabo, A. Radlińska, Machine learning in concrete science: applications, challenges, and best practices, Npj Comput. Mater. 8 (2022) 127. https://doi.org/10.1038/s41524-022-00810-x.
[23] F.J. Montáns, F. Chinesta, R. Gómez-Bombarelli, J.N. Kutz, Data-driven modeling and learning in science and engineering, C. R. Mec. 347 (2019) 845–855. https://doi.org/10.1016/j.crme.2019.11.009
[24] K. Takahashi, L. Takahashi, I. Miyazato, J. Fujima, Y. Tanaka, T. Uno, H. Satoh, K. Ohno, M. Nishida, K. Hirai, The rise of catalyst informatics: towards catalyst genomics, ChemCatChem 11 (2019) 1146–1152. https://doi.org/10.1002/cctc.201801956.
[25] Y. Guan, D. Chaffart, G. Liu, Z. Tan, D. Zhang, Y. Wang, J. Li, L. Ricardez-Sandoval, Machine learning in solid heterogeneous catalysis: Recent developments, challenges and perspectives, Chem. Eng. Sci. 248 (2022) 117224. https://doi.org/10.1016/j.ces.2021.117224.
[26] M. Erdem Günay, R. Yıldırım, Recent advances in knowledge discovery for heterogeneous catalysis using machine learning, Catal. Rev. 63 (2021) 120–164. https://doi.org/10.1080/01614940.2020.1770402.
[27] T. Taniike, A. Fujiwara, S. Nakanowatari, F. Garcia-Escobar, K. Takahashi, Automatic feature engineering for catalyst design using small data without prior knowledge of target catalysis, Commun. Chem. 7 (2024) 11. https://doi.org/10.1038/s42004-023-01086-y.
[28] R. Grainger, S. Whibley, A perspective on the analytical challenges encountered in high-throughput experimentation, Org. Process Res. Dev. 25 (2021) 354–364. https://doi.org/10.1021/acs.oprd.0c00463.
[29] A. Fujiwara, S. Nakanowatari, Y. Cho, T. Taniike, Acquiring and transferring comprehensive catalyst knowledge through integrated high-throughput experimentation and automatic feature engineering, Sci. Technol. Adv. Mater. (2025) 2454219.

https://doi.org/10.1080/14686996.2025.2454219.
[30] S. Mitchell, N.-L. Michels, J. Pérez-Ramírez, From powder to technical body: the undervalued science of catalyst scale up, Chem. Soc. Rev. 42 (2013) 6094–6112. https://doi.org/10.1039/C3CS60076A.
[31] J.E. Bauer, M.L. Occelli, P.M. Williams, P.C. McCaslin, Heterogeneous catalyst structure and function: Review and implications for the analysis of dissolved organic carbon and nitrogen in natural waters, Mar. Chem. 41 (1993) 75–89. https://doi.org/10.1016/0304-4203(93)90107-Y.
[32] A. Sundermann, O. Gerlach, High-throughput screening as a supplemental tool for the development of advanced emission control catalysts: methodological approaches and data processing, Catalysts 6 (2016) 23. https://doi.org/10.3390/catal6020023.
[33] C. Futter, L.T.A. Rupflin, N. Brem, R. Födisch, A. Haas, A.L. de Oliveira, M.L. Lejkowski, A. Müller, A. Sundermann, S. Titlbach, High throughput experimentation applied in the field of technical catalysis: past, present, future, in: Modern Applications of High Throughput R&D in Heterogeneous Catalysis, Bentham Science Publishers, 2014, pp. 3–88. https://doi.org/10.2174/97816080587231140101.
[34] T.N. Nguyen, S. Nakanowatari, T.P. Nhat Tran, A. Thakur, L. Takahashi, K. Takahashi, T. Taniike, Learning catalyst design based on bias-free data set for oxidative coupling of methane, ACS Catal. 11 (2021) 1797–1809. https://doi.org/10.1021/acscatal.0c04629.
[35] S.D. Le, N.N.T. Ton, K. Seenivasan, P. Chammingkwan, K. Higashimine, S. Praserthdam, T. Taniike, High-throughput screening of multimetallic catalysts for three-way catalysis, Sci. Technol. Adv. Mater. 4 (2024) 2284130. https://doi.org/10.1080/27660400.2023.2284130.
[36] H. Li, Y. Jiao, K. Davey, S.Z. Qiao, Data-driven machine learning for understanding surface structures of heterogeneous catalysts, Angew. Chem. Int. Ed. 62 (2023) e202216383. https://doi.org/10.1002/anie.202216383.
[37] Y. Yu, X. Wu, Q. Qian, Better utilization of materials' compositions for predicting their properties: Material composition visualization network, Eng. Appl. Artif. Intell. 117 (2023) 105539. https://doi.org/10.1016/j.engappai.2022.105539.
[38] Y. Minowa, Verification for generalizability and accuracy of a thinning-trees selection model with the ensemble learning algorithm and the cross-validation method, J. For. Res. 13 (2008) 275–285. https://doi.org/10.1007/s10310-008-0084-6.
[39] L.L. Schaaf, E. Fako, S. De, A. Schäfer, G. Csányi, Accurate energy barriers for catalytic reaction pathways: an automatic training protocol for machine learning force fields, Npj Comput. Mater. 9 (2023) 180. https://doi.org/10.1038/s41524-023-01124-2.
[40] A.M. Alhassan, I. Hussain, O.A. Taialla, M.M. Awad, A. Tanimu, K. Alhooshani, S.A. Ganiyu, Advances in catalytic dry reforming of methane (DRM): Emerging trends, current challenges, and future perspectives, J. Cleaner Prod. 423 (2023) 138638. https://doi.org/10.1016/j.jclepro.2023.138638.
[41] A.G. Hussien, K. Polychronopoulou, A review on the different aspects and challenges of the dry reforming of methane (DRM) reaction, Nanomaterials 12 (2022) 3400. https://doi.org/10.3390/nano12193400.
[42] H.J. Venvik, J. Yang, Catalysis in microstructured reactors: Short review on small-scale syngas production and further conversion into methanol, DME and Fischer-Tropsch products, Catal. Today 285 (2017) 135–146. https://doi.org/10.1016/j.cattod.2017.02.014.
[43] A. Das, S.D. Peu, A comprehensive review on recent advancements in

thermochemical processes for clean hydrogen production to decarbonize the energy sector, Sustainability 14 (2022) 11206. https://doi.org/10.3390/su141811206.
[44] A. Tanimu, B.O. Yusuf, S. Lateef, G. Tanimu, A.M. Alhassan, M.O. Azeez, K. Alhooshani, S.A. Ganiyu, Dry reforming of methane: advances in coke mitigation strategies via Siliceous catalyst formulations, J. Environ. Chem. Eng. (2024) 113873. https://doi.org/10.1016/j.jece.2024.113873.
[45] A. Mianowski, M. Szul, T. Radko, A. Sobolewski, T. Iluk, Literature review on thermodynamic and kinetic limitations of thermal decomposition of methane, Energies 17 (2024) 5007. https://doi.org/10.3390/en17195007.
[46] A.S. Al-Fatesh, N. Patel, A.H. Fakeeha, M.F. Alotibi, S.B. Alreshaidan, R. Kumar, Reforming of methane: effects of active metals, supports, and promoters, Catal. Rev. 66 (2024) 2209–2307. https://doi.org/10.1080/01614940.2023.2211447.
[47] R. Zhang, C. Wei, D. Li, Z. Jiang, B. Wang, L. Ling, M. Fan, The new role of surface adsorbed CH_s (x=1–3) intermediates as a co-adsorbed promoter in self-promoting syngas conversion to form CH_x intermediates and C_2 oxygenates on the Rh-doped Cu catalyst, J. Catal. 377 (2019) 1–12. https://doi.org/10.1016/j.jcat.2019.07.019.
[48] I.V. Yentekakis, P. Panagiotopoulou, G. Artemakis, A review of recent efforts to promote dry reforming of methane (DRM) to syngas production via bimetallic catalyst formulations, Appl. Catal. B-Environ. 296 (2021) 120210. https://doi.org/10.1016/j.apcatb.2021.120210.
[49] D. Pakhare, J. Spivey, A review of dry (CO_2) reforming of methane over noble metal catalysts, Chem. Soc. Rev. 43 (2014) 7813–7837. https://doi.org/10.1039/c3cs60395d.
[50] F. Sharifianjazi, A. Esmaeilkhanian, L. Bazli, S. Eskandarinezhad, S. Khaksar, P. Shafiee, M. Yusuf, B. Abdullah, P. Salahshour, F. Sadeghi, A review on recent advances in dry reforming of methane over Ni-and Co-based nanocatalysts, Int. J. Hydrogen Energ. 47 (2022) 42213–42233. https://doi.org/10.1016/j.ijhydene.2021.11.172.
[51] X. Zhao, S. Sun, Y. Wang, Y. Zhang, Y. Zhu, B. Zong, J. Hu, P. Williams, C. Wu, The role of reverse Boudouard reaction during integrated CO_2 capture and utilisation via dry reforming of methane, Chem. Eng. J. 491 (2024) 151668. https://doi.org/10.1016/j.cej.2024.151668.
[52] Y. Zhao, S. Liu, X. Feng, J. Wang, L. Chen, Y. Zhao, H. Wang, Q. Zhang, Highly porous Ni/MgO-ZrO_2 catalysts for dry reforming of methane and the effects of MgO addition on the mechanisms, Chem. Eng. J. 501 (2024) 157607. https://doi.org/10.1016/j.cej.2024.157607.
[53] X. Zhou, Y. Gao, J. Yang, W. Yi, Q. Pang, Z. Liu, B. Liu, M. Zhang, Unraveling the effects of Ce/Zr molar ratio in mesoporous $Ce_xZr_{1-x}O_2$ on the performance of dry reforming of methane over the supported Ni catalysts, Chem. Eng. Res. Des. 193 (2023) 626-640. https://doi.org/10.1016/j.cherd.2023.04.020.
[54] M. Li, Z. Sun, Y.H. Hu, Catalysts for CO_2 reforming of CH_4: A review, J. Mater. Chem. A 9 (2021) 12495–12520. https://doi.org/10.1039/D1TA00440A.
[55] P.K. Putanenko, N.V. Dorofeeva, T.S. Kharlamova, M.V. Grabchenko, S.A. Kulinich, O.V. Vodyankina, La_2O_3-CeO_2-Supported Bimetallic Cu-Ni DRM Catalysts, Materials 16 (2023) 7701. https://doi.org/10.3390/ma16247701.
[56] L. Wang, C. Qu, F. Meng, F. Yang, Q. Ye, Enhancement of carbon dioxide adsorption performance on mesoporous alumina modified with alkaline earth metals, Colloid. Surface. A 690 (2024) 133823. https://doi.org/10.1016/j.colsurfa.2024.133823.

[57] N. Czaplicka, A. Rogala, I. Wysocka, Metal (Mo, W, Ti) carbide catalysts: Synthesis and application as alternative catalysts for dry reforming of hydrocarbons—A review, Int. J. Mol. Sci. 22 (2021) 12337. https://doi.org/10.3390/ijms222212337.

Chapter 2 Unbiased dataset for methane dry reforming and catalyst design guidelines obtained by high-throughput experimentation and machine learning

Abstract

The conventional approach to solid catalyst design is predominantly empirical, relying on iterative trial-and-error experimentation informed by prior knowledge. Recently, the integration of high-throughput experimentation (HTE) and machine learning (ML) has emerged as a promising strategy for systematic catalyst design, eliminating the need for prior knowledge or assumptions about the target catalytic system. As an initial step, an unbiased HTE dataset was established for dry reforming of methane (DRM) at 500 °C, comprising 256 γ-Al_2O_3-supported multi-element catalysts synthesized via random combinations of 17 elements without prior assumptions. The resulting data and catalyst compositions were systematically analyzed to extract insights into catalyst design and reaction behavior. The results reveal that the presence of Ni or platinum group elements alone does not guarantee DRM activity; instead, careful combinations of elements are essential. Notably, the most active catalysts are Ni-based systems frequently incorporating Li, Al, and Nb—elements like Al and Nb being rarely acknowledged as promoters in existing literature. Experimental validation of the predictive ML models confirmed that the identified compositional patterns are transferable for designing other high-performance catalysts. Analysis of the top-performing Ni-based catalyst revealed the distinct roles of individual elements in enhancing activity and mitigating carbon deposition. In particular, the Al–Nb–Hf ternary combination proved effective in suppressing coke formation while boosting performance. Overall, the study underscores the effectiveness of unbiased exploration in generating foundational datasets for ML-driven discovery and deriving actionable catalyst design guidelines.

2.1. Introduction

A synergistic combination, a key factor in designing highly active and selective solid catalysts, is difficult to predict due to the complex interactions among multiple catalyst components and their intricate consequences [1–4]. As a result, typical catalyst development heavily relies on experimental trials and errors, iteratively preparing and evaluating catalysts based on hypotheses informed by intuition, prior knowledge, and characterizations [5–7]. This iterative process aims to enhance catalyst performance while continuously refining and generalizing design hypotheses. Numerous researchers are often involved, contributing to the discovery of better catalysts, new hypotheses, or trends. These discoveries, sometimes serendipitous, are then built upon by others [8–11]. Consequently, conventional catalyst development is a highly labor-intensive, ad hoc, and somewhat creative endeavor. The pathway of catalyst development traces a limited and biased route against the vast combinatorial and compositional space of catalysts [12–15]. This highlights the need for a paradigm shift in catalyst development methodologies.

With the rapid rise of catalyst informatics, data-driven approaches offer efficient tools for more systematic and rational catalyst exploration or design via statistical models that capture the intricate structure-performance relationships in solid catalysts [16–18]. However, the application of catalyst informatics to the vast combinatorial and compositional space is hindered by two main obstacles. The first obstacle is the lack of a proper dataset that serves as an empirical foundation for building models [19,20]. High-throughput experimentation (HTE), combined with strategic sampling, ensures the rapid

generation of sizable, process-consistent, and unbiased datasets, addressing the challenge of obtaining a substantial quantity of data within a short timeframe [2,3,21–23]. The second obstacle is the need for descriptors that capture the essence of catalysts, which are essential for building accurate and robust models [24–26]. This typically requires deep domain knowledge of target catalysis in the design process, which is challenging for insufficiently explored and/or complex combinations and compositions [27–29].

In a recent publication, Taniike et al. developed automatic feature engineering (AFE) to eliminate the reliance on specific knowledge or assumptions about the target catalysis when designing descriptors, leading to machine learning (ML) models that accurately describe complex and diverse catalyst designs [30]. It is believed that implementing HTE and AFE in active learning cycles would realize to explore the vast combinatorial and compositional space of solid catalysts, without necessitating any prior data and knowledge of the target system.

Dry reforming of methane (DRM) is an attractive process for converting two major greenhouse gases, methane and carbon dioxide, into syngas ($CH_4 + CO_2 \rightarrow 2CO + 2H_2$) [31,32]. Transition metal elements of groups 8 and 9, such as Ni, Co, Pt, Pd, Ru, Rh, and Ir, are often supported on thermally stable and high-surface area oxides (γ-Al_2O_3, ZrO_2, CeO_2, MgO, and SiO_2) [33–35]. Among these, Ni/γ-Al_2O_3 stands out as the preferred catalyst due to its commendable activity and cost-effectiveness [36,37].

The DRM process typically operates at high temperatures, usually between 700 and 800 °C, to activate the chemically inert CH_4 and CO_2 and to suppress carbon deposition

from the Boudouard reaction ($2CO \rightarrow C + CO_2$) [38–40]. Nevertheless, carbon deposition remains a serious issue. For instance, Wang et al. [41] observed 63 wt% carbon deposition on a 12 wt% Ni/Al_2O_3 catalyst after 2 hours of DRM reaction at 700 °C. Additionally, high temperatures can cause catalyst deactivation due to sintering and loss of H_2 through the reverse water-gas shift (RWGS), resulting in a lower H_2/CO ratio, which is detrimental for post-processes such as the Fischer-Tropsch process [42,43].

Implementing DRM at lower temperatures has the potential to minimize environmental impact and energy consumption [44]. However, it has been much less studied compared to high-temperature DRM due to challenges such as decreased yields and more severe carbon deposition (only 283 data points stored out of 5521 data points in the DRM literature data compiled by Şener et al. [45], **Figure 2.1a**). Despite the limited number of studies, the potential of multi-element catalysts has been reported. For example, He et al. [46] found that adding Ce to Ni/Al_2O_3 improved CH_4 conversion and catalyst stability at 550 °C by enhancing Ni dispersion and aiding the oxidation of carbon deposits. Song et al. [47] reported that Fe added to Ni/Al_2O_3 suppressed Ni oxidation and maintained improved conversion for 20 hours at 450 °C.

In general, the multi-element strategy has been widely studied across various temperatures, aimed at improving catalyst activity and longevity [48–50], where combinations of Ni with K, Ce, Ru, Co, or Pt are particularly popular (**Figure 2.1b**). These studies highlight several common promotion mechanisms, including: improving the dispersion of the main active element, facilitating the reduction of NiO, preventing

the formation of inactive phases (e.g., $NiAl_2O_4$), enhancing CO_2 adsorption, and suppressing coke deposition, several of which help maintain or increase active site availability during catalysis. Despite these well-known mechanisms, the scope of studied element combinations and compositions is extremely limited, with the number of combinations rarely exceeding 3 elements (**Figure 2.1c**). Additionally, multi-element catalysts specifically tailored for low-temperature DRM remain severely underexplored.

Recognizing these limitations, I sought to explore the vast combinatorial and compositional space of catalysts by selecting elements from the periodic table and depositing them onto γ-Al_2O_3 support, without relying on prior knowledge of the system. The focus is on discovering diverse, high-performing catalysts and establishing general design guidelines for low-temperature DRM. To achieve this, this chapter established a HTE protocol as a starting point to construct an initial dataset for this vast space. In detail, 256 catalysts were prepared with randomly determined combinations and compositions and evaluated their DRM performance at 500 °C. Statistical analyses and characterizations of the selected catalysts successfully derived heuristics on multi-element design for low-temperature DRM, including the identification of promising and previously underexplored elements such as Li, Al, Nb, and Hf. These elements were found to play critical roles in promoting activity and suppressing carbon deposition, demonstrating the effectiveness of unbiased exploration in uncovering novel catalyst design strategies.

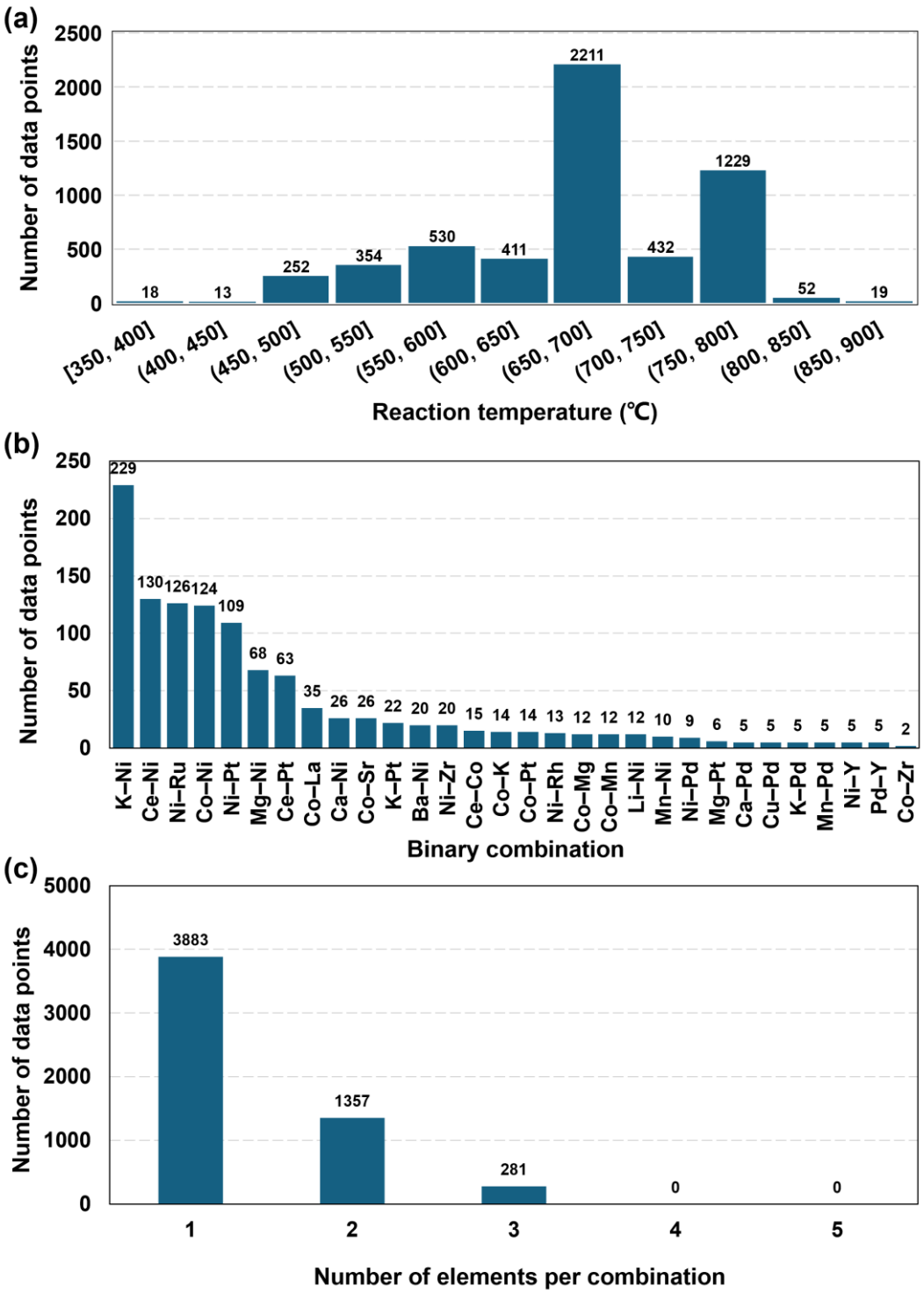

Figure 2.1. Statistics of literature DRM data: (a) Employed reaction temperature, (b) popular binary combinations of elements, and (c) number of elements per combination. The dataset curated by Şener [45] was analyzed.

2.2. Methods

2.2.1. Elemental library

For the exploration without assuming prior knowledge, I targeted the elements, including all typical metals, transition metals, *p*-block metals, and lanthanoids up to the 6th period of the periodic table, and assumed that any combination and composition of these elements could be supported on γ-Al_2O_3 as a catalyst. However, creating training data using all these elements is not practical due to reagent costs, safety concerns, and the physical similarities between elements. Therefore, representative elements were extracted according to the procedure illustrated in **Figure 2.2**. Specifically, the elements were represented using a comprehensive set of physicochemical properties obtained from the XenonPy library [51]. This library provides numerous features for each element, from H to Pu (a total of 94 elements), spanning a range of electronic, structural, and chemical attributes. For all target elements, 58 properties were utilized to ensure a thorough representation of their physicochemical characteristics, enabling unbiased and detailed analysis of potential catalytic combinations. The feature data were standardized and transformed into six principal components through principal component analysis (PCA) to eliminate potential collinearity among the 58 features and reduce the dimensionality of the dataset. These six components (PC1 to PC6) captured 85% of the original variance, as shown in the cumulative explained variance plot in **Figure 2.2**, effectively preserving the essential characteristics of the data. Then, farthest point sampling (FPS) was applied in the reduced-dimensional space obtained from PCA to systematically select

representative elements. The FPS process began by choosing an initial element from the dataset, typically the one farthest from the center of the feature space to maximize initial diversity. Subsequently, additional elements were iteratively selected based on their maximum distance from the elements already chosen, ensuring that each newly selected element was as physically dissimilar as possible from the existing set. To further refine the selection, additional rules were incorporated. Potentially risky elements, such as Hg, Cr, Pb, Tl, Be, and Os [52,53], were excluded due to safety and environmental concerns. Additionally, the number of elements from the same group in the periodic table was limited to less than three to maintain chemical diversity. This approach ensured that the final set of elements represented a broad range of physicochemical properties while minimizing sampling bias and redundancy. Through this workflow, 17 elements, Li, Al, Ca, V, Ni, Nb, Rh, Ag, Sn, Cs, Ba, Ce, Sm, Hf, Ir, Au, and Bi, were selected for the synthesis of DRM catalysts, which represents the vast combinatorial space while keeping the number of safely manageable reagents.

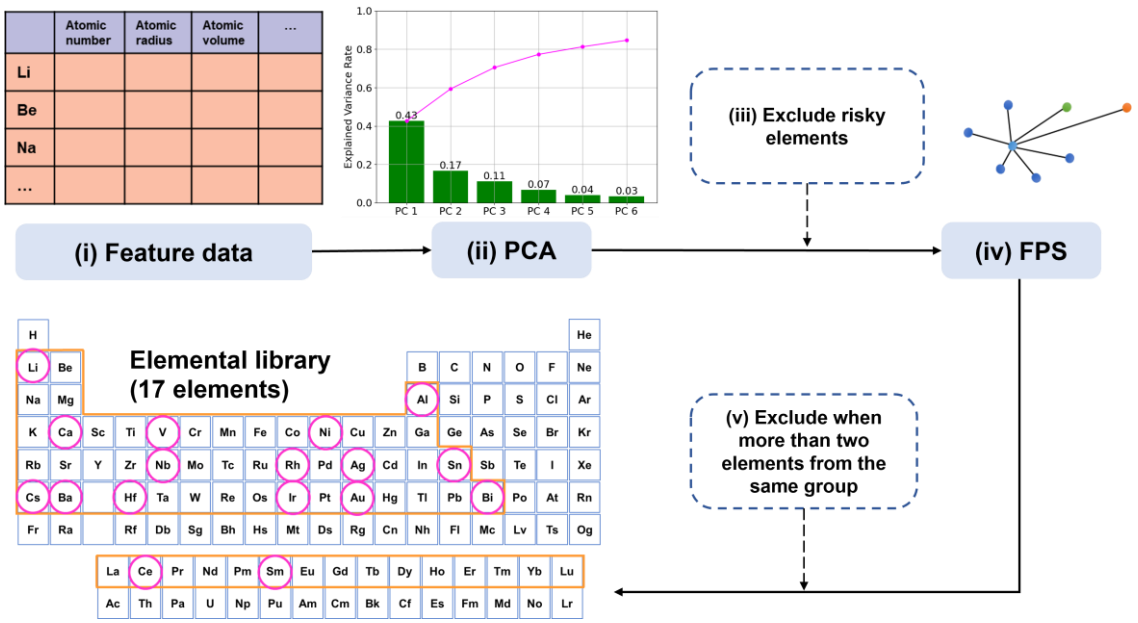

Figure 2.2. Workflow for extracting a representative set of elements from the target elements of the periodic table. (i) Feature data were collected from XenonPy; (ii) Feature data were reduced to 6 dimensions by principal component analysis (PCA); (iii) Risky elements were excluded; (iv) Farthest point sampling was made in the PCA space, where (v) entries from the same elemental group were restricted to at maximum two elements. Eventually, 17 representative elements, Li, Al, Ca, V, Ni, Nb, Rh, Ag, Sn, Cs, Ba, Ce, Sm, Hf, Ir, Au, and Bi, were carefully selected.

2.2.2. Materials

Metal precursors were purchased from commercially available sources: $LiNO_3$, $Ni(NO_3)_2{\cdot}6H_2O$, $AgNO_3$, $Sm(NO_3)_3{\cdot}6H_2O$, and $Bi(NO_3)_3{\cdot}5H_2O$ from FUJIFILM Wako Pure Chemical; $Al(NO_3)_3{\cdot}9H_2O$, and $Ca(NO_3)_2{\cdot}4H_2O$ from Kanto Chemical; $VOSO_4{\cdot}xH_2O$, $Nb(OC_2H_5)_5$, $Rh(NO_3)_3{\cdot}xH_2O$, $SnSO_4$, $CsNO_3$, $Ba(NO_3)_2$,

$Ce(NO_3)_3 \cdot 6H_2O$, $H_2IrCl_6 \cdot xH_2O$, and $HAuCl_4 \cdot 3H_2O$ from Sigma-Aldrich; $Hf(OC_2H_5)_4$ from Alfa Aesar. Aluminum oxide powder (γ-Al_2O_3, 164 m^2/g) was purchased from Sumitomo Chemical Industry and used as the catalyst support. Deionized (DI) water or ethanol (99.5%, FUJIFILM Wako Pure Chemical Corporation) was used to dissolve metal precursors.

2.2.3. Catalysts preparation

The catalysts were presented in the form of A–B–C–D–E/γ-Al_2O_3, with five elements (A–E) randomly selected from the elemental set selected in **2.2.1**, and their molar amounts were also randomly determined within the restrictions described below. The total amount of elements added to the support material, termed "total elemental loading", was varied within the range of 0.875–3.5 mmol per gram of support (mmol/g-support). The maximum loading of 3.5 mmol/g-support corresponds to a nickel loading of 17 wt%, while the minimum loading was set at 25% of the maximum to avoid excessively low loadings. The minimum loading of one element is 1% of the minimum total loading, i.e., 0.00875 mmol/g-support.

The catalyst preparation was conducted based on parallelized wet impregnation: 1.0 g of the support powder was impregnated in a 5.0 mL solution containing specified amounts of metal precursors for 6 hours at 50 °C [54,55], with the aid of a pipetting robot (Andrew+, Andrew Alliance) and a parallel thermal stirrer (ReactiTherm, Thermo Scientific). After vacuum drying in a centrifugal evaporator (CVE-3100, EYELA) at

90 °C for 4 hours, the catalyst was calcined under air at 500 °C for 4 hours. When water-sensitive precursors were involved, the impregnation was performed in the order of an aqueous solution for insensitive precursors and an ethanolic solution for sensitive ones. The calcined catalyst was thoroughly milled using an automated mortar and pestle (ALM-90DM, NITTO KAGAKU) prior to use. Twenty catalysts with different elemental combinations and compositions were prepared at the same time.

2.2.4. Catalyst evaluation

All the catalysts were evaluated in a process-consistent manner using an in-house high-throughput screening (HTS) instrument previously developed by Taniike et al. [2,3]. The instrument consists of a gas generator (MU-3504, HORIBA STEC), a flow distributor, an electric furnace, reaction tubes, an autosampler unit, and a quadrupole mass spectrometer (QMS, Transpector CPM 3, INFICON). The gas generator provides a reaction gas mixture of $CH_4/CO_2/Ar$ at controlled flow volumes. The gas mixture is then evenly distributed into 20 quartz reaction tubes through a gas distributor. The reaction tubes are made by fusing quartz tubes with inner diameters of 4 mm and 2 mm. A catalyst bed is positioned at the necked part of the reaction tube, supported by quartz wool. Twenty reaction tubes are symmetrically placed in a hollow furnace equipped with three temperature zones: T_1, T_2, and T_3. T_1 and T_3 serve as buffer layers to stabilize the temperature in the central catalyst bed. The effluent from each reaction tube is continuously transferred to QMS to determine its composition based on the mass signal

intensities of relevant mass fragments using external calibration. Twenty catalysts are tested at a time under each of programmed reaction conditions in an automated manner.

Catalyst powder, filled in a reaction tube as a 10-mm-high bed (roughly amounting to 60 mg), was subjected to the gas flow and temperature program depicted in **Figure 2.3**. Following in-line activation at 800 ºC for 1 hour under an H_2/Ar stream (10%/90% v/v), the catalysts were tested for 6 hours at 500 ºC using a CH_4/CO_2/Ar mixture of 3/3/4 mL/min/channel, corresponding to the contact time of 0.75 seconds or a gas hourly space velocity (GHSV) of approximately 10,000 $mL_{gas} \cdot h^{-1} \cdot g_{cat}^{-1}$. The reaction conditions in the evaluation process were determined with careful consideration of the literature data [45]. In particular, the temperature of 500 ºC presents a significant challenge, though it is not an unusual occurrence. A CO_2/CH_4 feed ratio of 1 is preferred from an industrial perspective, while a higher CO_2/CH_4 feed ratio greater than 1 is advantageous for avoiding carbon deposition. A duration of 6 hours is considered sufficient for screening purposes, although most of the literature adopts shorter durations. To avoid initial performance fluctuations and overscoring unstable catalysts, the time-on-stream data from 15,000 to 20,000 seconds were averaged to measure catalyst performance. The selected GHSV of 10,000 $mL \cdot h^{-1} \cdot g^{-1}$ is commonly used in the literature, offering a balanced tradeoff between promoting conversion and suppressing side reactions, making it suitable for comparative catalytic performance evaluation.

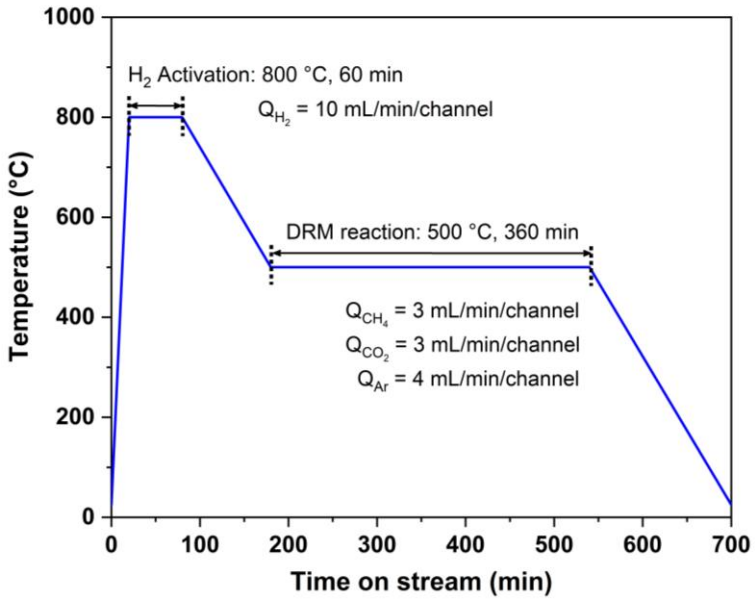

Figure 2.3. Sequence of gas flow and temperature conditions used in the evaluation process.

The conversion and yield of the relevant gases were calculated by the following equations:

$$CH_4 \text{ conversion } (\%) = \frac{P_{CH_4}^{in} - P_{CH_4}^{out}}{P_{CH_4}^{in}} \times 100 \quad (2.1),$$

$$CO_2 \text{ conversion } (\%) = \frac{P_{CO_2}^{in} - P_{CO_2}^{out}}{P_{CO_2}^{in}} \times 100 \quad (2.2),$$

$$H_2 \text{ yield } (\%) = \frac{P_{H_2}^{out}}{2P_{CH_4}^{in}} \times 100 \quad (2.3),$$

$$CO \text{ yield } (\%) = \frac{P_{CO}^{out}}{2P_{CO_2}^{in}} \times 100 \quad (2.4),$$

where $P^{in,out}$ represents the partial pressure in the influent and effluent, respectively.

2.2.5. Data analysis

Various data analyses were conducted on the obtained dataset, primarily employing ordinary statistical analysis methods using commonly available software such as Microsoft Excel or Python's Scikit-learn library. Particularly, decision tree classification was employed for its intuitive interpretability to derive comprehensive guidelines for catalyst design. Decision trees are constructed through recursive partitioning, starting with the root or parent node and subsequently dividing data into child nodes [56]. This recursive partitioning process continues as child nodes become parents for further splits, until a predetermined threshold is met. This approach facilitates the extraction of actionable guidelines for catalyst design. To be specific, the molar contents of individual elements were selected as descriptors to classify catalysts into different H_2 yield classes, based on the GINI impurity measure [57]. The random exploration led to an uneven distribution in catalyst performance, with non-catalysts prevailing in number. This class imbalance was addressed by adjusting the class weights inversely proportional to class frequencies. The resulting trees were pruned using cost-complexity pruning (CCP) with ccp_alpha set to 0.01, controlling the trade-off between fitting and simplicity by pruning branches with low importance [58].

ML models were built using experimental data as a training dataset to predict the performance of unknown catalysts. The models included a classifier to distinguish between non-catalysts (H_2 yield < 2%) and catalysts (H_2 yield ≥ 2%) and a regressor to predict continuous H_2 yield values for the catalyst class. The molar amounts of individual

elements served as explanatory variables. A random forest classifier was used for classification, and XGBoost for regression. Both models were hyperparameter-optimized to maximize classification accuracy and minimize the mean absolute error during 50-fold shuffle-split cross-validation (90% training, 10% test).

2.2.6. Characterization

The amount and nature of carbon deposits on the used catalysts was analyzed based on thermogravimetry differential thermal analysis (TG-DTA), measured on Thermo Plus EVO2 (Rigaku). A sample was placed in an Al_2O_3 crucible and heated from 30 °C to 900 °C at a ramping rate of 10 °C/min under dry air. The specific surface areas of the catalysts were determined using a BELSORP-mini II at 77 K and the Brunauer-Emmett-Teller (BET) method. Each catalyst sample was pretreated under vacuum at 523 K for 3 hours prior to the measurement [59]. The morphology of the catalysts was investigated using a JEOL JEM-2100Plus transmission electron microscope (TEM) operated at an accelerating voltage of 200 kV.

2.3. Results and discussion

2.3.1. Acquisition of DRM dataset and statistical analyses

Based on the rules described in section **2.1.1**, 256 five-element supported catalysts were prepared with randomly determined element combinations and compositions, generally denoted as A–B–C–D–E/γ-Al_2O_3, and their DRM performance was evaluated at 500 °C.

The preparation and evaluation were carried out according to the methods described in sections **2.2.3** and **2.2.4**, resulting in an unbiased and process-consistent DRM dataset, as exemplified in **Table 2.1**. The entire dataset is available in **Table A1** and is also digitally accessible on the Catalyst Acquisition by Data Science (CADS) web platform for public use [60].

Table 2.1. DRM dataset obtained by HTE (abbreviated). Individual catalysts are described by their elemental combinations, compositions and performances.[a,b,c] The entire dataset is available in Table A1.

No.	A (mmol)	B (mmol)	C (mmol)	D (mmol)	E (mmol)	M_{total} (mmol)	CH_4 conv. (%)	CO_2 conv. (%)	H_2 yield (%)	CO yield (%)
1	Al (0.837)	V (0.650)	Rh (0.293)	Ce (0.710)	Sm (0.248)	2.74	2.4	-2.6	0.1	0.7
2	Ca (0.681)	Nb (0.700)	Ag (0.402)	Cs (0.529)	Sm (0.373)	2.68	2.0	-3.1	0.0	0.2
3	Li (0.845)	Al (0.558)	Ni (0.282)	Nb (0.700)	Ce (0.426)	2.81	25.9	27.3	26.0	22.9
				...						
254	Ca (0.296)	V (0.298)	Ce (0.198)	Sm (0.257)	Hf (0.0406)	1.09	1.3	0.0	0.0	0.2
255	Ni (0.973)	Nb (0.351)	Ag (0.697)	Cs (0.114)	Ba (0.974)	3.11	1.4	0.8	0.0	0.3
256	Al (0.164)	Nb (0.147)	Rh (0.524)	Cs (0.446)	Ir (0.161)	1.44	14.1	21.3	15.4	19.0

[a] Individual catalysts are denoted as A–B–C–D–E/γ-Al_2O_3, where the elements A–E are ordered by atomic number, and the values in parentheses correspond to their amounts in mmol/g-support.

[b] M_{total} is the total amount in mmol/g-support.

[c] The conversions and yields were determined as the averages of the time-on-stream data from 15,000 to 20,000 seconds during the DRM reaction at 500 ºC under a CH_4/CO_2/Ar stream of 3/3/4 mL/min/channel (approx. 10000 $mL_{gas}\cdot h^{-1}\cdot g_{cat}^{-1}$ of GHSV) for 6 hours.

High-quality catalyst data of this scale is generally scarce. As previously demonstrated by Taniike et al. in oxidative coupling of methane, the analysis of such data is expected to yield valuable insights into catalysts and catalysis [2,3]. Hence, I first conducted a series of statistical analyses to understand the overall trends present in the data.

Figure 2.4a shows a bubble plot where H_2 yield is plotted along the catalyst number. The color of the bubbles represents the H_2 yield, and their size indicates the total loading amounts of the known active elements (Ni, Rh, Ir). It was observed that the H_2 yields were distributed up to 35%, while approximately 80% of the catalysts lacked notable catalytic performance. This is attributed to the random sampling method employed without any human intervention, ensuring the dataset's unbiased nature and objectivity. The inclusion of such negative results at a natural balance is also crucial for the accuracy and reliability of machine learning models [21]. In **Figure 2.4a**, all catalysts with non-zero yields contained the active elements, Ni, Rh, and Ir, i.e., no catalyst showed performance in the absence of these elements. However, based on the bubble size, there was no apparent correlation between the total amount of active elements and the H_2 yield. For instance, many catalysts involving these elements showed negligible yields. Several catalysts with low amounts of active elements achieved very high yields (No. 3, 135, and 209). This fact dictates the importance of synergistic and antagonistic interactions among elements in determining the overall performance.

The exploration identified seven catalysts with H_2 yields exceeding 25%, labeled in **Figure 2.4a** and **Table A1** as Nos. 3, 30, 53, 123, 135, 163, and 209. All of these catalysts

contained Ni, confirming that Ni is the most effective element for high yields when supported on Al_2O_3. It is also reasonable that platinum group metals, particularly Ir, which possesses DRM activity on its own and potential synergy with Ni [33,34], were included in four of these seven catalysts. On the other hand, elements that do not possess intrinsic DRM activity, such as Li, were found in six of the seven catalysts, while Al and Nb appeared in four. Other elements like Ca, Cs, Sm, and Hf were occasionally present, appearing in two catalysts each.

In the literature, there are only 16 entries with CH_4 conversion exceeding 25% at 500 °C or lower, with few known promoters for such low-temperature DRM [45]. Including entries above 500 °C, common promoters are K, Ce, Ca, Ba, and Zr (see **Figure 2.1b**). Specifically, K, Ca, and Ba are known to provide basic sites that promote CO_2 adsorption, leading to a moderate increase in activity and suppression of carbon deposition [61,62]. Ce plays multiple roles, including enhancing CO_2 adsorption, promoting CH_4 decomposition, aiding Ni dispersion, and improving both activity and durability by suppressing carbon deposition [63]. Zr, while increasing activity, also promotes carbon deposition [64]. Li, present in many of the high-performing catalysts in this study, is rarely mentioned in the literature dataset. However, a few recent studies have reported that the basicity introduced by Li can effectively promote DRM [65,66]. Al and Nb, which also appeared frequently, have no reported instances in the literature. Notably, Al and Nb were often found alongside Cs, another alkali metal like Li.

These observations on high-performing catalysts highlight the usefulness of combinatorial and compositional exploration without prior knowledge, leading to unexpected discoveries.

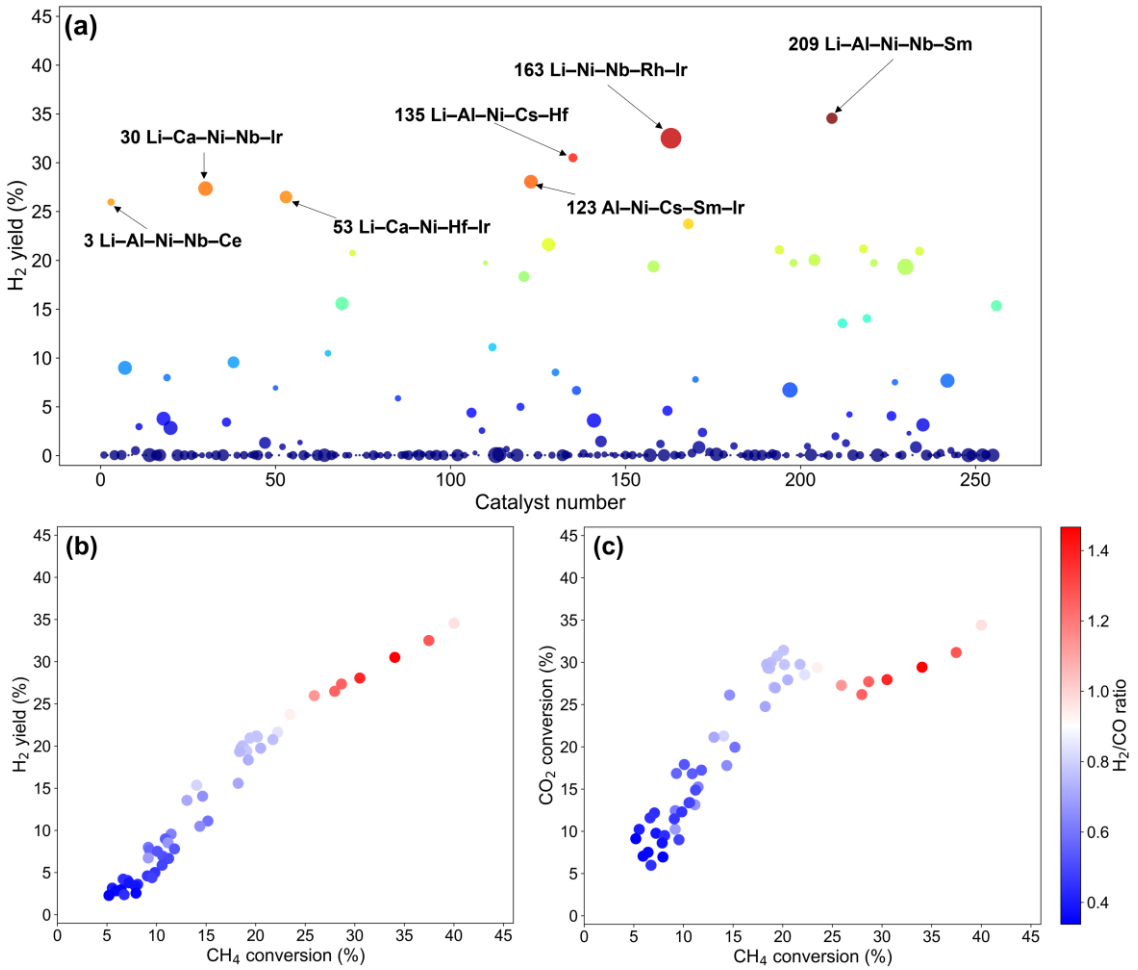

Figure 2.4. Visualization of the DRM dataset. (a) Bubble plot for the entire dataset, where the size of each bubble represents the total loading amounts of the active elements, Ni, Rh, and Ir. The color of the bubbles reflects the H_2 yield. It can be observed that the majority of catalysts exhibited negligible yields, while particularly high-performing catalysts are labeled with their elemental combinations. Scatter plots for catalysts with H_2 yields ≥2% are shown in terms of (b) CH_4 conversion vs. H_2 yield and (c) CH_4 conversion

vs. CO_2 conversion, where the H_2/CO ratio is indicated by the color. These plots represent trends intrinsic to low-temperature DRM.

The exploration yielded a reasonable amount of data with meaningful H_2 yields. Analyzing this data provides insights into the low-temperature DRM reaction. F**igures 2.4b** and **2.4c** plot the relationships between CH_4 conversion and H_2 yield, and between CH_4 conversion and CO_2 conversion, with the color axis indicating the H_2/CO yield ratio.

Ideally, DRM consumes one mole of CH_4 and CO_2 to produce two moles of H_2 and CO, resulting in identical values for conversion and yield. Any deviation from this indicates the occurrence of side reactions. From **Figures 2.4b** and **2.4c**, several key observations can be made. First, the H_2 yield was always lower than the CH_4 conversion. Additionally, at lower CH_4 conversions, the CO_2 conversion was higher than the CH_4 conversion; however, as CH_4 conversion increased, this relationship reversed. This resulted in a monotonous increase in the H_2/CO ratio with increasing CH_4 conversion, crossing unity at around 25% CH_4 conversion.

These observations suggest that the main side reaction at lower CH_4 conversions is the methanation of CO_2 by H_2, which consumes H_2 and CO_2 to produce CH_4, thereby lowering the CH_4 conversion and the H_2/CO ratio [67]. At higher CH_4 conversions, the Boudouard reaction becomes more evident [38], where CO disproportionates into C and CO_2, lowering the CO_2 conversion while raising the H_2/CO ratio. The unity of the H_2/CO ratio at around 25% CH_4 conversion does not indicate the absence of side reactions but

rather a coincidental balance between H_2 consumption due to methanation and CO consumption due to disproportionation.

The interrelation between reactants and products described above appears largely independent of the catalysts used, suggesting a thermodynamic origin. Thus, suppressing the side reactions through catalyst design is likely impractical. However, this inherent limitation does not undermine the pivotal role of catalysts in re-gasifying the deposited carbon and ensuring catalyst longevity. This aspect will be discussed in the next section.

The 256 five-element supported catalysts correspond to a total of 1280 individual element selections and 2560 binary element combinations. By analyzing the obtained dataset, we attempted to extract catalyst design heuristics for low-temperature DRM. As seen in **Figure 2.5a**, it is clear that each element was sampled evenly without significant bias. Even the least frequently sampled element, Sn, appeared 64 times, which was deemed sufficient to obtain reliable trends.

The dataset was then divided into four subsets based on H_2 yield thresholds of 2%, 13%, and 20% to analyze the relationship between the elements and performance. The number of catalysts in each subset was: 205 with H_2 yield < 2%, 27 with 2% ≤ H_2 yield < 13%, 10 with 13% ≤ H_2 yield < 20%, and 14 with H_2 yield ≥ 20%, with the majority of catalysts belonging to the non-catalyst group with negligible H_2 yields. Note that the number of high-performing catalysts was not large, and the catalyst design heuristics identified in this chapter should not be regarded as comprehensive. Nevertheless, this does not

underscore the value of the identified heuristics, considering the scarcity of literature exploring multi-element catalyst design in DRM [45].

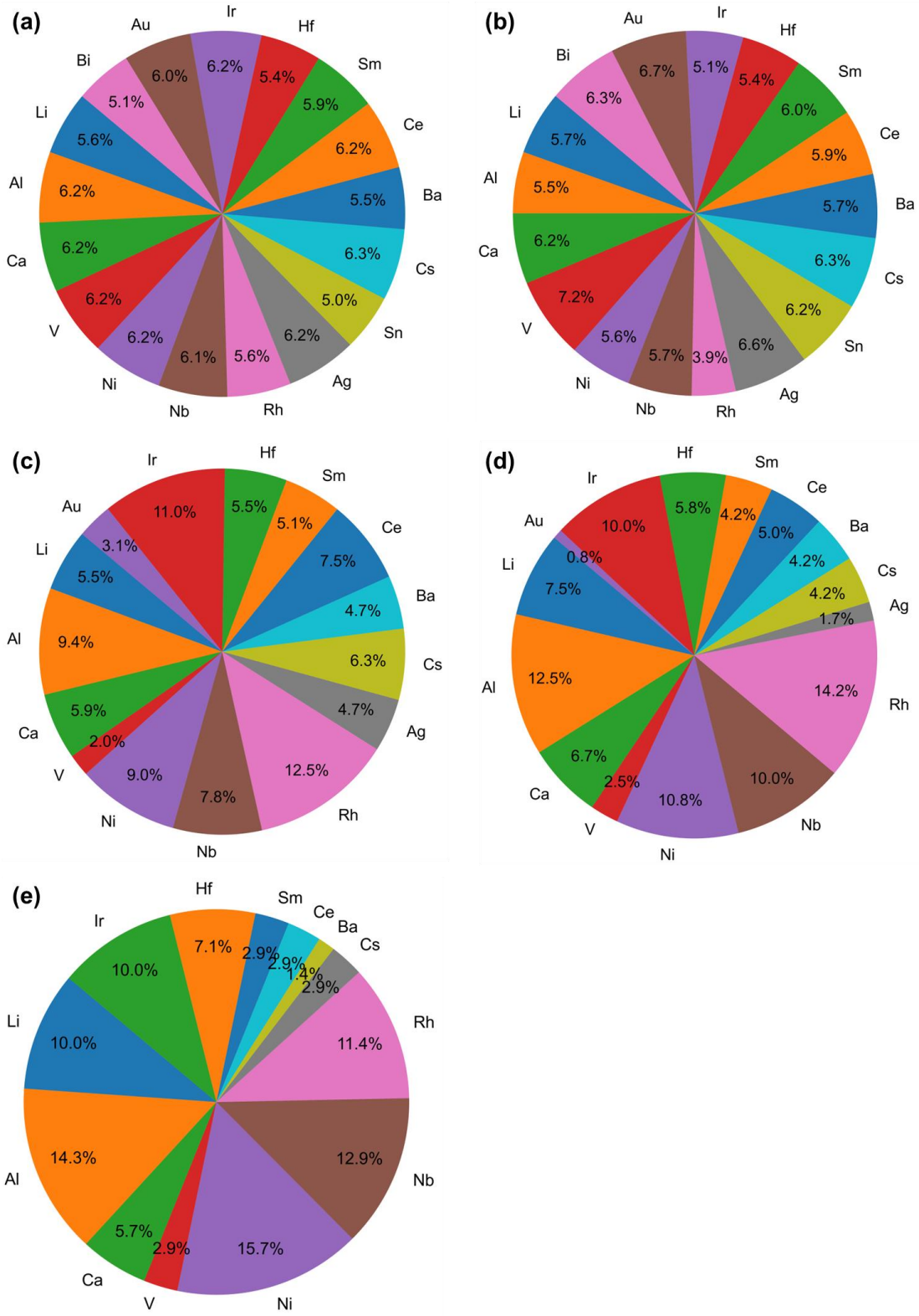

Figure 2.5. Percentage of appearances of individual elements. (a) Entire dataset, and subsets with (b) H_2 yield < 2%, (c) H_2 yield ≥ 2%, (d) H_2 yield ≥ 13%, and (e) H_2 yield ≥ 20%. The number of appearances of elements in each subset is normalized by the subset size.

Figure 2.6 shows the distribution of performance classes for individual elements. This is better understood when viewed alongside **Figures 2.5b**–**e**, which show the percentage of appearances of individual elements in each performance class. For all the elements, H_2 yield < 2% was the most dominant class, suggesting that the presence of a certain element alone does not assure DRM performance. However, the probability of a catalyst belonging to a specific performance class notably changed with the inclusion of certain elements. For instance, all the catalysts containing Sn or Bi belonged to the non-catalyst group. The inclusion of post-transition metals such as Au and Ag increased the likelihood of non-catalysts and eliminated the probability of obtaining catalysts with H_2 yield ≥ 20%, indicating that these elements inhibit low-temperature DRM.

On the positive side, the probability of yielding catalysts with H_2 yield ≥ 2% was highest for Rh, followed by Ir, Al, Ni, Nb, and Ce. Among these, Rh, Ir, and Ni are known to be DRM-active. While Rh and Ir were more likely than Ni to yield catalysts with H_2 yield ≥ 2%, Ni was more significant in achieving H_2 yield ≥ 20%. This suggests that Ni is more specific to combinations than Rh and Ir, but can yield better catalysts when combinations are carefully selected. Among DRM-inactive elements, the most frequently

contained element was Al, followed by Nb and Ce. Of these, only Ce is known to be effective in promoting DRM in the literature [63]. Notably, Al stood out compared to the other rather inhibiting p-block metals and was frequently found in catalysts with H_2 yield ≥ 20%. Nb showed similar effectiveness to Al, in contrast to V from the same group. Additionally, elements such as Li and Hf, though not recognized as promoters, also have a high probability of being included in catalysts with H_2 yield ≥ 20%.

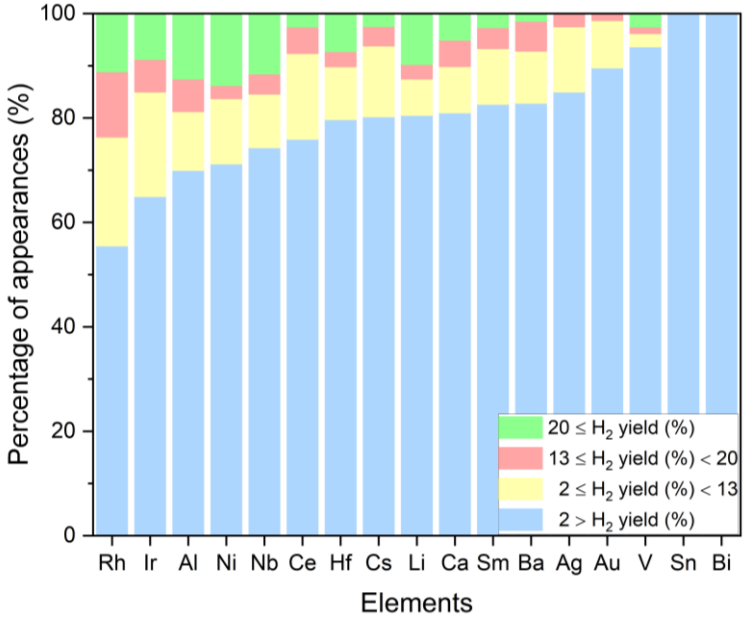

Figure 2.6. Normalized distribution of performance classes for individual elements. This represents the percentage of catalysts containing a specific element that fell into a specific performance class. The colors represent the H_2 yield classes associated with these appearances.

Next, I analyzed the relationship between elemental combinations and catalytic performance. Specifically, I compared the probability of each binary combination

appearing in catalysts within specified H_2 yield ranges (**Figure 2.7**). For instance, in **Figure 2.7a**, Li–V appears in 13% of the catalysts with H_2 yields below 2% (it should be noted that each five-element catalyst contains 10 binary combinations, so the total percentage of appearances sums to 1000%). Among the catalysts with H_2 yields below 2%, no prominent binary combinations were observed, suggesting that negative catalysts are numerous and specifying binary combinations alone is insufficient to obtain active DRM catalysts. Nonetheless, it is noteworthy that a subset containing active elements such as Ni, Rh, or Ir included one or more of V, Ag, Sn, or Bi in 97% of cases.

In catalysts with H_2 yields of 2% or higher, the appearance of elemental combinations began to show specificity, with Al–Rh, Ni–Ir, Rh–Ir, and Nb–Ir being the most frequent combinations (**Figure 2.7b**). As the performance threshold was raised to 13%, specific elemental combinations became more pronounced: Al–Rh, Ni–Nb, Ni–Ir, Nb–Rh, and Rh–Ir (**Figure 2.7c**). Among them, the combinations of Ni–Nb and Nb–Rh newly emerged. Once the threshold reached 20%, binary combinations such as Ni–Nb, Al–Ni, Li–Ni, Al–Nb, Ni–Ir, Nb–Rh, and Ni–Rh became dominant (**Figure 2.7d**). Many of these combinations involved Ni, suggesting that promoting Ni is the most effective strategy for achieving high activity in low-temperature DRM, consistent with the observation in **Figure 2.4b**. The binary combination of inactive elements, Al–Nb, suggests their synergy when combined with the active element, Ni. It is also noteworthy that Al and Nb frequently appeared with Rh.

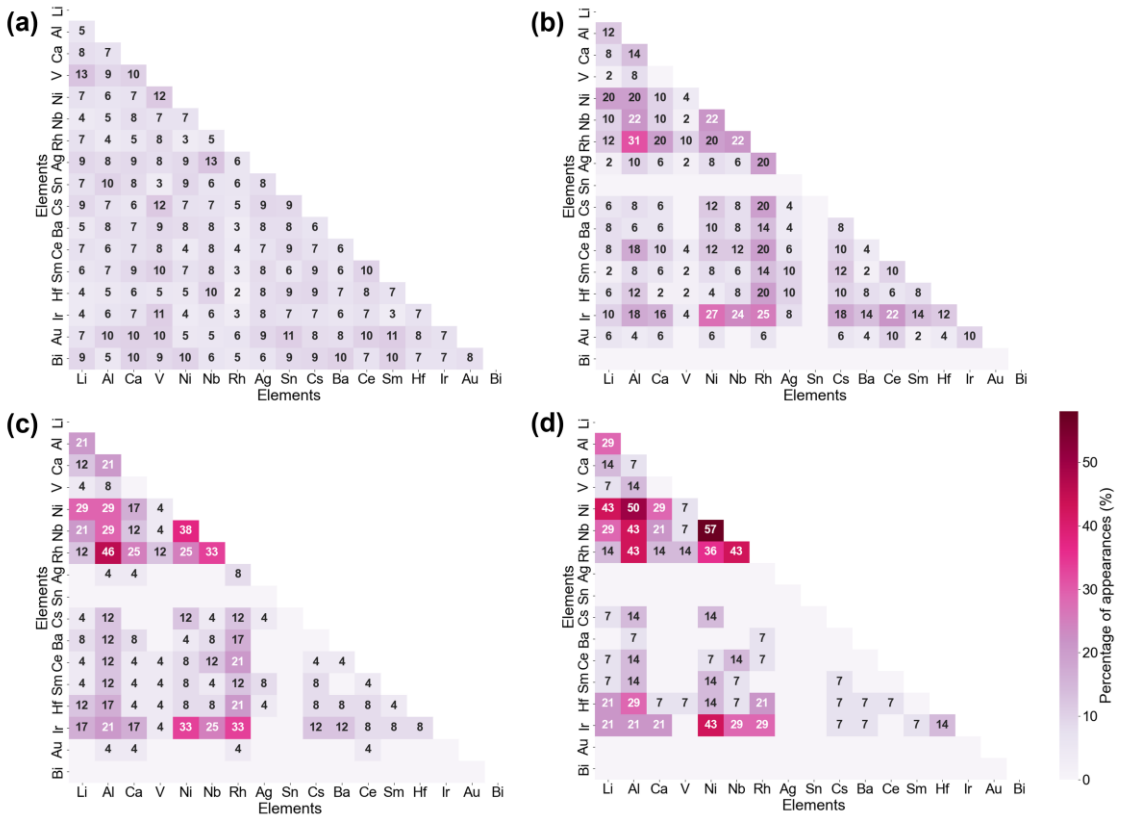

Figure 2.7. Percentage of appearances of individual binary combinations of elements. (a) H_2 yield < 2%, (b) H_2 yield ≥ 2%, (c) H_2 yield ≥ 13%, (d) H_2 yield ≥ 20%. The number of appearances of binary combinations in each subset is normalized by the subset size.

Decision tree classification, an interpretable machine learning algorithm, offers an intuitive display of feature importance and the decision-making process, thus holding significant value for visualizing catalyst design [68]. Here, I performed classification using the loading amounts of individual elements as descriptors and the H_2 yield as the target variable to establish catalyst design guidelines for low-temperature DRM and to comprehend the impact of elemental compositions on performance. The H_2 yields of catalysts were categorized into four classes: <2%, 2–13%, 13–20%, and ≥20%, similar to

Figure 2.6. This categorization focuses on high-performing catalysts, but the substantial presence of catalysts with H_2 yields < 2% may bias the classification model towards this specific class. To address this class imbalance issue, I set the class weights inversely proportional to class frequencies. Furthermore, to prevent the classification tree from becoming overly complex, a CCP technique was used to omit less decisive splits [58].

Figure 2.8 shows the obtained classification tree result. Initially, the top node classifies the 256 catalysts into 205 with H_2 yields < 2%, 27 with 2–13%, 10 with 13–20%, and 14 with ≥20%. The first split is based on the amount of Rh. By recursively performing such splits, the purity of the nodes—i.e., the proportion of catalysts in each node belonging to a specific H_2 yield class—increases, leading to catalyst design guidelines.

When catalysts contain a high amount of Rh, achieving a yield of ≥20% also requires having high amounts of Nb and Ni or Hf and Al. These rules involve the frequent combinations of Rh–Nb and Rh–Al identified in **Figure 2.7**, along with the need for a third element (Ni or Hf, respectively). When Nb and Hf amounts are low, excluding Ag is necessary to increase the chance of achieving yields of 13–20%. These observations suggest that Rh alone is insufficient for high performance without promoters.

When the Rh content was insufficient, two significant branches emerged, differing in Ni content. The right branch is associated with high Ni content, where the primary design guideline for achieving H_2 yields ≥20% is to avoid specific elements such as Cs, Ag, and V. This suggests that Ni can achieve high performance without promoters, although it does not imply that promoters do not enhance performance beyond 20%. The other branch

is related to low Ni content, where the only way to increase the chance of achieving yields ≥20% is to exclude Bi and include high amounts of both Nb and Al. As seen in **Figure 2.7**, Nb and Al were frequently associated with both Ni and Rh.

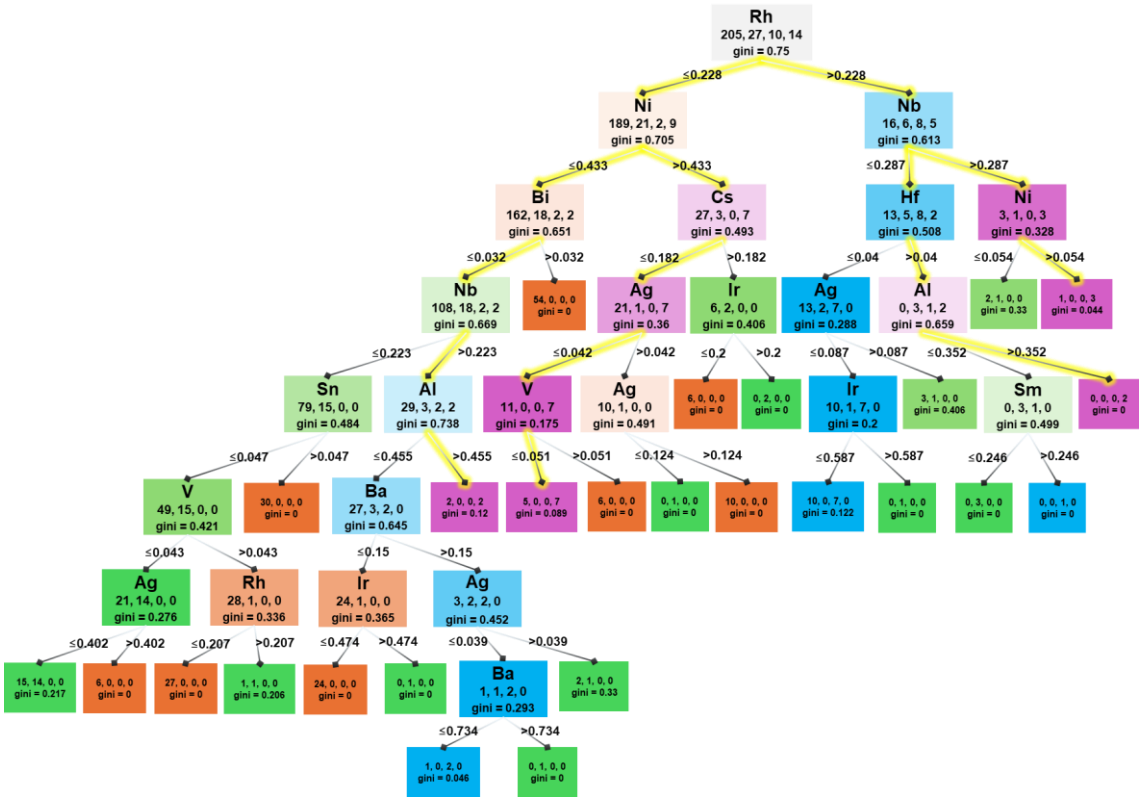

Figure 2.8. Classification tree result. The 256 catalysts were classified based on the loading amounts of the elements into four H_2 yield classes: < 2%, 2–13%, 13–20%, and ≥20%. The class weights were adjusted to be inversely proportional to the class frequencies. The tree was pruned based on cost complexity pruning (CCP). The four numbers written in each node correspond to the numbers of samples in the < 2%, 2–13%, 13–20%, and ≥20% H_2 yield classes, respectively. The nodes are colored according to the class with the largest weighted frequency. The splits were made based on specific

threshold loading amounts of elements in mmol/g-support. The yellow highlight traces the routes for catalysts with H_2 yields ≥20%.

A direct application of the unbiased dataset is predicting the performance of untested catalysts using ML models trained on it. Here, ML models were built using the dataset in **Table 2.1**, supplemented with data from **Tables 2.3** and **2.4** (**Figures 2.9a and 2.9b**). The models comprised a random forest classifier and an XGBoost regressor. The classifier differentiated between non-catalysts (H_2 yield < 2%) and catalysts (H_2 yield ≥ 2%), while the regressor predicted continuous H_2 yield values for the catalyst class. After hyperparameter optimization, the classifier achieved an accuracy of 0.99 during training and 0.89 during cross-validation, while the regressor achieved a mean absolute error of 0.29% during training and 4.1% during cross-validation. Despite slight overfitting due to the limited dataset size, the regressor's prediction error of 4.1% is sufficient for practical applications, such as distinguishing between catalysts with yields of 10% and 20%.

The predictive power of the ML models was validated experimentally. Catalysts were generated as combinations of 1–5 elements from the library of 17 elements, with individual loadings varied from 0.2 to 3.4 mmol/g-support in 0.2 mmol/g-support increments, within a total loading limit of 3.5 mmol/g-support. A total of 20 catalysts were sampled, consisting of 5 each in the predicted yield ranges of H_2 yield < 2%, 2–13%, 13–20%, and ≥20%. Note that the catalysts for which the regressor predicted the H_2 yield were limited to those assigned to the catalyst class (H_2 yield ≥ 2%) by the classifier. To

ensure diversity and avoid extreme extrapolation, random sampling was performed in regions within a minimum Euclidean distance between 0.2 to 1.0 mmol/g-support from the training data in the 17-dimensional compositional space. The correspondence between predicted and experimentally observed H_2 yields for these 20 catalysts (**Table 2.2**) is shown in **Figure 2.9c**.

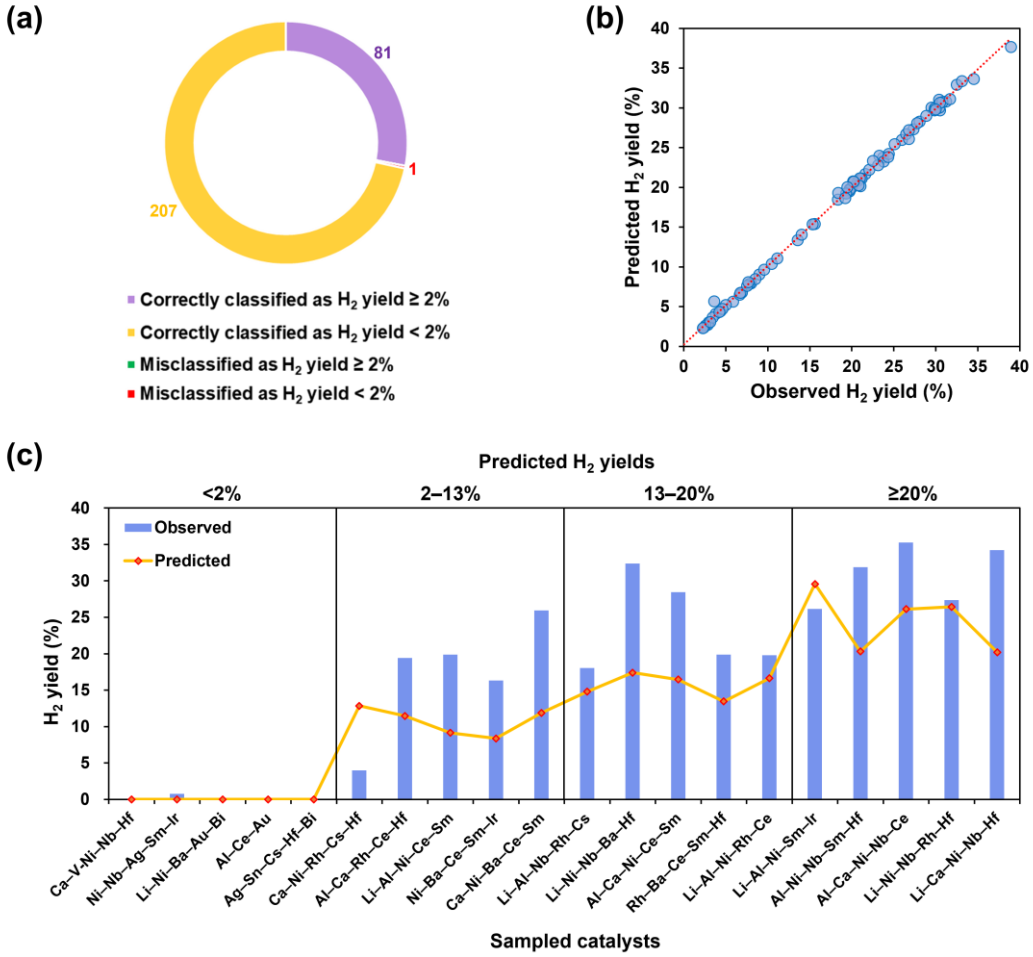

Figure 2.9. Results for the training of the machine learning models and experimental validation. (a) Classification of catalysts into the non-catalyst class (H_2 yield < 2%) and catalyst class (H_2 yield ≥ 2%) using a random forest classifier. (b) XGBoost regression of H_2 yields for catalysts with H_2 yield ≥ 2%. (c) Experimental validation of prediction

results from the developed models. 20 catalysts were selected by restricted random sampling, consisting of 5 from each predicted yield range: H_2 yield < 2%, 2–13%, 13–20%, and ≥ 20%. The restriction was based on the distance representing compositional similarity to the catalysts in the training data.

Table 2.2. DRM performance of the catalysts used to validate the machine learning models.[a]

No.	A (mmol)	B (mmol)	C (mmol)	D (mmol)	E (mmol)	M_{total} (mmol)	CH_4 conv. (%)	CO_2 conv. (%)	H_2 yield (%)	CO yield (%)
1	Ca (0.200)	V (0.600)	Ni (0.600)	Nb (0.400)	Hf (0.800)	2.60	1.6	0.5	0.0	0.2
2	Ni (0.800)	Nb (0.200)	Ag (0.200)	Sm (0.200)	Ir (0.200)	1.60	3.0	3.5	0.8	2.2
3	Li (0.400)	Ni (1.000)	Ba (0.400)	Au (0.200)	Bi (1.200)	3.20	1.2	-0.9	0.0	0.1
4	Al (0.200)	Ce (1.400)	Au (0.800)			2.40	2.3	-0.2	0.0	0.1
5	Ag (0.600)	Sn (0.400)	Cs (0.200)	Hf (1.000)	Bi (0.800)	3.00	2.6	0.3	0.1	0.2
6	Ca (0.800)	Ni (0.400)	Rh (0.400)	Cs (1.000)	Hf (0.400)	3.00	7.2	13.6	4.0	9.9
7	Al (0.200)	Ca (0.200)	Rh (1.200)	Ce (0.800)	Hf (0.400)	2.80	19.6	31.0	19.4	26.6
8	Li (0.800)	Al (0.400)	Ni (0.400)	Ce (0.600)	Sm (0.600)	2.80	20.3	30.5	19.9	24.7
9	Ni (0.600)	Ba (0.200)	Ce (0.800)	Sm (1.200)	Ir (0.600)	3.40	16.6	26.8	16.3	22.7
10	Ca (0.200)	Ni (0.800)	Ba (0.800)	Ce (0.400)	Sm (1.000)	3.20	26.2	32.3	25.9	22.3
11	Li (0.200)	Al (0.600)	Nb (0.200)	Rh (1.200)	Cs (0.200)	2.40	19.0	29.9	18.0	25.9
12	Li (0.200)	Ni (0.800)	Nb (0.600)	Ba (1.200)	Hf (0.200)	3.00	36.7	37.9	32.4	38.3
13	Al (0.400)	Ca (0.200)	Ni (0.800)	Ce (0.200)	Sm (0.600)	2.20	28.9	33.5	28.5	22.0
14	Rh (0.800)	Ba (0.800)	Ce (0.800)	Sm (0.400)	Hf (0.600)	3.40	19.4	31.3	19.9	27.0
15	Li (0.400)	Al (0.200)	Ni (0.400)	Rh (1.000)	Ce (0.600)	2.60	19.9	31.5	19.8	26.9
16	Li (0.400)	Al (1.200)	Ni (1.200)	Sm (0.200)	Ir (0.200)	3.20	25.8	31.4	26.2	23.1
17	Al (0.200)	Ni (0.800)	Nb (0.400)	Sm (0.600)	Hf (1.200)	3.20	35.5	36.4	31.9	19.9
18	Al (0.200)	Ca (0.200)	Ni (1.800)	Nb (0.600)	Ce (0.600)	3.40	42.7	39.2	35.3	24.2
19	Li (0.400)	Ni (1.200)	Nb (0.800)	Rh (0.200)	Hf (0.400)	3.00	27.9	30.7	27.4	21.9
20	Li (1.400)	Ca (0.600)	Ni (0.800)	Nb (0.200)	Hf (0.200)	3.20	41.0	39.9	34.2	37.3

[a] The 20 catalysts were selected, consisting of 5 each in the predicted yield ranges of H_2 yield < 2%, 2–13%, 13–20%, and ≥20%.

The performance of the classifier was found to be perfect: all 5 catalysts predicted as non-catalysts indeed had H_2 yields < 2%, while the remaining 15 catalysts predicted as catalysts all exhibited H_2 yields ≥ 2%. Notably, the non-catalysts contained either of the elements V, Ag, Sn, Au, and Bi, which were previously identified as detrimental to DRM. The mean absolute error between the predicted and observed H_2 yields for the 15 catalysts was 8.6%, reflecting the quantitative limitation of the regressor, likely due to the overfitting tendency caused by the small sample size of the catalyst class. Despite the limitation, the regressor demonstrated practical utility for predicting the composition of high-performance catalysts. Specifically, among the 5 catalysts with predicted H_2 yields in the range of 13–20%, 3 exhibited observed H_2 yields within the same range. Furthermore, all 5 catalysts with predicted H_2 yields ≥ 20% also had observed yields ≥ 20%. Among the 8 catalysts with observed H_2 yields ≥ 20%, all contained Ni as the main active element, frequently coupled with Nb > Li, Al, Ca, Sm, and Hf > Ce. Furthermore, 4 out of these 8 included the combination Ni–Nb–Hf, while 3 contained combinations such as Li–Ni–Nb, Li–Ni–Hf, Al–Ni–Sm, and Ni–Ca–Ce. These patterns were identified by the earlier data science analyses as frequent in high-performance catalysts. This demonstrates that the predictive models successfully learned these patterns and can apply them directly to the design of high-performance catalysts.

This section concludes that exploration without assumptions on elemental combinations and compositions enabled the clear revisiting of heuristics scattered across diverse literature and facilitated the discovery of unexpected catalyst design guidelines.

The former includes side reactions intrinsic to DRM and the effectiveness of Ni as the primary element, while the latter involves pairing uncommon elements such as Al, Nb, and Hf, which may enhance the activity of Ni and Rh. Most importantly, the obtained data, characterized by its large scale, process consistency, and unbiased nature, holds significant value as a subject for machine learning. This perspective was partly realized in this chapter through the development of predictive models and their experimental validation, demonstrating the practical applicability of the approach.

2.3.2. Catalyst design to mitigate carbon deposition

DRM catalysts are susceptible to carbon deposition from three mechanisms: methane cracking, CO disproportionation, and CO hydrogenation [69,70]. The CO disproportionation is particularly relevant at the studied temperature (cf. **2.3.1**). The accumulation of carbon deposits not only causes the blockage of active sites that deteriorates long-term stability and reaction efficiency, but also disrupts reactant flow, leading to an increase in pressure drop and potential safety issues.

To facilitate the design of multi-element catalysts with enhanced resistance to carbon formation, the top three performing catalysts identified during the random exploration (Nos. 135, 163, and 209 in **Table A1**) were subjected to TG-DTA analysis after 6 hours on-stream at 500 °C. **Table 2.3** (entries 1–3) provides a summary of the catalyst performance, including the carbon deposition amount and reactivity. Notably, all three catalysts exhibited carbon deposition amounts exceeding 34 wt%, comparable to

previously reported values, such as 47 wt% for Ni/Al_2O_3 after just 1 hour on stream [71], and 18–52 wt% for modified Ni catalysts after 5 hours [72]. Nonetheless, the catalysts exhibited relatively stable activity over 6 hours on stream (**Figure 2.10**), and the surface areas of the fresh and spent catalysts were comparable (120 vs. 126 $m^2\ g^{-1}$) for Li–Al–Ni13–Cs–Hf/γ-Al_2O_3. It was reported in the literature that low-temperature DRM is prone to filamentous whisker carbon formation on Ni surfaces [73,74], but such carbon hardly deactivate the catalysts as long as no excessive carbon is accumulated or polymerized into film to encapsulate the Ni particles [74,75]. Among the three catalysts, Li–Al–Ni13–Cs–Hf demonstrated the lowest carbon deposition, although it shared some common elements with the other two.

Table 2.3. DRM performance of selected and additionally prepared catalysts with an emphasis of carbon formation.[a,b]

No.	Catalyst name	A (mmol)	B (mmol)	C (mmol)	D (mmol)	E (mmol)	CH_4 conv. (%)	CO_2 conv. (%)	H_2 yield (%)	CO yield (%)	Weight loss (wt%)	DTA peak temp. (°C)
1	Li–Al–Ni13–Cs–Hf	Li (0.865)	Al (0.193)	Ni (0.443)	Cs (0.080)	Hf (0.424)	34.0	29.4	30.5	20.8	34.8	555
2	Li–Ni64–Nb–Rh3–Ir3	Li (0.096)	Ni (2.255)	Nb (0.101)	Rh (0.114)	Ir (0.096)	37.5	31.2	32.5	25.5	36.2	586
3	Li–Al–Ni20–Nb–Sm	Li (0.350)	Al (0.545)	Ni (0.704)	Nb (0.102)	Sm (0.058)	40.0	34.4	34.5	35.5	38.4	581
4	Ni13	Ni (0.443)					19.1	30.8	18.4	22.5	30.2	580
5	Li–Ni13	Li (0.865)	Ni (0.443)				22.7	30.1	22.1	23.8	31.6	541
6	Al–Ni13	Al (0.193)	Ni (0.443)				21.1	32.2	21.0	23.6	10.3	565
7	Ni13–Cs	Ni (0.443)	Cs (0.080)				17.8	29.4	19.2	23.0	21.5	557
8	Ni13–Hf	Ni (0.443)	Hf (0.424)				22.2	33.6	20.8	24.4	26.3	572
9	Li–Al–Ni13	Li (0.865)	Al (0.193)	Ni (0.443)			24.4	30.6	23.8	22.8	31.8	545
10	Li–Ni13–Cs	Li (0.865)	Ni (0.443)	Cs (0.080)			25.3	30.4	24.4	22.6	32.2	545
11	Li–Ni13–Hf	Li (0.865)	Ni (0.443)	Hf (0.424)			21.7	31.2	23.1	24.0	30.5	533
12	Al–Ni13–Cs	Al (0.193)	Ni (0.443)	Cs (0.080)			18.5	29.1	20.2	23.4	25.7	593
13	Al–Ni13–Hf	Al (0.193)	Ni (0.443)	Hf (0.424)			21.4	31.6	20.2	23.0	16.4	564
14	Ni13–Cs–Hf	Ni (0.443)	Cs (0.080)	Hf (0.424)			18.5	30.3	19.5	23.6	15.0	549
15	Li–Al–Ni13–Cs	Li (0.865)	Al (0.193)	Ni (0.443)	Cs (0.080)		28.3	30.3	26.8	21.2	42.7	546

16	Li–Al–Ni13–Hf	Li (0.865)	Al (0.193)	Ni (0.443)	Hf (0.424)	22.7	30.3	22.5	24.5	31.6	540
17	Li–Al–Cs–Hf	Li (0.865)	Al (0.193)	Cs (0.080)	Hf (0.424)	1.8	-1.0	0.1	0.1	5.4	n.a.
18	Li–Ni13–Cs–Hf	Li (0.865)	Ni (0.443)	Cs (0.080)	Hf (0.424)	26.1	29.8	25.1	22.5	34.1	533
19	Al–Ni13–Cs–Hf	Al (0.193)	Ni (0.443)	Cs (0.080)	Hf (0.424)	23.7	35.1	24.3	23.1	13.9	549

[a] Nos. 1–3 correspond to the top-performing catalysts identified during the random exploration (corresponding to Nos. 135, 163, and 209 in Table A1). Nos. 4–19 include variants of No. 1 with some elements intentionally omitted. Note that the relative loadings of the active elements are indicated after their respective element symbols, with 100 corresponding to 3.5 mmol/g-support.

[b] Catalysts used in the DRM reaction at 500 °C for 6 hours on stream were subjected to TG-DTA analysis. The weight loss corresponds to the difference in sample weight at the onset and termination temperatures of the exothermic peak on the DTA curve, with the DTA peak temperature being the temperature at its maximum.

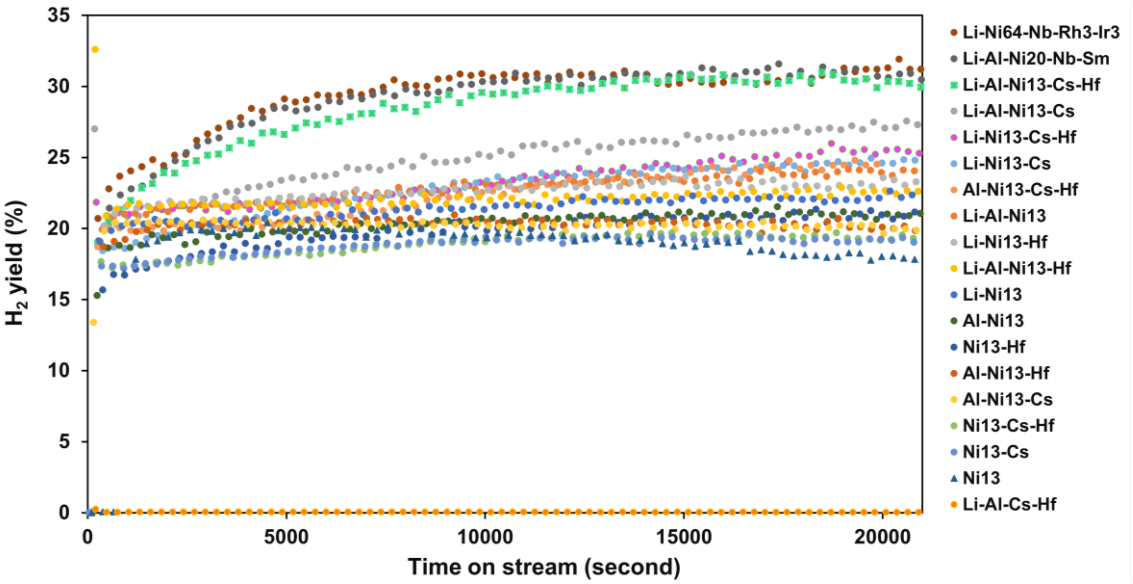

Figure 2.10. Time-on-stream performance of selected catalysts. These catalysts are listed in Table 2. The DRM reaction was performed at 500 ºC under a CH_4/CO_2/Ar stream of 3/3/4 mL/min/channel (approx. 10000 $mL_{gas}{\cdot}h^{-1}{\cdot}g_{cat}^{-1}$ of GHSV).

To investigate the roles of elemental combinations in catalytic performance, a series of catalysts were additionally prepared and evaluated. These catalysts comprised variants of

Li–Al–Ni13–Cs–Hf with some elements intentionally omitted. The results of catalysis and TG-DTA analysis are summarized in **Table 2.3** (from entry 4 onwards), with representative TG-DTA curves provided in **Figure 2.11**. TEM images of Li–Al–Ni13–Cs–Hf and Ni13 are shown in **Figure 2.12**.

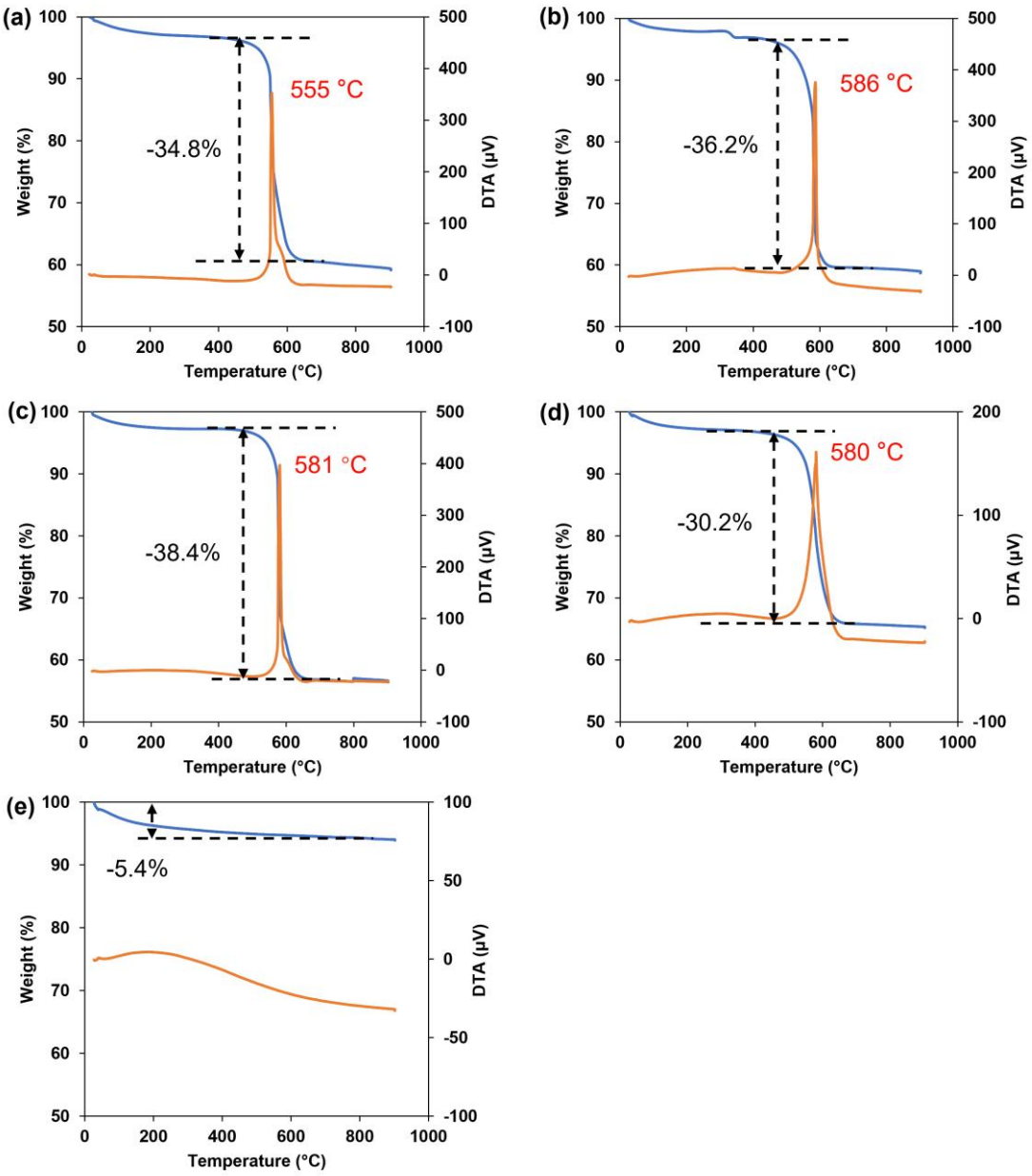

Figure 2.11. Representative TG-DTA curves for selected catalysts after the use in the DRM reaction at 500 °C for 6 hours on stream: (a) Li–Al–Ni13–Cs–Hf, (b) Li–Ni64–Nb–Rh3–Ir3, (c) Li–Al–Ni20–Nb–Sm, (d) Ni13, (e) Li–Al–Cs–Hf.

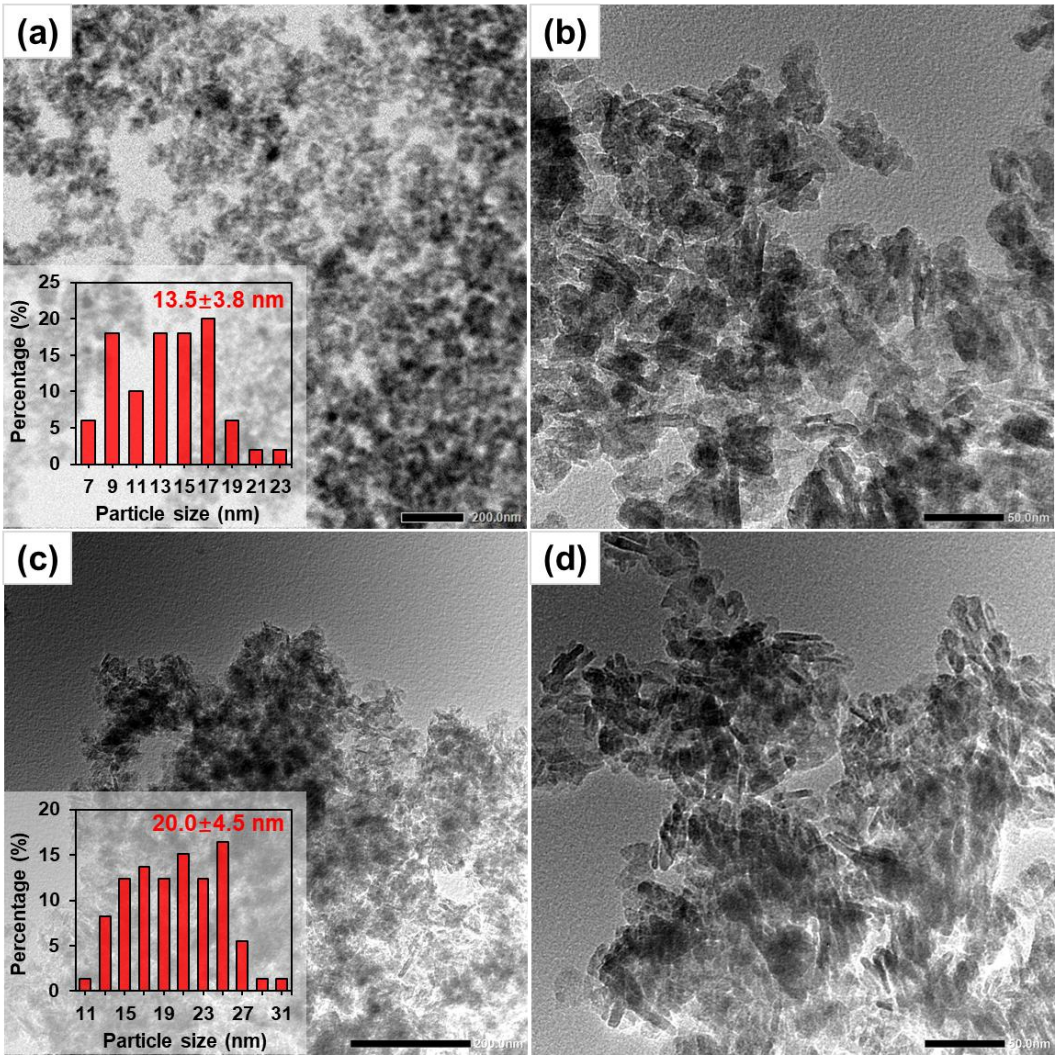

Figure 2.12. TEM images and particle size distribution: (a,b) Li–Al–Ni13–Cs–Hf and (c,d) Ni13. The images were taken after activation under an H_2 stream. The particle size distribution was acquired by analyzing randomly selected particles at a fixed magnification.

Analysis on additional data revealed the essentiality of Ni for promoting DRM reaction. However, its presence and the increase in its loading amount significantly raised the carbon deposition. The introduction of additional elements either suppressed or promoted the carbon formation, depending on their specific combinations. **Figure 2.13** visualizes the observed trends compiled in a tree diagram segmented by elements, alongside a heat map illustrating the H_2 yield, H_2/CO ratio, weight loss, and combustion peak temperature from TG-DTA. First of all, the presence or absence of Li led to distinct responses to additional elements, and therefore, the tree was divided by it at its root node. In the presence of Li, the addition of third and subsequent elements significantly enhanced the H_2 yield, while moderately increasing carbon deposition, accompanied with a rise in the H_2/CO ratio. The yield enhancement was most pronounced with Cs, followed by Al and Hf. When two elements were added to Li–Ni, higher H_2 yields, and increased carbon deposition were generally observed compared to the addition of only one element. However, the combination of all three elements, Al, Cs, and Hf, unexpectedly resulted in the best performance, with a significant reduction in carbon deposition. Without Li, the introduction of second and subsequent elements moderately promoted the H_2 yield but greatly suppressed carbon deposition. The synergistic effect was evident also in this context, where the combination of Al, Cs, and Hf significantly enhanced the H_2 yield while inhibiting carbon formation.

Note that the amount of carbon deposits exhibited an inverse relationship with the peak combustion temperature. In particular, the combustion temperature remained relatively

low for Li-containing catalysts, although the inclusion of Li increased carbon deposition. This suggests the formation of less stable carbon species, or the ease of regeneration that may compromise the increase in carbon deposition.

Experiments removing specific elements were also conducted on another high-performing catalyst (corresponding to No. 209 in **Table A1**). The results, presented in **Table 2.4**, reaffirmed the essential role of Ni and demonstrated that Li and Nb act as promoters for Ni. Moreover, in both **Tables 2.3** and **2.4**, the most active catalysts were consistently the original five-element compositions, with H_2 yields showing a declining trend as elements other than Ni were removed. Notably, in **Table 2.3**, all two-element catalysts were more active than Ni alone, strongly suggesting that most of the constituents play a promotional role for Ni.

In this section, it was revealed that the activity of catalysts and their propensity for carbon formation in low-temperature DRM are greatly influenced by the combination of elements. The discovery of unexpectedly effective new combinations, in particular, demonstrates the usefulness of large-scale exploration of multi-element catalysts. Further exploration and the development of rules from these findings may pave the way to addressing carbon deposition, the biggest issue in DRM.

Table 2.4. DRM performance after removing specific elements from Li–Al–Ni20–Nb–Sm.[a]

No.	Catalyst name	A (mmol)	B (mmol)	C (mmol)	D (mmol)	E (mmol)	CH_4 conv. (%)	CO_2 conv. (%)	H_2 yield (%)	CO yield (%)
1	Li–Al–Ni20–Nb–Sm	Li (0.350)	Al (0.545)	Ni (0.704)	Nb (0.102)	Sm (0.058)	40.0	34.4	34.5	35.5
2	Ni20	Ni (0.704)					30.3	25.1	29.5	20.2
3	Li–Ni20	Li (0.350)	Ni (0.704)				33.7	25.3	31.2	19.4
4	Al–Ni20	Al (0.545)	Ni (0.704)				26.8	26.2	26.8	22.2
5	Ni20–Nb	Ni (0.704)	Nb (0.102)				32.8	25.9	30.4	19.8
6	Ni20–Sm	Ni (0.704)	Sm (0.058)				31.5	25.3	29.9	19.6
7	Li–Al–Ni20	Li (0.350)	Al (0.545)	Ni (0.704)			29.6	25.4	28.9	21.0
8	Li–Ni20–Nb	Li (0.350)	Ni (0.704)	Nb (0.102)			35.4	26.8	30.8	19.8
9	Li–Ni20–Sm	Li (0.350)	Ni (0.704)	Sm (0.058)			34.0	25.7	31.7	19.4
10	Al–Ni20–Nb	Al (0.545)	Ni (0.704)	Nb (0.102)			32.9	26.9	30.5	20.0
11	Al–Ni20–Sm	Al (0.545)	Ni (0.704)	Sm (0.058)			23.7	24.4	23.3	20.9
12	Ni20–Nb–Sm	Ni (0.704)	Nb (0.102)	Sm (0.058)			31.4	26.1	30.0	20.2
13	Li–Al–Ni20–Nb	Li (0.350)	Al (0.545)	Ni (0.704)	Nb (0.102)		36.2	27.3	33.1	19.4
14	Li–Al–Ni20–Sm	Li (0.350)	Al (0.545)	Ni (0.704)	Sm (0.058)		28.5	25.2	27.8	21.4
15	Li–Al–Nb–Sm	Li (0.350)	Al (0.545)	Nb (0.102)	Sm (0.058)		-0.2	-4.9	0.1	0.2
16	Li–Ni20–Nb–Sm	Li (0.350)	Ni (0.704)	Nb (0.102)	Sm (0.058)		34.2	26.1	30.4	18.7
17	Al–Ni20–Nb–Sm	Al (0.545)	Ni (0.704)	Nb (0.102)	Sm (0.058)		31.9	25.2	29.9	19.8

[a] No. 1 corresponds to catalyst No. 209 in Table S1, which was identified during the random exploration. Nos. 2–17 include variants of No. 1 with some elements intentionally omitted. Note that the relative loadings of the active elements are indicated after their respective element symbols, with 100 corresponding to 3.5 mmol/g-support.

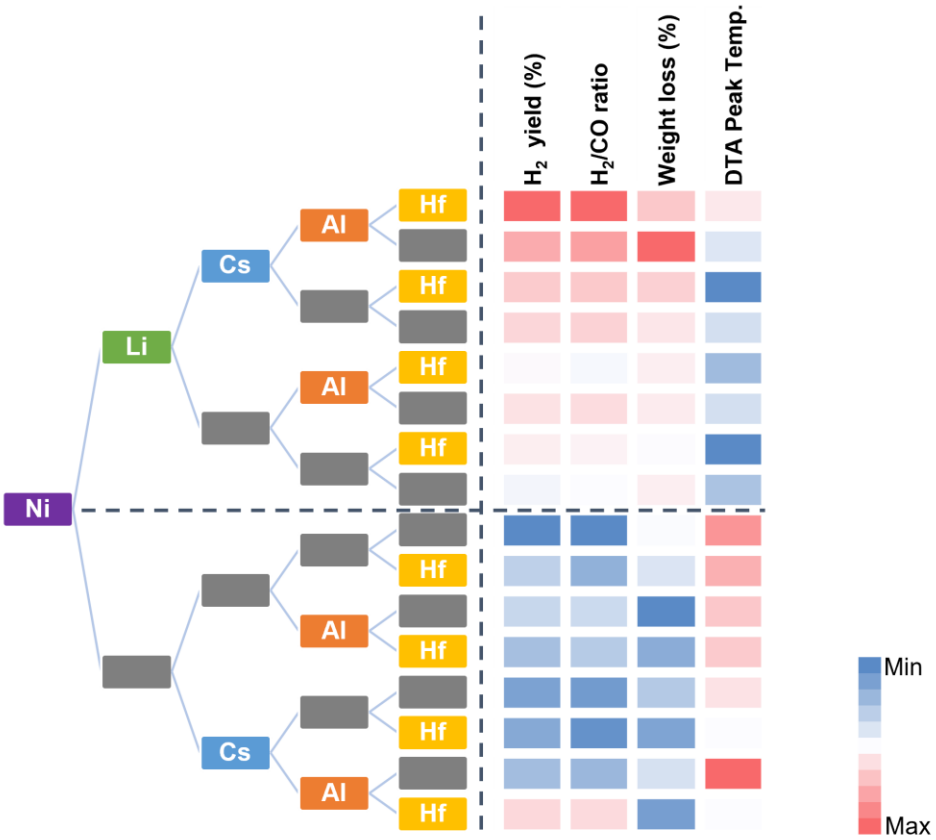

Figure 2.13. Tree diagram segmented by elements, alongside a heat map illustrating the H_2 yield, H_2/CO ratio, weight loss, and combustion peak temperature in TG-DTA. The heat map displays normalized values for each property, ranging from minimum (blue) to maximum (red).

2.4. Conclusion

The design of multi-element catalysts for the DRM has not been thoroughly explored in the literature. Here, 256 γ-Al_2O_3-supported five-element catalysts with randomly determined elemental combinations and compositions were prepared and evaluated for

DRM at 500 °C in a high-throughput mode. The major findings, derived from various analyses of the obtained unbiased dataset and the selected catalysts, are as follows:

- Out of the 256 catalysts, 205 were inactive for DRM. This means the majority of the catalyst design space belongs to negative data, and including such data in natural proportion is believed to be important.
- Many of the inactive catalysts contained elements, such as Ni and platinum group elements, that are known to be DRM-active. Indeed, no significant correlation was observed between the amount of these elements and activity, highlighting the essentiality of careful elemental combinations.
- DRM at 500 °C, regardless of the catalysts used, was limited by two side reactions: CO_2 methanation and CO disproportionation. The former was more pronounced at lower conversions, while the latter at higher conversions, causing the H_2/CO ratio to increase monotonically with conversion.
- Catalysts that exhibited DRM activity contained either Ni or platinum group elements, while their performance depended on the types and amounts of other combined elements. Rh and Ir were less sensitive to the combinations for activity, whereas Ni achieved the highest performance with the right combinations. Notably, Li, Al, Nb, Ca, Cs, Sm, Ce, and Hf frequently appeared in high-performance catalysts containing Ni. These frequent patterns were demonstrated to be practically useful for the direct prediction of high-performance catalysts using machine learning models.

- The promoters affected not only activity but also carbon deposition. Notably, the ternary combination of Al, Cs, and Hf with Ni significantly suppressed carbon deposition while enhancing activity.

Thus, exploration without prior knowledge, while not efficient for pinpointing high-performing catalysts or optimization, is beneficial for unexpected discoveries from unexplored catalyst design spaces. The inefficiency can be compensated by high-throughput experimentation, and the findings offer new perspectives for DRM catalyst design. Sized and qualified datasets are still scarce in the field of heterogeneous catalysis. The dataset publicized here will contribute to data-driven catalysis as benchmark and training data for further catalyst development.

Reference

[1] Q. Wei, X. Gao, L. Wang, Q. Ma, Rational design of nickel-based catalyst coupling with combined methane reforming to steadily produce syngas, Fuel 271 (2020) 117631. https://doi.org/10.1016/j.fuel.2020.117631.

[2] T.N. Nguyen, S. Nakanowatari, T.P. Nhat Tran, A. Thakur, L. Takahashi, K. Takahashi, T. Taniike, Learning catalyst design based on bias-free data set for oxidative coupling of methane, ACS Catal. 11 (2021) 1797–1809. https://doi.org/10.1021/acscatal.0c04629.

[3] T.N. Nguyen, T.T.P. Nhat, K. Takimoto, A. Thakur, S. Nishimura, J. Ohyama, I. Miyazato, L. Takahashi, J. Fujima, K. Takahashi, T. Taniike, High-throughput experimentation and catalyst informatics for oxidative coupling of methane, ACS Catal. 10 (2019) 921–932. https://doi.org/10.1021/acscatal.9b04293.

[4] I.V. Yentekakis, P. Panagiotopoulou, G. Artemakis, A review of recent efforts to promote dry reforming of methane (DRM) to syngas production via bimetallic catalyst formulations, Appl. Catal. B: Environ. 296 (2021) 120210. https://doi.org/10.1016/j.apcatb.2021.120210.

[5] L. He, Y. Fan, J. Bellettre, J. Yue, L. Luo, A review on catalytic methane combustion at low temperatures: Catalysts, mechanisms, reaction conditions and reactor designs, Renew. and Sust. Energ. Rev. 119 (2020) 109589. https://doi.org/10.1016/j.rser.2019.109589.

[6] T. Gensch, M.J. James, T. Dalton, F. Glorius, Increasing catalyst efficiency in C-H activation catalysis, Angew. Chem. Int. Ed. Engl. 57 (2018) 2296–2306. https://doi.org/10.1002/anie.201710377.

[7] J. Ashok, S. Pati, P. Hongmanorom, Z. Tianxi, C. Junmei, S. Kawi, A review of recent catalyst advances in CO_2 methanation processes, Catal. Today 356 (2020) 471–489. https://doi.org/10.1016/j.cattod.2020.07.023.

[8] N.A.K. Aramouni, J.G. Touma, B.A. Tarboush, J. Zeaiter, M.N. Ahmad, Catalyst design for dry reforming of methane: Analysis review, Renew. Sust. Energ. Rev. 82 (2018) 2570–2585. https://doi.org/10.1016/j.rser.2017.09.076.

[9] S. Furukawa, T. Komatsu, K.-i. Shimizu, Catalyst design concept based on a variety of alloy materials: a personal account and relevant studies, J. Mater. Chem. A 8 (2020) 15620–15645. https://doi.org/10.1039/d0ta03733h.

[10] E.-J. Ras, G. Rothenberg, Heterogeneous catalyst discovery using 21st century tools: a tutorial, RSC Adv. 4 (2014) 5963–5974. https://doi.org/10.1039/c3ra45852k.

[11] K. McCullough, T. Williams, K. Mingle, P. Jamshidi, J. Lauterbach, High-throughput experimentation meets artificial intelligence: a new pathway to catalyst discovery, Phys. Chem. Chem. Phys. 22 (2020) 11174–11196. https://doi.org/10.1039/d0cp00972e.

[12] S. Ahn, M. Hong, M. Sundararajan, D.H. Ess, M.H. Baik, Design and optimization of catalysts based on mechanistic insights derived from quantum chemical reaction

modeling, Chem. Rev. 119 (2019) 6509–6560. https://doi.org/10.1021/acs.chemrev.9b00073.
[13] Y. Nakaya, S. Furukawa, Catalysis of alloys: Classification, principles, and design for a variety of materials and reactions, Chem. Rev. 123 (2023) 5859–5947. https://doi.org/10.1021/acs.chemrev.2c00356.
[14] H. Vuong, A.J. Binder, J.E. Sutton, T. Toops, A. Savara, Experimental data based combinatorial kinetic simulations for predictions of synergistic catalyst mixtures, Catal. Today 338 (2019) 117–127. https://doi.org/10.1016/j.cattod.2019.04.026.
[15] S.L. González-Cortés, F.E. Imbert, Fundamentals, properties and applications of solid catalysts prepared by solution combustion synthesis (SCS), Appl. Catal. A: Gen. 452 (2013) 117–131. https://doi.org/10.1016/j.apcata.2012.11.024.
[16] K. Takahashi, L. Takahashi, S.D. Le, T. Kinoshita, S. Nishimura, J. Ohyama, Synthesis of heterogeneous catalysts in catalyst informatics to bridge experiment and high-throughput calculation, J. Am. Chem. Soc. 144 (2022) 15735–15744. https://doi.org/10.1021/jacs.2c06143.
[17] M. Wang, H. Zhu, Machine learning for transition-metal-based hydrogen generation electrocatalysts, ACS Catal. 11 (2021) 3930–3937. https://doi.org/10.1021/acscatal.1c00178.
[18] H. Li, Y. Jiao, K. Davey, S.Z. Qiao, Data-driven machine learning for understanding surface structures of heterogeneous catalysts, Angew. Chem. Int. Ed. Engl. 62 (2023) e202216383. https://doi.org/10.1002/anie.202216383.
[19] J.T. Margraf, H. Jung, C. Scheurer, K. Reuter, Exploring catalytic reaction networks with machine learning, Nat. Catal. 6 (2023) 112–121. https://doi.org/10.1038/s41929-022-00896-y.
[20] A. Kolluru, M. Shuaibi, A. Palizhati, N. Shoghi, A. Das, B. Wood, C.L. Zitnick, J.R. Kitchin, Z.W. Ulissi, Open challenges in developing generalizable large-scale machine-learning models for catalyst discovery, ACS Catal. 12 (2022) 8572–8581. https://doi.org/10.1021/acscatal.2c02291.
[21] T. Taniike, K. Takahashi, The value of negative results in data-driven catalysis research, Nat. Catal. 6 (2023) 108–111. https://doi.org/10.1038/s41929-023-00920-9.
[22] T.P. Jayakumar, S.P. Suresh Babu, T.N. Nguyen, S.D. Le, R.P. Manchan, P. Phulkerd, P. Chammingkwan, T. Taniike, Exploration of ethanol-to-butadiene catalysts by high-throughput experimentation and machine learning, Appl. Catal. A: Gen. 666 (2023) 119427. https://doi.org/10.1016/j.apcata.2023.119427.
[23] S.D. Le, N.N.T. Ton, K. Seenivasan, P. Chammingkwan, K. Higashimine, S. Praserthdam, T. Taniike, High-throughput screening of multimetallic catalysts for three-way catalysis, Sci. Technol. Adv. Mater. Meth. 4 (2024) 2284130. https://doi.org/10.1080/27660400.2023.2284130.
[24] J.A. Esterhuizen, B.R. Goldsmith, S. Linic, Interpretable machine learning for knowledge generation in heterogeneous catalysis, Nat. Catal. 5 (2022) 175–184. https://doi.org/10.1038/s41929-022-00744-z.

[25] L.H. Mou, T. Han, P.E.S. Smith, E. Sharman, J. Jiang, Machine learning descriptors for data-driven catalysis study, Adv. Sci. 10 (2023) e2301020. https://doi.org/10.1002/advs.202301020.
[26] S. Ishioka, A. Fujiwara, S. Nakanowatari, L. Takahashi, T. Taniike, K. Takahashi, Designing catalyst descriptors for machine learning in oxidative coupling of methane, ACS Catal. 12 (2022) 11541–11546. https://doi.org/10.1021/acscatal.2c03142.
[27] N.S. Lai, Y.S. Tew, X. Zhong, J. Yin, J. Li, B. Yan, X. Wang, Artificial intelligence (AI) workflow for catalyst design and optimization, Ind. Eng. Chem. Res. 62 (2023) 17835–17848. https://doi.org/10.1021/acs.iecr.3c02520.
[28] T. Mou, H.S. Pillai, S. Wang, M. Wan, X. Han, N.M. Schweitzer, F. Che, H. Xin, Bridging the complexity gap in computational heterogeneous catalysis with machine learning, Nat. Catal. 6 (2023) 122–136. https://doi.org/10.1038/s41929-023-00911-w.
[29] J. Roh, H. Park, H. Kwon, C. Joo, I. Moon, H. Cho, I. Ro, J. Kim, Interpretable machine learning framework for catalyst performance prediction and validation with dry reforming of methane, Appl. Catal. B: Environ. 343 (2024) 123454. https://doi.org/10.1016/j.apcatb.2023.123454.
[30] T. Taniike, A. Fujiwara, S. Nakanowatari, F. Garcia-Escobar, K. Takahashi, Automatic feature engineering for catalyst design using small data without prior knowledge of target catalysis, Commun. Chem. 7 (2024) 11. https://doi.org/10.1038/s42004-023-01086-y.
[31] C. Palmer, D.C. Upham, S. Smart, M.J. Gordon, H. Metiu, E.W. McFarland, Dry reforming of methane catalysed by molten metal alloys, Nat. Catal. 3 (2020) 83–89. https://doi.org/10.1038/s41929-019-0416-2.
[32] L. Wang, F. Wang, Design strategy, synthesis, and mechanism of Ni catalysts for methane dry reforming reaction: Recent advances and future perspectives, Energy Fuels 36 (2022) 5594–5621. https://doi.org/10.1021/acs.energyfuels.2c01007.
[33] W.-J. Jang, J.-O. Shim, H.-M. Kim, S.-Y. Yoo, H.-S. Roh, A review on dry reforming of methane in aspect of catalytic properties, Catal. Today 324 (2019) 15–26. https://doi.org/10.1016/j.cattod.2018.07.032.
[34] A.G.S. Hussien, K. Polychronopoulou, A review on the different aspects and challenges of the dry reforming of methane (DRM) reaction, Nanomaterials 12 (2022) 3400. https://doi.org/10.3390/nano12193400.
[35] C. Shi, S. Wang, X. Ge, S. Deng, B. Chen, J. Shen, A review of different catalytic systems for dry reforming of methane: Conventional catalysis-alone and plasma-catalytic system, J. CO_2 Util. 46 (2021) 101462. https://doi.org/10.1016/j.jcou.2021.101462.
[36] M.S. Ferrandon, C. Byron, G. Celik, Y. Zhang, C. Ni, J. Sloppy, R.A. McCormick, K. Booksh, A.V. Teplyakov, M. Delferro, Grafted nickel-promoter catalysts for dry reforming of methane identified through high-throughput experimentation, Appl. Catal. A: Gen. 629 (2022) 118379. https://doi.org/10.1016/j.apcata.2021.118379.
[37] L. Zhou, L. Li, N. Wei, J. Li, J.M. Basset, Effect of $NiAl_2O_4$ formation on Ni/Al_2O_3 stability during dry reforming of methane, ChemCatChem 7 (2015) 2508–2516. https://doi.org/10.1002/cctc.201500379.

[38] X. Zhao, S. Sun, Y. Wang, Y. Zhang, Y. Zhu, B. Zong, J. Hu, P. Williams, C. Wu, The role of reverse Boudouard reaction during integrated CO_2 capture and utilisation via dry reforming of methane, Chem. Eng. J. 491 (2024) 151668. https://doi.org/10.1016/j.cej.2024.151668.
[39] D. Pakhare, J. Spivey, A review of dry (CO_2) reforming of methane over noble metal catalysts, Chem. Soc. Rev. 43 (2014) 7813–7837. https://doi.org/10.1039/c3cs60395d.
[40] D. Wang, P. Littlewood, T.J. Marks, P.C. Stair, E. Weitz, Coking can enhance product yields in the dry reforming of methane, ACS Catal. 12 (2022) 8352–8362. https://doi.org/10.1021/acscatal.2c02045.
[41] S. Wang, G.Q. Lu, A comprehensive study on carbon dioxide reforming of methane over Ni/γ-Al_2O_3 catalysts, Ind. Eng. Chem. Res. 38 (1999) 2615–2625. https://doi.org/10.1021/ie980489t.
[42] Z. Li, Q. Lin, M. Li, J. Cao, F. Liu, H. Pan, Z. Wang, S. Kawi, Recent advances in process and catalyst for CO_2 reforming of methane, Renew. Sust. Energ. Rev. 134 (2020) 110312. https://doi.org/10.1016/j.rser.2020.110312.
[43] Y. Kathiraser, U. Oemar, E.T. Saw, Z. Li, S. Kawi, Kinetic and mechanistic aspects for CO_2 reforming of methane over Ni based catalysts, Chem. Eng. J. 278 (2015) 62–78. https://doi.org/10.1016/j.cej.2014.11.143.
[44] Y. Wang, L. Yao, Y. Wang, S. Wang, Q. Zhao, D. Mao, C. Hu, Low-temperature catalytic CO_2 dry reforming of methane on Ni-Si/ZrO_2 catalyst, ACS Catal. 8 (2018) 6495–6506. https://doi.org/10.1021/acscatal.8b00584.
[45] A.N. Şener, M.E. Günay, A. Leba, R. Yıldırım, Statistical review of dry reforming of methane literature using decision tree and artificial neural network analysis, Catal. Today 299 (2018) 289–302. https://doi.org/10.1016/j.cattod.2017.05.012.
[46] L. He, X. Chen, Y. Ren, B. Yue, S.C.E. Tsang, H. He, Improving catalytic stability and coke resistance of Ni/Al_2O_3 catalysts with Ce promoter for relatively low temperature dry reforming of methane reaction, Chem. Res. Chin. Univ. 38 (2021) 1032–1040. https://doi.org/10.1007/s40242-021-1281-5.
[47] Z. Song, Q. Wang, C. Guo, S. Li, W. Yan, W. Jiao, L. Qiu, X. Yan, R. Li, Improved effect of Fe on the stable NiFe/Al_2O_3 catalyst in low-temperature dry reforming of methane, Ind. Eng. Chem. Res. 59 (2020) 17250–17258. https://doi.org/10.1021/acs.iecr.0c01204.
[48] A.H.K. Owgi, A.A. Jalil, M.A.A. Aziz, M. Alhassan, H.U. Hambali, W. Nabgan, R. Saravanan, A.H. Hatta, Effect of promoters (Ce, Sr, Cs, and Sm) on the activity and coke formation of FSA support Ni in the dry reforming of methane, Fuel 340 (2023) 127592. https://doi.org/10.1016/j.fuel.2023.127592.
[49] N. Wang, K. Shen, L. Huang, X. Yu, W. Qian, W. Chu, Facile route for synthesizing ordered mesoporous Ni–Ce–Al oxide materials and their catalytic performance for methane dry reforming to hydrogen and syngas, ACS Catal. 3 (2013) 1638–1651. https://doi.org/10.1021/cs4003113.

[50] F. Jin, Y. Fu, W. Kong, J. Wang, F. Cai, C. Yuan, B. Pan, J. Zhang, Y. Sun, Stable trimetallic NiFeCu catalysts with high carbon resistance for dry reforming of methane, Chempluschem 85 (2020) 1120–1128. https://doi.org/10.1002/cplu.202000217.
[51] R. Yoshida, XenonPy is a python software for materials informatics. https://github.com/yoshida-lab/XenonPy.
[52] M.K. Silver, A.L. Arain, J. Shao, M. Chen, Y. Xia, B. Lozoff, J.D. Meeker, Distribution and predictors of 20 toxic and essential metals in the umbilical cord blood of Chinese newborns, Chemosphere 210 (2018), 1167–1175. https://doi.org/10.1016/j.chemosphere.2018.07.124.
[53] A. Stojsavljevic, M. Rovcanin, B. Rovcanin, Z. Mikovic, A. Jeremic, M. Perovic, D. Manojlovic, Human biomonitoring of essential, nonessential, rare earth, and noble elements in placental tissues, Chemosphere 285 (2021) 131518. https://doi.org/10.1016/j.chemosphere.2021.131518.
[54] B.A.T. Mehrabadi, S. Eskandari, U. Khan, R.D. White, J.R. Regalbuto, A review of preparation methods for supported metal catalysts, Adv. Catal. 61 (2017) 1–35. https://doi.org/10.1016/bs.acat.2017.10.001.
[55] S. Kawi, Y. Kathiraser, J. Ni, U. Oemar, Z. Li, E.T. Saw, Progress in synthesis of highly active and stable nickel-based catalysts for carbon dioxide reforming of methane, ChemSusChem 8 (2015) 3556–3575. https://doi.org/10.1002/cssc.201500390.
[56] M. Baysal, M.E. Günay, R. Yıldırım, Decision tree analysis of past publications on catalytic steam reforming to develop heuristics for high performance: A statistical review, Int. J. Hydrogen Energ. 42 (2017) 243–254. https://doi.org/10.1016/j.ijhydene.2016.10.003.
[57] T. Daniya, M. Geetha, K.S. Kumar, Classification and regression trees with Gini index, Adv. Math. Sci. J. 9 (2020) 8237–8247. https://doi.org/10.37418/amsj.9.10.53.
[58] L. Luo, X. Zhang, H. Peng, W. Lv, Y. Zhang, A new pruning method for decision tree based on structural risk of leaf node, Neural Comput. Appl. 22 (2013) 17–26. https://doi.org/10.1007/s00521-012-1055-6.
[59] S. Weber, K.L. Abel, R.T. Zimmermann, X. Huang, J. Bremer, L.K. Rihko-Struckmann, D. Batey, S. Cipiccia, J. Titus, D. Poppitz, C. Kübel, K. Sundmacher, R. Gläser, T.L. Sheppard, Porosity and structure of hierarchically porous Ni/Al_2O_3 catalysts for CO_2 methanation, Catalysts 10 (2020) 1471. https://doi.org/10.3390/catal10121471.
[60] J. Fujima, Y. Tanaka, I. Miyazato, L. Takahashi, K. Takahashi, Catalyst Acquisition by Data Science (CADS): a web-based catalyst informatics platform for discovering catalysts, React. Chem. Eng. 5 (2020) 903−911. https://doi.org/10.1039/d0re00098a.
[61] Z. Alipour, M. Rezaei, F. Meshkani, Effects of support modifiers on the catalytic performance of Ni/Al_2O_3 catalyst in CO_2 reforming of methane, Fuel 129 (2014) 197−203. https://doi.org/10.1016/j.fuel.2014.03.045.
[62] J. Juan-Juan, M.C. Román-Martínez, M.J. Illán-Gómez, Effect of potassium content in the activity of K-promoted Ni/Al_2O_3 catalysts for the dry reforming of methane, Appl. Catal. A: Gen. 301 (2006) 9−15. https://doi.org/10.1016/j.apcata.2005.11.006.

[63] M. Rezaei, S.M. Alavi, S. Sahebdelfar, Z.-F. Yan, A highly stable catalyst in methane reforming with carbon dioxide, Scripta Mater. 61 (2009) 173−176. https://doi.org/10.1016/j.scriptamat.2009.03.033.
[64] L. Yao, J. Zhu, X. Peng, D. Tong, C. Hu, Comparative study on the promotion effect of Mn and Zr on the stability of Ni/SiO_2 catalyst for CO_2 reforming of methane, Int. J. Hydrogen Energ. 38 (2013) 7268−7279. https://doi.org/10.1016/j.ijhydene.2013.02.126.
[65] V. Pérez-Madrigal, E. Ríos-Valdovinos, E. Rojas-García, M.A. Valenzuela, F. Pola-Albores, Dry reforming of methane over Li-doped Ni/TiO_2 catalysts: Effect of support basicity, Methane 2 (2023) 452–469. https://doi.org/10.3390/methane2040031.
[66] C.M. Steffens, O.W. Perez-Lopez, Biogas dry reforming over Li–Ni–Al LDH-derived catalysts, Int. J. Hydrogen Energy 71 (2024) 205–216. https://doi.org/10.1016/j.ijhydene.2024.05.285.
[67] M.K. Nikoo, N.A.S. Amin, Thermodynamic analysis of carbon dioxide reforming of methane in view of solid carbon formation, Fuel Process. Technol. 92 (2011) 678−691. https://doi.org/10.1016/j.fuproc.2010.11.027.
[68] I.D. Mienye, Y. Sun, Z. Wang, Prediction performance of improved decision tree-based algorithms: A review, Procedia Manuf. 35 (2019) 698–703. https://doi.org/10.1016/j.promfg.2019.06.011.
[69] L.A. Schulz, L.C.S. Kahle, K.H. Delgado, S.A. Schunk, A. Jentys, O. Deutschmann, J.A. Lercher, On the coke deposition in dry reforming of methane at elevated pressures, Appl. Catal. A: Gen. 504 (2015) 599–607. https://doi.org/10.1016/j.apcata.2015.03.002.
[70] O. Muraza, A. Galadima, A review on coke management during dry reforming of methane, Int. J. Energy Res. 39 (2015) 1196–1216. https://doi.org/10.1002/er.3295.
[71] W.Y. Kim, Y.H. Lee, H. Park, Y.H. Choi, M.H. Lee, J.S. Lee, Coke tolerance of Ni/Al_2O_3 nanosheet catalyst for dry reforming of methane, Catal. Sci. Technol. 6 (2016) 2060–2064. https://doi.org/10.1039/c6cy00017g.
[72] H. Wang, W. Mo, X. He, X. Fan, F. Ma, S. Liu, D. Tax, Effect of Ca promoter on the structure, performance, and carbon deposition of Ni-Al_2O_3 catalyst for CO_2-CH_4 reforming, ACS Omega 5 (2020) 28955–28964. https://doi.org/10.1021/acsomega.0c02558.
[73] J.H. Kim, D.J. Suh, T.J. Park, K.L. Kim, Effect of metal particle size on coking during CO_2 reforming of CH_4 over Ni–alumina aerogel catalysts, Appl. Catal. A: Gen. 197 (2000) 191–200. https://doi.org/10.1016/S0926-860X(99)00487-1.
[74] J.M. Ginsburg, J. Piña, T. El Solh, H.I. de Lasa, Coke formation over a nickel catalyst under methane dry reforming conditions: Thermodynamic and kinetic models, Ind. Eng. Chem. Res. 44 (2005) 4846–4854. https://doi.org/10.1021/ie0496333.
[75] L. Baharudin, N. Rahmat, N.H. Othman, N. Shah, S.S.A. Syed-Hassan, Formation, control, and elimination of carbon on Ni-based catalyst during CO_2 and CH_4 conversion via dry reforming process: A review, J. CO_2 Util. 61 (2022) 102050. https://doi.org/10.1016/j.jcou.2022.102050.

Chapter 3 Scaling up catalyst discovery by breaking human constraints through high-throughput experimentation and automatic feature engineering

Abstract

Catalyst discovery is often bottlenecked by the vastness of compositional space and the inefficiencies of conventional trial-and-error approaches. In this chapter, I present a data-driven discovery framework that combines high-throughput experimentation (HTE), automatic feature engineering (AFE), and an adaptive active learning loop to identify high-performance dry reforming of methane (DRM) catalysts at 500 °C. Unlike conventional methods that rely on handcrafted descriptors, AFE automatically generates features from general physicochemical properties, enabling unbiased exploration and reducing reliance on domain-specific assumptions. Starting from an initial dataset of 277 multi-element γ-Al_2O_3-supported catalysts generated primarily through random sampling, I conducted 13 active learning loops that progressively expanded the elemental design space to 45 elements. Through strategic sampling, a total of 420 new catalysts were synthesized and evaluated. Catalyst phylogenetic tree was constructed to visualize over 100 high-performance DRM catalysts discovered through the adaptive learning process. The compositions span three major lineages: alkali-promoted systems, platinum-group metal (PGM)-based systems, and Ni- or Co-based active metal systems. Catalysts achieving H_2 yields ≥30% reaffirm the central role of Ni as the active component and reveal expanded elemental diversity, highlighting the role of alkali metals (Li, K, Cs, Rb), transition metals (Sc, Ti, Mn, Y, Nb, Hf, Ta), and the rare earth element Sm as effective promoters for enhancing DRM catalytic performance. Overall, this chapter highlights the powerful capability of adaptive active learning to overcome human intuition, systematically explore vast and previously inaccessible catalyst spaces, and accelerate the discovery of novel high-performance formulations.

3.1. Introduction

Catalysts lie at the core of modern chemical industries, playing a crucial role in energy production, environmental protection, and materials synthesis [1–3]. However, the discovery of new catalysts remains a formidable scientific challenge. This difficulty arises from the intricate nature of catalytic systems, where the activity, selectivity, and stability are governed by a complex interplay of structural, electronic, and kinetic factors [4,5]. In addition, the space of possible compositions and combinations is extraordinarily vast, as catalysts are typically composed of multiple elements in varying proportions [6].

Conventional catalyst development has largely relied on trial-and-error experiments to identify the optimal catalyst compositions and reaction conditions, which are time-consuming and costly [7,8]. Therefore, catalyst design space has long been confined to a narrow "known space" (**Figure 3.1**), where discoveries are typically restricted to regions close to the origin, characterized by simpler catalyst designs. For example, conventional systems like Ni/Al_2O_3, Rh/CeO_2, or Pt/ZrO_2, commonly used in reforming reactions, involve only a single active metal with typical support. However, beyond this known space lies a vast, unexplored "unknown space" that may harbor materials capable of revolutionizing catalysis. Although researchers often seek breakthroughs, traditional methods remain confined to known territories because hypothesis generation depends heavily on prior knowledge, naturally biasing exploration toward familiar regions and limiting access to novel catalyst compositions [9]. As a result, the search for new catalysts remains confined by the boundary between the known and the unknown. Although

accidental discoveries, while responsible for many major breakthroughs in catalysis, are inherently unpredictable and reliant heavily on chance [10]. Their randomness and lack of systematic guidance make them an inefficient approach for discovering novel catalysts. In this case, a paradigm shift in catalyst design strategies has become imperative.

Advances in materials informatics have led to the widespread adoption of data-driven approaches in materials development [11–14]. By integrating catalysts knowledge with techniques like machine learning (ML), researchers have accelerated the exploration and discovery of new materials. Traditional hypothesis-driven strategies rely on existing knowledge to formulate new assumptions but often struggle to transcend the boundaries of established material domains and exhibit limited capability in exploring uncharted catalyst spaces [15,16]. In contrast, data-driven approaches are free from the constraints of prior intuition or predefined relationships. ML algorithms can autonomously extract hidden patterns and complex correlations from large datasets, thereby expanding the scope of catalyst discovery beyond the limitations of conventional human inference [17]. For example, studies have explored design guidelines for oxidative coupling of methane catalysts with the aid of supervised ML, indicating its effectiveness in exploring high-performance catalysts for better C_2 yields [18,19]. Additionally, by incorporating general physicochemical features such as the electronic and geometric properties of elements in ammonia decomposition catalysts into the training data, novel catalyst formulations can be predicted beyond the original material parameter space [20].

However, the implementation of data-driven approaches across the vast combinatorial and compositional space remains challenged by two fundamental limitations [21]. First, it is undeniable that datasets in catalysis are typically limited in size, rarely exceeding a thousand observations. Moreover, these datasets often exhibit inconsistency and bias. Such constraints present significant challenges for constructing robust and generalizable ML models, which generally require numerous tunable parameters to capture complex trends [22,23]. The emergence of high-throughput experimentation (HTE), which can quickly generate high-quality, large-scale, and highly consistent catalyst datasets, has provided an effective approach to addressing the issue of insufficient experimental data in catalysis research [18,19,24,25]. Second, the inherent complexity and diversity of catalytic materials make it challenging to design robust descriptors based on researchers' physicochemical insights, as it typically requires in-depth domain knowledge of the target catalytic system [26]. Current ML approaches primarily rely on manually engineered descriptors thereby constraining their ability to uncover novel chemical insights. A major drawback is that the resulting models often fail to identify or generalize to materials entirely outside the training domain [27,28].

In a recent work [21,24], Taniike et al. introduced an automatic feature engineering (AFE) technique that automatically generates descriptors that effectively capture the essential physicochemical characteristics of catalytic systems, without the need of prior knowledge of the catalytic system This approach enables the identification of meaningful data trends using relatively simple ML models, substantially improving predictive

accuracy and efficiency, particularly when dealing with small catalyst datasets. Briefly, AFE constructs an extensive set of features by transforming the physicochemical properties of catalyst components and selects those most relevant to the target catalysis. Combining AFE with HTE and strategic sampling in an adaptive active learning loop, enables systematic refinement and optimization of catalyst descriptors. Through iterative training and experimental validation, it is expected to develop robust models that identify and recommend high-performance catalysts, while comprehensively exploring the vast unknown materials space.

To overcome the limitations of conventional catalyst discovery and expand the scope of catalyst discovery beyond established domains, I focus on methane dry reforming (DRM) as a representative case study—a crucial reaction which addresses both sustainable energy production and greenhouse gas mitigation by converting two major greenhouse gases (CH_4 and CO_2) into syngas [29–32]. An adaptive active learning iterative loop integrating HTE, AFE, and strategic sampling was implemented to progressively and efficiently expand the scope of exploration. By selecting representative elements from the periodic table, I constructed an unbiased dataset containing 277 multi-element catalysts supported on γ-Al_2O_3 as a starting point for training, with no reliance on prior knowledge. Throughout the iterative process, data sampling strategies were also dynamically adjusted based on model predictions to maximize exploration efficiency. Through 13 iterative loops, an additional 420 DRM catalysts were synthesized and evaluated. To the end, I successfully developed a well-validated robust ML model, which

enabled pinpointing various high-performance catalysts from a huge space comprising of arbitrary combinations and compositions of a total of 45 elements, totaling ca. 10^9 catalysts.

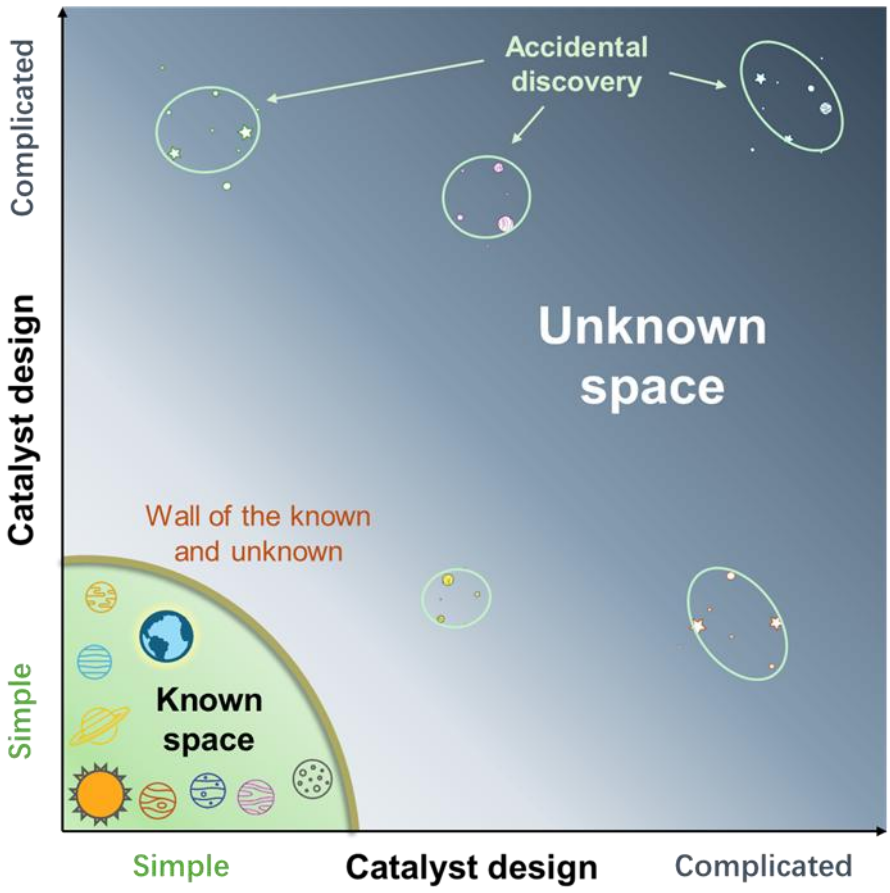

Figure 3.1. Schematic illustration of the catalyst design space.

3.2. Methods

3.2.1. Adaptive active learning loop

In catalyst design, when the training data are limited or lack diversity in elemental composition, AFE tends to generate multiple models with similar performance on the training set. However, these models frequently exhibit significant variability when predicting the performance of unknown catalysts. This inconsistency arises because the models are prone to fitting localized patterns rather than capturing global ones essential for reliable predictions. To address this issue, I implemented a customized active learning loop to enhance the AFE process (**Figure 3.2**). It started with an initial training dataset comprising 277 DRM catalysts, primarily obtained through HTE and random sampling. Subsequently, AFE was employed to generate descriptors most relevant to the target catalysis, encompassing feature collection, assignment, synthesis, and selection.

During the feature selection, a two-step procedure was implemented to address the substantial variability in feature values associated with non-catalysts (H_2 yield < 2%). First, a random forest classifier was applied to the entire dataset, using H_2 yield as the target variable. Descriptors that maximized balanced accuracy were selected. In the second step, a refined dataset was constructed by excluding samples predicted to be non-catalysts. Huber regression was then applied to identify descriptors that minimized the mean absolute error (MAE). This process ultimately yielded a robust predictive model. To improve the robustness of the generated descriptors and model, it employed FPS to select new catalysts that were most dissimilar to those in the training set within the

descriptor space. The sampled catalysts were then synthesized and evaluated using HTE, and the resulting data were added to reinforce the training set and update the descriptors and model through AFE. During this process, the elemental set gradually expanded. The final elemental set comprised 45 elements from the periodic table, which significantly enhanced the diversity of the training data. This expansion reduced the risk of overfitting to local patterns and progressively guided the model toward global applicability. Once such a model was established, FPS could be performed within catalysts predicted to be high-performing, called seeds generation. Finally, through the experimental evaluation of 420 new catalysts predicted by the ML models over 13 iterations of the closed-loop discovery system, diverse high-performing catalysts were identified, and deeper insights into the principles governing catalyst design were also gained.

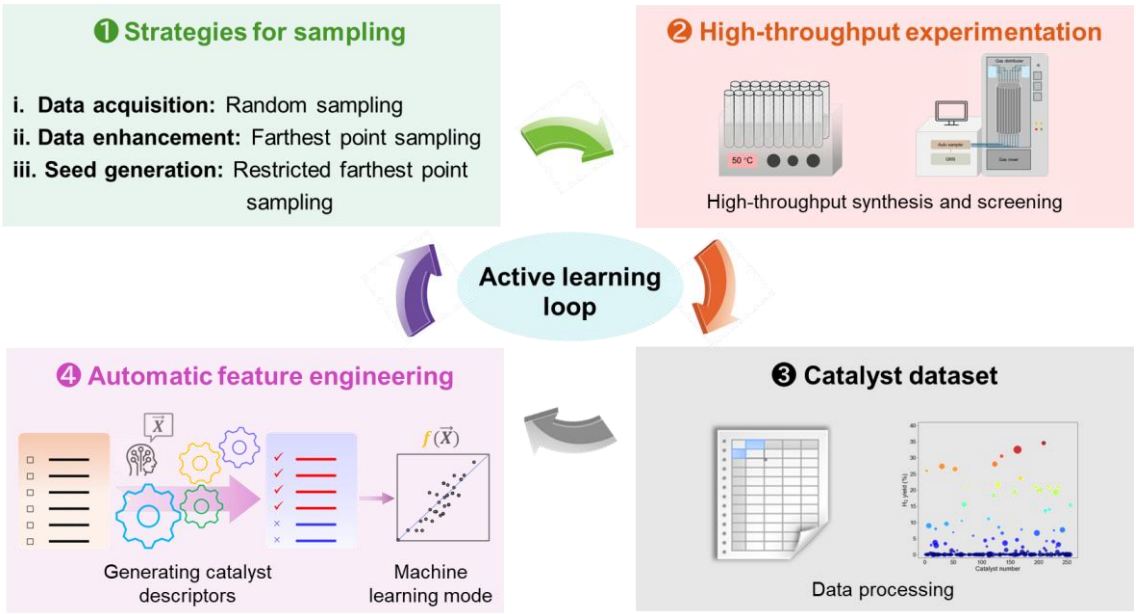

Figure 3.2. Workflow of adaptive active learning loop. (1) Three kinds of sampling strategies were employed: Initial training dataset was obtained mainly by random sampling; farthest point sampling (FPS) was implemented to pick up catalysts for training data enhancement; restricted FPS was applied to identify the most promising candidate catalysts, serving as seed generation. In this process, FPS targeted catalysts predicted to catalyst class (H_2 yield ≥ 2%) and within the 25–50% performance range. (2) Synthesis and performance evaluation of the catalysts were performed on the in-house developed high-throughput experimentation (HTE) platform. (3) High-quality catalyst dataset for model training and correction. (4) Automatic feature engineering (AFE) generated descriptors most relevant to the target catalysis, by producing a predictive model capable of identifying candidates with novel performance potential. New catalysts were sampled, synthesized and evaluated, and fed back into the dataset to retrain the descriptors and model, thereby completing the data-driven discovery loop.

3.2.2. Elemental library

My initial scope encompassed 61 elements from the periodic table, including all typical metals, transition metals, *p*-block metals, and lanthanides up to the 6th period, which was motivated by the intent to explore the widest possible compositional and combinatorial space of potential catalysts supported on γ-Al_2O_3, ensuring no promising candidate was overlooked due to preconceived notions or biases. In practice, I adopted a stepwise strategy to cover the 61 elements, rather than attempting to span the entire space at once. As the first step in this incremental approach, I previously developed and published a systematic element selection strategy [33]. This strategy combined physicochemical diversity optimization via principal component analysis (PCA) and farthest point sampling (FPS), while also considering practical factors such as cost, safety, and redundancy. Following these criteria, the initial element set comprising 17 elements was established: Li, Al, Ca, V, Ni, Nb, Rh, Ag, Sn, Cs, Ba, Ce, Sm, Hf, Ir, Au, and Bi.

In this adaptive active learning loop, the primary objective was to accelerate the convergence of the model toward a comprehensive global model capable of accurately capturing the unknown catalyst design space. Expanding the element set within the dataset played a critical role in achieving this objective, as it eliminated potential alternative models that might fail to generalize effectively and reduced the risk of overfitting to a limited subset of elements. Therefore, I extended the elemental set during testing in Loops 4, 7, and 12, corresponding to the second, third and final elemental sets, respectively. To facilitate the effective expansion of the elemental set, I also established

a method for adding a specified number of new elements while simultaneously removing an equivalent number from the current element library. This approach allows us to control the rate of knowledge expansion and minimize the loss of potentially important elemental combinations.

The element set was updated to the second one at Loop 4. The newly added elements were selected to be distant from the first element set and also from each other, where FPS was performed on top of the first element set within the PCA-contracted elemental feature space. Based on this, 8 new elements were incorporated, including Mg, K, Mn, Cu, Ga, Zr, Pd, and W, while the same number of elements were removed from the first element set to maintain the size of the test set. The selection of the removed elements was performed based on an elemental importance analysis. In this analysis, the predictive models generated during the iterative process were used to evaluate both the frequency of each element's occurrence in the positive list (defined as catalysts with H_2 yield ≥2%) and the average H_2 yield associated with each element within this list. The product of these two metrics was defined as the elemental importance. The average of the elemental importance over Loops 3 and 4 was used to remove 8 elements with lower importance: V, Ag, Sn, Cs, Ba, Ce, Sm, and Bi (**Figures 3.3a**). These elements were predicted to occur less frequently in high-performing catalysts compared with the retained elements, ensuring that the removal minimally impacts the identification of optimal catalyst compositions. The refined second elemental set thus consisted of 17 elements: Li, Mg, Al, K, Ca, Mn, Ni, Cu, Ga, Zr, Nb, Rh, Pd, Hf, W, Ir, and Au.

A similar refinement process was performed at Loop 7, leading to the third element set. According to the average elemental importance across Loops 6 and 7 (**Figures 3.3b**), elements with lower importance, namely Mg, K, Ca, Cu, Ga, Zr, Hf, and Au, were excluded. The third elemental set was consequently established, consisting of 17 elements: Li, Al, Sc, Mn, Fe, Co, Ni, Zn, Y, Nb, Mo, Rh, Pd, Ta, W, Ir, and Pt.

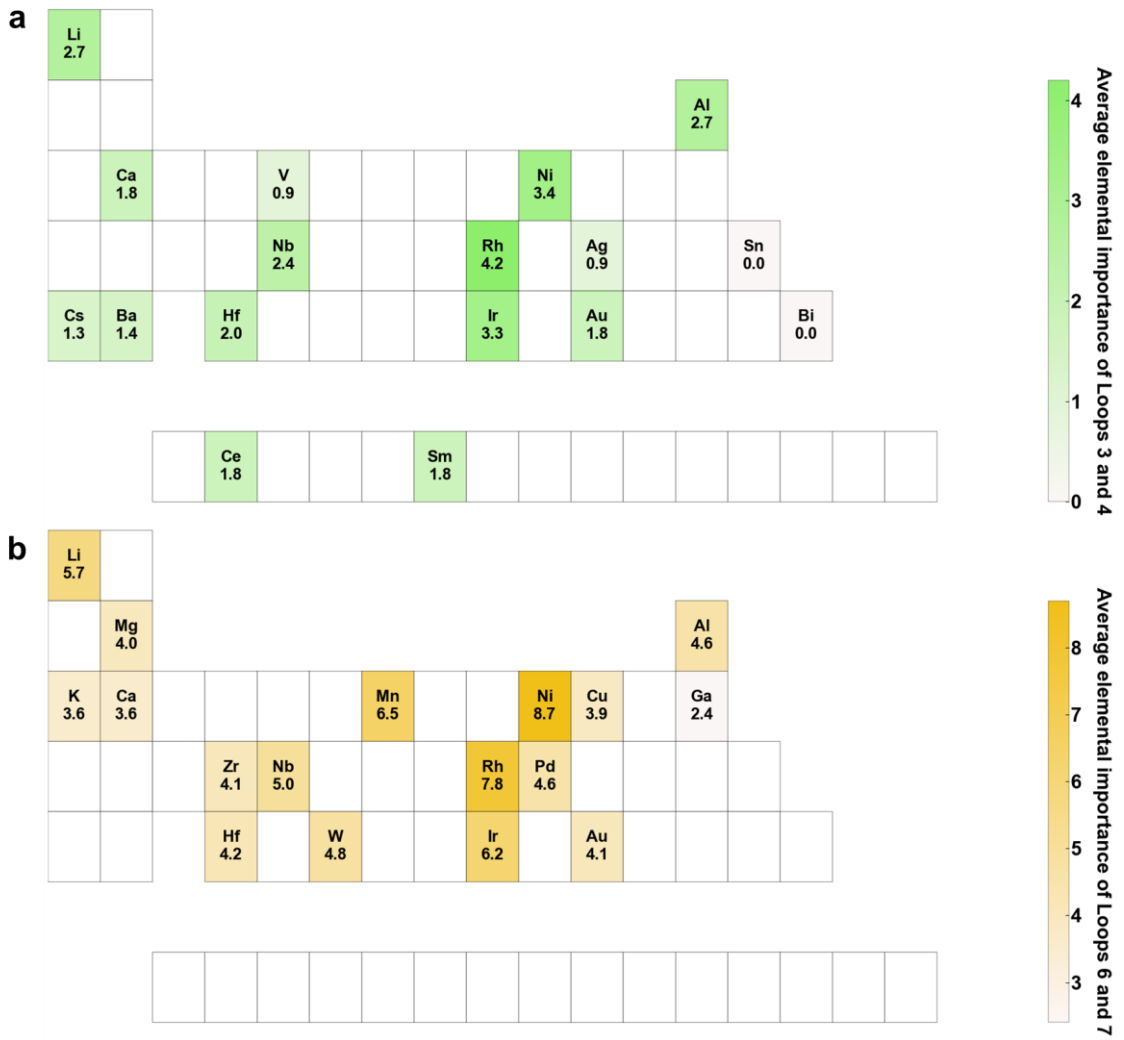

Figure 3.3. Elemental importance analysis during the active learning loop, where the elemental importance is defined as the product of an element's frequency of appearance in the positive list and its average H_2 yield in the positive list, scaled by 10^{-5}. (a) Average

elemental importance of Loops 3 and 4, (b) average elemental importance of Loops 6 and 7.

Eventually after Loop 12, the elemental set was expanded to 45 elements, removing 16 elements from the original 61 that were too costly and/or risky (Be, Cr, Tc, Ru, Cd, Pm, Dy, Ho, Tm, Yb, Lu, Re, Os, Hg, Tl, and Pb).

3.2.3. Automatic feature engineering

3.2.3.1. Feature collection

I collected 58 features of elements from XenonPy. These features involve a wide range of properties that could influence catalytic behavior, such as atomic radius, electronegativity, and bond energies.

3.2.3.2. Feature assignment

A series of mathematical operations were applied to the aforementioned elemental features, assigning primary features for individual catalysts. These features account for the elemental composition of individual catalysts using commutative operations, including maximum, minimum, weighted sum, weighted average, weighted sum of squared distance, weighted average squared distance, weighted product, and weighted geometric mean. Through this process, a total of 464 primary features were assigned to each catalyst.

3.2.3.3. Feature synthesis

To capture nonlinear relationships between elemental features and catalytic behavior, first-order features were synthesized by applying 12 mathematical functions (x, $x^{1/2}$, x^2, x^3, $\ln(x)$, $\exp(x)$, and their reciprocals) to each of the primary features, resulting in a total of 5,568 first-order features.

3.2.3.4. Feature selection

Feature selection is crucial for constructing reliable predictive models, particularly when dealing with a large number of synthesized high-order features [21,38]. Additionally, to address the issue of various non-catalysts, where feature values widely ranged despite the target performance being constant (zero), a two-step feature selection process was implemented.

In the first step, I employed random forest classification across the entire dataset. During this process, the H_2 yield served as the target variable. A genetic algorithm (GA) was used in conjunction with leave-one-out cross-validation (LOOCV) to identify 8 features that maximized balanced accuracy, a metric that accounts for class imbalances and ensures equitable consideration of all classes in the dataset. Subsequently, Huber regression was applied to the refined dataset that excluded non-catalysts with predicted H_2 yields below 2% from the entire dataset. GA was also utilized to select 8 or 12 features that minimized the MAE in LOOCV. Huber regression was adopted for its robustness in balancing sensitivity to subtle variations with resilience against the distorting effects of

outliers [39]. The number of features retained at each stage was empirically determined to balance cross-validation performance with computational efficiency.

3.2.4. Strategies for sampling

In this chapter, I implemented three sampling strategies to construct and expand my dataset, demonstrating the effectiveness of an active learning iterative loop combined with AFE for catalyst development. The dataset was obtained through a standardized protocol, ensuring consistent data collection—critical for reliable machine learning. A brief overview of the sampling strategies is given below.

3.2.4.1. Random sampling

Random sampling is widely employed in statistics and data science to ensure that every sample has an equal probability of being selected, reducing human bias. It is particularly useful when there is no prior knowledge or when the data distribution is unknown [18,34]. In this chapter, the initial dataset comprised 277 catalysts, each defined by elemental composition and performance, primarily generated through random sampling. The catalysts were structured as A–B–C–…/γ-Al_2O_3, where elements (up to five) were randomly selected from the initial elemental set defined in **3.2.2**. Their molar amounts were also randomly assigned within specified constraints. The total elemental loading ranged from 0.875 to 3.5 mmol per gram of support (mmol/g-support). The upper limit of 3.5 mmol/g-support corresponds to a nickel loading of 17 wt%, while the lower limit,

set at 25% of the maximum, ensured sufficient loading for meaningful results. Each individual element's loading was randomly determined but required a minimum of 0.00875 mmol/g-support, which represents 1% of the minimum total loading.

3.2.4.2. Farthest point sampling

To validate and refine the obtained machine learning model, each active learning loop incorporated 20 or 40 new catalysts for experimental testing. The resulting data were fed back into the AFE process, iteratively updating the descriptor space. In this process, PCA was applied to the descriptors selected by the two-step supervised machine learning model, representing each catalyst in a three-dimensional space and mitigating potential collinearity among descriptors [35]. FPS was employed within this contracted descriptor space to select catalysts that were most dissimilar to the catalysts contained in the training data.

3.2.4.3. Seed generation

The seed generation utilized both classification and regression models, rigorously validated through active learning loops, to capture key features of high-performance catalysts and propose the most promising candidates. During this process, FPS sampling targets a predicted class as catalyst (H_2 yield $\geq$ 2%) and performance range of 25–50%, with the upper limit set to avoid unphysical entries rooted to classification failures. To further enhance the seed generation efficiency, data from the recommended candidates

were also fed back into the AFE process, improving the model's generalization. This iterative approach ultimately established robust descriptors and model, facilitating the identification of various promising catalysts and a deeper understanding of their fundamental design principles.

3.2.5. High-throughput experimentation

In this study, all catalysts were prepared and evaluated using the same experimental procedures and conditions as those employed during the acquisition of the initial training data. The detail is provided below.

3.2.5.1. Chemicals

The metal precursors utilized in this chapter were sourced from commercially available suppliers: $LiNO_3$, KNO_3, $Mn(NO_3)_2{\cdot}6H_2O$, $Ni(NO_3)_2{\cdot}6H_2O$, $Ga(NO_3)_3{\cdot}xH_2O$, $AgNO_3$, $In(NO_3)_3{\cdot}3H_2O$, $Sm(NO_3)_3{\cdot}6H_2O$, $Gd(NO_3)_3{\cdot}6H_2O$, and $Bi(NO_3)_3{\cdot}5H_2O$ from FUJIFILM Wako Pure Chemical; $Mg(NO_3)_2{\cdot}6H_2O$, $Al(NO_3)_3{\cdot}9H_2O$, $Ca(NO_3)_2{\cdot}4H_2O$, $Fe(NO_3)_3{\cdot}9H_2O$, $Sr(NO_3)_2$, $(NH_4)_6Mo_7O_{24}{\cdot}4H_2O$, $5(NH_4)_2O{\cdot}12WO_3{\cdot}5H_2O$, $La(NO_3)_3{\cdot}6H_2O$, $Eu(NO_3)_3{\cdot}6H_2O$, and $Tb(NO_3)_3{\cdot}6H_2O$ from Kanto Chemical; $NaNO_3$, $Sc(NO_3)_3{\cdot}xH_2O$, $Ti(OC_2H_5)_4$, $VOSO_4{\cdot}xH_2O$, $Co(NO_3)_2{\cdot}6H_2O$, $Cu(NO_3)_2{\cdot}3H_2O$, $Zn(NO_3)_2{\cdot}6H_2O$, $RbNO_3$, $Y(NO_3)_3{\cdot}6H_2O$, $ZrO(NO_3)_2{\cdot}xH_2O$, $Nb(OC_2H_5)_5$, $Rh(NO_3)_3{\cdot}xH_2O$, $Pd(NO_3)_2{\cdot}2H_2O$, $SnSO_4$, $CsNO_3$, $Ba(NO_3)_2$, $Ce(NO_3)_3{\cdot}6H_2O$, $Pr(NO_3)_3{\cdot}6H_2O$, $Nd(NO_3)_3{\cdot}6H_2O$, $Er(NO_3)_3{\cdot}5H_2O$, $Ta(OC_2H_5)_5$, $H_2IrCl_6{\cdot}xH_2O$,

$H_2PtCl_6 \cdot 6H_2O$, and $HAuCl_4 \cdot 3H_2O$ from Sigma-Aldrich; $Hf(OC_2H_5)_4$ from Alfa Aesar. Aluminum oxide powder (γ-Al_2O_3, 164 m^2/g) was purchased from Sumitomo Chemical Industry and used as the catalyst support. Deionized (DI) water or ethanol (99.5%, FUJIFILM Wako Pure Chemical Corporation) was used to dissolve metal precursors.

3.2.5.2. Catalyst synthesis

The catalysts were synthesized following parallelized wet impregnation established in Chapter 2 [36,37]. Support powder (1.0 g) was impregnated with a 5.0 mL solution containing a specified amount of metal precursors with the aid of a pipetting robot (Andrew+, Andrew Alliance). The mixture was stirred for 6 hours at 50 °C on a parallel hot stirrer (ReactiTherm, Thermo Scientific), followed by vacuum drying in a centrifugal evaporator (CVE-3100, EYELA) at 90 °C for 4 hours and calcination in air at 500 °C for 4 hours using a muffle furnace (FT-001W, FULL-TECH). The catalyst thus obtained was milled using an automated mortar and pestle (ALM-90DM, NITTO KAGAKU) before any subsequent use. Each batch of preparation involved 20 or 40 catalysts. For water-sensitive precursors, the impregnation process was performed in two steps: first, in an aqueous solution of non-sensitive precursors , followed by an ethanol solution of sensitive precursors.

3.2.5.3. Evaluation of catalysts

All catalysts were evaluated using a previously developed in-house high-throughput screening (HTS) platform designed by Taniike et al. [18,19]. The setup comprises a gas mixing unit (MU-3504, HORIBA STEC), a flow distributor, 20 quartz reaction tubes, an auto sampling module, and a quadrupole mass spectrometer (QMS, Transpector CPM 3, INFICON). A predefined gas mixture was generated and equally divided among the 20 parallel channels, each containing a 10 mm catalyst bed supported on quartz wool. The reaction tubes were arranged within a hollow tubular furnace segmented into three zones, with the outer zones acting as thermal buffers to maintain a stable temperature in the central zone where the catalyst is located. Prior to testing, catalysts were reduced under a hydrogen/argon atmosphere (10/90 v/v) at 800 °C for 1 hour. The dry reforming of methane (DRM) reaction was then carried out at 500 °C using a CH_4/CO_2/Ar mixture (3/3/4 mL/min/channel), resulting in a gas hourly space velocity (GHSV) of approximately 10,000 mL gas$\cdot h^{-1}\cdot g^{-1}_{cat}$. To ensure data consistency and minimize the influence of transient behavior, catalytic performance was assessed by averaging the signal between 15,000 and 20,000 seconds on stream. This steady-state window enabled reliable comparisons across the 20 catalysts evaluated simultaneously.

3.2.6. Catalyst phylogenetic tree

Originally developed to depict evolutionary relationships among biological species, the catalyst phylogenetic tree has recently been adapted as a powerful visualization framework for complex catalyst datasets [40]. The catalyst phylogenetic tree

systematically organizes catalysts based on their elemental compositions and encodes their physicochemical similarity into a hierarchical structure. This approach provides a global overview of catalyst diversity and enables intuitive interpretation of design trends, evolutionary trajectories, and compositional novelty within expansive catalyst design spaces [41].

Therefore, I applied the phylogenetic tree analysis to systematically compare the catalysts discovered through the active learning loop with literature-reported catalysts for DRM at 500 °C that were previously compiled by Şener et al. (2002–2014) [42]. By projecting both datasets onto the same phylogenetic tree, I was able to compare the variety of catalysts discovered in this work against history. Specifically, a unified representation and distance-based similarity approach were established. Each catalyst was represented as a combination of minor and support elements, sorted by atomic number. Then, a chemically informed distance matrix was constructed to quantify similarities between catalyst formulations. Using the derived distance matrix, a hierarchical phylogenetic tree was constructed via the neighbor-joining algorithm. This tree provides an intuitive visualization of the compositional relationships among catalysts. Each node represents a unique formulation, and visual enhancements such as color-coded metadata were applied to improve interpretability and reveal patterns across the catalyst space.

3.3. Results and discussion

3.3.1. Adaptive active learning exploration of DRM catalysts

In this chapter, I conducted a comprehensive and systematic exploration of A(X_1)–B(X_2)–C(X_3)–…/γ-Al_2O_3-type catalysts for DRM, where each formulation contained no more than five elements. Each catalyst was defined by a unique set of element loadings X, with the total loading constrained to a maximum of 3.5 mmol/g-support. The catalyst design space encompassed 45 elements, including 7 main active elements (Fe, Co, Ni, Rh, Pd, Ir, Pt), 38 promoter or additive elements, and one support material. Even when restricted to five-element combinations, and assuming individual elemental loadings ranging from 0.1 to 3.5 mmol/g-support (with a step size of 0.1), the number of possible catalyst candidates easily exceeds 10^{11}. As a starting point, 277 catalysts in the initial dataset were predominantly generated through random sampling within the compositional space defined by the initial 17 elements and were labeled as “Loop 0”. Subsequently, a subset of candidate catalysts was selected for experimental validation based on the predicted performance classification and expected H_2 yields generated by two-step ML models trained on the initial dataset using AFE. To ensure compositional diversity, the selection process was further guided by FPS strategy. Detailed procedures are also provided in the Methods section. Through this iterative approach, I progressively refined the dataset by eliminating descriptors not applicable to unseen catalysts, ultimately establishing more reliable and globally applicable catalyst design strategies. The complete DRM dataset is provided in **Table A1**. **Table A2** provides a summary of the

selected descriptors and the corresponding model performances during the training and cross-validation stages for each iteration of the active learning loop.

Figure 3.4 provides a summary of the performance scores associated with the two-step ML training process, consisting of classification followed by regression. Notably, during the classification stage, the balanced accuracy scores obtained in both the training and cross-validation were highly consistent across all active learning loops, ranging narrowly between 0.90 and 0.96. Balanced accuracy is particularly well-suited, as it compensates for class imbalance by averaging the recall across both classes. This metric ensures that the model maintains strong performance not only on the majority class (H_2 yield < 2%) but also retains sensitivity to the minority class (H_2 yield ≥ 2%), thereby offering a more equitable and comprehensive assessment of classification performance. In the subsequent regression stage, the MAE obtained from cross-validation closely matched that from the training phase, indicating the absence of overfitting. Both MAE_{train} and MAE_{CV} remained below 4.0%, suggesting that the regression model achieved reasonable predictive accuracy despite the limited dataset size. This level of error is sufficiently low for practical applications, such as distinguishing between catalysts with H_2 yields of 10% and 20%. Notably, a slight upward trend in MAE was observed over the course of the active learning loops. This increase can be attributed to the progressive expansion of the elemental set that introduced greater catalyst diversity. FPS specifically prioritized the inclusion of compositions that were maximally distinct within the defined descriptor space [24]. While such diversity inevitably led to a moderate rise in prediction error, it

played a critical role in filtering out models lacking global generalizability. Importantly, the overall variation in MAE remained relatively small, indicating that the model's predictive behavior became increasingly stable as the dataset expanded.

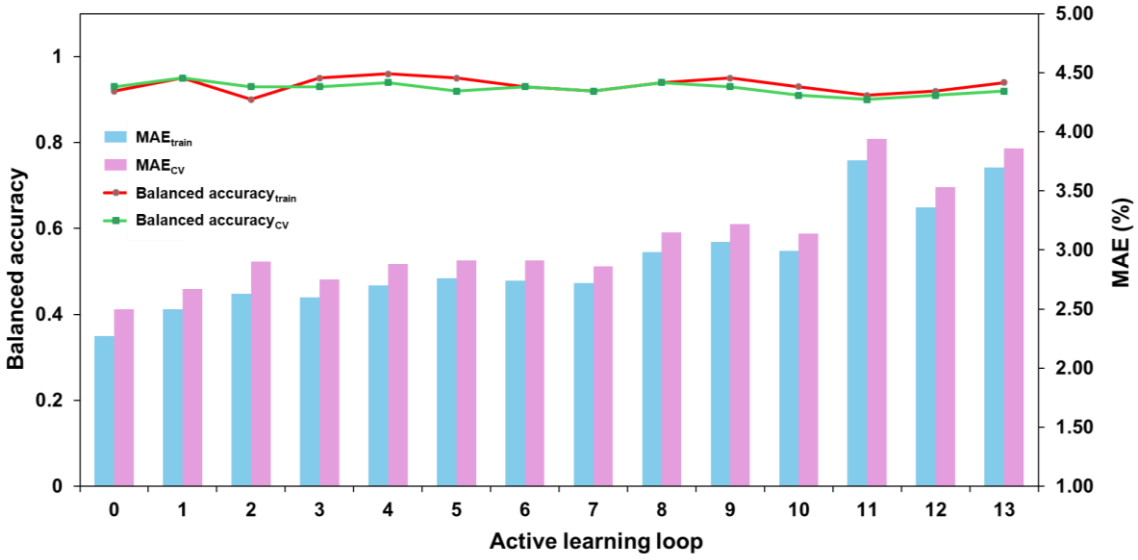

Figure 3.4. The model scores during classification and regression across active learning loops. Balanced accuracy reflects the performance of the classification model on the entire catalyst dataset within each loop, accounting for class imbalance. The mean absolute error (MAE) was calculated for the regression models trained in each loop using catalysts with predicted H_2 yields $\geq 2\%$. A lower MAE indicates greater predictive accuracy of the model in estimating the H_2 yield.

Through the experimental evaluation of 420 catalysts across the above 13 active learning loops, the performance of both the classification and regression models during the testing phase was assessed and more than 100 high-performing catalysts for low-

temperature DRM were identified. A detailed description of this exploration process is presented below.

First, a key aspect of this workflow lies in the progressive expansion of the elemental design space. In this work, I employed an elemental feature-based representation to encode each catalyst, accounting for both the compositional makeup and the invariance to elemental order, rather than directly treating elements as discrete categorical symbols. To construct this representation, I leveraged the XenonPy library to systematically collect 58 descriptors for 94 elements, ranging from H to Pu, drawing from all available data sources [43]. These features include a broad range of elemental properties such as electronegativity, atomic radius, density, and melting point. At the outset, all features were assumed to carry equal prior importance. AFE was then employed to generate a large number of derived features and, within a supervised machine learning, to recommend feature combinations that optimize model performance (see **Table A2**). This enables the obtained model to capture feature-based chemical similarities between elements, thereby allowing for the inclusion of elements that were not present in the training data. While previous studies have typically relied on manually pre-selected elemental features to describe multi-element catalysts [44], such approaches often suffer from limited coverage and potential human bias, which constrain the model's ability to explore unknown regions of the materials space.

Accordingly, strategic updates to the elemental library were implemented in Loops 4, 7, and 12. As a result, four distinct elemental sets were applied across different stages of

the active learning process: Loops 0–3, 4–6, 7–11, and 12–13, as defined in Section 3.2.1. Correspondingly, the catalyst test sets were adjusted based on the evolving elemental selection strategy throughout the active learning loops (**Table A3**).

In addition, strategic sampling represents another critical component of active learning loop exploration. The initial dataset was primarily constructed through random sampling to minimize human bias. To develop more robust ML models, FPS was employed to identify catalysts that are most dissimilar in physicochemical properties from the existing training data, thereby promoting iterative refinement of the descriptor space. Seed generation, essentially a constrained form of FPS, was introduced to propose the most promising candidate catalysts. Together, FPS and seed generation contributed to data augmentation and improved the generalization performance of the model.

Therefore, starting from Loop 7, seed generation was partially introduced, accounting for half of the 40 selected candidates. By Loop 10, seed generation was fully integrated into the sampling strategy.

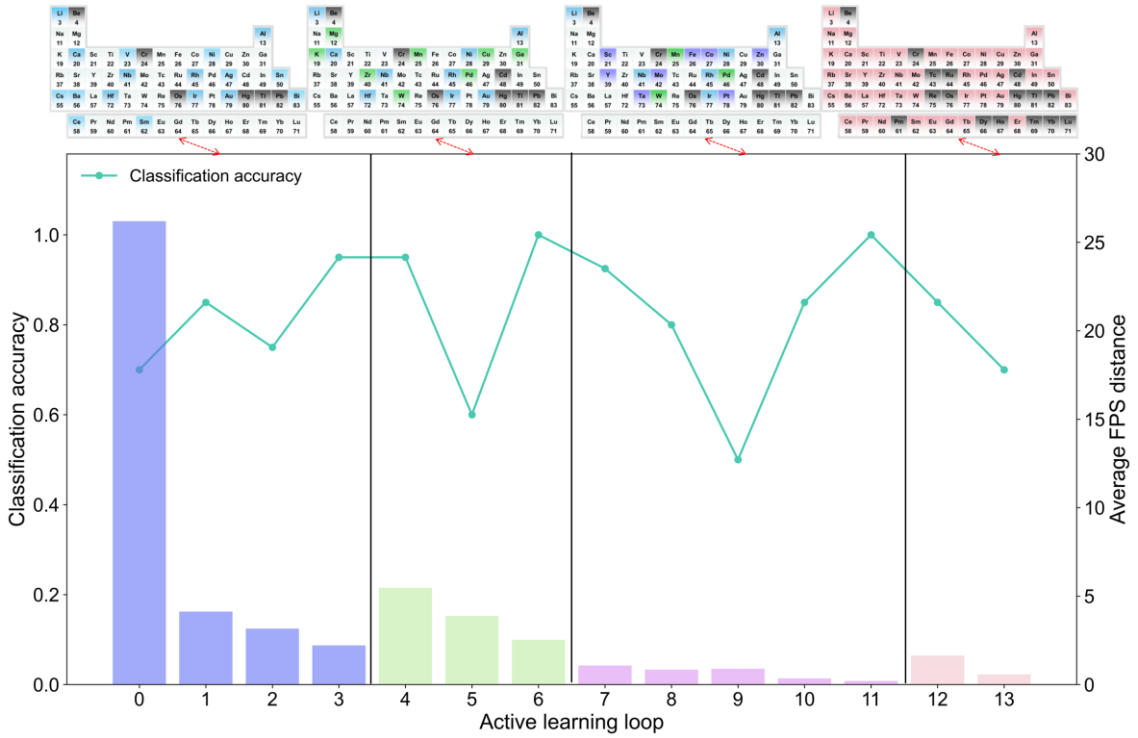

Figure 3.5. Model performance during the testing phases of classification and regression across active learning loops. Line chart illustrates the classification accuracy of the model during the testing phase for each active learning loop. The bar chart displays the mean FPS (Farthest point sampling) distance of the test catalysts in each loop, reflecting their physicochemical similarity from the training dataset in feature space. As the active learning loop progressed, the elemental space was expanded from an initial set of 17 elements to a final set of 45. Further details on the test sets and elemental sets are provided in Table A3.

Figure 3.5 shows the model's performance during the testing phases. Classification accuracy was used to evaluate the ability of the random forest classifier to distinguish between non-catalysts (H_2 yield < 2%) and catalysts (H_2 yield ≥ 2%). Additionally, average FPS distance was used as an estimate of the diversity introduced at each loop.

It can be observed that the classification accuracy tends to decrease when the elemental set is updated. This indicates that the classifier's ability to generalize to previously unseen catalyst compositions remain limited, and additional learning cycles may be required to achieve higher predictive accuracy. Loop 0 exhibited the largest average FPS distance, indicating maximum compositional diversification. As the active learning process progressed, the FPS distances gradually declined, reflecting improved coverage of the explored space. However, when the elemental space was expanded, FPS distances increased accordingly, indicating that the introduction of new elements effectively broadened the diversity of the selected catalysts. Ultimately, the active learning process was terminated at Loop 13, by which point the model's average FPS distance had substantially decreased. This suggests that the remaining novelty within the explored space was limited, and that the vast catalyst space constructed from the final set of 45 elements had been effectively and comprehensively sampled. Most chemically meaningful regions of the design space had been successfully captured. In the following, a detailed visualization of the discovered catalysts and their performance profiles is presented.

Figure 3.6 visualizes the H_2 yield of all 420 newly tested catalysts throughout the active learning loops. To distinguish different sampling strategies, catalysts selected through seed generation are marked with diamond-shaped symbols. It is evident that, as the iterative loops progressed, the maximum H_2 yield of the tested catalysts increased in a stepwise manner, eventually exceeding 35%. This trend validates the effectiveness of the proposed workflow in discovering high-performance catalysts. In Loops 0–6, all catalysts were selected using unconstrained FPS, resulting in a limited number of high-yielding catalysts. However, these early data points played a crucial role in establishing a robust foundation for model training. A notable shift in performance was observed following the introduction of seed generation in Loop 7. From this point onward, the trend of H_2 yield clearly improved, with an increasing number of high-performance catalysts successfully identified in subsequent loops.

Overall, the combination of strategic sampling and progressive elemental expansion enabled the AFE process to capture a broad and diverse catalyst space. This, in turn, facilitated the generation of descriptors most relevant to high-performance catalyst discovery and contributed to the development of a robust, globally applicable predictive model. As a result, a wide range of promising DRM catalysts were effectively identified.

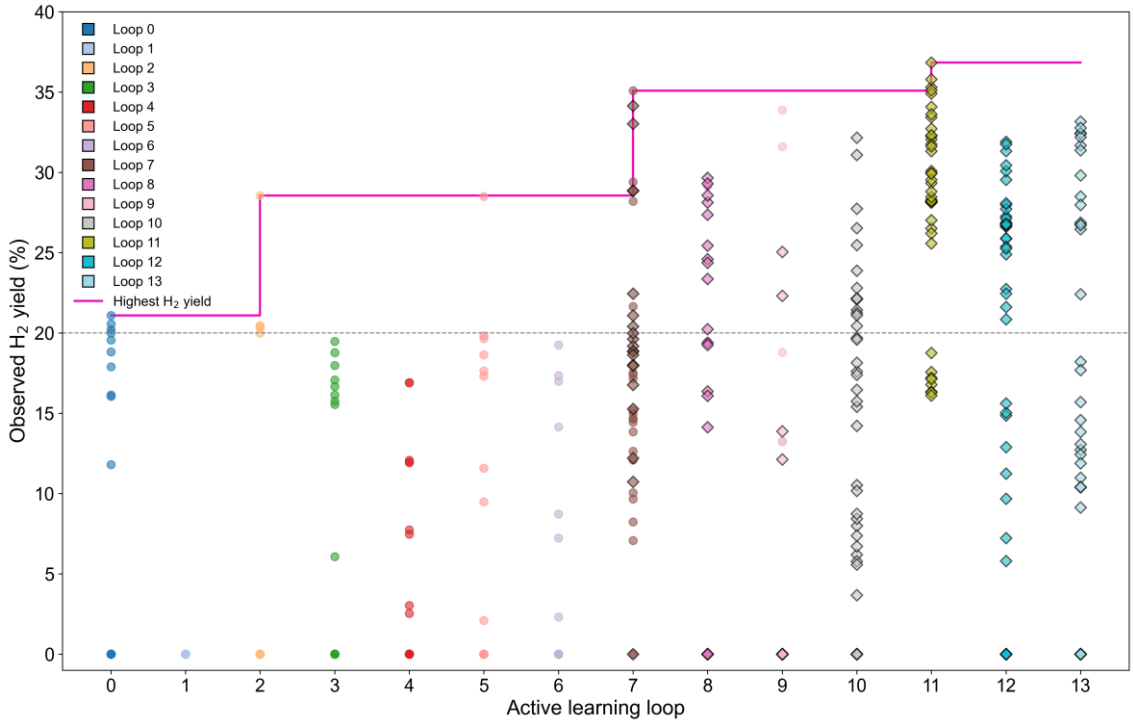

Figure 3.6. Visualization of DRM catalyst datasets. AFE-assisted active learning exploration of DRM catalysts. A total of 420 catalysts were newly added during the active learning loops. Catalysts sampled for seed generation in each loop are represented by diamond markers, while those added via general data enhancement using farthest point sampling (FPS) are shown as circles. The pink solid line indicates the highest observed H_2 yield in each loop.

In this section, the developed active learning strategy enabled systematic exploration of an ultra-large catalyst design space through an adaptive, data-driven process. By strategically diversifying compositions and progressively expanding the elemental set, the framework achieved a balance between exploration of unknown regions and

exploitation of high-performing areas. This approach not only ensured that the ML models progressively improved in generalizability and robustness but also accelerated the discovery of various promising DRM catalysts under low-temperature conditions.

3.3.2. Visualization of phylogenetic tree

To construct the catalyst phylogenetic tree, I first collected a curated DRM dataset compiled by Şener et al. [42], which contains 5,521 experimental data points published between 2005 and 2014. This dataset encompasses a wide range of catalyst types tested under various reaction temperatures, durations, and preparation conditions. For a meaningful comparison of catalyst performance under low-temperature DRM conditions (500 °C), I selected 252 data points from the dataset as representative literature references. These were subsequently combined with the 697 data points obtained from the active learning-driven discovery. As detailed in section 3.2.6, all catalysts were grouped according to their elemental compositions. Each group could contain multiple data entries, reflecting the common practice of repeated testing on identical compositions for optimization or validation purposes.

Since many literature-reported data points lack explicit H_2 yield values, I first established a linear relationship between CH_4 conversion and H_2 yield based on my 697-catalyst dataset (**Figure 3.7**). This model was then used to estimate the H_2 yield values for the literature catalysts. By excluding catalyst groups with an average H_2 yield below 20%, the final phylogenetic tree visualizes 109 catalyst groups, mapping the relationship

between their elemental compositions and corresponding average H_2 yields (**Figure 3.8a**). Among them, 102 groups were identified in this work, and 7 were derived from literature sources.

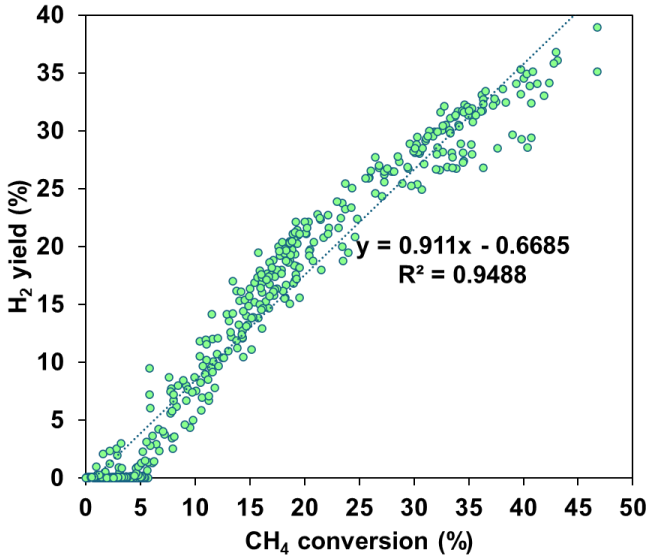

Figure 3.7. Relationship between CH_4 conversion and H_2 yield based on the 697-catalyst dataset.

A clear comparison reveals that the number of high-performance catalysts identified in this work far exceeds those discovered over the past decade, highlighting the power of the adaptive active learning loop in overcoming the limitations of conventional discovery paradigms and expediting the search for superior catalyst formulations. Based on the structure of the phylogenetic tree, three distinct catalyst lineages emerge: (1) the active metal lineage, represented by transition metals such as Fe, Ni, and Co; (2) the platinum-group metal (PGM) lineage; (3) the alkali metal lineage. In general, PGMs function as highly active centers for methane activation, whereas alkali elements increase surface

basicity and facilitate CO_2 adsorption. transition metals such as Fe, Ni, and Co, by contrast, serve as more economical alternatives and frequently exhibit synergistic effects when integrated into bimetallic or multimetallic systems.

In addition, distinct trends emerge within each lineage. It is evident that the alkali metal lineage constitutes the predominant structure within the phylogenetic tree. In the alkali metal lineage, several of the most outstanding catalysts were identified, including Li-Mn-Ni-Nb/Al and Li-Ni-Ta/Al (both achieving H_2 yields of 35.1%), as well as Li-Al-Ni-Nb/Al (33.6%). A notable trend in this lineage is the frequent incorporation of Li, which contrasts with its limited representation in historical literature datasets. Nevertheless, emerging studies have underscored Li's capacity to enhance surface basicity and facilitate DRM activity, positioning it as a promising alkaline promoter for future catalyst development [45].

Another important branch corresponds to the PGM-based lineage. Within this group, the Co–Rh/Al catalyst exhibits the highest H_2 yield (29.2%), followed by Al–Co–Ni–Pd/Al with a yield of 28.2%. For high performance, PGMs are often used in combination with active elements such as Co and Ni. Notably, many high-performing catalysts reported in the literature are also located within this lineage, indicating that previous studies on low-temperature DRM catalysts have largely remained within this compositional domain. This finding underscores the effectiveness of the adaptive discovery framework, which combines HTE and AFE, in accelerating the identification of novel and efficient DRM catalysts beyond conventionally explored regions. Within the

active metal (Fe, Ni, Co) lineage, Ni-Y/Al stands out with a H_2 yield of 33.4%, while other elements such as Al, Nb, Mn, and Ti also emerge as effective promoters, offering valuable insights for the development of cost-efficient and sustainable DRM catalysts.

In addition, **Figure 3.8a** highlights the high-performance catalysts with H_2 yields ≥30%, marked by asterisks. These catalyst combinations exhibit both notable commonality and compositional diversity. First, all catalysts contain Ni, confirming its role as the core active element. This observation aligns with the established understanding that Ni serves as an economically efficient and catalytically active component in DRM. Among the promoter elements, Li and Nb each appear 13 times, indicating their frequent use in enhancing catalyst performance when combined with Ni. Li, an alkali metal from Group I, increases the surface basicity of the catalyst, thereby promoting CO_2 adsorption and activation, which in turn facilitates the DRM reaction [46]. Nb contributes by increasing the surface area and improving the dispersion of Ni, leading to improved catalytic activity [47]. Other frequently occurring elements include Al and Co. Although Al is rarely reported in the literature for DRM, Co is a commonly used active metal. Notably, representative ternary combinations such as Li–Ni–Nb, Al–Ni–Nb, and Li–Al–Ni were frequently designed and tested, suggesting their high-performance potential. Furthermore, these high-performance catalysts with H_2 yields ≥30% discovered through active learning loop reveal expanded elemental diversity. In addition to known DRM-active elements, the compositional space also explored includes alkali metals (Li, K, Cs, Rb), transition metals (Sc, Ti, Mn, Y, Nb, Hf, Ta), and rare earth elements (Sm). Overall, these catalysts

maintain Ni as the central active component while incorporating a wide range of promoter elements across different categories. This reflects the potential of systematic exploration and data-driven methodologies beyond conventional empirical approaches.

In **Figure 3.8b**, the same tree structure used in **Figure 3.8a** is retained, while the number of active learning cycles is represented through a color gradient. This allows the progress of catalyst discovery throughout the adaptive learning process. This representation helps differentiate catalysts discovered in early versus later stages of the study. Literature-derived catalysts, which were not included in the active learning workflow, are assigned a cycle index of "–1" to indicate their external origin. At the initial stage of training, only a limited number of high-performance catalysts were identified. This is primarily due to the reliance on random exploration in the absence of prior knowledge, which is inherently inefficient for accurately locating optimal compositions. Therefore, early candidates were largely concentrated around formulations containing active elements such as Ni, Rh, and Ir, along with promoters like Li, Al, Nb, and Sm.

As the active learning process progressed, the number of high-performing catalysts increased significantly. In the later stages of the active learning process, catalysts with H_2 yields ≥30% began to appear more frequently, particularly from Loops 10 to 13. This improvement is primarily attributed to the seed generation strategy, which directed the model toward unexplored yet promising regions of the compositional space. Notably, several newly discovered high-performance catalysts incorporated K and Rb, such as K–Co–Ni–Rb–Nb/Al, K–Ni–Rb/Al, and Co–Ni–Rb/Al. These compositions were entirely

absent in the early stages of active learning, underscoring the model's capacity to uncover beneficial elements that were previously overlooked. In addition, catalysts containing rare earth elements (Y, Sc) and early transition metals (Ti, Ta, Mn) in combination with Ni were successfully identified in this phase, reflecting a broadening of the elemental scope driven by data-guided exploration.

While the earlier stages of active learning loop had already recognized the performance-enhancing roles of elements such as Li, Nb, and Cs when paired with active metals, the later-discovered combinations—such as Li–Mn–Ni–Nb, Li–Al–Sc–Ni–Nb, and Ni–Y–Cs—represent novel compositional frameworks that had not been observed previously. These findings demonstrate the power of iterative model refinement and strategic sampling in discovering non-intuitive yet highly effective catalyst designs beyond conventional empirical knowledge.

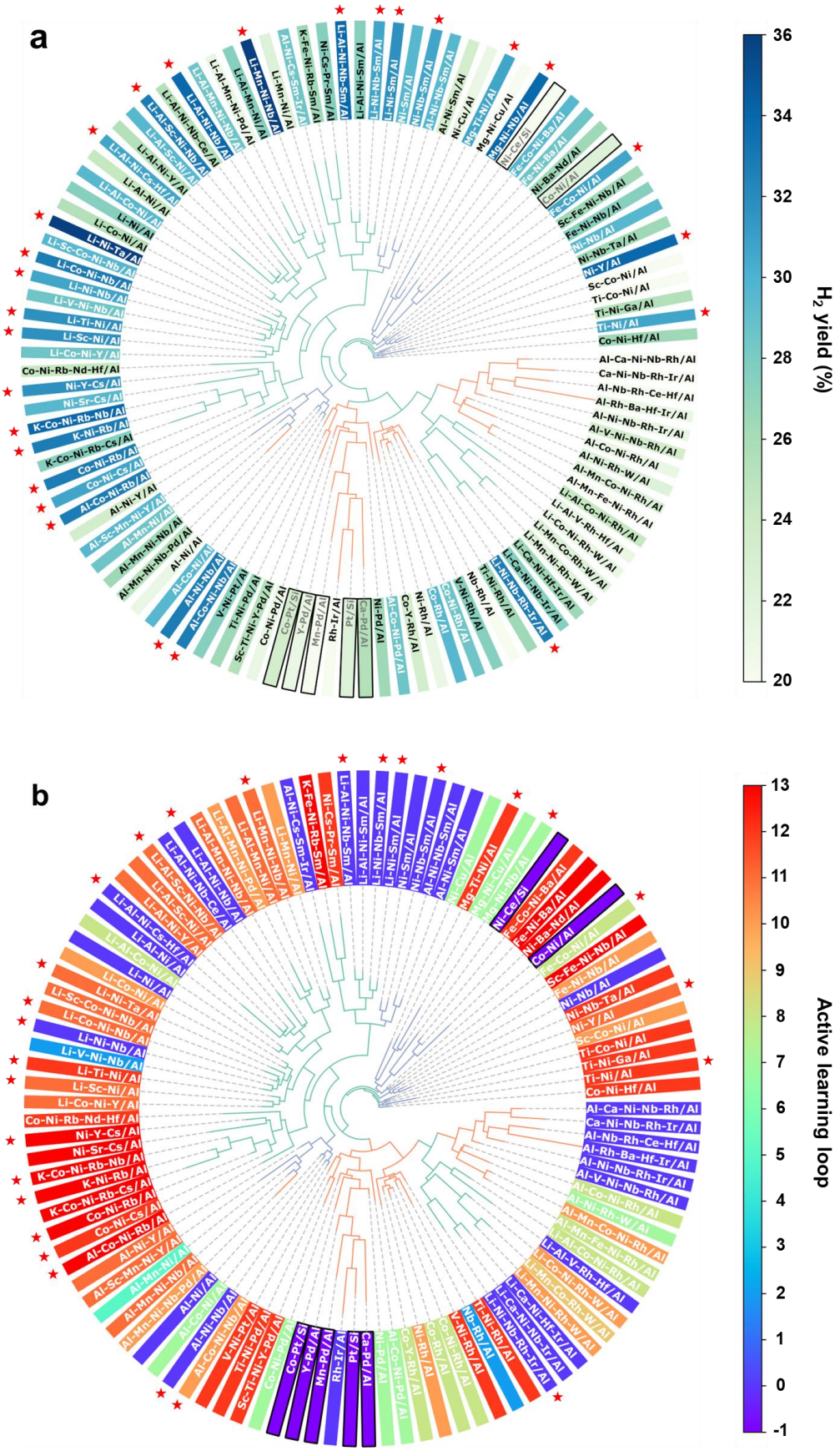
a
b
H2 yield (%)
Active learning loop
36
34
32
30
28
26
24
22
20
13
12
11
10
9
8
7
6
5
4
3
2
1
0
-1

Figure 3.8. Phylogenetic tree analysis for DRM catalysts. Catalysts are labeled using the format "elemental combination/support", where Al_2O_3 is abbreviated as Al. Zeolites are approximated as SiO_2 due to the absence of explicit Si/Al ratios in the literature dataset. This tree visualizes 109 catalysts with H_2 yields ≥ 20%, comprising 7 literature-reported catalysts (outlined in black) and 102 catalysts identified in this work. The background color of each node represents **a** average H_2 yield and **b** the corresponding active learning loop. Catalysts from the literature, which were not part of the active learning process, were assigned a loop index of "–1" to denote their external origin. Catalysts achieving exceptionally high H_2 yields above 30% are marked with red pentagrams. Branch colors reflect the structure of the phylogenetic tree: blue for the active metal lineage (Fe, Ni, Co), orange for the platinum-group metal (PGM) lineage, and green for the alkali metal lineage.

3.4. Conclusion

This chapter demonstrates the transformative potential of an adaptive active learning framework for catalyst discovery. By integrating HTE, AFE, and strategically guided sampling, I established a closed-loop discovery process capable of systematically navigating the vast uncharted compositional space of multi-element catalysts. Unlike conventional approaches constrained by prior knowledge and human intuition, this data-driven strategy enables the iterative refinement of descriptors based on experimental feedback, thereby accelerating the identification of high-performance catalysts.

Furthermore, I introduced a catalyst phylogenetic tree as an intuitive visualization tool to capture the evolutionary trajectories of elemental combinations, offering new insights into catalyst design strategies and the temporal emergence of superior compositions across the active learning loops. This revealed clear lineage structures associated with different catalyst classes, such as platinum group metal rich systems, alkali promoted catalysts, and transition metal-based formulations, and illuminated how high-performing catalysts emerged progressively over time.

Reference

[1] B. Hauer, Embracing nature's catalysts: a viewpoint on the future of biocatalysis, ACS Catal. 10 (2020) 8418–8427. https://doi.org/10.1021/acscatal.0c01708.
[2] I. Fechete, Y. Wang, J.C. Védrine, The past, present and future of heterogeneous catalysis, Catal. Today 189 (2012) 2–27. https://doi.org/10.1016/j.cattod.2012.04.003.
[3] C. Vogt, B.M. Weckhuysen, The concept of active site in heterogeneous catalysis, Nat. Rev. Chem. 6 (2022) 89–111. https://doi.org/10.1038/s41570-021-00340-y.
[4] M. Salciccioli, M. Stamatakis, S. Caratzoulas, D.G. Vlachos, A review of multiscale modeling of metal-catalyzed reactions: Mechanism development for complexity and emergent behavior, Chem. Eng. Sci. 66 (2011) 4319–4355. https://doi.org/10.1016/j.ces.2011.05.050.
[5] C. Spöri, J.T.H. Kwan, A. Bonakdarpour, D.P. Wilkinson, P. Strasser, The stability challenges of oxygen evolving catalysts: towards a common fundamental understanding and mitigation of catalyst degradation, Angew. Chem. Int. Ed. 56 (2017) 5994–6021. https://doi.org/10.1002/anie.201608601.
[6] Y. Nakaya, S. Furukawa, Catalysis of alloys: classification, principles, and design for a variety of materials and reactions, Chem. Rev. 123 (2022) 5859–5947. https://doi.org/10.1021/acs.chemrev.2c00356.
[7] E.S. Isbrandt, R.J. Sullivan, S.G. Newman, High throughput strategies for the discovery and optimization of catalytic reactions, Angew. Chem. Int. Ed. 58 (2019) 7180–7191. https://doi.org/10.1002/anie.201812534.
[8] J. Benavides-Hernández, F. Dumeignil, From characterization to discovery: artificial intelligence, machine learning and high-throughput experiments for heterogeneous catalyst design, ACS Catal. 14 (2024) 11749–11779. https://doi.org/10.1021/acscatal.3c06293.
[9] T.C. Le, D.A. Winkler, Discovery and optimization of materials using evolutionary approaches, Chem. Rev. 116 (2016) 6107–6132. https://doi.org/10.1021/acs.chemrev.5b00691.
[10] K.D. Collins, T. Gensch, F. Glorius, Contemporary screening approaches to reaction discovery and development, Nat. Chem. 6 (2014) 859–871. https://doi.org/10.1038/nchem.2062.
[11] L. Himanen, A. Geurts, A.S. Foster, P. Rinke, Data-driven materials science: status, challenges, and perspectives, Adv. Sci. 6 (2019) 1900808. https://doi.org/10.1002/advs.201900808.
[12] Z. Wang, Z. Sun, H. Yin, X. Liu, J. Wang, H. Zhao, C.H. Pang, T. Wu, S. Li, Z. Yin, Data-driven materials innovation and applications, Adv. Mater. 34 (2022) 2104113. https://doi.org/10.1002/adma.202104113.
[13] R. Ramprasad, R. Batra, G. Pilania, A. Mannodi-Kanakkithodi, C. Kim, Machine learning in materials informatics: recent applications and prospects, Npj Comput. Mater. 3 (2017) 54. https://doi.org/10.1038/s41524-017-0056-5.
[14] W. Chaikittisilp, Y. Yamauchi, K. Ariga, Material evolution with nanotechnology, nanoarchitectonics, and materials informatics: what will be the next paradigm shift in nanoporous materials?, Adv. Mater. 34 (2022) 2107212. https://doi.org/10.1002/adma.202107212.
[15] A.M. Mroz, V. Posligua, A. Tarzia, E.H. Wolpert, K.E. Jelfs, Into the unknown: how computation can help explore uncharted material space, J. Am. Chem. Soc. 144

(2022) 18730–18743. https://doi.org/10.1021/jacs.2c06833.
[16] I.M.S. Anekwe, S.O. Akpasi, E.M. Enemuo, D. Ashiegbu, S.I. Mustapha, Y.M. Isa, Innovations in catalytic understanding: A journey through advanced characterization, Mater. Today Catal. (2024) 100061. https://doi.org/10.1016/j.mtcata.2024.100061.
[17] M. Suvarna, J. Pérez-Ramírez, Embracing data science in catalysis research, Nat. Catal. 7 (2024) 624–635. https://doi.org/10.1038/s41929-024-01150-3.
[18] T.N. Nguyen, S. Nakanowatari, T.P. Nhat Tran, A. Thakur, L. Takahashi, K. Takahashi, T. Taniike, Learning catalyst design based on bias-free data set for oxidative coupling of methane, ACS Catal. 11 (2021) 1797–1809. https://doi.org/10.1021/acscatal.0c04629.
[19] T.N. Nguyen, T.T.P. Nhat, K. Takimoto, A. Thakur, S. Nishimura, J. Ohyama, I. Miyazato, L. Takahashi, J. Fujima, K. Takahashi, T. Taniike, High-throughput experimentation and catalyst informatics for oxidative coupling of methane, ACS Catal. 10 (2019) 921–932. https://doi.org/10.1021/acscatal.9b04293.
[20] W.A. Saidi, W. Shadid, G.t. Veser, Optimization of high-entropy alloy catalyst for ammonia decomposition and ammonia synthesis, The Journal of Physical Chemistry Letters, 12 (2021) 5185–5192. https://doi.org/10.1021/acs.jpclett.1c01242.
[21] T. Taniike, A. Fujiwara, S. Nakanowatari, F. Garcia-Escobar, K. Takahashi, Automatic feature engineering for catalyst design using small data without prior knowledge of target catalysis, Commun. Chem. 7 (2024) 11. https://doi.org/10.1038/s42004-023-01086-y.
[22] T. Mou, H.S. Pillai, S. Wang, M. Wan, X. Han, N.M. Schweitzer, F. Che, H. Xin, Bridging the complexity gap in computational heterogeneous catalysis with machine learning, Nat. Catal. 6 (2023) 122–136. https://doi.org/10.1038/s41929-023-00911-w.
[23] T. Toyao, Z. Maeno, S. Takakusagi, T. Kamachi, I. Takigawa, K.-i. Shimizu, Machine learning for catalysis informatics: recent applications and prospects, ACS Catal. 10 (2019) 2260–2297. https://doi.org/10.1021/acscatal.9b04186.
[24] A. Fujiwara, S. Nakanowatari, Y. Cho, T. Taniike, Acquiring and transferring comprehensive catalyst knowledge through integrated high-throughput experimentation and automatic feature engineering, Sci. Technol. Adv. Mater. (2025) 2454219. https://doi.org/10.1080/14686996.2025.2454219.
[25] Z. Huang, Z. Chen, J. Cheng, J. Zhang, S. Wang, T. Chen, X. Zhang, H. Pang, Recent progress in high-throughput on-chip synthesis, screening, and data-driven optimization: toward an electrocatalyst chip for catalysis universe exploration, Adv. Funct. Mater. 35 (2025) 2416117. https://doi.org/10.1002/adfm.202416117.
[26] J. Liu, W. Luo, L. Wang, J. Zhang, X.Z. Fu, J.L. Luo, Toward excellence of electrocatalyst design by emerging descriptor-oriented machine learning, Adv. Funct. Mater. 32 (2022) 2110748. https://doi.org/10.1002/adfm.202110748.
[27] G. Wang, S. Mine, D. Chen, Y. Jing, K.W. Ting, T. Yamaguchi, M. Takao, Z. Maeno, I. Takigawa, K. Matsushita, Accelerated discovery of multi-elemental reverse water-gas shift catalysts using extrapolative machine learning approach, Nat. Commun. 14 (2023) 5861. https://doi.org/10.1038/s41467-023-41341-3.
[28] S.M. Moosavi, K.M. Jablonka, B. Smit, The role of machine learning in the understanding and design of materials, J. Am. Chem. Soc. 142 (2020) 20273–20287. https://doi.org/10.1021/jacs.0c09105.
[29] K. Wittich, M. Krämer, N. Bottke, S.A. Schunk, Catalytic dry reforming of methane: insights from model systems, ChemCatChem 12 (2020) 2130–2147.

https://doi.org/10.1002/cctc.201902142.
[30] R.-J. Zhang, G.-F. Xia, M.-F. Li, W. Yu, N. Hong, D.-D. Li, Effect of support on the performance of Ni-based catalyst in methane dry reforming, J. Fuel Chem. Technol. 43 (2015) 1359–1365. https://doi.org/10.1016/S1872-5813(15)30040-2.
[31] C. Palmer, D.C. Upham, S. Smart, M.J. Gordon, H. Metiu, E.W. McFarland, Dry reforming of methane catalysed by molten metal alloys, Nat. Catal. 3 (2020) 83–89. https://doi.org/10.1038/s41929-019-0416-2.
[32] L. Zhou, J.M.P. Martirez, J. Finzel, C. Zhang, D.F. Swearer, S. Tian, H. Robatjazi, M. Lou, L. Dong, L. Henderson, Light-driven methane dry reforming with single atomic site antenna-reactor plasmonic photocatalysts, Nat. Energy 5 (2020) 61–70. https://doi.org/10.1038/s41560-019-0517-9.
[33] W. Du, P. Chammingkwan, K. Takahashi, T. Taniike, Unbiased dataset for methane dry reforming and catalyst design guidelines obtained by high-throughput experimentation and machine learning, J. Catal. 442 (2025) 115930. https://doi.org/10.1016/j.jcat.2024.115930.
[34] U. Zavyalova, M. Holena, R. Schlögl, M. Baerns, Statistical analysis of past catalytic data on oxidative methane coupling for new insights into the composition of high-performance catalysts, ChemCatChem 3 (2011) 1935–1947. https://doi.org/10.1002/cctc.201100186.
[35] W. Guo, A. Shafizadeh, H. Shahbeik, S. Rafiee, S. Motamedi, S.A.G. Nia, M.H. Nadian, F. Li, J. Pan, M. Tabatabaei, Machine learning for predicting catalytic ammonia decomposition: An approach for catalyst design and performance prediction, J. Energy Storage 89 (2024) 111688. https://doi.org/10.1016/j.est.2024.111688.
[36] L. Villegas, F. Masset, N. Guilhaume, Wet impregnation of alumina-washcoated monoliths: Effect of the drying procedure on Ni distribution and on autothermal reforming activity, Appl. Catal. A: Gen. 320 (2007) 43–55. https://doi.org/10.1016/j.apcata.2006.12.011.
[37] R. Guil-Lopez, R. Navarro, J. Fierro, Controlling the impregnation of nickel on nanoporous aluminum oxide nanoliths as catalysts for partial oxidation of methane, Chem. Eng. J. 256 (2014) 458–467. https://doi.org/10.1016/j.cej.2014.05.146.
[38] M. Okada, Y. Amamoto, J. Kikuchi, Designing sustainable hydrophilic interfaces via feature selection from molecular descriptors and time-domain nuclear magnetic resonance relaxation curves, Polymers 16 (2024) 824. https://doi.org/10.3390/polym16060824.
[39] Huber, P. J. Robust estimation of a location parameter. Ann. Math. Stat. 35 (1964) 73–101. https://doi.org/10.1007/978-1-4612-4380-9_35.
[40] J.B. Procter, J. Thompson, I. Letunic, C. Creevey, F. Jossinet, G.J. Barton, Visualization of multiple alignments, phylogenies and gene family evolution, Nat. Methods 7 (2010) 16–25. https://doi.org/10.1038/nmeth.1434.
[41] S. Nakanowatari, T. Taniike, Catalyst phylogenetic tree: a visualization tool for exploring catalyst research and development from tabular data. ChemRxiv. 2025 https://doi.org/10.26434/chemrxiv-2025-jr3p6.
[42] A.N. Şener, M.E. Günay, A. Leba, R. Yıldırım, Statistical review of dry reforming of methane literature using decision tree and artificial neural network analysis, Catal. Today 299 (2018) 289–302. https://doi.org/10.1016/j.cattod.2017.05.012.
[43] R. Yoshida, XenonPy is a python software for materials informatics. https://github.com/yoshida-lab/XenonPy.

[44] Z. Lin, Y. Cui, Y. Wang, Y. Wu, B. He, D. Liu, Machine learning reveals structure-performance relationships of dry reforming of methane catalysts and the potential influencing mechanisms, Int. J. Hydrogen Energy 122 (2025) 332–347. https://doi.org/10.1016/j.ijhydene.2025.03.363.
[45] C.M. Steffens, O.W. Perez-Lopez, Biogas dry reforming over Li–Ni–Al LDH-derived catalysts, Int. J. Hydrogen Energy 71 (2024) 205–216. https://doi.org/10.1016/j.ijhydene.2024.05.285.
[46] V. Pérez-Madrigal, E. Ríos-Valdovinos, E. Rojas-García, M.A. Valenzuela, F. Pola-Albores, Dry reforming of methane over Li-doped Ni/TiO_2 catalysts: effect of support basicity, Methane 2 (2023) 452–469. https://doi.org/10.3390/methane2040031.
[47] N.A. Abd Ghani, A. Azapour, A.F.a.S. Muhammad, B. Abdullah, Dry reforming of methane for hydrogen production over NiCo catalysts: Effect of NbZr promoters, Int. J. Hydrogen Energy 44 (2019) 20881–20888. https://doi.org/10.1016/j.ijhydene.2018.05.153.

Chapter 4 Data-driven catalyst design for mitigating carbon deposition in low-temperature dry reforming of methane

Abstract

Dry reforming of methane (DRM) represents a sustainable pathway for converting methane into syngas, but catalyst deactivation due to carbon accumulation, particularly under low-temperature operations, remains a major challenge. Building upon a previous active learning-driven exploration, a dataset comprising 141 high-performing catalysts was constructed. These catalysts were subjected to DRM at 500 °C, and their carbon formation behaviors were quantitatively assessed using thermogravimetric–differential thermal analysis (TG-DTA). Systematic data analysis revealed that carbon deposition is primarily influenced by side reactions such as CO disproportionation. Catalysts with high loadings of Ni and Co tended to accumulate greater amounts of carbon, whereas those enriched in Rh or Ir exhibited excellent carbon resistance. However, these noble metals often required the assistance of additional active or promoter elements to sustain sufficient catalytic activity. To derive interpretable design principles, a decision tree classifier and SHAP (Shapley Additive Explanations) analysis were employed. These models identified Rh loading as the most critical factor in minimizing carbon formation. In cases where Rh content was limited, the incorporation of Pt, Cu, or Y was found to be effective in mitigating carbon accumulation. Meanwhile, Li, Nb, and Ta were consistently associated with moderate to severe carbon deposition. Overall, these insights offer a data-driven foundation for the rational design of carbon-resistant multi-element catalysts tailored for low-temperature DRM conditions.

.

4.1. Introduction

Dry reforming of methane (DRM), which converts methane (CH_4) and carbon dioxide (CO_2) into syngas, has attracted considerable attention as a promising route for greenhouse gas utilization and value-added chemical production [1–2]. However, the DRM reaction is highly endothermic, typically requiring temperatures above 700 °C to achieve meaningful conversions [3]. While significant progress has been made in high-temperature DRM catalysis, operating under such harsh conditions remains energy-intensive and often leads to undesirable effects such as metal nanoparticle sintering, which contribute to catalyst deactivation and reduced process stability [4]. In contrast, low-temperature DRM (≤500 °C) offers notable advantages, including improved energy efficiency, lower operational costs, and enhanced compatibility with renewable heat sources [5]. Nevertheless, carbon accumulation is widely recognized as a major cause of catalyst deactivation, particularly under low-temperature conditions where slower kinetics and insufficient carbon gasification, along with the thermodynamic favorability of the exothermic CO disproportionation, collectively promote the buildup of carbonaceous species on the catalyst surface [6–8]. Therefore, while the mechanisms of carbon formation are relatively well understood, the rational design of catalysts that can effectively tolerate or suppress carbon accumulation remains an ongoing challenge.

Carbon accumulation during DRM predominantly proceeds through three mechanistic pathways: methane cracking ($CH_4 \rightarrow C + 2H_2$), CO disproportionation ($2CO \rightarrow C + CO_2$),

and CO hydrogenation ($CO + H_2 \rightarrow C + H_2O$) [9,10]. Among these, methane cracking and CO disproportionation are regarded as the major contributors to coke formation on Ni-based catalysts, which are the most commonly used due to their low cost and high activity in C–H bond activation [11]. Thermodynamically, CO disproportionation is strongly favored at lower temperatures and is thus a dominant source of carbon under mild DRM conditions. This reaction can be suppressed at temperatures exceeding 820 °C, but remains active and detrimental at ≤500 °C [12]. In contrast, methane cracking becomes more favorable above 527 °C and tends to dominate carbon formation at high temperatures [13]. CO hydrogenation also contributes to carbon buildup, though to a lesser extent, and is influenced by the local H_2 partial pressure and catalyst surface chemistry [14]. For example, Sokolov et al. reported that Ni/La_2O_3–ZrO_2 catalysts exhibited excellent stability at 400 °C for 180 hours [15]. Catalyst deactivation was attributed primarily to carbon layers and NiO shell formation, rather than metal sintering, highlighting the relevance of CO disproportionation as a major carbon formation pathway at low temperatures.

In general, multi-element strategies have been extensively explored across a wide range of temperatures to enhance catalyst activity and stability. Several studies suggest that the introduction of lattice defects, particularly oxygen vacancies, can significantly improve carbon tolerance [16–18]. These defects facilitate the oxidation of deposited carbon and inhibit key carbon-forming pathways at active sites. However, despite their demonstrated

potential, systematic studies on multi-element catalysts specifically designed for low-temperature DRM applications remain scarce.

Multi-element systems offer promising solutions for mitigating carbon accumulation. However, the vast combinatorial space and nonlinear interactions among components make their optimization inherently complex, rendering conventional trial-and-error approaches insufficient for identifying optimal formulations [19,20]. In this context, data-driven methodologies [21–23], especially those incorporating machine learning [24–28], provide distinct advantages by uncovering hidden correlations between elemental composition, catalytic performance, and carbon resistance. Such approaches enable the systematic analysis of complex, high-dimensional datasets, thereby facilitating the rational design of catalysts that not only exhibit high activity but also maintain long-term stability against carbon buildup.

Therefore, to address the aforementioned challenges and facilitate the rational design of carbon-resistant multi-element catalysts, this chapter systematically investigated the carbon deposition behavior of 141 high-performing catalysts identified in the Chapters 2 and 3. These catalysts were subjected to DRM at 500 °C for 6 hours, and their carbon accumulation was quantitatively analyzed using thermogravimetric–differential thermal analysis (TG-DTA). Through comprehensive data analysis combined with model-guided interpretation, I elucidated the relationships among catalytic activity, carbon deposition

tendencies, and multi-element composition, ultimately providing practical design principles for the development of durable and high-performance DRM catalysts.

4.2. Methods

4.2.1. Dataset

Within Chapters 2 and 3, a total of 697 multi-element catalysts, denoted as A–B–C–D–E/γ-Al_2O_3, were evaluated for DRM at 500 °C using a consistent HTE protocol. These catalysts were generated through random selection or an active learning process integrated with AFE. The notations A–E represent the elements supported on γ-Al_2O_3, which were selected from a predefined set of 45 elements (with repetition allowed), including Li, Na, Mg, Al, K, Ca, Sc, Ti, V, Mn, Fe, Co, Ni, Cu, Zn, Ga, Rb, Sr, Y, Zr, Nb, Mo, Rh, Pd, Ag, In, Sn, Cs, Ba, La, Ce, Pr, Nd, Sm, Eu, Gd, Tb, Er, Hf, Ta, W, Ir, Pt, Au, and Bi.

In this chapter, to address the challenges posed by carbon deposition and to facilitate the design of multi-element catalysts with enhanced carbon resistance, a subset comprising 141 high-performing catalysts (H_2 yield ≥ 20%) were extracted from the entire dataset (**Table A1**) for further analysis. Among them, 15 originated from the initial training dataset, which was primarily generated via random sampling of the compositional space [29]. The remaining 126 were iteratively selected and evaluated as part of the active learning process to refine and retrain the ML model.

4.2.2. Data acquisition.

To investigate the carbon deposition behavior of the selected high-performance catalysts and gain deeper insight into their carbon resistance, thermogravimetric–differential thermal analysis (TG-DTA) was employed. This technique enables the quantitative evaluation of the amount and thermal characteristics of carbonaceous species formed on the catalyst surface after DRM. TG-DTA analysis was performed on all 141 catalysts described in Section 4.2.1, which had previously undergone DRM at 500 °C for 6 hours, to assist in identifying compositional features associated with enhanced resistance to carbon deposition. The measurements were carried out on a Thermo Plus EVO2 system (Rigaku) under dry air. Approximately 5–10 mg of each used catalyst was placed in an alumina crucible and subjected to a controlled heating program from 30 °C to 900 °C at a constant ramp rate of 10 °C min^{-1} under a dry air atmosphere.

4.2.3. Data analysis

Comprehensive data analysis was conducted to extract meaningful insights from the experimental data and to establish interpretable design principles for carbon-resistant catalysts. Most analyses were performed using conventional statistical methods and machine learning techniques implemented in standard software environments such as Microsoft Excel and the Scikit-learn library in Python.

The decision tree classification algorithm played a central role due to its inherent interpretability and capability to generate rule-based insights [30]. Decision trees operate by recursively partitioning the dataset into subsets, starting from a root node and progressing through internal nodes to terminal leaves. At each node, the data are split based on a single input variable that maximizes a selected criterion, namely GINI impurity. This process creates branches that correspond to increasingly homogeneous subsets with respect to the target variable. In this study, individual elemental molar contents were used as input features to classify catalysts into discrete categories of carbon deposition levels. To address class imbalance in the carbon deposition data, class weights were adjusted to be inversely proportional to class frequencies. This ensured that the model treated minority classes with sufficient importance and avoided bias toward the dominant class. To enhance generalizability and prevent overfitting, cost-complexity pruning (CCP) was applied.

The final model was analyzed using Shapley Additive Explanations (SHAP) to quantify the contribution of each input feature to the model's predictions. This approach provided a unified framework for interpreting the influence of individual elemental loadings on the classification outcomes, allowing the identification of key elements that govern carbon deposition behavior.

4.3. Results and discussion

4.3.1. Carbon formation of high-performance catalysts

Based on the dataset described in Section 4.2.1, a total of 141 high-performance catalysts, typically denoted as A–B–C–D–E/γ-Al_2O_3, had been previously synthesized and evaluated for DRM at 500 °C for 6 hours in Chapters 2 and 3. The spent catalysts from these tests were subsequently collected and subjected to TG-DTA to quantify carbon deposition. Finally, a high-quality dataset on carbon formation behavior for high-performing DRM catalysts was established (**Table 4.1**).

Table 4.1. Catalytic performance of the selected DRM catalysts with H_2 yield ≥ 20%, emphasizing carbon deposition behavior.[a]

No.	A (mmol)	B (mmol)	C (mmol)	D (mmol)	E (mmol)	CH_4 conv. (%)	CO_2 conv. (%)	H_2 yield (%)	CO yield (%)	Weight loss (%)
1	Li (0.845)	Al (0.558)	Ni (0.282)	Nb (0.700)	Ce (0.426)	25.9	27.3	26.0	22.9	29.4
2	Li (0.627)	Ca (0.171)	Ni (0.792)	Nb (0.175)	Ir (0.413)	28.7	27.7	27.3	21.8	45.4
3	Li (0.408)	Ca (0.354)	Ni (0.759)	Hf (0.129)	Ir (0.144)	28.0	26.2	26.5	21.2	56.6
4	Al (0.470)	Nb (0.484)	Rh (0.221)	Ce (0.428)	Hf (0.389)	21.7	29.8	20.8	27.3	0.0
5	Al (0.096)	Ni (0.975)	Cs (0.160)	Sm (0.365)	Ir (0.092)	30.5	27.9	28.1	20.3	36.1
6	Al (0.193)	Ni (0.620)	Nb (0.626)	Rh (0.105)	Ir (0.275)	22.2	28.5	21.6	25.8	15.8
7	Li (0.865)	Al (0.193)	Ni (0.443)	Cs (0.080)	Hf (0.424)	34.0	29.4	30.5	20.8	34.8
8	Li (0.096)	Ni (2.255)	Nb (0.101)	Rh (0.114)	Ir (0.096)	37.5	31.2	32.5	25.5	36.2
9	Al (0.086)	V (0.663)	Ni (0.282)	Nb (0.811)	Rh (0.343)	23.5	29.4	23.7	25.4	17.5
10	Al (0.582)	Rh (0.398)	Ba (0.338)	Hf (0.557)	Ir (0.074)	20.2	29.7	21.1	27.3	0.0
11	Ca (0.914)	Ni (0.352)	Nb (0.306)	Rh (0.259)	Ir (0.203)	18.7	29.3	20.0	26.2	2.4
12	Li (0.350)	Al (0.545)	Ni (0.704)	Nb (0.102)	Sm (0.058)	40.0	34.4	34.5	35.5	56.1
13	Li (0.264)	Al (0.416)	V (0.450)	Rh (0.422)	Hf (0.138)	20.1	31.4	21.2	27.7	0.0
14	Al (0.749)	Ca (0.565)	Ni (0.108)	Nb (0.434)	Rh (0.316)	19.4	30.7	20.9	27.2	1.2
15	Ni (3.500)					46.8	35.7	39.0	33.6	58.0
16	Ni (0.704)					30.3	29.9	29.5	20.2	55.9
17	Ni (1.750)					41.2	35.1	34.1	26.1	57.2
18	Ni (2.625)					43.1	35.6	36.1	30.8	47.0

19	Li (0.350)	Al (0.545)	Ni (0.704)	Nb (0.102)	Sm (0.058)	36.3	32.4	31.7	20.1	56.1
20	Li (0.350)	Al (0.545)	Ni (0.704)	Nb (0.102)		36.2	32.1	33.1	19.4	53.7
21	Li (0.350)	Al (0.545)	Ni (0.704)	Sm (0.058)		28.5	30.0	27.8	21.4	47.0
22	Li (0.350)	Ni (0.704)	Nb (0.102)	Sm (0.058)		34.2	30.9	30.4	18.7	61.4
23	Al (0.545)	Ni (0.704)	Nb (0.102)	Sm (0.058)		31.9	30.0	29.9	19.8	52.2
24	Li (0.350)	Ni (0.704)				33.7	30.1	31.2	19.4	47.7
25	Al (0.545)	Ni (0.704)				26.8	31.0	26.8	22.2	40.3
26	Ni (0.704)	Nb (0.102)				32.8	30.7	30.4	19.8	53.0
27	Ni (0.704)	Sm (0.058)				31.5	30.2	29.9	19.6	48.0
28	Li (0.350)	Al (0.545)	Ni (0.704)			29.6	30.2	28.9	21.0	51.4
29	Li (0.350)	Ni (0.704)	Nb (0.102)			35.4	31.6	30.8	19.8	52.0
30	Li (0.350)	Ni (0.704)	Sm (0.058)			34.0	30.5	31.7	19.4	55.0
31	Al (0.545)	Ni (0.704)	Nb (0.102)			32.9	31.7	30.5	20.0	52.8
32	Al (0.545)	Ni (0.704)	Sm (0.058)			23.7	29.2	23.3	20.9	40.9
33	Ni (0.704)	Nb (0.102)	Sm (0.058)			31.4	30.9	30.0	20.2	52.7
34	Ir (3.000)	Au (0.500)				18.5	29.8	20.2	26.0	0.0
35	Rh (0.500)	Ir (2.000)				19.1	31.1	20.6	26.9	0.0
36	Ir (2.000)	Au (0.500)				18.3	28.8	20.0	25.2	0.0
37	Rh (3.000)	Ir (0.500)				19.0	31.0	21.1	27.0	0.0
38	Rh (0.500)					17.6	33.6	20.0	27.6	0.0
39	Rh (1.000)					18.0	33.8	20.4	28.2	0.0
40	Rh (1.500)					18.7	34.7	20.5	28.1	0.0
41	Nb (0.500)	Rh (0.500)				18.7	34.8	20.3	28.2	0.0
42	Li (2.000)	V (0.500)	Ni (0.500)	Nb (0.500)		32.2	36.1	28.6	22.6	40.0
43	Al (0.500)	Mn (2.000)	Ni (1.000)			37.6	40.3	28.5	42.4	34.8
44	Ni (2.500)	Pd (1.000)				34.3	34.1	28.9	19.4	35.5
45	Ni (2.500)	Cu (0.500)				22.2	29.4	21.1	21.3	14.6
46	Ni (2.000)	Pd (0.500)				35.3	35.2	28.9	38.0	38.2
47	Mg (0.500)	Ni (2.500)	Cu (0.500)			20.9	28.9	20.4	22.2	38.3
48	Al (0.500)	Ni (2.000)	Rh (0.500)	W (0.500)		23.3	29.7	22.5	22.2	26.2
49	Mg (0.500)	Ni (2.500)	Nb (0.500)			41.9	35.4	33.0	24.9	48.0
50	Al (0.500)	Ni (2.500)	Nb (0.500)			42.4	37.0	34.2	32.2	40.6
51	Al (0.500)	Co (0.500)	Ni (2.500)			40.7	40.4	29.4	40.2	33.5
52	Co (0.500)	Ni (1.000)	Pd (2.000)			23.1	29.5	21.7	22.9	29.2
53	Al (0.500)	Co (1.000)	Ni (1.000)	Pd (1.000)		32.6	34.5	28.2	32.7	23.8
54	Co (0.500)	Ni (3.000)				46.8	37.7	35.1	35.5	49.4
55	Co (2.500)	Rh (1.000)				31.0	35.8	29.2	21.4	29.6
56	Co (1.500)	Ni (1.500)	Rh (0.500)			33.5	38.5	28.1	22.2	23.5
57	Al (0.500)	Co (0.500)	Ni (2.000)	Rh (0.500)		26.4	34.8	24.6	22.4	32.4
58	Al (2.000)	Ni (0.500)				29.0	38.3	25.4	23.4	27.2
59	Li (0.500)	Al (0.500)	Co (1.000)	Ni (1.000)	Rh (0.500)	27.1	37.1	24.4	23.0	17.1
60	Al (0.500)	Mn (0.500)	Fe (0.500)	Ni (1.500)	Rh (0.500)	19.3	34.6	20.2	26.0	20.2
61	Mn (1.000)	Co (0.500)	Ni (0.500)	Nb (0.500)		40.4	41.9	28.6	30.7	33.8
62	Fe (0.500)	Co (1.000)	Ni (2.000)			39.0	39.6	29.7	23.2	33.9
63	Li (0.500)	Al (0.500)	Co (0.500)	Ni (2.000)		39.8	41.2	29.3	21.6	17.4
64	Co (2.000)	Y (0.500)	Rh (1.000)			24.2	36.8	23.4	23.9	15.8
65	Al (0.500)	Ni (0.500)				34.6	39.2	27.4	23.2	30.6
66	Co (3.000)	Zn (0.500)				32.4	30.3	31.6	18.7	36.5
67	Co (3.000)	Nb (0.500)				40.6	38.4	33.9	28.6	32.6
68	Li (0.200)	Mn (0.400)	Co (0.600)	Rh (0.200)	W (0.200)	21.4	31.4	22.3	26.7	2.1
69	Co (0.600)	Ni (0.200)				24.3	31.0	25.1	23.4	27.5

70	Al (0.200)	Ni (0.800)				23.0	32.8	23.9	23.4	42.3
71	Ni (0.600)	Rh (0.200)				19.3	33.5	21.4	26.8	4.3
72	Li (0.400)	Co (0.200)	Ni (0.400)	Rh (0.200)	W (0.200)	19.2	33.2	21.3	26.5	4.9
73	Li (0.200)	Mn (0.600)	Ni (0.800)			21.2	32.9	22.8	24.4	33.2
74	Ni (0.600)	Pd (0.200)				20.4	31.4	22.1	23.7	30.1
75	Li (0.200)	Al (0.200)	Mn (0.400)	Ni (0.600)	Pd (0.200)	19.6	32.2	21.1	24.6	23.6
76	Li (0.600)	Ni (0.800)				33.3	37.2	31.1	21.3	39.3
77	Li (0.200)	Co (0.200)	Ni (0.600)			26.0	34.7	26.5	38.4	33.4
78	Sc (0.200)	Co (0.400)	Ni (0.400)			18.9	29.5	20.4	23.9	26.8
79	Li (0.400)	Mn (0.200)	Ni (0.600)	Rh (0.200)	W (0.200)	19.2	31.8	22.1	27.4	2.1
80	Fe (0.200)	Ni (0.600)	Nb (0.400)			26.4	32.3	27.7	22.2	32.2
81	Al (0.400)	Mn (0.400)	Co (0.200)	Ni (0.400)	Rh (0.200)	20.0	32.1	22.1	27.4	2.5
82	Al (0.400)	Mn (0.200)	Ni (0.400)	Nb (0.200)	Pd (0.200)	23.7	32.8	25.5	24.0	30.9
83	Al (0.400)	Co (0.200)	Ni (0.600)	Nb (0.200)		32.8	36.3	32.2	21.6	36.0
84	Li (0.600)	Ni (0.600)				30.1	30.9	28.2	19.6	38.0
85	Li (0.200)	Al (0.400)	Mn (0.200)	Ni (0.800)		28.2	30.7	26.5	21.1	25.8
86	Li (0.400)	Al (0.200)	Mn (0.200)	Ni (0.800)		30.1	31.2	28.1	19.7	34.5
87	Li (0.400)	Ni (0.600)	Nb (0.400)			32.6	31.7	30.1	18.4	31.3
88	Li (0.600)	Ni (0.600)	Nb (0.200)			30.3	31.0	28.3	19.7	30.9
89	Li (0.200)	Al (0.200)	Mn (0.200)	Ni (0.800)	Nb (0.200)	30.6	31.8	28.3	19.2	26.4
90	Li (0.400)	Al (0.200)	Sc (0.200)	Ni (0.800)		33.3	34.1	30.0	20.7	31.7
91	Li (0.200)	Co (0.400)	Ni (0.400)	Y (0.200)		30.3	31.2	28.1	18.7	27.9
92	Li (0.800)	Ni (0.800)				34.6	32.7	32.3	18.4	25.5
93	Li (0.400)	Al (0.400)	Ni (0.600)			30.0	31.6	28.2	20.8	30.6
94	Al (0.400)	Ni (0.600)	Y (0.200)			31.1	32.2	29.3	19.8	26.1
95	Al (0.200)	Sc (0.200)	Mn (0.200)	Ni (0.800)	Y (0.200)	31.8	32.8	29.5	19.1	26.8
96	Ni (0.800)	Nb (0.200)				30.8	31.1	28.5	19.7	32.0
97	Al (0.200)	Mn (0.400)	Ni (0.800)	Nb (0.200)		27.3	31.0	26.2	21.8	26.4
98	Li (0.200)	Al (0.400)	Ni (0.800)	Y (0.200)		27.3	31.0	25.6	20.5	21.0
99	Li (0.400)	Ni (0.600)	Nb (0.200)			34.9	33.4	32.1	18.3	27.3
100	Ni (0.600)	Y (0.200)				36.5	36.4	33.4	19.1	40.0
101	Li (0.200)	Al (0.200)	Sc (0.200)	Ni (0.800)	Nb (0.200)	36.3	35.8	32.7	18.8	41.1
102	Li (0.600)	Co (0.400)	Ni (0.400)	Nb (0.200)		34.9	37.5	31.3	19.1	42.8
103	Li (0.400)	Ni (0.800)	Ta (0.200)			39.8	40.4	35.3	29.6	39.2
104	Li (0.200)	Al (0.400)	Sc (0.200)	Ni (0.800)		30.2	34.8	28.8	20.1	37.2
105	Li (0.600)	Ni (0.600)	Ta (0.200)			36.3	37.5	32.3	18.8	45.4
106	Al (0.600)	Ni (0.800)	Nb (0.200)			34.4	35.8	31.7	18.6	40.0
107	Li (0.400)	Sc (0.200)	Co (0.200)	Ni (0.600)	Nb (0.200)	32.2	34.6	29.9	19.0	44.5
108	Li (0.600)	Al (0.200)	Ni (0.800)			40.3	39.2	34.9	36.3	36.9
109	Li (0.400)	Mn (0.200)	Ni (0.800)	Nb (0.200)		40.8	40.0	35.1	20.2	42.4
110	Li (0.200)	Al (0.400)	Ni (0.800)	Nb (0.200)		39.4	39.3	34.1	17.6	39.5
111	Li (0.200)	Al (0.600)	Ni (0.800)			26.8	31.9	27.0	22.1	41.8
112	Li (0.600)	Ni (0.800)	Ta (0.200)			43.0	40.8	36.8	28.5	38.0
113	Li (0.200)	Sc (0.200)	Ni (0.800)			34.5	36.2	31.6	18.7	49.3
114	Li (0.400)	Co (0.200)	Ni (0.600)	Nb (0.400)		38.1	38.9	33.6	18.4	44.7
115	Li (0.400)	Ni (0.800)	Ta (0.400)			42.8	42.0	35.8	19.8	40.3
116	Co (0.400)	Ni (0.800)				35.3	37.8	31.9	36.2	38.6
117	Fe (0.100)	Co (0.500)	Ni (0.800)			33.8	35.9	31.3	18.4	48.7
118	Fe (0.200)	Co (0.100)	Ni (0.800)	Ba (0.500)		31.2	33.6	29.5	19.5	42.3
119	Mn (0.200)	Ni (0.800)				22.1	32.2	22.7	23.0	37.1
120	Ti (0.200)	Ni (0.800)	Ga (0.100)			25.8	34.3	25.9	21.9	43.8

121	Li (0.100)	Ti (0.100)	Ni (0.800)			35.1	37.3	31.7	20.0	47.6
122	Sc (0.400)	Ti (0.100)	Ni (0.800)	Y (0.100)	Pd (0.100)	25.6	33.6	25.9	23.0	43.2
123	Mn (0.800)	Ni (0.800)				21.4	32.7	22.4	24.6	34.3
124	Ni (0.800)	Rh (0.200)				20.2	32.7	21.6	25.9	19.5
125	Mg (0.100)	Ti (0.100)	Ni (0.800)			33.2	37.3	30.1	41.5	41.0
126	Ti (0.100)	Ni (0.800)				32.6	37.1	30.4	19.9	46.4
127	Co (0.100)	Ni (0.800)	Cs (0.100)			35.3	40.7	28.0	21.7	43.7
128	Ni (0.800)	Nb (0.100)	Ta (0.200)			33.0	38.6	26.9	18.5	40.7
129	V (0.100)	Ni (0.800)	Rh (0.100)			34.5	39.6	27.3	20.2	2.2
130	Co (0.200)	Ni (0.800)	Hf (0.100)			36.4	37.5	26.8	15.5	40.3
131	Co (0.100)	Ni (0.800)	Rb (0.400)	Nd (0.200)	Hf (0.100)	30.7	35.1	24.9	19.1	42.7
132	Co (0.100)	Ni (0.800)	Sr (0.600)			32.4	36.9	26.6	18.3	41.0
133	Mn (0.100)	Co (0.600)	Ni (0.800)			30.3	35.7	25.4	18.9	44.2
134	Ni (0.800)	Cs (0.400)	Pr (0.200)	Sm (0.200)		30.9	41.0	27.1	24.9	42.1
135	Ti (0.100)	Ni (0.800)	Pd (0.100)			32.0	36.5	26.7	18.4	40.5
136	Li (0.100)	Co (0.100)	Ni (0.800)			29.7	35.6	25.3	19.3	45.8
137	Mn (0.300)	Ni (0.800)				33.9	36.5	26.7	17.1	43.9
138	V (0.300)	Ni (0.800)	Pt (0.100)			33.6	40.2	27.7	21.4	0.0
139	Co (0.600)	Ni (0.800)				34.5	40.3	28.1	19.6	44.3
140	Ti (0.200)	Co (0.200)	Ni (0.800)			24.6	31.9	20.9	22.2	40.6
141	Ti (0.100)	Ni (0.800)	Rh (0.100)			33.5	38.2	26.8	17.4	9.0

[a] Nos. 1–15 originated from the initial training dataset, which was primarily generated via random sampling. Nos. 16–141 were iteratively selected and evaluated as part of the active learning process to progressively refine and retrain the ML model.

[b] Catalysts used in the DRM reaction at 500 °C for 6 h on stream were subjected to TG-DTA analysis. The weight loss corresponds to the difference in sample weight at the onset and termination temperatures of the exothermic peak on the DTA curve.

Most studies have focused on noble metal catalysts such as Pt, Pd, Rh and Ir, which exhibit high activity and strong resistance to carbon accumulation. These noble metals possess excellent catalytic activity for CH_4 and CO_2 activation, enabling rapid turnover rates that minimize the surface residence time of carbonaceous intermediates. In addition, strong metal–support interactions enhance metal dispersion and thermal stability, thereby mitigating sintering and localized carbon buildup. Moreover, their pronounced redox properties allow activation of surface oxygen species or utilization of support-derived

oxygen to oxidize carbon intermediates in situ [31]. In addition to noble metals, transition metals such as Ni, Co, and Fe, which are more cost-effective than noble metals, have also been extensively investigated. Depending on the catalyst formulation and reaction conditions, the carbon formed can manifest as either desirable structures, such as carbon nanotubes, or detrimental graphitic layers that lead to catalyst deactivation [8]. Although significant progress has been made in understanding carbon formation during the DRM reaction, large-scale, high-quality datasets systematically evaluating carbon deposition across a broad range of catalysts remain scarce.

To address this gap, I performed a series of data analyses and ML model training on the carbon deposition dataset obtained from high-performing catalysts identified through a previous active learning process, aiming to extract actionable design principles for the development of durable multi-element catalysts.

To explore the potential correlation between reactant utilization and carbon formation, I analyzed the ratio of CH_4 conversion to CO_2 conversion as an indicator of the surface carbon balance during DRM. This ratio reflects the relative rates at which methane is activated, and carbon dioxide is consumed, and has direct implications for the likelihood of carbon deposition via side reactions. From a mechanistic perspective, methane cracking and CO disproportionation are the dominant pathways leading to carbon accumulation under DRM conditions. While the DRM reaction itself is carbon-neutral at the stoichiometric ratio, a CH_4/CO_2 conversion ratio significantly greater than 1 suggests

that methane is being consumed at a faster rate than CO_2, which may indicate CO_2-deficient conditions. Such conditions can suppress the gasification of surface carbon species and promote the thermodynamically favorable carbon-forming side reactions, especially CO disproportionation at low temperatures. Conversely, a CH_4/CO_2 conversion ratio closer to 1, or below, implies sufficient CO_2 availability to oxidize carbon intermediates and suppress coke accumulation. Therefore, this ratio serves as a useful proxy to evaluate the redox environment surrounding the active sites and the catalyst's tendency toward either carbon formation or self-cleaning. Therefore, **Figure 4.1a** and **Figure 4.1b** illustrate the relationships between CH_4 conversion/CO_2 conversion and H_2 yield, and between CH_4 conversion/CO_2 conversion and weight loss, respectively. To capture the influence of different metal elements on catalytic activity and carbon deposition behavior, I adopted a composition-based visualization strategy. In this approach, each catalyst is color-coded based on the relative proportions of three elemental categories: blue represents the combined percentage of transition metals Ni and Co, pink indicates the percentage of platinum-group metals (PGMs), and green corresponds to other additional elements. For consistency, the total metal content of each catalyst is normalized to 100%.

Analysis of **Figures 4.1a** and **4.1b** reveals several important trends regarding the catalytic behavior of the studied catalysts. First, a strong positive correlation is observed between H_2 yield and the CH_4 conversion to CO_2 conversion ratio, indicating that H_2

production generally increases with higher CH_4 conversion. However, not all elemental combinations yield the same benefit. Catalysts with a high fraction of PGMs (pink) tend to cluster near the H_2 yield threshold of 20%, suggesting that PGMs alone are insufficient for achieving high performance if the catalyst lacks adequate amounts of Ni, Co, or key additive elements. In contrast, catalysts with a higher proportion of Ni and Co (blue) display a broader and more upward-spread distribution in H_2 yield, indicating their stronger contribution to CH_4 activation. This observation aligns with findings in Chapter 2 and suggests that Ni and Co, when combined with carefully selected additives, can deliver more effective catalytic performance than PGMs alone.

In **Figure 4.1b**, when the CH_4 conversion is lower than the CO_2 conversion, methane formation via CO_2 methanation becomes significant. This secondary reaction consumes H_2 and CO_2 to regenerate CH_4, thereby lowering the CH_4 conversion and reducing the CH_4/CO_2 conversion ratio [32]. Conversely, when CH_4 conversion exceeds CO_2 conversion, the Boudouard reaction becomes more prominent, leading to the disproportionation of CO into C and CO_2 and thereby decreasing CO_2 conversion disproportionately [33]. A generally positive correlation is also observed between the CH_4/CO_2 conversion ratio and carbon deposition. However, this positive trend is not absolute. Certain catalysts exhibit CH_4/CO_2 conversion ratios approaching unity yet possess relatively high weight loss, suggesting that carbon accumulation does not necessarily increase monotonically with time. Instead, carbon buildup may reach a

saturation point beyond which further accumulation is suppressed, resulting in CH_4/CO_2 conversion ratios stabilizing near stoichiometric values.

Moreover, catalysts containing a high proportion of Ni and Co tend to exhibit more substantial carbon deposition overall (**Figure 4.1b**). Interestingly, several catalysts combine high catalytic activity with negligible carbon deposition (further visualized in **Figure 4.1c**). These carbon-tolerant catalysts are primarily composed of high PGM loadings (particularly Rh, Ir, and Pt) or specific additive elements, which is consistent with the well-documented carbon resistance of PGMs. However, these carbon-free catalysts are mostly located in the CH_4 conversion/CO_2 conversion < 1 region, suggesting that CO_2 methanation may play a role in enhancing CO_2 utilization while suppressing CH_4 conversion, thereby reducing the carbon formation potential.

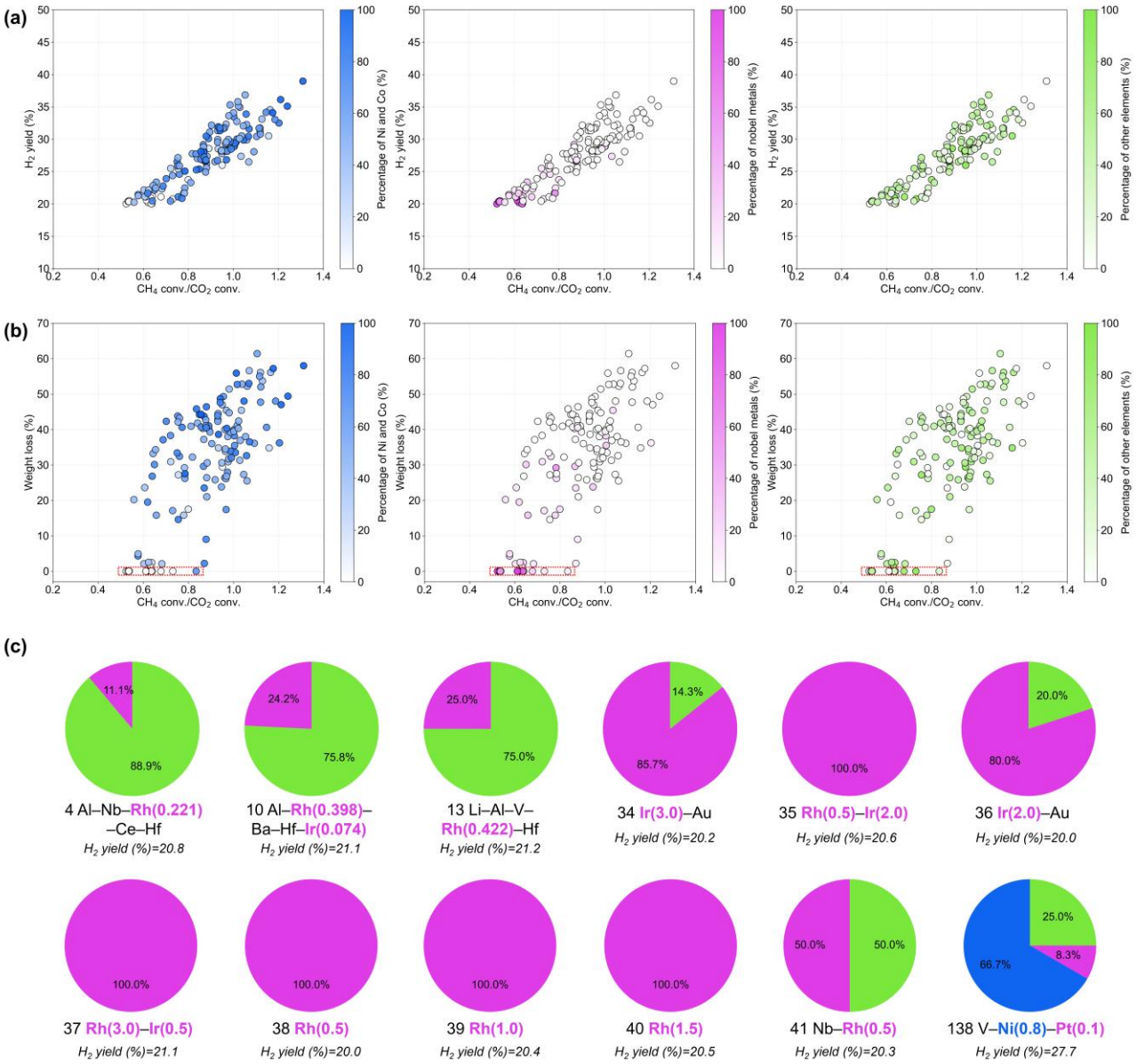

Figure 4.1. Visualization of the high-performance DRM catalyst dataset. Scatter plots for catalyst performance and carbon deposition are shown in terms of (a) CH_4 conversion/CO_2 conversion versus H_2 yield and (b) CH_4 conversion/CO_2 conversion versus weight loss (as a measure of carbon deposition determined by TG-DTA). Catalysts are color-coded based on their elemental composition: blue represents the relative content of transition metals (Ni and Co), pink corresponds to platinum-group metals (PGMs), and

green indicates the proportion of other added elements. The total metal content for each catalyst is normalized to 100%. (c) Pie chart showing the elemental composition of catalysts with no detectable carbon deposition, selected from Figure 4.1b. The values in parentheses indicate the loading amounts of elements in mmol per gram of support. The corresponding H_2 yields for each composition are also annotated.

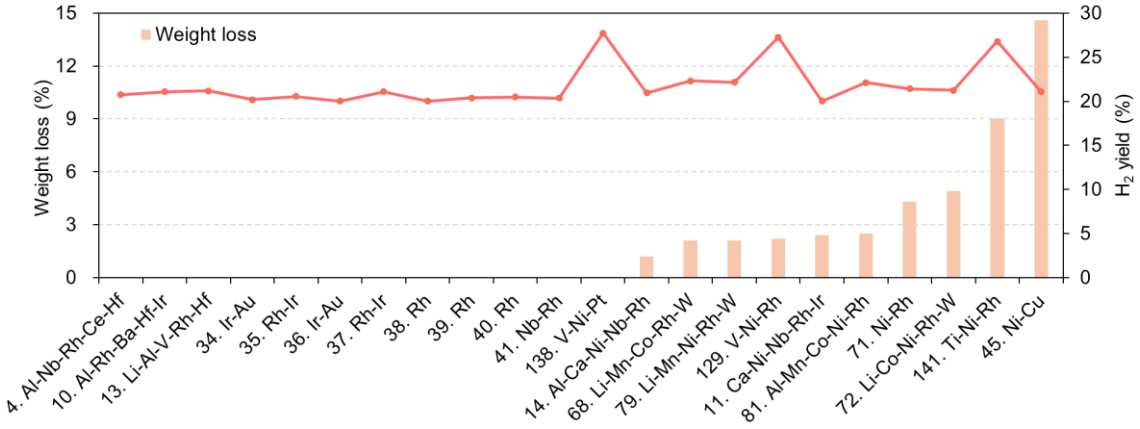

Figure 4.2. Histograms showing catalysts with less than 15% carbon deposition based on TG-DTA analysis. Catalyst names are abbreviated using the ordinal numbers corresponding to the detailed compositions listed in Table 4.1.

To further elucidate the compositional trends associated with low carbon deposition, **Figure 4.2** summarizes the formulations and catalytic performance of the 22 catalysts exhibiting carbon deposition below 15%. Among these, Rh appeared most frequently, being present in 18 compositions, confirming its effectiveness as a noble metal

component for achieving carbon-resistant catalysts when supported on γ-Al_2O_3. Ir was also observed in 6 compositions, further highlighting the role of PGMs in mitigating carbon accumulation. In contrast, Ni, though generally associated with increased carbon formation due to its high intrinsic activity for CH_4 dissociation and limited ability to activate CO_2 [34], was present in 10 of the low-carbon catalysts. This suggests a functional complementarity: while Ni enables high H_2 yields, PGMs like Rh suppress carbon formation, allowing their combinations to balance activity and stability under low-temperature DRM conditions.

Given this interplay between catalytic performance and carbon resistance, a meaningful interpretation of carbon deposition trends must account for the underlying selection bias imposed by the 20% H_2 yield threshold. Since all catalysts included in the present dataset are high-performing by design, elements that contribute to high activity, such as Ni, are inherently overrepresented. In contrast, elements that may suppress carbon deposition but perform poorly in terms of activity, such as isolated PGMs, tend to be underrepresented. Consequently, any analysis of the relationship between individual elements and carbon formation must first consider their association with catalytic activity. To address this complexity, the dataset was partitioned into four subsets based on carbon deposition thresholds of 15%, 30%, and 45%. Specifically, catalysts were classified into four groups: 22 catalysts with carbon deposition <15%, 26 catalysts with deposition between 15% and 30%, 65 catalysts between 30% and 45%, and 28 catalysts with deposition >45%. This

stratification enables a more nuanced examination of how elemental distributions correlate with varying levels of carbon deposition among already high-performing catalysts.

Figure 4.3 illustrates the distribution of elemental occurrences across different carbon deposition categories among high-performance DRM catalysts. The frequency of each element provides a clear indication of its prevalence within the high-performing catalyst dataset (**Figure 4.3a**). Firstly, Ni appears most frequently, being present in more than 85% of all catalysts (125 out of 141), reaffirming its essential role in achieving H_2 yields above the 20% threshold, , followed by Li, Al, Nb, Co, Rh, Mn, Ir, Sm, and Pd in descending order of frequency. Among them, Co, Rh, Ir, and Pd are well-known for their intrinsic catalytic activity in DRM. In contrast, elements such as Li, Al, Nb, Mn, and Sm do not exhibit catalytic activity when loaded individually onto support and are therefore likely functioning as promoters. In other words, when carefully combined with active metals such as Ni, these elements can enhance catalytic performance through mechanisms such as improving the dispersion of the primary active phase or increasing surface basicity to promote CO_2 adsorption. This promotional effect is consistent with the findings in Chapter 2, where elements such as Li, Al, Nb, and Sm frequently appeared in high-performance Ni-based catalysts.

In **Figure 4.3b**, the percentage distribution of each element across the four carbon deposition levels reveals compositional trends related to carbon formation. As expected,

Rh and Ir exhibit the strongest resistance to carbon deposition, whereas Ni and Co are more prone to carbon accumulation. Promoter elements such as Li, Al, Nb, and Mn show variable carbon resistance, likely depending on the specific combination and loading used in each formulation. Notably, catalysts containing Sm tend to fall into higher carbon deposition categories, suggesting that Sm may function as a potential inhibitor to carbon suppression. Surprisingly, Pd-containing catalysts also show relatively high carbon deposition, despite Pd being a platinum-group metal. Moreover, although elements such as Au, Pt, W, Ce and V appear infrequently across the dataset, they are often associated with low-carbon-deposition catalysts. This observation suggests their potential role in suppressing carbon accumulation when appropriately incorporated into catalyst formulations.

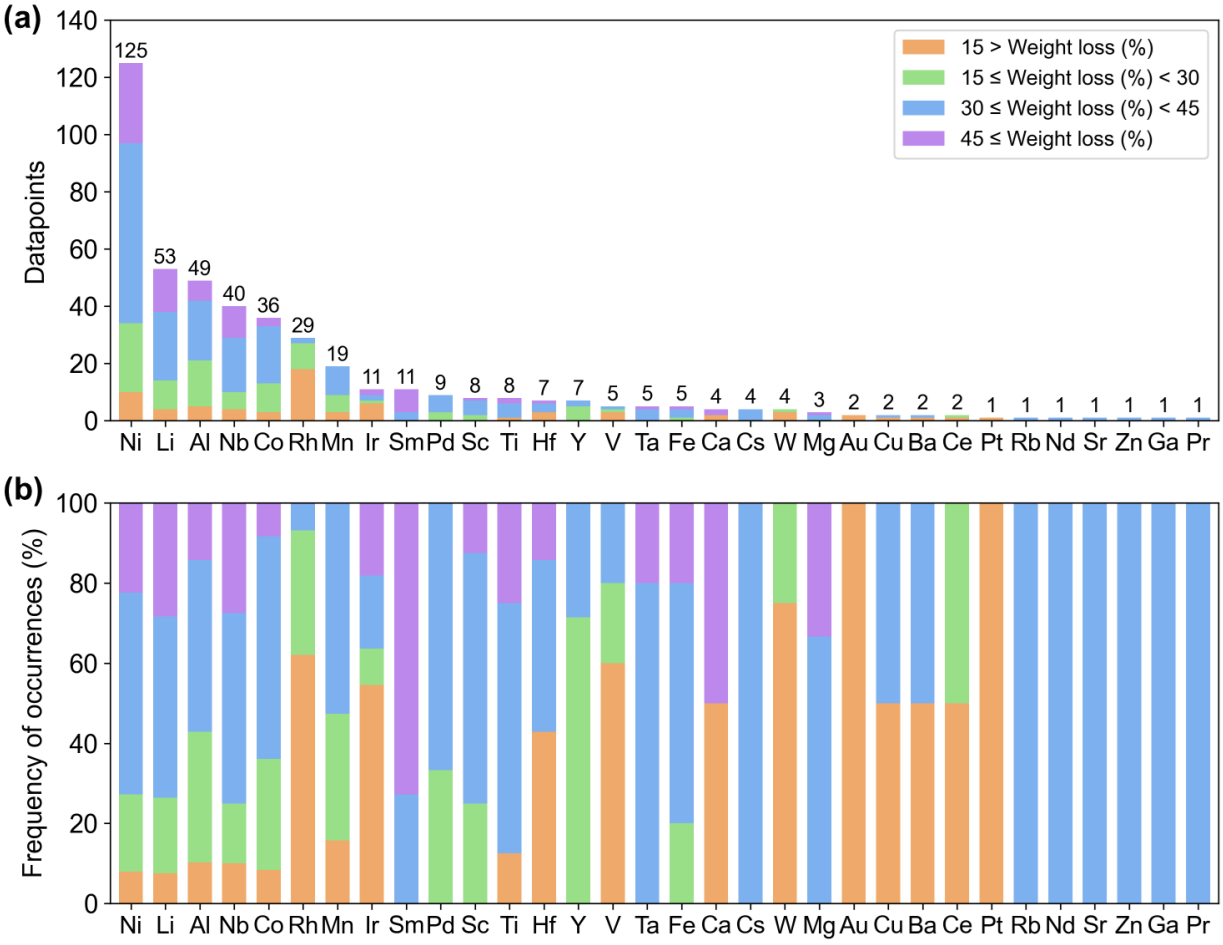

Figure 4.3. Histograms showing the elemental distribution among high-performance DRM catalysts (H_2 yield ≥ 20%), categorized by carbon deposition levels. The dataset was partitioned into four classes based on carbon deposition thresholds: <15%, 15–30%, 30–45%, and >45%. The upper panel (a) displays the absolute occurrence count of each element within each carbon deposition category, while the lower panel (b) presents the corresponding percentage distribution, normalized by the total number of occurrences for each element.

In this section, a comprehensive analysis of carbon deposition behavior across high-performing DRM catalysts was conducted by integrating TG-DTA data with elemental composition and reactant conversion metrics. Key trends were identified linking catalyst formulations to both H_2 yields and carbon accumulation. While Ni and Co were confirmed as essential components for high H_2 yields, their use often coincided with increased carbon deposition. In contrast, PGMs such as Rh and Ir exhibit excellent resistance to carbon deposition, although they generally need to be functionally complemented by active or promoter elements to achieve sufficient catalytic activity. Promoters like Li, Al, Nb, and Mn showed variable carbon resistance, depending on their pairing with active metals. To further clarify the design guidelines for carbon-resistant catalysts, the next section will address this issue through more advanced ML techniques.

4.3.2. Design guidelines for carbon-resistant catalysts

To establish interpretable guidelines linking elemental composition to carbon deposition under low-temperature DRM conditions, a decision tree classification method was employed. In this study, the elemental loadings were used as input features, and carbon deposition served as the target variable. This classification scheme mirrors the thresholds adopted in **Figure 4.4** to ensure consistency across analyses. To address the inherent class imbalance within the dataset, class weights were adjusted inversely proportional to the frequency of each class, ensuring that minority classes exerted

appropriate influence during model training. Additionally, to prevent overfitting and enhance the generalizability of the decision tree, cost complexity pruning was applied. The optimal pruning parameter was determined through cross-validation, where 90% of the data was allocated to training and 10% to testing, repeated over 50 iterations. The accuracy score was employed as the evaluation metric, and the best *ccp_alpha* was identified as 0.0057, ensuring a balanced trade-off between model complexity and classification performance.

Figure 4.4 presents the resulting classification tree for carbon deposition. At the top root node, the classification tree initially splits based on the Rh loading. The 141 catalysts were divided into four carbon deposition classes: 22 catalysts with <15%, 26 catalysts with 15–30%, 65 catalysts with 30–45%, and 28 catalysts with ≥45%. The "value" associated with each node indicates the weighted number of samples belonging to each class, where the class weights were adjusted to be inversely proportional to class frequencies. As the total number of samples is 141 and equal class weights were applied, the value for each class at the root node is standardized to 32.25, ensuring that the sum across all classes matches the dataset size. Through recursive splitting at each node, the decision tree ultimately enables the extraction of interpretable design principles for the rational development of carbon-resistant DRM catalysts.

When the catalyst contains a relatively high loading of Rh, it is necessary to reduce the contents of Co and Ni to achieve carbon deposition below 15%. Notably, when the Ni

loading exceeds a certain threshold, the Rh content must be carefully controlled to maintain carbon resistance. In addition, it is worth mentioning that in specific samples, an increased V loading also correlates with higher levels of carbon deposition.

When the Rh content in the catalyst is insufficient, two major branches emerge depending on the Ni loading. On the left branch, where the Ni content is relatively low, achieving carbon deposition below 15% requires the incorporation of Au, while simultaneously avoiding the excessive use of Ta, Nb, and Li, which tend to promote carbon formation. On the other branch, associated with higher Ni loadings, suppressing carbon deposition necessitates the addition of substantial amounts of Pt and Cu. Furthermore, Al and Y also contribute to mitigating carbon accumulation to some extent.

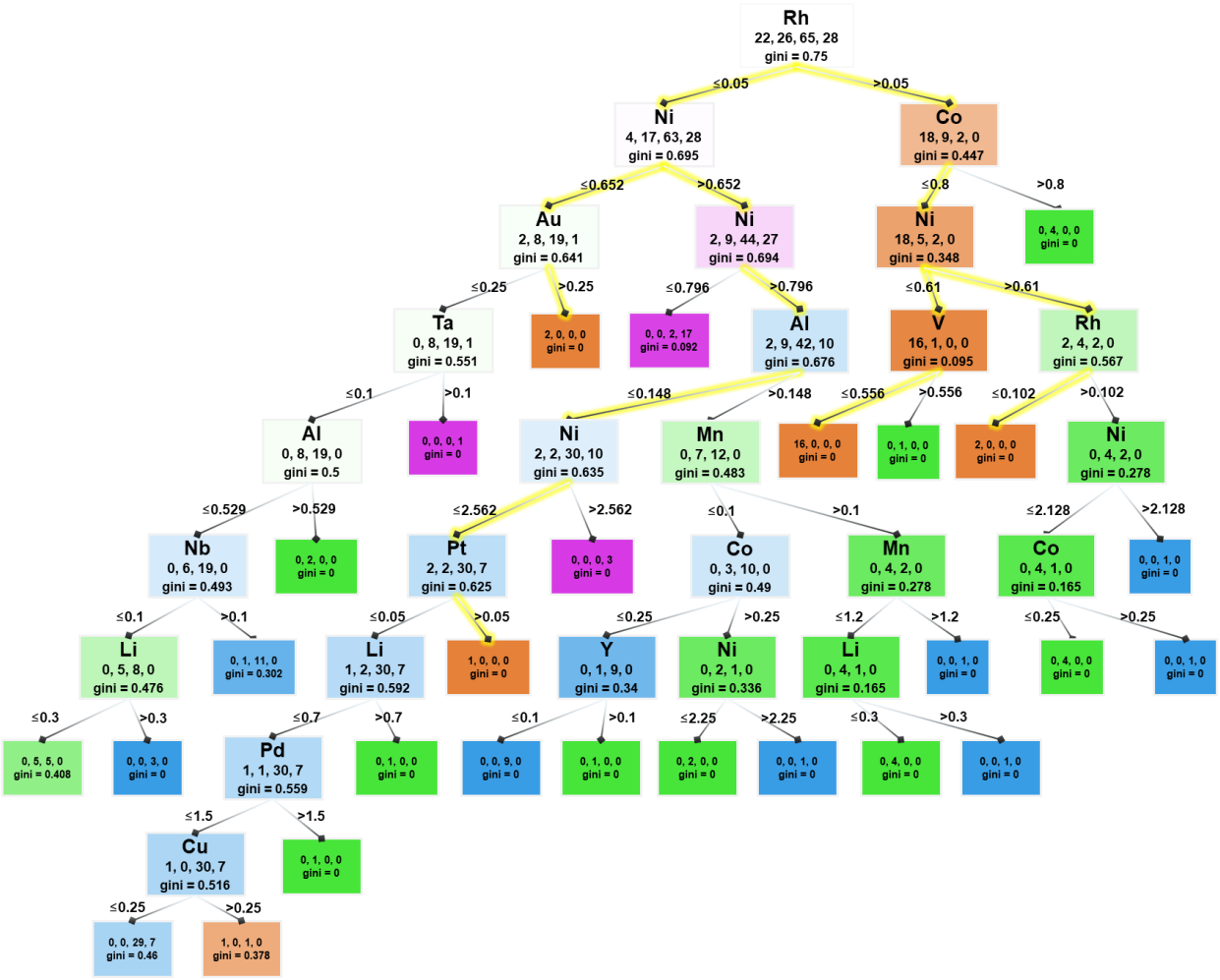

Figure 4.4. Classification tree based on elemental loadings and carbon deposition. The 141 catalysts were classified based on the loading amounts of the elements into four carbon formation classes: 0–15%, 15–30%, 30–45%, and ≥ 45%, represented by orange, green, blue, and purple, respectively. Class weights were assigned inversely proportional to class frequencies to address imbalance. The tree was pruned using cost complexity pruning (CCP) to optimize generalizability. The nodes are colored according to the class with the largest weighted frequency. The yellow highlight traces the routes for catalysts with carbon deposition <15%.

Subsequently, the resulting model was analyzed using SHAP analysis. This approach is particularly well-suited for capturing complex non-monotonic relationships within the data. It quantifies the contribution of each feature, specifically the elemental loading, to the predicted carbon deposition, thereby enabling global interpretability [35]. **Figure 4.5a** presents the global feature importance ranking based on the mean absolute SHAP values. A higher mean absolute SHAP value indicates a greater influence of the corresponding elemental loading on determining carbon formation. In addition, the distribution of SHAP values reveals how each element contributes across different levels of carbon deposition. It is evident that among all the elements investigated, the relative importance in influencing carbon formation follows the order of Ni > Rh > Al > Li > Co > Mn > Nb > Au > Ta > Y > Cu > Pt > Pd > V. Other elements showed lower overall importance and were therefore not explicitly discussed.

Figure 4.5b–e illustrates the local feature contributions, where the x-axis represents the SHAP values of individual data points, and the color scale reflects the corresponding elemental loading. This visualization enables a detailed understanding of how variations in elemental content influence carbon deposition behavior. In the 0–15% carbon deposition class (**Figure 4.5b**), the most influential elements are Rh > Ni > Co > Au > Cu, Pt, V. Notably, higher Rh loadings are predominantly associated with positive SHAP values (red points on the right), indicating that Rh strongly suppresses carbon formation.

Conversely, low Rh loadings correlate with negative SHAP values (blue points on the left), implying that insufficient Rh may promote carbon accumulation. Additionally, high Ni and Co loadings consistently contribute positively to carbon formation. Elements such as Au, Cu, and Pt appear in only a few catalysts, exhibiting limited but notable influence. These observations also align with the classification patterns in **Figure 4.4**.

In the 15–30% carbon deposition class (**Figure 4.5c**), Al emerges as a prominent contributor. Catalysts with higher Al loadings tend to exhibit positive SHAP values, suggesting that elevated Al content may moderately promote carbon formation. However, this trend becomes less clear in the 30–45% class (**Figure 4.5d**). Instead, Li and Nb emerge as more significant contributors to higher carbon formation in this range. Furthermore, elements such as Co, Mn, and Y show increased association with the 15–30% class, implying a possible role in sustaining intermediate carbon deposition levels. In the ≥45% carbon deposition class (**Figure 4.5e**), catalysts containing high Ta loadings are distinctly visible, suggesting that Ta probably serves as a driving factor for severe carbon deposition under the studied reaction conditions.

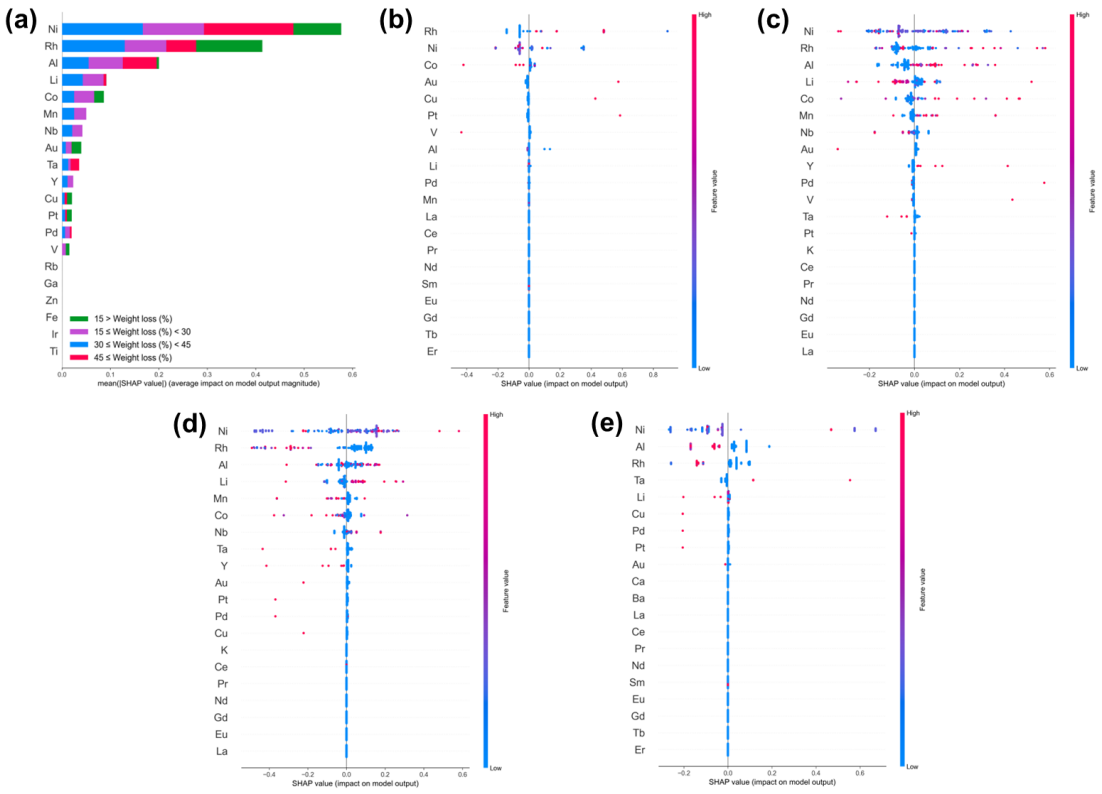

Figure 4.5. Feature importance analysis based on SHAP values. (a) Global feature importance was assessed using the mean absolute SHAP (Shapley Additive Explanations) values to identify the most influential elements contributing to carbon formation. (b)–(e) Local feature importance plots illustrate how each element influences the predicted carbon formation within specific carbon deposition classes: (b) 0–15%, (c) 15–30%, (d) 30–45%, and (e) ≥45%. Each dot corresponds to a single catalyst. The horizontal position represents the SHAP value, while the color indicates the magnitude of elemental loading in millimoles, with darker red reflecting higher values. A positive SHAP value implies that an increase in the corresponding elemental loading is associated with greater carbon formation.

4.4. Conclusion

In this chapter, the carbon deposition behavior of high-performance multi-element catalysts for low-temperature DRM was systematically investigated. A carbon deposition dataset comprising 141 catalysts was successfully constructed by performing DRM at 500 °C and quantitatively analyzing their carbon deposition behavior via TG-DTA. These catalysts were previously identified as high-performing candidates through an active learning loop that combined AFE with HTE to explore unknown compositional spaces.

Initial analyses revealed that while Ni and Co are indispensable for achieving high H_2 yields, their elevated loadings tend to promote carbon deposition. In contrast, Rh and Ir exhibit strong resistance to carbon accumulation but require the presence of active or promoter elements to complement their limited intrinsic activity.

To derive generalized design principles, a decision tree classifier and SHAP-based feature interpretation were applied. The tree revealed that high Rh loadings are essential for minimizing carbon deposition, while in Rh-deficient systems, alternative mitigation strategies involving Pt, Cu, and Y can be effective. SHAP analysis further quantified element-specific contributions and uncovered class-specific trends, such as the strong influence of Li, Nb, and Ta in promoting moderate to severe carbon accumulation. Overall, this chapter provides critical insights and actionable guidelines for the rational design of carbon-resistant multi-element catalysts for low-temperature DRM applications.

Reference

[1] B. Agún, A. Abánades, Comprehensive review on dry reforming of methane: Challenges and potential for greenhouse gas mitigation, Int. J. Hydrog. Energy 103 (2025) 395–414. https://doi.org/10.1016/j.ijhydene.2025.01.160.
[2] Z. Navas-Anguita, P.L. Cruz, M. Martin-Gamboa, D. Iribarren, J. Dufour, Simulation and life cycle assessment of synthetic fuels produced via biogas dry reforming and Fischer-Tropsch synthesis, Fuel 235 (2019) 1492–1500. https://doi.org/10.1016/j.fuel.2018.08.147.
[3] A.G. Hussien, K. Polychronopoulou, A review on the different aspects and challenges of the dry reforming of methane (DRM) reaction, Nanomaterials 12 (2022) 3400. https://doi.org/10.3390/nano12193400.
[4] B. Yuan, T. Zhu, Y. Han, X. Zhang, M. Wang, C. Li, Deactivation mechanism and anti-deactivation measures of metal catalyst in the dry reforming of methane: a review, Atmosphere 14 (2023) 770. https://doi.org/10.3390/atmos14050770.
[5] C. Wang, Y. Wang, M. Chen, D. Liang, Z. Yang, W. Cheng, Z. Tang, J. Wang, H. Zhang, Recent advances during CH_4 dry reforming for syngas production: A mini review, Int. J. Hydrog. Energy 46 (2021) 5852–5874. https://doi.org/10.1016/j.ijhydene.2020.10.240.
[6] J. Ren, J.-P. Cao, F.-L. Yang, Y.-L. Liu, W. Tang, X.-Y. Zhao, Understandings of catalyst deactivation and regeneration during biomass tar reforming: A crucial review, ACS Sustainable Chem. Eng. 9 (2021) 17186–17206. https://doi.org/10.1021/acssuschemeng.1c07483.
[7] C.H. Bartholomew, Mechanisms of catalyst deactivation, Appl. Catal. A: Gen. 212 (2001) 17–60. https://doi.org/10.1016/S0926-860X(00)00843-7.
[8] S. Arora, R. Prasad, An overview on dry reforming of methane: strategies to reduce carbonaceous deactivation of catalysts, RSC Adv. 6 (2016) 108668–108688. https://doi.org/10.1039/c6ra20450c.
[9] X. Cai, Y.H. Hu, Advances in catalytic conversion of methane and carbon dioxide to highly valuable products, Energy Sci. Eng. 7 (2019) 4–29. https://doi.org/10.1002/ese3.278.
[10] S. Chen, J. Zaffran, B. Yang, Dry reforming of methane over the cobalt catalyst: Theoretical insights into the reaction kinetics and mechanism for catalyst deactivation, Appl. Catal. B: Environ. 270 (2020) 118859. https://doi.org/10.1016/j.apcatb.2020.118859.
[11] E. Akbari, S.M. Alavi, M. Rezaei, CeO_2 Promoted Ni-MgO-Al_2O_3 nanocatalysts for carbon dioxide reforming of methane, J. CO_2 Util. 24 (2018) 128–138. https://doi.org/10.1016/j.jcou.2017.12.015.
[12] D.L. Nguyen, A.V. Tran, D.-V.N. Vo, H.T. Nguyen, N. Rajamohan, T.H. Trinh, T.L. Nguyen, Q.V. Le, T.M. Nguyen, Methane dry reforming: A catalyst challenge awaits, J. Ind. Eng. Chem. 140 (2024) 169–189. https://doi.org/10.1016/j.jiec.2024.06.017.
[13] S. Kawi, Y. Kathiraser, J. Ni, U. Oemar, Z. Li, E.T. Saw, Progress in synthesis of highly active and stable nickel-based catalysts for carbon dioxide reforming of methane, ChemSusChem 8 (2015) 3556–3575. https://doi.org/10.1002/cssc.201500390.
[14] L. Baharudin, N. Rahmat, N.H. Othman, N. Shah, S.S.A. Syed-Hassan, Formation, control, and elimination of carbon on Ni-based catalyst during CO_2 and CH_4 conversion via dry reforming process: A review, J. CO_2 Util. 61 (2022) 102050.

https://doi.org/10.1016/j.jcou.2022.102050.
[15] S. Sokolov, E.V. Kondratenko, M.-M. Pohl, A. Barkschat, U. Rodemerck, Stable low-temperature dry reforming of methane over mesoporous La_2O_3-ZrO_2 supported Ni catalyst, Appl. Catal. B: Environ. 113 (2012) 19–30. https://doi.org/10.1016/j.apcatb.2011.09.035.
[16] L. Wu, X. Xie, H. Ren, X. Gao, A short review on nickel-based catalysts in dry reforming of methane: Influences of oxygen defects on anti-coking property, Mater. Today: Proc. 42 (2021) 153–160. https://doi.org/10.1016/j.matpr.2020.10.697.
[17] K. Sutthiumporn, T. Maneerung, Y. Kathiraser, S. Kawi, CO_2 dry-reforming of methane over $La_{0.8}Sr_{0.2}Ni_{0.8}M_{0.2}O_3$ perovskite (M= Bi, Co, Cr, Cu, Fe): Roles of lattice oxygen on C–H activation and carbon suppression, Int. J. Hydrog. Energy 37 (2012) 11195–11207. https://doi.org/10.1016/j.ijhydene.2012.04.059.
[18] S.N.A. Rosli, S.Z. Abidin, O.U. Osazuwa, X. Fan, Y. Jiao, The effect of oxygen mobility/vacancy on carbon gasification in nano catalytic dry reforming of methane: A review, J. CO_2 Util. 63 (2022) 102109. https://doi.org/10.1016/j.jcou.2022.102109.
[19] L. Wang, Z. He, B. Ouyang, Data driven design of compositionally complex energy materials, Comput. Mater. Sci. 230 (2023) 112513. https://doi.org/10.1016/j.commatsci.2023.112513.
[20] C. Tian, T. Li, J. Bustillos, S. Bhattacharya, T. Turnham, J. Yeo, A. Moridi, Data-driven approaches toward smarter additive manufacturing, Adv. Intell. Syst. 3 (2021) 2100014. https://doi.org/10.1002/aisy.202100014.
[21] T. Toyao, Z. Maeno, S. Takakusagi, T. Kamachi, I. Takigawa, K.-i. Shimizu, Machine learning for catalysis informatics: recent applications and prospects, ACS Catal. 10 (2019) 2260–2297. https://doi.org/10.1021/acscatal.9b04186.
[22] J. Benavides-Hernández, F. Dumeignil, From characterization to discovery: artificial intelligence, machine learning and high-throughput experiments for heterogeneous catalyst design, ACS Catal. 14 (2024) 11749–11779. https://doi.org/10.1021/acscatal.3c06293.
[23] T. Taniike, A. Fujiwara, S. Nakanowatari, F. Garcia-Escobar, K. Takahashi, Automatic feature engineering for catalyst design using small data without prior knowledge of target catalysis, Commun. Chem. 7 (2024) 11. https://doi.org/10.1038/s42004-023-01086-y.
[24] S. Zhu, K. Jiang, B. Chen, S. Zheng, Data-driven design of electrocatalysts: principle, progress, and perspective, J. Mater. Chem. A 11 (2023) 3849–3870. https://doi.org/10.1039/D2TA09278F.
[25] L.H. Mou, T. Han, P.E. Smith, E. Sharman, J. Jiang, Machine learning descriptors for data-driven catalysis study, Adv. Sci. 10 (2023) 2301020. https://doi.org/10.1002/advs.202301020.
[26] A. Fujiwara, S. Nakanowatari, Y. Cho, T. Taniike, Acquiring and transferring comprehensive catalyst knowledge through integrated high-throughput experimentation and automatic feature engineering, Sci. Technol. Adv. Mater. (2025) 2454219. https://doi.org/10.1080/14686996.2025.2454219.
[27] T.N. Nguyen, T.T.P. Nhat, K. Takimoto, A. Thakur, S. Nishimura, J. Ohyama, I. Miyazato, L. Takahashi, J. Fujima, K. Takahashi, High-throughput experimentation and catalyst informatics for oxidative coupling of methane, ACS Catal. 10 (2019) 921–932. https://doi.org/10.1021/acscatal.9b04293.

[28] T.P. Jayakumar, S.P.S. Babu, T.N. Nguyen, S.D. Le, R.P. Manchan, P. Phulkerd, P. Chammingkwan, T. Taniike, Exploration of ethanol-to-butadiene catalysts by high-throughput experimentation and machine learning, Appl. Catal. A: Gen. 666 (2023) 119427. https://doi.org/10.1016/j.apcata.2023.119427.
[29] W. Du, P. Chammingkwan, K. Takahashi, T. Taniike, Unbiased dataset for methane dry reforming and catalyst design guidelines obtained by high-throughput experimentation and machine learning, J. Catal. 442 (2025) 115930. https://doi.org/10.1016/j.jcat.2024.115930.
[30] M. Baysal, M.E. Günay, R. Yıldırım, Decision tree analysis of past publications on catalytic steam reforming to develop heuristics for high performance: A statistical review, Int. J. Hydrog. Energy 42 (2017) 243–254. https://doi.org/10.1016/j.ijhydene.2016.10.003.
[31] Y. Li, Y. Fu, C. Lai, L. Qin, B. Li, S. Liu, H. Yi, F. Xu, L. Li, M. Zhang, Porous materials confining noble metals for the catalytic reduction of nitroaromatics: controllable synthesis and enhanced mechanism, Environ. Sci. Nano 8 (2021) 3067–3097. https://doi.org/10.1039/D1EN00628B.
[32] S. Nieß, U. Armbruster, S. Dietrich, M. Klemm, Recent advances in catalysis for methanation of CO_2 from biogas, Catalysts 12 (2022) 374. https://doi.org/10.3390/catal12040374.
[33] A.M. Alsawadi, R. Marsh, J.M. Steer, D. Morgan, A study of the mechanisms associated with CO_2 utilisation via the reverse Boudouard reaction, Fuel 381 (2025) 133448. https://doi.org/10.1016/j.fuel.2024.133448.
[34] C. Vogt, M. Monai, E.B. Sterk, J. Palle, A.E. Melcherts, B. Zijlstra, E. Groeneveld, P.H. Berben, J.M. Boereboom, E.J. Hensen, Understanding carbon dioxide activation and carbon–carbon coupling over nickel, Nat. Commun. 10 (2019) 5330. https://doi.org/10.1038/s41467-019-12858-3.
[35] J. Qi, Y. Wang, P. Xu, T. Huhe, X. Ling, H. Yuan, Y. Chen, J. Li, Study on biomass and polymer catalytic co-pyrolysis product characteristics using machine learning and shapley additive explanations (SHAP), Fuel 380 (2025) 133165. https://doi.org/10.1016/j.fuel.2024.133165.

Chapter 5 General conclusion

The rational design of solid catalysts remains one of the most formidable challenges in heterogeneous catalysis, primarily due to the immense compositional complexity and intricate interdependencies among active metals, supports, and promoters. Traditional development strategies have largely depended on iterative experimentation guided by chemical intuition, which inherently restricts exploration to familiar systems and limits the potential for discovering novel and high-performing catalysts. In recent years, data-driven approaches have gained increasing traction in catalyst development. However, they still face two major limitations. First, in complex material systems such as solid catalysts, there is often a lack of sufficient high-quality experimental data. Second, designing universal and informative descriptors typically requires deep domain expertise and system-specific assumptions. Dry reforming of methane (DRM) is an important catalytic reaction, but it conventionally requires high temperatures above 700 °C to achieve adequate conversion. Operating at lower temperatures, such as 500 °C, is an attractive alternative. However, under such mild conditions, undesired side reactions become more severe, posing significant challenges for catalyst stability. Addressing this issue which often requires the careful integration of multiple elements. To overcome these limitations, this dissertation proposes a systematic, data-driven strategy for the design of multi-element catalysts for low-temperature DRM, under the assumption of no prior knowledge. By integrating HTE, ML, and AFE within an adaptive experimental design framework, it enables efficient exploration of high-dimensional catalyst spaces and accelerates the identification of active and carbon-resistant formulations.

In **Chapter 2**, the research commenced with the construction of a large-scale, compositionally unbiased dataset consisting of 256 γ-Al_2O_3-supported catalysts. These catalysts were synthesized through random sampling from a representative library of 17 elements and systematically evaluated for DRM at 500 °C. This dataset served as a foundational platform for subsequent ML applications by capturing diverse compositional patterns without imposing prior assumptions. Statistical analyses revealed that superior catalytic performance was not exclusively associated with the inclusion of conventionally active metals such as Ni or platinum group elements. Rather, unexpected synergies involving elements such as Al, Nb, and Hf were found to play pivotal roles in enhancing H_2 yield and mitigating carbon deposition. These findings underscored the effectiveness of an unbiased experimental design strategy in uncovering non-obvious but chemically meaningful design principles.

In **Chapter 3**, the research expanded upon the initial dataset by establishing an adaptive active learning framework that systematically guided catalyst exploration. This framework integrated AFE to generate thousands of composition-based descriptors and employed farthest point sampling (FPS) to strategically select candidates from underexplored regions of the compositional space. Through successive loops of model retraining and HTE validation, the elemental design space was expanded from 17 to 45 elements. This iterative strategy led to the identification of more than 100 previously unreported catalysts exhibiting outstanding H_2 yields. Catalysts with H_2 yields of 30% or higher not only reaffirm the pivotal role of Ni as the core active element but also

demonstrate a broadened promoter landscape. Notably, elements including alkali metals (Li, K, Cs, Rb), early transition metals (Sc, Ti, Mn, Y, Nb, Hf, Ta), and the rare earth element Sm emerged as effective contributors to enhanced DRM performance. Overall, this chapter underscores the powerful capability of adaptive active learning to overcome the limitations of human intuition and accelerate the discovery of novel high-performance DRM catalysts.

In **Chapter 4**, the focus shifted to one of the most critical challenges in low-temperature DRM: carbon deposition. Using thermogravimetric and differential thermal analysis, this chapter systematically investigated the carbon deposition behavior of the high-performing catalysts identified through the adaptive learning loop presented in Chapter 3. The results revealed that carbon deposition was primarily governed by the Boudouard reaction, and its severity strongly depended on catalyst composition. Preliminary analysis revealed that Ni and Co are indispensable for achieving high H_2 yields, yet their high loadings tend to promote carbon deposition. In contrast, Rh and Ir exhibit strong resistance to carbon accumulation but require the presence of active or promoter elements to compensate for their limited intrinsic activity. Decision tree analysis indicated that high Rh loadings are critical for minimizing carbon formation, while in systems with low Rh content, the incorporation of Pt, Cu, or Y proved to be effective alternatives. SHAP analysis further revealed the strong contributions of Li, Nb, and Ta to moderate and severe carbon accumulation. Overall, this chapter provides valuable insights and practical

guidelines for the rational design of carbon-resistant multi-element catalysts for low-temperature DRM applications.

I believe that this dissertation presents a robust adaptive catalyst design strategy that integrates HTE, AFE, and ML to accelerate the discovery of high-performance multi-element DRM catalysts without requiring prior system-specific knowledge. Moreover, it is also expected to provide practical and generalizable guidelines for the rational design of catalysts in other complex catalytic systems, especially those involving high-dimensional compositional spaces.

List of Publications and Other Achievements

A) Publications

1. **Wentao Du**, Patchanee Chammingkwan, Keisuke Takahashi, Toshiaki Taniike, Unbiased dataset for methane dry reforming and catalyst design guidelines obtained by high-throughput experimentation and machine learning, *Journal of Catalysis* **2024**, *442*, 115930. https://doi.org/10.1016/j.jcat.2024.115930.

B) Conferences

Domestic Conference

1. **Wentao Du**, Sunao Nakanowatari, Ken Takimoto, Toshiaki Taniike, High-throughput experimentation and machine learning for exploring multi-element catalysts in low-temperature dry reforming of methane, The Chemical Society of Japan, Kinki Branch, Hokuriku District Lecture Meeting and Research Presentation, Kanazawa, Japan, Nov. 17, 2023, poster.

International Conferences

1. **Wentao Du**, Sunao Nakanowatari, Ken Takimoto, Toshiaki Taniike, Unbiased dataset for methane dry reforming and catalyst design heuristics obtained by high-throughput experimentation and machine learning, International Symposium on Materials Informatics 2023, Multidisciplinary approach to olefin polymerization catalysis, Nomi, Japan, Dec. 8, 2023, poster.

C) Patents

1. 谷池 俊明, ト ブントウ, 新規メタンドライリフォーミング触媒の網羅的な探索と製造, 特願 2024-147988.

Appendix A – Catalyst dataset, descriptors and test set

Table A1. Entire DRM dataset obtained by HTE. Individual catalysts are described by their elemental combinations, compositions and performances.[a,b,c,d]

No.	A (mmol)	B (mmol)	C (mmol)	D (mmol)	E (mmol)	M_{total} (mmol/g-support)	CH_4 conv. (%)	CO_2 conv. (%)	H_2 yield (%)	CO yield (%)
1	Al (0.837)	V (0.650)	Rh (0.293)	Ce (0.710)	Sm (0.248)	2.74	2.4	-2.6	0.1	0.7
2	Ca (0.681)	Nb (0.700)	Ag (0.402)	Cs (0.529)	Sm (0.373)	2.68	2.0	-3.1	0.0	0.2
3	Li (0.845)	Al (0.558)	Ni (0.282)	Nb (0.700)	Ce (0.426)	2.81	25.9	27.3	26.0	22.9
4	Ca (0.545)	Ni (0.565)	Ba (0.913)	Sm (0.373)	Au (0.371)	2.77	2.7	-3.4	0.0	0.3
5	Al (0.837)	V (0.390)	Cs (0.661)	Sm (0.248)	Bi (0.452)	2.59	2.3	-4.0	0.0	0.1
6	Li (0.704)	Ca (0.273)	Ni (0.565)	Ag (0.803)	Hf (0.421)	2.77	2.2	-3.1	0.1	0.4
7	Al (0.558)	Ni (0.706)	Cs (0.529)	Ce (0.568)	Ir (0.400)	2.76	10.9	16.8	9.0	16.5
8	Al (0.279)	Ca (0.818)	Ag (0.536)	Sm (0.621)	Au (0.371)	2.62	2.3	-3.4	0.0	0.1
9	Nb (0.700)	Ce (0.426)	Sm (0.745)	Hf (0.421)	Au (0.371)	2.66	2.6	-3.3	0.1	0.3
10	Li (1.126)	Nb (0.420)	Rh (0.440)	Ag (0.670)	Hf (0.140)	2.80	3.1	-2.7	0.5	1.0
11	Nb (0.280)	Cs (0.793)	Ba (0.760)	Ce (0.710)	Ir (0.267)	2.81	6.4	7.5	3.0	8.3
12	Li (0.704)	Cs (0.396)	Ce (0.568)	Sm (0.373)	Hf (0.701)	2.74	2.2	-3.1	0.0	0.2
13	Ca (0.409)	Nb (1.120)	Ag (0.536)	Hf (0.421)	Au (0.248)	2.73	1.9	-3.2	0.0	0.1
14	Ca (1.226)	V (0.260)	Ni (0.847)	Hf (0.140)	Ir (0.267)	2.74	2.5	-2.7	0.1	0.5
15	V (0.260)	Nb (0.420)	Ag (0.536)	Cs (0.793)	Hf (0.701)	2.71	2.5	-3.5	0.0	0.1
16	Al (0.279)	V (0.520)	Cs (0.529)	Ir (0.667)	Bi (0.565)	2.56	2.3	-3.7	0.0	0.1
17	Li (0.845)	Ca (0.273)	V (0.130)	Ni (0.847)	Ag (0.670)	2.76	2.2	-3.7	0.0	0.3
18	Ni (0.706)	Nb (0.140)	Cs (0.661)	Sm (0.745)	Ir (0.400)	2.65	7.2	9.8	3.8	9.9
19	Al (0.837)	Nb (0.700)	Rh (0.293)	Ag (0.402)	Hf (0.561)	2.79	9.2	12.4	8.0	13.2
20	Ni (0.424)	Rh (0.440)	Ag (0.937)	Ce (0.710)	Ir (0.267)	2.78	5.9	7.1	2.8	8.0
21	Ca (0.514)	Nb (0.175)	Ce (0.198)	Sm (0.678)	Bi (0.354)	1.92	3.0	-3.3	0.0	0.0
22	Al (0.295)	Ni (0.792)	Ag (0.358)	Sn (0.233)	Cs (0.615)	2.29	2.9	-2.6	0.0	0.1
23	Ag (0.358)	Sn (0.698)	Ba (0.849)	Sm (0.226)	Hf (0.286)	2.42	3.3	-2.9	0.0	0.0
24	Al (0.591)	V (0.158)	Ni (0.528)	Sm (0.678)	Bi (0.354)	2.31	3.2	-3.0	0.0	0.0
25	Ca (0.171)	Ag (0.179)	Sn (0.698)	Sm (0.452)	Bi (0.531)	2.03	3.1	-3.0	0.0	0.0
26	Ni (0.528)	Nb (0.175)	Ag (0.536)	Sm (0.452)	Hf (0.572)	2.26	3.1	-2.6	0.0	0.3
27	Sn (0.465)	Ba (0.566)	Hf (0.858)	Ir (0.207)	Bi (0.354)	2.45	2.7	-3.2	0.0	0.1
28	Li (0.209)	Ca (0.342)	V (0.316)	Au (0.325)	Bi (0.531)	1.72	3.2	-3.1	0.0	0.0
29	Al (0.591)	V (0.158)	Rh (0.172)	Sn (0.698)	Cs (0.615)	2.23	3.4	-2.7	0.0	0.1
30	Li (0.627)	Ca (0.171)	Ni (0.792)	Nb (0.175)	Ir (0.413)	2.18	28.7	27.7	27.3	21.8
31	V (0.316)	Ni (0.264)	Ag (0.536)	Ce (0.395)	Au (0.325)	1.84	3.3	-2.5	0.0	0.1
32	V (0.316)	Cs (0.615)	Ba (0.283)	Sm (0.452)	Bi (0.354)	2.02	3.4	-3.1	0.0	0.0
33	Al (0.886)	Ni (0.528)	Ag (0.179)	Sn (0.233)	Sm (0.678)	2.50	3.0	-3.2	0.0	0.1
34	Al (0.295)	Ca (0.342)	Ba (0.849)	Sm (0.678)	Bi (0.177)	2.34	3.4	-3.4	0.0	0.0

35	Li (0.418)	Al (0.295)	Ni (0.792)	Sn (0.698)	Cs (0.205)	2.41	3.7	-2.7	0.0	0.4
36	Ca (0.514)	Ni (0.264)	Ba (0.849)	Ir (0.207)	Au (0.325)	2.16	7.9	8.6	3.4	9.0
37	Ca (0.514)	V (0.316)	Cs (0.205)	Ba (0.283)	Sm (0.678)	2.00	4.5	-3.0	0.0	0.1
38	Ca (0.514)	Nb (0.175)	Rh (0.172)	Cs (0.410)	Ir (0.620)	1.89	11.5	15.2	9.6	15.2
39	Ni (0.264)	Sn (0.233)	Ce (0.593)	Sm (0.452)	Hf (0.858)	2.40	2.9	-3.1	0.0	0.1
40	Li (0.209)	Ag (0.715)	Sn (0.465)	Au (0.163)	Bi (0.354)	1.91	2.7	-3.3	0.0	0.0
41	Li (0.612)	V (0.614)	Ni (0.380)	Cs (0.188)	Bi (0.159)	1.95	3.5	-3.2	0.0	0.1
42	Sn (0.148)	Cs (0.376)	Ce (0.770)	Sm (0.249)	Au (0.165)	1.71	3.8	-3.1	0.0	0.1
43	Li (0.408)	Rh (0.223)	Ag (0.490)	Sn (0.443)	Ce (0.192)	1.76	4.1	-2.1	0.1	0.8
44	Al (0.306)	V (0.205)	Rh (0.446)	Ba (0.589)	Ce (0.385)	1.93	3.9	-1.7	0.1	0.9
45	Al (0.459)	Ni (0.569)	Nb (0.128)	Ag (0.163)	Sn (0.295)	1.61	3.5	-2.9	0.0	0.1
46	Ag (0.327)	Sn (0.148)	Cs (0.376)	Hf (0.386)	Au (0.331)	1.57	3.1	-3.1	0.0	0.1
47	Li (0.408)	V (0.410)	Ni (0.569)	Rh (0.223)	Ag (0.327)	1.94	6.1	4.1	1.3	5.3
48	Ca (0.531)	V (0.410)	Nb (0.128)	Hf (0.257)	Ir (0.288)	1.61	3.5	-3.0	0.0	0.2
49	Al (0.306)	Ca (0.531)	Sn (0.148)	Cs (0.188)	Ba (0.589)	1.76	4.1	-3.3	0.0	0.1
50	Li (0.408)	Ca (0.354)	Ce (0.577)	Ir (0.144)	Au (0.331)	1.81	10.6	13.4	6.9	13.4
51	V (0.205)	Nb (0.384)	Ag (0.327)	Cs (0.376)	Bi (0.317)	1.61	3.5	-3.0	0.0	0.1
52	Al (0.459)	Rh (0.223)	Ag (0.490)	Sm (0.249)	Au (0.165)	1.59	4.7	0.4	0.9	2.5
53	Li (0.408)	Ca (0.354)	Ni (0.759)	Hf (0.129)	Ir (0.144)	1.79	28.0	26.2	26.5	21.2
54	Nb (0.384)	Sn (0.295)	Ba (0.392)	Ce (0.385)	Ir (0.144)	1.60	4.0	-2.9	0.0	0.2
55	Ca (0.177)	Ni (0.380)	Ba (0.392)	Sm (0.249)	Bi (0.476)	1.67	3.7	-3.6	0.0	0.1
56	Al (0.153)	Ca (0.531)	Ag (0.327)	Sn (0.443)	Au (0.165)	1.62	3.6	-3.3	0.0	0.1
57	Al (0.306)	Nb (0.511)	Ce (0.385)	Hf (0.129)	Ir (0.144)	1.47	5.7	3.8	1.3	5.0
58	V (0.205)	Ni (0.569)	Cs (0.564)	Ba (0.392)	Bi (0.159)	1.89	3.6	-2.8	0.0	0.2
59	Li (0.612)	Ni (0.190)	Sn (0.148)	Sm (0.373)	Bi (0.317)	1.64	3.5	-3.0	0.0	0.1
60	Al (0.313)	Ca (0.166)	Sn (0.786)	Ce (0.642)	Au (0.203)	2.11	5.1	-1.5	0.0	0.1
61	Ca (0.332)	Ag (0.352)	Cs (0.810)	Hf (0.195)	Bi (0.191)	1.88	5.2	-1.0	0.0	0.1
62	Rh (0.221)	Ag (0.352)	Sm (0.693)	Ir (0.500)	Bi (0.191)	1.96	5.2	-1.6	0.0	0.1
63	Nb (0.726)	Ag (0.176)	Ba (0.707)	Ce (0.214)	Hf (0.389)	2.21	5.3	-1.5	0.0	0.1
64	Li (0.231)	V (0.661)	Ni (0.804)	Rh (0.221)	Bi (0.382)	2.30	5.6	-1.2	0.0	0.1
65	Al (0.627)	Ca (0.166)	Rh (0.221)	Ag (0.352)	Ce (0.428)	1.79	14.4	17.8	10.5	16.2
66	Ni (0.536)	Nb (0.726)	Sn (0.524)	Ba (0.471)	Hf (0.195)	2.45	5.1	-1.6	0.0	0.1
67	V (0.441)	Nb (0.968)	Sm (0.173)	Ir (0.250)	Au (0.407)	2.24	5.5	-1.1	0.1	0.4
68	Al (0.157)	Ca (0.332)	V (0.441)	Au (0.203)	Bi (0.765)	1.90	5.5	-1.9	0.0	0.0
69	Li (0.463)	Ni (0.268)	Nb (0.242)	Ba (0.707)	Ir (0.750)	2.43	18.2	24.8	15.6	22.1
70	Ca (0.497)	Rh (0.221)	Ba (0.471)	Ce (0.642)	Bi (0.191)	2.02	4.9	-1.6	0.0	0.1
71	Li (0.463)	Rh (0.221)	Sn (0.786)	Cs (0.607)	Bi (0.191)	2.27	4.9	-1.3	0.0	0.1
72	Al (0.470)	Nb (0.484)	Rh (0.221)	Ce (0.428)	Hf (0.389)	1.99	21.7	29.8	20.8	27.3
73	Ca (0.166)	Ag (0.352)	Sn (0.786)	Sm (0.520)	Au (0.203)	2.03	5.5	-2.2	0.0	0.0
74	Al (0.470)	Cs (0.405)	Sm (0.520)	Hf (0.195)	Au (0.203)	1.79	5.7	-1.5	0.0	0.1
75	Li (0.463)	Al (0.470)	Ca (0.166)	V (0.661)	Au (0.203)	1.96	5.4	-1.6	0.0	0.0
76	Ni (0.268)	Ag (0.176)	Sn (0.786)	Cs (0.405)	Ce (0.642)	2.28	4.9	-1.4	0.0	0.1
77	Li (0.463)	Ca (0.332)	Nb (0.484)	Ag (0.352)	Sm (0.347)	1.98	4.9	-1.7	0.0	0.1
78	V (0.441)	Ni (0.536)	Ag (0.176)	Sm (0.520)	Bi (0.382)	2.05	5.1	-1.7	0.0	0.0
79	Al (0.218)	Ni (0.166)	Nb (0.708)	Sn (0.373)	Sm (0.238)	1.70	4.4	-2.2	0.0	0.1
80	Li (0.485)	V (0.244)	Rh (0.203)	Cs (0.517)	Ce (0.741)	2.19	4.5	-0.9	0.0	0.2

81	Li (0.728)	V (0.733)	Nb (0.177)	Cs (0.259)	Sm (0.476)	2.37	4.8	-1.7	0.0	0.1
82	Al (0.218)	Ca (0.449)	V (0.977)	Sn (0.124)	Ir (0.344)	2.11	4.7	-1.3	0.0	0.2
83	Al (0.218)	Ca (0.449)	Nb (0.708)	Ag (0.451)	Sm (0.238)	2.06	4.5	-1.6	0.0	0.2
84	Li (0.243)	Ca (0.674)	Ba (0.621)	Sm (0.714)	Au (0.217)	2.47	4.1	-2.1	0.0	0.1
85	Ca (0.674)	Rh (0.203)	Ag (0.226)	Cs (0.776)	Sm (0.476)	2.35	10.6	13.4	5.9	12.1
86	V (0.489)	Sn (0.248)	Ce (0.370)	Ir (0.344)	Bi (0.444)	1.90	4.5	-1.9	0.0	0.1
87	Ni (0.332)	Nb (0.177)	Ag (0.451)	Ba (0.311)	Ce (0.741)	2.01	5.0	-1.5	0.1	0.7
88	Ca (0.449)	Ni (0.332)	Rh (0.203)	Sn (0.497)	Au (0.217)	1.70	5.0	-1.7	0.0	0.2
89	Li (0.485)	V (0.733)	Ag (0.226)	Ba (0.621)	Bi (0.444)	2.51	4.9	-2.2	0.0	0.1
90	Li (0.485)	Al (0.654)	Rh (0.203)	Sn (0.248)	Au (0.434)	2.02	5.3	0.8	0.2	1.7
91	Li (0.243)	V (0.244)	Ag (0.226)	Sn (0.373)	Ir (0.689)	1.77	4.8	-0.7	0.1	0.6
92	Li (0.728)	Al (0.436)	Rh (0.203)	Ag (0.451)	Au (0.434)	2.25	4.8	-1.5	0.1	0.4
93	Li (0.728)	Al (0.436)	V (0.244)	Ce (0.370)	Au (0.434)	2.21	5.0	-1.9	0.0	0.2
94	Ni (0.498)	Nb (0.354)	Ag (0.451)	Ce (0.370)	Sm (0.238)	1.91	5.4	-1.4	0.1	0.4
95	V (0.489)	Nb (0.354)	Rh (0.203)	Sm (0.476)	Au (0.650)	2.17	5.2	0.5	0.2	1.5
96	Ca (0.449)	Ni (0.664)	Nb (0.177)	Sn (0.248)	Bi (0.222)	1.76	4.3	-2.0	0.0	0.1
97	Ca (0.225)	Nb (0.531)	Ag (0.451)	Cs (0.517)	Ba (0.621)	2.35	4.2	-2.2	0.0	0.2
98	Ca (0.225)	Rh (0.203)	Cs (0.517)	Ir (0.344)	Bi (0.888)	2.18	4.0	-2.2	0.0	0.1
99	Ba (0.654)	Ce (0.211)	Sm (0.153)	Hf (0.220)	Au (0.519)	1.76	4.9	-2.5	0.0	0.2
100	Al (0.232)	Nb (0.204)	Cs (0.242)	Ce (1.267)	Hf (0.220)	2.16	4.2	-2.7	0.0	0.2
101	Li (0.692)	Sn (0.203)	Cs (1.088)	Hf (0.329)	Ir (0.114)	2.43	4.7	-2.6	0.0	0.2
102	V (0.926)	Ni (0.379)	Nb (0.204)	Ba (0.374)	Ir (0.455)	2.34	4.8	-2.8	0.0	0.2
103	Li (0.138)	Sn (1.521)	Ce (0.106)	Hf (0.220)	Au (0.074)	2.06	4.6	-3.1	0.0	0.1
104	Rh (0.227)	Sn (0.608)	Cs (0.363)	Ba (0.374)	Au (0.371)	1.94	4.1	-3.0	0.0	0.2
105	Nb (0.816)	Sn (0.203)	Ce (0.317)	Sm (0.076)	Bi (0.159)	1.57	4.6	-2.8	0.0	0.1
106	Rh (0.227)	Cs (0.846)	Hf (0.549)	Ir (0.341)	Au (0.223)	2.19	9.6	9.0	4.4	9.1
107	Li (0.553)	Nb (0.612)	Rh (0.113)	Ag (0.821)	Ba (0.093)	2.19	4.8	-2.0	0.3	0.7
108	Li (0.830)	Al (0.232)	Sn (0.811)	Ba (0.187)	Ce (0.211)	2.27	4.4	-2.7	0.0	0.1
109	Li (0.415)	Rh (0.227)	Cs (1.329)	Ce (0.211)	Au (0.148)	2.33	7.9	7.0	2.6	7.4
110	Nb (1.020)	Rh (0.113)	Ba (0.187)	Ce (0.633)	Hf (0.110)	2.06	20.5	27.9	19.7	26.9
111	Ca (0.774)	Nb (0.714)	Ba (0.187)	Ce (0.211)	Bi (0.219)	2.11	4.4	-3.3	0.0	0.2
112	Li (0.830)	Ni (0.253)	Rh (0.113)	Cs (0.483)	Ba (0.654)	2.33	15.2	19.9	11.1	18.8
113	Ca (0.442)	V (0.529)	Ni (1.010)	Rh (0.227)	Ir (0.227)	2.44	4.7	-2.6	0.1	0.4
114	Al (0.232)	Ni (0.126)	Sn (0.507)	Ir (1.023)	Au (0.223)	2.11	5.2	-0.8	0.1	1.3
115	Sn (0.304)	Cs (0.242)	Ba (0.841)	Hf (0.439)	Bi (0.071)	1.90	4.4	-2.7	0.0	0.2
116	Li (1.798)	V (0.265)	Ag (0.205)	Cs (0.121)	Ir (0.227)	2.62	5.7	1.2	0.7	2.9
117	Li (0.415)	V (0.529)	Rh (0.227)	Cs (0.725)	Hf (0.549)	2.44	4.3	-2.9	0.0	0.2
118	Li (0.433)	Ag (0.469)	Cs (0.160)	Ba (0.380)	Hf (0.424)	1.87	4.2	-1.8	0.1	0.2
119	Ni (0.886)	Sn (0.633)	Cs (0.160)	Ir (0.092)	Bi (0.106)	1.88	3.9	-1.6	0.0	0.2
120	Li (0.649)	Al (0.193)	Ni (0.354)	Ce (0.575)	Au (0.057)	1.83	9.8	12.3	5.0	10.9
121	V (0.854)	Rh (0.314)	Ce (0.411)	Sm (0.073)	Ir (0.367)	2.02	19.3	27.0	18.3	25.4
122	Ca (0.181)	Nb (0.089)	Cs (0.400)	Ba (0.951)	Hf (0.212)	1.83	4.4	-2.1	0.0	0.1
123	Al (0.096)	Ni (0.975)	Cs (0.160)	Sm (0.365)	Ir (0.092)	1.69	30.5	27.9	28.1	20.3
124	Li (0.865)	V (0.244)	Ba (0.380)	Sm (0.292)	Bi (0.271)	2.05	4.3	-1.6	0.0	0.2
125	Ca (0.271)	Ag (0.703)	Sn (0.311)	Cs (0.080)	Ir (0.367)	1.73	4.2	-1.9	0.0	0.2
126	Cs (0.320)	Ce (0.411)	Sm (0.365)	Hf (0.212)	Au (0.226)	1.53	4.4	-1.9	0.0	0.1

127	Nb (0.089)	Ag (0.469)	Ba (0.665)	Ce (0.082)	Au (0.283)	1.59	4.8	-1.8	0.0	0.1
128	Al (0.193)	Ni (0.620)	Nb (0.626)	Rh (0.105)	Ir (0.275)	1.82	22.2	28.5	21.6	25.8
129	Li (0.433)	Ca (0.090)	Ni (0.266)	Sn (0.279)	Bi (0.093)	1.16	4.4	-2.0	0.0	0.2
130	Al (0.289)	Nb (0.268)	Rh (0.314)	Ag (0.625)	Hf (0.318)	1.81	11.2	13.1	8.5	12.7
131	Ca (0.903)	Cs (0.320)	Ce (0.329)	Sm (0.073)	Au (0.057)	1.68	4.0	-1.8	0.1	0.3
132	Ni (0.798)	Sn (0.122)	Cs (0.240)	Hf (0.424)	Bi (0.122)	1.71	4.7	-2.0	0.0	0.2
133	Al (0.193)	Ca (0.181)	Rh (0.418)	Sn (0.332)	Ce (0.657)	1.78	5.0	-0.6	0.1	0.8
134	V (0.366)	Cs (0.720)	Sm (0.219)	Ir (0.183)	Au (0.170)	1.66	4.3	-2.1	0.0	0.2
135	Li (0.865)	Al (0.193)	Ni (0.443)	Cs (0.080)	Hf (0.424)	2.01	34.0	29.4	30.5	20.8
136	Ni (0.089)	Ce (0.164)	Sm (0.877)	Ir (0.367)	Au (0.057)	1.55	11.2	14.9	6.7	13.4
137	Ca (0.632)	Nb (0.089)	Rh (0.105)	Hf (0.424)	Bi (1.176)	2.43	4.4	-1.7	0.0	0.1
138	Li (0.823)	Ca (0.130)	V (0.613)	Ce (0.254)	Ir (0.373)	2.19	4.7	1.6	0.2	1.6
139	Ca (0.130)	Nb (0.405)	Sn (0.869)	Cs (0.411)	Ir (0.093)	1.91	3.7	0.0	0.0	0.2
140	Li (0.137)	Ca (0.909)	V (0.102)	Rh (0.138)	Cs (0.924)	2.21	3.9	-0.8	0.0	0.1
141	Li (0.137)	Ni (1.099)	Rh (0.069)	Ag (0.084)	Ba (0.057)	1.45	8.1	9.5	3.6	8.2
142	Cs (0.513)	Ce (0.338)	Hf (0.165)	Ir (0.280)	Bi (0.465)	1.76	4.0	-0.3	0.1	0.5
143	Ca (0.909)	Ni (0.481)	Ag (0.168)	Ce (0.085)	Ir (0.280)	1.92	6.2	6.0	1.5	5.0
144	Al (0.210)	Sn (0.095)	Ce (0.846)	Hf (0.221)	Ir (0.187)	1.56	4.2	0.8	0.1	1.2
145	Al (0.105)	Nb (0.243)	Sn (1.572)	Ba (0.057)	Bi (0.393)	2.37	3.7	-0.7	0.0	0.1
146	V (0.511)	Ag (0.336)	Sm (1.090)	Ir (0.093)	Au (0.067)	2.10	4.2	0.3	0.1	1.1
147	Ni (0.206)	Nb (0.486)	Sn (0.143)	Cs (0.616)	Ba (0.114)	1.56	4.0	-0.9	0.0	0.1
148	Li (0.549)	V (0.307)	Ag (0.840)	Cs (0.103)	Bi (0.064)	1.86	3.7	-0.9	0.0	0.1
149	Al (0.315)	Ca (0.649)	Ni (0.069)	Cs (0.924)	Sm (0.242)	2.20	3.6	-1.0	0.0	0.1
150	Al (0.525)	V (0.204)	Rh (0.413)	Ba (0.114)	Au (0.335)	1.59	3.6	-0.6	0.0	0.4
151	Al (1.155)	V (0.307)	Ni (0.137)	Ag (0.252)	Ba (0.057)	1.91	3.7	-0.8	0.0	0.2
152	Nb (0.486)	Ba (0.057)	Hf (0.165)	Ir (0.373)	Bi (0.165)	1.25	4.0	-0.9	0.0	0.1
153	Al (0.105)	Sn (0.265)	Ba (0.398)	Ce (0.254)	Au (0.268)	1.29	3.9	-1.2	0.0	0.1
154	Li (1.235)	Nb (0.324)	Rh (0.138)	Ce (0.085)	Bi (0.618)	2.40	3.7	-1.1	0.0	0.1
155	Ca (0.519)	Ag (0.252)	Sn (0.446)	Ce (0.254)	Au (0.402)	1.87	3.4	-0.9	0.0	0.2
156	Li (2.058)	V (0.102)	Ni (0.069)	Ce (0.085)	Sm (0.242)	2.56	3.9	-0.7	0.0	0.2
157	Li (0.137)	Ca (0.260)	V (0.102)	Ni (1.030)	Au (0.067)	1.60	3.7	-0.8	0.0	0.1
158	Al (0.172)	Ca (0.135)	Rh (0.229)	Ba (0.783)	Ir (0.577)	1.90	19.1	27.0	19.4	24.9
159	V (0.331)	Cs (0.112)	Ce (0.104)	Sm (0.813)	Au (0.346)	1.71	3.5	-0.2	0.0	0.2
160	Al (0.600)	Nb (0.709)	Ag (0.118)	Sm (0.068)	Ir (0.385)	1.88	5.0	2.7	1.2	3.1
161	Li (0.482)	Ni (0.846)	Ag (0.118)	Cs (0.224)	Bi (0.663)	2.33	4.2	-1.0	0.0	0.1
162	Al (0.086)	Ca (0.203)	Nb (0.912)	Ce (0.104)	Ir (0.577)	1.88	9.1	11.5	4.6	10.0
163	Li (0.096)	Ni (2.255)	Nb (0.101)	Rh (0.114)	Ir (0.096)	2.66	37.5	31.2	32.5	25.5
164	V (0.442)	Ni (0.423)	Sm (0.271)	Au (0.231)	Bi (1.008)	2.37	3.7	-1.1	0.0	0.1
165	Li (0.675)	Ca (0.068)	Ir (0.192)	Au (0.231)	Bi (1.084)	2.25	3.6	-1.1	0.0	0.1
166	Al (0.686)	V (0.442)	Ni (0.141)	Ba (0.489)	Ir (0.192)	1.95	3.8	-0.9	0.0	0.2
167	Ca (0.203)	Sn (0.412)	Ba (0.293)	Au (0.461)	Bi (0.103)	1.47	3.7	-1.5	0.0	0.1
168	Al (0.086)	V (0.663)	Ni (0.282)	Nb (0.811)	Rh (0.343)	2.18	23.5	29.4	23.7	25.4
169	V (0.221)	Ni (0.423)	Nb (0.405)	Sm (0.407)	Au (0.576)	2.03	4.8	1.6	0.3	1.8
170	Rh (0.229)	Cs (0.672)	Ba (0.587)	Sm (0.203)	Hf (0.302)	1.99	11.8	17.2	7.8	14.6
171	Nb (0.101)	Rh (0.343)	Ag (0.236)	Cs (0.896)	Ir (0.577)	2.15	4.6	1.2	0.8	1.8
172	Cs (0.336)	Ba (0.293)	Hf (0.201)	Ir (0.481)	Au (0.807)	2.12	6.7	6.0	2.4	5.4

173	Ca (0.271)	Ag (0.118)	Ce (0.728)	Hf (0.403)	Bi (0.202)	1.72	3.8	-1.0	0.0	0.2
174	V (0.221)	Ag (1.180)	Cs (0.112)	Ce (0.312)	Ir (0.385)	2.21	4.6	2.2	0.4	2.2
175	Li (0.482)	Ca (0.203)	Ce (0.104)	Sm (0.474)	Bi (0.064)	1.33	3.5	-0.9	0.0	0.2
176	Rh (0.457)	Ag (0.472)	Sn (0.248)	Ir (0.577)	Au (0.461)	2.22	4.1	0.4	0.1	1.3
177	Ca (0.203)	Ba (0.293)	Ce (0.936)	Au (0.461)	Bi (0.162)	2.06	3.8	-1.3	0.0	0.1
178	Ca (0.053)	V (0.261)	Nb (0.744)	Ce (0.415)	Ir (0.370)	1.84	3.7	-0.2	0.1	1.0
179	Al (0.582)	V (0.087)	Cs (0.808)	Sm (0.593)	Hf (0.159)	2.23	3.6	0.0	0.0	0.3
180	Al (0.233)	Sn (0.188)	Ba (0.113)	Hf (0.398)	Au (0.586)	1.52	3.3	-1.0	0.0	0.2
181	Al (0.466)	Ag (0.225)	Ba (1.015)	Ir (0.296)	Au (0.073)	2.08	4.8	1.7	1.0	2.6
182	Cs (0.462)	Ce (0.104)	Sm (0.356)	Hf (0.637)	Au (0.293)	1.85	3.5	-1.4	0.0	0.2
183	V (0.435)	Ni (0.186)	Cs (0.115)	Ce (0.622)	Sm (0.711)	2.07	3.6	-0.7	0.0	0.2
184	Li (0.178)	Ca (0.265)	V (0.695)	Ce (0.311)	Ir (0.148)	1.60	3.8	-0.9	0.0	0.2
185	Ca (0.212)	V (0.261)	Hf (0.080)	Ir (0.666)	Au (0.220)	1.44	3.7	-1.0	0.0	0.3
186	Ni (0.093)	Sn (0.406)	Ba (0.451)	Au (0.367)	Bi (0.609)	1.93	4.0	-1.0	0.0	0.2
187	Li (0.624)	V (0.261)	Ni (0.464)	Rh (0.298)	Ba (0.226)	1.87	4.1	-0.7	0.0	0.3
188	V (0.087)	Nb (0.213)	Ba (0.226)	Sm (0.711)	Bi (1.292)	2.53	3.3	-1.6	0.0	0.1
189	Li (0.357)	V (0.261)	Ni (0.649)	Cs (0.231)	Au (0.293)	1.79	3.7	-1.3	0.0	0.2
190	Al (0.233)	Nb (0.425)	Ag (0.789)	Cs (0.692)	Au (0.073)	2.21	3.5	-1.3	0.0	0.2
191	Li (0.178)	Ni (0.278)	Ag (0.451)	Ba (0.789)	Bi (0.328)	2.02	3.2	-1.9	0.0	0.2
192	Al (0.233)	V (0.087)	Sn (0.149)	Hf (0.637)	Ir (0.444)	1.55	4.5	1.1	0.2	1.5
193	Ni (0.186)	Nb (0.850)	Rh (0.398)	Ag (0.225)	Bi (0.256)	1.92	3.4	-1.3	0.0	0.2
194	Al (0.582)	Rh (0.398)	Ba (0.338)	Hf (0.557)	Ir (0.074)	1.95	20.2	29.7	21.1	27.3
195	Al (0.116)	Ca (0.106)	Hf (0.398)	Au (0.513)	Bi (0.383)	1.52	3.2	-1.1	0.0	0.2
196	Al (0.815)	V (0.174)	Rh (0.199)	Sn (0.738)	Ba (0.338)	2.26	3.4	-1.2	0.0	0.3
197	Rh (0.597)	Ag (0.225)	Sm (0.119)	Hf (0.080)	Ir (0.740)	1.76	9.2	10.2	6.7	9.9
198	Al (0.623)	Ca (0.114)	Rh (0.345)	Ce (0.314)	Au (0.160)	1.56	18.5	29.3	19.7	26.3
199	Nb (0.306)	Ag (0.082)	Sn (0.256)	Ce (0.314)	Hf (0.267)	1.22	1.2	0.0	0.0	0.3
200	Ce (0.126)	Hf (0.623)	Ir (0.135)	Au (0.480)	Bi (0.281)	1.64	1.1	-0.9	0.0	0.2
201	Li (0.210)	Ca (0.229)	V (0.764)	Ba (0.342)	Au (0.320)	1.86	0.9	-1.1	0.0	0.1
202	V (0.109)	Nb (1.019)	Rh (0.259)	Cs (0.294)	Au (0.240)	1.92	3.0	4.2	0.9	3.8
203	V (0.218)	Rh (0.517)	Cs (0.588)	Ir (0.338)	Au (0.080)	1.74	0.9	-0.4	0.1	0.6
204	Ca (0.914)	Ni (0.352)	Nb (0.306)	Rh (0.259)	Ir (0.203)	2.03	18.7	29.3	20.0	26.2
205	Li (0.140)	Al (0.156)	Cs (0.588)	Ce (0.126)	Au (0.640)	1.65	1.2	-1.0	0.0	0.1
206	Rh (0.086)	Ag (0.576)	Cs (0.588)	Au (0.080)	Bi (0.648)	1.98	1.3	-1.1	0.0	0.1
207	V (0.109)	Ni (0.117)	Nb (0.306)	Cs (1.175)	Hf (0.267)	1.97	1.2	-1.0	0.0	0.2
208	Al (0.311)	Ca (0.114)	V (0.218)	Ni (0.469)	Ba (0.770)	1.88	1.2	-1.4	0.0	0.2
209	Li (0.350)	Al (0.545)	Ni (0.704)	Nb (0.102)	Sm (0.058)	1.76	40.0	34.4	34.5	35.5
210	Al (0.623)	Ag (0.082)	Ba (0.342)	Ir (0.338)	Au (0.160)	1.55	2.9	3.9	2.0	3.7
211	Ba (0.513)	Ce (0.063)	Sm (0.289)	Ir (0.203)	Bi (0.183)	1.25	0.8	-0.9	0.0	0.2
212	Rh (0.517)	Ag (0.247)	Cs (0.098)	Sm (0.289)	Hf (0.445)	1.60	13.1	21.1	13.6	19.1
213	Li (0.280)	Al (0.156)	Ag (0.329)	Ba (0.428)	Ir (0.338)	1.53	2.2	1.3	1.3	2.3
214	Al (0.467)	Nb (0.102)	Ce (0.377)	Sm (0.231)	Ir (0.203)	1.38	6.6	11.6	4.2	9.5
215	Li (0.140)	Ca (0.571)	V (0.437)	Rh (0.517)	Ir (0.203)	1.87	1.1	-0.5	0.0	0.4
216	Ca (0.229)	Nb (0.510)	Sn (0.372)	Hf (0.356)	Au (0.480)	1.95	1.2	-0.7	0.0	0.2
217	Ca (0.343)	V (0.655)	Ni (0.352)	Ba (0.257)	Bi (0.673)	2.28	1.0	-1.3	0.0	0.1
218	Li (0.264)	Al (0.416)	V (0.450)	Rh (0.422)	Hf (0.138)	1.69	20.1	31.4	21.2	27.7

219	Li (0.264)	Al (0.083)	Ca (0.424)	Rh (0.422)	Ba (1.092)	2.28	14.7	26.1	14.0	21.3
220	Sn (0.140)	Sm (0.533)	Hf (0.275)	Au (0.105)	Bi (0.280)	1.33	2.1	0.2	0.0	0.1
221	Al (0.333)	Ca (0.706)	Rh (0.316)	Ag (0.077)	Sm (0.747)	2.18	18.8	30.0	19.7	26.0
222	Al (0.333)	Ni (0.108)	Ce (0.195)	Ir (0.900)	Bi (0.228)	1.76	1.7	0.1	0.0	0.2
223	Li (0.132)	Nb (0.434)	Sm (0.213)	Hf (0.963)	Bi (0.918)	2.66	1.5	0.3	0.0	0.2
224	Ca (0.141)	Nb (1.158)	Rh (0.211)	Sn (0.497)	Hf (0.825)	2.83	1.9	1.7	0.1	1.0
225	Li (0.330)	Nb (0.290)	Ag (0.540)	Ce (0.391)	Sm (0.213)	1.76	1.8	0.4	0.0	0.2
226	Al (0.166)	V (0.675)	Ni (0.325)	Rh (0.211)	Ag (0.308)	1.69	7.1	12.2	4.1	9.2
227	Ca (0.706)	Rh (0.211)	Cs (0.738)	Ce (0.586)	Sm (0.107)	2.35	10.1	17.9	7.5	14.3
228	Li (0.066)	Ni (0.217)	Sn (0.615)	Cs (1.107)	Hf (0.413)	2.42	1.8	0.4	0.0	0.1
229	V (0.375)	Ba (0.546)	Ce (0.586)	Ir (0.450)	Au (0.105)	2.06	1.3	0.0	0.0	0.3
230	Ni (0.325)	Rh (0.843)	Cs (0.492)	Ce (0.195)	Ir (0.337)	2.19	18.4	29.8	19.3	25.9
231	Ag (0.231)	Ce (0.586)	Sm (0.747)	Hf (0.413)	Ir (0.112)	2.09	5.2	9.1	2.3	6.8
232	Li (0.595)	Al (0.333)	Cs (0.246)	Ce (0.098)	Bi (0.132)	1.40	1.9	-0.1	0.0	0.1
233	Ag (0.231)	Cs (0.369)	Ba (0.136)	Hf (0.825)	Ir (0.787)	2.35	3.3	3.5	0.9	2.6
234	Al (0.749)	Ca (0.565)	Ni (0.108)	Nb (0.434)	Rh (0.316)	2.17	19.4	30.7	20.9	27.2
235	Ni (0.325)	Nb (1.014)	Ag (0.077)	Ba (0.409)	Ir (0.675)	2.50	5.5	10.2	3.1	7.8
236	Sn (1.044)	Cs (0.246)	Ce (0.488)	Ir (0.675)	Au (0.105)	2.56	1.6	0.0	0.0	0.3
237	Sm (0.640)	Hf (1.100)	Ir (0.112)	Au (0.105)	Bi (0.636)	2.59	1.3	-0.1	0.0	0.1
238	V (0.585)	Ag (0.073)	Ce (0.419)	Hf (0.676)	Au (0.471)	2.22	1.5	0.3	0.1	0.1
239	Al (0.160)	V (0.227)	Ni (0.285)	Ba (0.167)	Hf (0.078)	0.92	1.0	1.2	0.0	0.2
240	Nb (1.069)	Ag (1.097)	Ba (0.053)	Hf (0.249)	Ir (0.354)	2.82	1.0	0.3	0.3	0.5
241	Cs (0.200)	Ba (1.096)	Sm (0.698)	Au (0.152)	Bi (1.192)	3.34	1.2	-0.1	0.0	0.1
242	Al (0.283)	V (0.036)	Rh (0.564)	Ce (0.075)	Ir (0.578)	1.54	9.3	16.8	7.7	13.7
243	Al (0.092)	Ca (0.381)	Nb (0.368)	Ag (0.117)	Ir (0.253)	1.21	1.8	1.9	0.5	1.5
244	Ca (0.037)	V (0.695)	Rh (0.234)	Ag (0.097)	Sm (0.781)	1.84	1.4	1.2	0.1	0.7
245	Rh (0.229)	Sn (0.500)	Ce (0.134)	Sm (0.595)	Au (0.480)	1.94	1.5	0.9	0.1	0.7
246	Al (0.440)	Nb (0.425)	Ag (0.536)	Hf (0.321)	Au (0.540)	2.26	1.1	-0.4	0.1	0.2
247	Li (1.013)	Al (0.348)	Cs (0.619)	Sm (0.849)	Bi (0.202)	3.03	1.4	-0.2	0.0	0.1
248	Li (0.600)	Sn (1.059)	Ir (1.119)	Au (0.182)	Bi (0.495)	3.45	1.3	0.3	0.0	0.1
249	Ni (0.626)	Sn (0.465)	Ba (0.040)	Hf (0.580)	Bi (0.728)	2.44	1.0	-0.1	0.0	0.2
250	Li (0.193)	Al (0.550)	V (0.443)	Nb (0.552)	Ag (0.210)	1.95	1.3	0.1	0.0	0.2
251	Li (0.358)	V (0.158)	Nb (0.113)	Sn (0.350)	Ce (0.049)	1.03	1.1	0.2	0.0	0.2
252	Ni (0.662)	Nb (0.055)	Rh (0.372)	Au (1.188)	Bi (0.913)	3.19	1.3	-0.1	0.0	0.2
253	Li (0.556)	Ca (0.458)	Rh (0.481)	Sn (0.394)	Sm (0.200)	2.09	2.2	2.0	0.1	1.0
254	Ca (0.296)	V (0.298)	Ce (0.198)	Sm (0.257)	Hf (0.041)	1.09	1.3	0.0	0.0	0.2
255	Ni (0.973)	Nb (0.351)	Ag (0.697)	Cs (0.114)	Ba (0.974)	3.11	1.4	0.8	0.0	0.3
256	Al (0.164)	Nb (0.147)	Rh (0.524)	Cs (0.446)	Ir (0.161)	1.44	14.1	21.3	15.4	19.0
257	Ni (3.500)					3.50	46.8	35.7	39.0	33.6
258	Ni (0.704)					0.70	30.3	29.9	29.5	20.2
259	Ni (0.443)					0.44	19.1	30.8	18.4	22.5
260	Ni (1.750)					1.75	41.2	35.1	34.1	26.1
261	Ni (2.625)					2.63	43.1	35.6	36.1	30.8
262	Li (0.350)	Al (0.545)	Ni (0.704)	Nb (0.102)	Sm (0.058)	1.76	36.3	32.4	31.7	20.1
263	Li (0.350)	Al (0.545)	Ni (0.704)	Nb (0.102)		1.70	36.2	32.1	33.1	19.4
264	Li (0.350)	Al (0.545)	Ni (0.704)	Sm (0.058)		1.66	28.5	30.0	27.8	21.4

265	Li (0.350)	Ni (0.704)	Nb (0.102)	Sm (0.058)	1.21	34.2	30.9	30.4	18.7
266	Al (0.545)	Ni (0.704)	Nb (0.102)	Sm (0.058)	1.41	31.9	30.0	29.9	19.8
267	Li (0.350)	Ni (0.704)			1.05	33.7	30.1	31.2	19.4
268	Al (0.545)	Ni (0.704)			1.25	26.8	31.0	26.8	22.2
269	Ni (0.704)	Nb (0.102)			0.81	32.8	30.7	30.4	19.8
270	Ni (0.704)	Sm (0.058)			0.76	31.5	30.2	29.9	19.6
271	Li (0.350)	Al (0.545)	Ni (0.704)		1.60	29.6	30.2	28.9	21.0
272	Li (0.350)	Ni (0.704)	Nb (0.102)		1.16	35.4	31.6	30.8	19.8
273	Li (0.350)	Ni (0.704)	Sm (0.058)		1.11	34.0	30.5	31.7	19.4
274	Al (0.545)	Ni (0.704)	Nb (0.102)		1.35	32.9	31.7	30.5	20.0
275	Al (0.545)	Ni (0.704)	Sm (0.058)		1.31	23.7	29.2	23.3	20.9
276	Ni (0.704)	Nb (0.102)	Sm (0.058)		0.86	31.4	30.9	30.0	20.2
277	Li (0.350)	Al (0.545)	Nb (0.102)	Sm (0.058)	1.05	-0.2	-0.1	0.1	0.2
278	Cs (0.500)				0.50	0.8	0.6	0.1	0.2
279	Ir (3.500)				3.50	16.1	28.2	16.1	23.3
280	Li (0.500)				0.50	-0.1	-0.2	0.1	0.2
281	Cs (0.500)	Ba (3.000)			3.50	0.4	0.1	0.1	0.2
282	Ir (3.000)	Au (0.500)			3.50	18.5	29.8	20.2	26.0
283	Sm (3.500)				3.50	0.5	0.8	0.1	0.5
284	Rh (0.500)	Ir (2.000)			2.50	19.1	31.1	20.6	26.9
285	Ca (0.500)	Cs (0.500)	Ba (0.500)		1.50	0.3	-0.1	0.0	0.2
286	Ir (1.000)	Au (2.000)			3.00	13.8	20.4	16.1	18.8
287	Sn (0.500)	Cs (0.500)	Sm (2.500)		3.50	0.3	0.1	0.0	0.2
288	Ir (2.000)	Au (0.500)			2.50	18.3	28.8	20.0	25.2
289	Cs (0.500)	Ba (0.500)	Sm (0.500)		1.50	0.4	0.3	0.1	0.2
290	Ag (0.500)	Ir (2.000)	Au (1.000)		3.50	10.4	17.5	11.8	15.4
291	Ir (2.500)	Au (1.000)			3.50	17.9	28.7	19.6	25.0
292	Li (0.500)	Cs (3.000)			3.50	0.4	0.2	0.1	0.3
293	Ir (1.500)	Au (1.000)			2.50	17.1	26.9	18.8	23.7
294	Rh (3.000)	Ir (0.500)			3.50	19.0	31.0	21.1	27.0
295	Bi (2.500)				2.50	0.1	0.2	0.0	0.2
296	Ag (3.500)				3.50	0.1	-0.1	0.0	0.3
297	Rh (1.500)	Au (0.500)			2.00	15.9	24.6	17.9	21.9
298	Cs (3.500)				3.50	0.1	3.3	0.1	0.8
299	Ba (0.500)				0.50	0.4	2.0	0.1	0.5
300	Nb (0.500)				0.50	0.5	2.3	0.1	0.4
301	Cs (3.000)	Hf (0.500)			3.50	0.3	2.1	0.0	0.4
302	Cs (2.000)	Au (0.500)			2.50	0.3	1.6	0.0	0.5
303	Nb (3.500)				3.50	0.4	1.4	0.1	0.3
304	Sm (0.500)				0.50	0.4	1.5	0.1	0.3
305	Au (0.500)				0.50	0.7	1.7	0.1	0.3
306	Cs (1.000)				1.00	0.7	2.0	0.0	0.3
307	Ba (2.500)				2.50	0.0	1.5	0.0	0.3
308	Ni (0.500)	Cs (3.000)			3.50	-2.3	1.8	0.0	0.6
309	Ce (2.000)				2.00	-2.0	2.0	0.0	0.6
310	Al (0.500)	V (2.500)	Nb (0.500)		3.50	-1.7	1.6	0.1	0.5

311	Al (1.000)					1.00	-2.3	1.7	0.1	0.5
312	Cs (1.500)	Ce (0.500)	Sm (0.500)			2.50	-2.1	2.6	0.0	0.7
313	V (0.500)	Cs (2.000)	Ba (1.000)			3.50	-1.9	2.0	0.0	0.4
314	Ce (0.500)					0.50	-2.2	1.8	0.0	0.4
315	Sn (1.500)	Cs (1.000)	Ba (1.000)			3.50	-2.2	2.3	0.0	0.6
316	Ca (0.500)					0.50	-2.0	1.8	0.1	0.5
317	Cs (3.000)	Ce (0.500)				3.50	-2.1	2.3	0.0	0.5
318	Sn (0.500)					0.50	-3.3	2.8	0.0	1.2
319	Cs (3.000)	Sm (0.500)				3.50	-3.2	3.1	0.0	0.7
320	Cs (0.500)	Sm (0.500)				1.00	-3.8	2.4	0.1	1.2
321	Li (1.500)	Cs (0.500)				2.00	-3.7	2.2	0.0	0.5
322	Sn (3.500)					3.50	-3.4	2.5	0.0	0.5
323	Sn (0.500)	Cs (3.000)				3.50	-4.0	2.4	0.0	0.5
324	Bi (0.500)					0.50	-3.9	2.6	0.0	0.7
325	Nb (1.000)					1.00	-3.8	2.4	0.0	0.6
326	Li (0.500)	Al (0.500)	Cs (1.000)	Ba (1.000)	Sm (0.500)	3.50	-3.4	3.0	0.0	0.7
327	Li (1.000)	Sm (0.500)				1.50	-3.8	2.4	0.1	0.5
328	Rh (0.500)					0.50	17.6	33.6	20.0	27.6
329	V (0.500)					0.50	-3.2	2.8	0.1	0.7
330	Ni (0.500)	Cs (2.000)	Ba (0.500)	Hf (0.500)		3.50	-3.6	2.4	0.0	0.7
331	Rh (0.500)	Cs (2.000)				2.50	-0.7	10.5	1.6	6.6
332	Rh (1.000)					1.00	18.0	33.8	20.4	28.2
333	Rh (1.500)					1.50	18.7	34.7	20.5	28.1
334	V (0.500)	Nb (0.500)				1.00	-3.8	2.4	0.1	0.5
335	Nb (0.500)	Rh (0.500)				1.00	18.7	34.8	20.3	28.2
336	Rh (0.500)	Cs (3.000)				3.50	-1.7	8.2	0.8	4.6
337	Li (2.000)	V (0.500)	Ni (0.500)	Nb (0.500)		3.50	32.2	36.1	28.6	22.6
338	Cs (3.000)	Ba (0.500)				3.50	-1.7	6.0	0.1	47.6
339	Cs (1.500)	Ba (0.500)				2.00	-4.3	4.3	0.1	2.1
340	Cs (2.000)					2.00	-1.8	6.1	0.1	74.6
341	Ca (1.500)					1.50	-4.2	4.2	0.1	2.4
342	Au (1.500)					1.50	-4.3	4.6	0.1	5.5
343	Cs (2.000)	Au (1.500)				3.50	-4.3	4.1	0.0	1.9
344	Li (0.500)	Au (0.500)				1.00	-4.3	4.1	0.1	1.3
345	Li (1.500)					1.50	-5.0	3.0	0.1	1.5
346	Ca (3.000)					3.00	-4.8	3.0	0.1	1.4
347	Cs (1.500)	Ba (0.500)	Sm (1.000)	Au (0.500)		3.50	-4.4	3.4	0.0	1.8
348	Ni (0.500)	Au (0.500)				1.00	24.0	33.4	19.5	24.4
349	Hf (1.500)	Ir (2.000)				3.50	19.1	36.3	17.1	30.1
350	Ni (0.500)	Au (1.500)				2.00	21.5	34.0	18.0	25.9
351	Nb (0.500)	Rh (0.500)	Ir (0.500)	Au (2.000)		3.50	18.3	35.2	16.7	29.1
352	Hf (2.500)	Ir (1.000)				3.50	17.2	33.7	15.8	28.2
353	Li (0.500)	Ni (0.500)	Au (1.500)			2.50	23.5	34.1	18.8	25.5
354	Ni (0.500)	Ir (0.500)	Au (2.000)			3.00	18.2	34.3	15.5	27.4
355	Ni (0.500)	Ag (0.500)	Au (1.000)			2.00	-2.5	7.5	0.8	5.2
356	Ba (1.500)	Sm (0.500)	Ir (0.500)	Au (1.000)		3.50	5.9	20.7	6.1	15.7

357	Ce (0.500)	Ir (1.500)	Au (1.500)		3.50	18.1	35.0	16.1	29.1
358	K (3.500)				3.50	-2.3	0.5	0.0	0.3
359	Mn (0.500)				0.50	-2.0	1.1	0.1	0.5
360	Ca (0.500)	Mn (3.000)			3.50	-2.3	0.9	0.0	0.5
361	K (2.500)	Mn (1.000)			3.50	-2.5	0.7	0.0	0.7
362	K (3.000)	Nb (0.500)			3.50	-1.8	1.0	0.0	0.3
363	K (3.000)	Au (0.500)			3.50	-2.1	1.3	0.0	0.3
364	K (3.000)	Mn (0.500)			3.50	-2.0	0.8	0.0	0.3
365	K (2.500)	Mn (0.500)	Ga (0.500)		3.50	-1.8	1.4	0.1	0.8
366	Mn (3.000)	Ga (0.500)			3.50	-1.9	0.8	0.0	0.4
367	K (0.500)	Mn (2.500)	Ga (0.500)		3.50	-1.9	1.0	0.0	0.4
368	K (3.000)	Ir (0.500)			3.50	2.8	11.4	2.5	7.9
369	K (2.500)	Rh (0.500)	Ir (0.500)		3.50	7.8	18.7	7.7	14.6
370	K (1.000)	Ir (2.500)			3.50	15.4	28.3	16.9	24.5
371	K (1.500)	Nb (0.500)	Rh (0.500)	Ir (1.000)	3.50	11.6	24.1	12.0	19.9
372	K (2.000)	Rh (1.500)			3.50	12.1	24.7	12.1	20.6
373	K (0.500)	Pd (2.000)			2.50	11.0	21.4	11.9	18.1
374	K (1.000)	Rh (0.500)	W (0.500)	Ir (1.000)	3.00	7.7	19.2	7.5	15.1
375	Al (0.500)	Mn (2.500)	Au (0.500)		3.50	-2.0	0.9	0.1	0.5
376	K (0.500)	Nb (0.500)	Ir (2.500)		3.50	16.1	29.6	16.9	24.9
377	Li (1.000)	K (2.000)	Ir (0.500)		3.50	3.3	11.9	3.0	8.5
378	Ni (1.000)	W (2.500)			3.50	-3.0	1.0	0.1	0.7
379	Mn (0.500)	Nb (1.000)	W (2.000)		3.50	-3.3	0.5	0.0	0.6
380	Pd (0.500)				0.50	5.9	10.5	9.5	9.6
381	K (1.000)	Nb (0.500)	W (2.000)		3.50	-2.6	1.0	0.0	0.5
382	Mn (3.500)				3.50	-2.9	0.4	0.1	0.5
383	Mg (0.500)	Nb (1.000)	W (2.000)		3.50	-2.6	1.3	0.0	23.2
384	Mn (3.000)	Cu (0.500)			3.50	-2.5	0.4	0.0	0.8
385	Mn (0.500)	Nb (0.500)	Hf (0.500)	W (2.000)	3.50	-2.0	0.9	0.0	0.5
386	Mn (1.000)	Ni (1.000)	W (0.500)	Ir (1.000)	3.50	18.4	31.4	19.6	27.1
387	Mn (1.500)	Ir (0.500)			2.00	11.1	23.9	11.6	19.8
388	K (0.500)				0.50	-3.0	0.3	0.1	0.6
389	Al (0.500)	K (3.000)			3.50	-2.7	0.5	0.0	0.6
390	K (1.000)	Nb (0.500)	Rh (1.000)	Pd (0.500)	3.00	15.7	29.5	17.3	26.1
391	Rh (2.500)	W (0.500)			3.00	18.3	33.0	19.8	28.4
392	Nb (0.500)	Hf (0.500)	W (2.000)	Ir (0.500)	3.50	-1.8	2.0	0.5	1.8
393	Al (1.500)	Mn (1.500)	Ga (0.500)		3.50	-2.3	0.8	0.1	0.6
394	K (3.000)	Pd (0.500)			3.50	1.6	9.7	2.1	7.3
395	Mn (2.000)	Cu (0.500)	Rh (0.500)	Hf (0.500)	3.50	16.6	30.3	17.6	26.1
396	Li (0.500)	Rh (2.000)	Pd (0.500)	Ir (0.500)	3.50	16.8	30.1	18.6	26.1
397	Al (0.500)	Mn (2.000)	Ni (1.000)		3.50	37.6	40.3	28.5	42.4
398	K (0.500)	Au (3.000)			3.50	-1.7	1.2	0.0	0.2
399	W (0.500)				0.50	-1.1	1.0	0.0	0.2
400	Au (3.500)				3.50	-1.1	1.0	0.1	0.4
401	Al (0.500)	K (0.500)	Ca (0.500)		1.50	-1.0	0.4	0.0	0.2
402	Mg (0.500)	K (2.000)			2.50	-1.1	0.7	0.0	0.2

403	Al (0.500)	K (0.500)	Au (2.500)		3.50	-0.7	1.1	0.0	0.3
404	W (0.500)	Ir (3.000)			3.50	17.7	31.5	19.3	26.7
405	Mg (0.500)	Ca (1.000)			1.50	-0.3	1.2	0.0	0.2
406	Mg (0.500)	Al (1.000)			1.50	-0.8	0.7	0.1	0.2
407	Ni (0.500)	W (0.500)			1.00	12.9	22.7	14.2	19.1
408	W (1.500)	Ir (0.500)			2.00	2.2	8.1	2.3	5.6
409	K (1.000)	Rh (0.500)	Au (2.000)		3.50	7.6	14.9	8.7	12.1
410	Al (0.500)	Ca (0.500)	Ga (0.500)		1.50	-0.8	1.2	0.1	0.4
411	Mn (1.000)				1.00	-0.6	1.8	0.4	0.8
412	Ir (1.000)				1.00	13.5	22.6	17.0	20.6
413	Hf (0.500)	Ir (1.500)	Au (1.000)		3.00	16.1	28.5	17.3	24.0
414	Pd (0.500)	Au (3.000)			3.50	5.9	11.6	7.2	9.4
415	K (2.500)	Ni (0.500)	Ga (0.500)		3.50	-1.0	1.4	0.0	0.2
416	Ga (0.500)				0.50	-1.0	0.7	0.0	0.3
417	K (0.500)	Ni (1.000)	Cu (0.500)	Ga (1.500)	3.50	1.0	6.8	1.0	4.2
418	Ni (2.500)	Pd (1.000)			3.50	34.3	34.1	28.9	19.4
419	Al (0.500)	Ni (2.500)	Cu (0.500)		3.50	20.4	29.0	19.6	22.2
420	Ni (2.000)	Ga (1.000)	Rh (0.500)		3.50	16.8	28.6	16.8	24.3
421	Ni (2.500)	Cu (0.500)			3.00	22.2	29.4	21.1	21.3
422	Ni (2.000)	Pd (0.500)			2.50	35.3	35.2	28.9	38.0
423	Mg (0.500)	Ni (2.500)	Cu (0.500)		3.50	20.9	28.9	20.4	22.2
424	Al (0.500)	Ni (2.000)	Rh (0.500)	W (0.500)	3.50	23.3	29.7	22.5	22.2
425	Mn (2.000)	Ga (0.500)	Zr (1.000)		3.50	0.5	0.7	0.1	0.3
426	Mn (1.000)	Ni (1.000)	Ga (0.500)		2.50	18.4	30.1	18.9	25.5
427	Mg (0.500)	Ni (2.500)	Nb (0.500)		3.50	41.9	35.4	33.0	24.9
428	Ni (1.500)	Ga (2.000)			3.50	17.9	30.7	18.0	34.7
429	Mn (0.500)	Ni (2.000)	Cu (0.500)		3.00	20.4	27.7	19.2	20.4
430	Ni (0.500)	Ga (0.500)	Rh (1.000)		2.00	16.5	25.3	15.3	22.5
431	Ni (1.500)	Ga (0.500)	Rh (0.500)	Pd (0.500)	3.00	17.5	29.4	18.0	25.4
432	Ni (1.000)	Zr (0.500)	Rh (1.500)		3.00	18.6	31.0	18.9	26.4
433	Ni (2.500)	Cu (0.500)	Nb (0.500)		3.50	23.4	29.3	20.0	19.6
434	Mn (1.000)	Ni (1.000)	Ga (1.500)		3.50	13.3	22.9	12.2	18.5
435	Mn (0.500)	Ni (2.500)	Ga (0.500)		3.50	18.5	28.8	18.6	24.2
436	Al (0.500)	Ni (2.500)	Nb (0.500)		3.50	42.4	37.0	34.2	32.2
437	Mn (2.000)	Ni (0.500)	Ga (1.000)		3.50	12.0	21.7	10.7	17.7
438	Pd (3.500)				3.50	16.9	27.6	17.5	23.7
439	Co (0.500)	Pd (3.000)			3.50	17.2	29.0	17.4	24.6
440	Li (0.500)	Pd (3.000)			3.50	16.5	27.0	17.2	23.3
441	Al (0.500)	Co (0.500)	Ni (2.500)		3.50	40.7	40.4	29.4	40.2
442	Pd (3.000)	Ta (0.500)			3.50	15.5	20.9	15.2	19.4
443	Li (3.000)	Al (0.500)			3.50	3.1	-0.7	0.0	0.1
444	Li (0.500)	Pd (2.500)	Ta (0.500)		3.50	13.3	16.0	12.6	15.4
445	Co (0.500)	Ni (1.000)	Pd (2.000)		3.50	23.1	29.5	21.7	22.9
446	Co (0.500)	Mo (0.500)	Pd (2.500)		3.50	15.8	23.7	13.9	20.6
447	Li (0.500)	Mn (0.500)	Mo (0.500)	Pd (2.000)	3.50	10.5	17.3	8.2	14.4
448	Co (0.500)	Pd (2.500)			3.00	16.7	24.0	14.7	20.4

449	Mn (0.500)	Ni (0.500)	Mo (0.500)	Pd (2.000)		3.50	11.3	15.5	7.1	11.1
450	Mn (0.500)	Pd (2.500)	Pt (0.500)			3.50	11.7	15.5	10.1	13.9
451	Al (0.500)	Co (1.000)	Ni (1.000)	Pd (1.000)		3.50	32.6	34.5	28.2	32.7
452	Ta (1.000)	Pt (2.000)				3.00	15.9	23.7	15.0	21.5
453	Ta (2.000)	Pt (1.000)				3.00	14.4	20.8	12.1	18.3
454	Co (0.500)	Ni (3.000)				3.50	46.8	37.7	35.1	35.5
455	Li (1.500)	Pd (2.000)				3.50	14.4	18.2	14.4	17.3
456	Y (2.500)	Pd (1.000)				3.50	16.2	24.2	14.7	21.4
457	Mn (0.500)	Nb (0.500)	Pd (2.000)	Ta (0.500)		3.50	12.1	15.7	9.7	13.4
458	Al (0.500)	Mn (0.500)				1.00	-3.7	3.0	0.1	0.4
459	Al (0.500)					0.50	-3.5	3.4	0.1	0.4
460	Y (1.000)	W (2.500)				3.50	-3.8	3.6	0.1	0.6
461	Al (3.500)					3.50	-4.0	3.1	0.1	0.3
462	Y (1.000)	W (1.000)				2.00	-3.5	3.9	0.1	0.3
463	Mn (1.500)					1.50	-3.6	3.5	0.1	0.4
464	Y (2.000)	W (1.000)				3.00	-3.6	3.3	0.1	0.4
465	Co (2.500)	Rh (1.000)				3.50	31.0	35.8	29.2	21.4
466	Al (1.000)	Zn (0.500)				1.50	-3.5	3.2	0.1	0.3
467	Y (0.500)	Ta (0.500)	W (1.500)	Pt (0.500)		3.00	-3.8	3.9	0.1	0.5
468	Y (1.000)	Nb (1.500)	Ta (0.500)	W (0.500)		3.50	-3.7	4.0	0.1	0.4
469	Y (0.500)	W (3.000)				3.50	-4.1	3.3	0.1	0.4
470	Y (3.500)					3.50	-3.1	5.3	0.3	1.5
471	Li (1.000)	Fe (0.500)	W (2.000)			3.50	-4.1	3.0	0.1	0.3
472	Al (1.500)					1.50	-3.8	3.1	0.1	0.3
473	Ta (1.000)					1.00	-3.7	2.9	0.1	0.4
474	Li (0.500)	Nb (0.500)	Mo (0.500)	Pd (1.000)	W (1.000)	3.50	-2.3	5.8	1.1	2.3
475	Li (0.500)	Y (1.500)	Mo (1.000)	W (0.500)		3.50	-4.1	3.1	0.1	0.3
476	Li (0.500)	Y (0.500)	Ta (1.500)	W (1.000)		3.50	-3.8	3.5	0.1	0.3
477	Mn (0.500)	Rh (0.500)	W (2.500)			3.50	15.7	31.4	19.5	25.1
478	Co (1.500)	Ni (1.500)	Rh (0.500)			3.50	33.5	38.5	28.1	22.2
479	Al (0.500)	Co (0.500)	Ni (2.000)	Rh (0.500)		3.50	26.4	34.8	24.6	22.4
480	Fe (0.500)	Co (1.500)	Ni (0.500)	Y (0.500)	Ir (0.500)	3.50	15.0	32.1	16.4	25.3
481	Al (1.500)	Mn (0.500)	Zn (1.000)			3.00	-3.6	5.6	0.9	2.0
482	Al (0.500)	Co (1.000)	Ni (0.500)	Rh (1.500)		3.50	18.2	35.4	19.4	27.3
483	Al (2.000)	Ni (0.500)				2.50	29.0	38.3	25.4	23.4
484	Al (3.000)	Pt (0.500)				3.50	11.5	27.1	14.1	20.7
485	Li (0.500)	Al (0.500)	Co (1.000)	Ni (1.000)	Rh (0.500)	3.50	27.1	37.1	24.4	23.0
486	Mn (0.500)	Zn (3.000)				3.50	-4.6	3.8	0.2	0.5
487	Al (0.500)	Mn (0.500)	Fe (0.500)	Ni (1.500)	Rh (0.500)	3.50	19.3	34.6	20.2	26.0
488	Pt (2.500)					2.50	14.2	30.2	16.1	23.2
489	Mn (1.000)	Co (0.500)	Ni (0.500)	Nb (0.500)		2.50	40.4	41.9	28.6	30.7
490	Fe (0.500)	Co (1.000)	Ni (2.000)			3.50	39.0	39.6	29.7	23.2
491	Li (0.500)	Al (0.500)	Co (0.500)	Ni (2.000)		3.50	39.8	41.2	29.3	21.6
492	Co (2.000)	Y (0.500)	Rh (1.000)			3.50	24.2	36.8	23.4	23.9
493	Al (0.500)	Ni (0.500)				1.00	34.6	39.2	27.4	23.2
494	Li (0.500)	Fe (1.500)	Ni (1.000)	Ir (0.500)		3.50	-2.2	9.3	0.9	4.3

495	Al (2.000)	Mn (0.500)	Ni (0.500)	Rh (0.500)		3.50	18.7	36.0	19.3	27.7
496	Li (0.500)	Al (1.000)	Mn (1.000)	Zn (1.000)		3.50	-4.9	3.7	0.2	0.6
497	Sc (0.500)	Mn (1.500)	Zn (1.500)			3.50	-5.0	3.6	0.1	0.4
498	Mn (1.000)	Fe (1.500)				2.50	3.2	0.6	0.0	0.3
499	Co (3.000)	Zn (0.500)				3.50	32.4	30.3	31.6	18.7
500	Co (0.500)	Ni (0.500)	Y (2.500)			3.50	18.3	28.3	18.8	23.8
501	Li (0.500)	Al (0.500)	Zn (1.500)	Rh (0.500)	Pt (0.500)	3.50	14.0	21.1	13.2	18.1
502	Li (1.000)	Al (0.500)	Sc (0.500)	Fe (0.500)	Y (1.000)	3.50	2.8	0.4	0.1	0.2
503	Ta (3.500)					3.50	3.4	1.1	0.1	0.3
504	Mn (2.000)	Fe (0.500)	Co (0.500)	W (0.500)		3.50	2.9	0.2	0.1	0.3
505	Co (1.000)	Ni (0.500)	Nb (0.500)	Rh (0.500)	W (1.000)	3.50	14.8	23.3	13.3	18.8
506	Al (0.500)	Sc (0.500)	Mn (2.500)			3.50	3.0	0.6	0.1	0.4
507	Co (3.000)	Nb (0.500)				3.50	40.6	38.4	33.9	28.6
508	Zn (0.500)	Y (3.000)				3.50	3.3	0.5	0.1	0.3
509	Li (1.000)	Co (0.500)	Mo (0.500)	Ta (0.500)	W (1.000)	3.50	3.6	1.3	0.0	0.2
510	Co (0.500)	Y (3.000)				3.50	3.1	0.4	0.1	1.3
511	Y (0.500)	Ta (2.500)				3.00	2.8	0.8	0.1	0.3
512	Li (0.500)	Sc (0.500)	Fe (0.500)	Y (1.500)	Mo (0.500)	3.50	2.6	0.4	0.0	0.3
513	Fe (0.500)	Y (3.000)				3.50	3.0	0.7	0.0	0.3
514	Al (0.500)	Mo (0.500)	Ta (2.000)	W (0.500)		3.50	2.9	0.7	0.0	0.2
515	Li (0.500)	Fe (0.500)	Mo (0.500)	Ta (1.500)	W (0.500)	3.50	3.1	0.8	0.0	0.3
516	Li (0.500)	Fe (1.500)	Co (0.500)	Mo (0.500)	W (0.500)	3.50	3.4	0.0	0.0	0.3
517	Mn (0.500)	Y (3.000)				3.50	2.4	0.6	0.0	0.3
518	Co (0.800)	Zn (0.200)				1.00	3.4	0.7	0.0	0.3
519	Co (0.800)	Nb (0.200)				1.00	3.7	1.1	0.1	0.2
520	Co (0.400)					0.40	3.0	0.6	0.1	0.3
521	Li (0.200)	Al (0.200)	Co (0.200)	Ni (0.600)	Zn (0.400)	1.60	15.3	23.7	13.9	19.4
522	Co (0.800)	Zn (0.200)	Nb (0.200)			1.20	3.3	0.7	0.0	0.2
523	Al (0.200)	Mn (0.400)	Co (0.800)	Nb (0.200)		1.60	2.6	1.9	0.1	0.1
524	Al (0.200)	Co (0.800)				1.00	3.3	0.3	0.0	0.2
525	Li (0.200)	Mn (0.200)	Co (0.800)	Nb (0.200)	Mo (0.200)	1.60	3.0	0.9	0.1	0.2
526	Mn (0.200)	Fe (0.400)	Co (0.400)			1.00	2.9	0.3	0.1	0.2
527	Fe (0.200)	Co (0.400)	Ni (0.200)	Y (0.200)		1.00	3.1	0.3	0.0	0.3
528	Fe (0.200)	Co (0.400)	Ni (0.200)	Zn (0.600)		1.40	2.8	-0.2	0.0	0.3
529	Al (0.200)	Sc (0.200)	Fe (0.200)	Co (0.600)		1.20	2.8	0.8	0.0	0.2
530	Mn (0.200)	Co (0.400)	Ni (0.200)	Zn (0.400)	Y (0.200)	1.40	3.4	1.3	0.1	0.3
531	Al (0.200)	Sc (0.400)	Mn (0.200)	Co (0.400)	Ni (0.200)	1.40	2.8	0.9	0.0	0.2
532	Li (0.400)	Mn (0.200)	Co (0.800)	Nb (0.200)		1.60	3.2	0.7	0.1	0.2
533	Li (0.200)	Mn (0.400)	Co (0.600)	Rh (0.200)	W (0.200)	1.60	21.4	31.4	22.3	26.7
534	Al (0.200)	Co (0.800)	Zn (0.200)			1.20	14.4	22.9	12.1	18.3
535	Co (0.600)	Ni (0.200)				0.80	24.3	31.0	25.1	23.4
536	Al (0.200)	Mn (0.200)	Fe (0.800)	Zn (0.200)	Nb (0.200)	1.60	3.5	0.9	0.1	0.3
537	Sc (0.200)	Fe (0.600)	Ni (0.200)			1.00	3.3	0.6	0.1	0.2
538	Mn (0.200)	Co (0.200)	Ni (0.600)			1.00	-0.7	3.0	0.1	0.3
539	Mn (0.600)	Co (0.200)	Ni (0.600)			1.40	-0.7	2.7	0.1	0.3
540	Co (0.400)	Ni (0.400)				0.80	18.3	30.9	19.7	23.9

541	Al (0.200)	Ni (0.800)				1.00	23.0	32.8	23.9	23.4
542	Ni (0.600)	Rh (0.200)				0.80	19.3	33.5	21.4	26.8
543	Li (0.400)	Co (0.200)	Ni (0.400)	Rh (0.200)	W (0.200)	1.40	19.2	33.2	21.3	26.5
544	Mn (0.200)	Fe (0.200)	Co (0.200)	Ni (0.400)		1.00	13.4	26.5	14.2	20.5
545	Li (0.200)	Mn (0.600)	Ni (0.800)			1.60	21.2	32.9	22.8	24.4
546	Ni (0.600)	Pd (0.200)				0.80	20.4	31.4	22.1	23.7
547	Fe (0.200)	Ni (0.600)				0.80	16.0	30.1	17.6	23.4
548	Al (0.200)	Mn (0.200)	Co (0.200)	Ni (0.400)	Nb (0.200)	1.20	-0.7	3.1	0.1	0.2
549	Sc (0.200)	Ni (0.600)				0.80	8.5	20.1	8.0	14.1
550	Al (0.200)	Mn (0.600)	Co (0.400)	Ni (0.200)	Pd (0.200)	1.60	14.6	27.4	15.4	20.8
551	Li (0.200)	Al (0.400)	Ni (0.600)			1.20	10.4	23.1	10.5	16.6
552	Li (0.200)	Al (0.200)	Mn (0.400)	Ni (0.600)	Pd (0.200)	1.60	19.6	32.2	21.1	24.6
553	Co (0.200)	Ni (0.400)				0.60	-0.4	2.6	0.1	0.2
554	Li (0.600)	Ni (0.800)				1.40	33.3	37.2	31.1	21.3
555	Li (0.200)	Co (0.200)	Ni (0.600)			1.00	26.0	34.7	26.5	38.4
556	Mn (0.400)	Co (0.400)	Ni (0.200)	Nb (0.200)		1.20	-0.5	2.5	0.1	0.3
557	Al (0.200)	Fe (0.400)	Ni (0.400)	Nb (0.200)		1.20	8.9	20.3	8.4	14.7
558	Al (0.200)	Ni (0.400)				0.60	8.3	16.3	6.2	12.0
559	Mn (0.600)	Co (0.400)	Nb (0.200)	Pd (0.200)		1.40	6.1	10.8	3.7	7.2
560	Co (0.200)	Ni (0.200)	Nb (0.200)	Pd (0.400)		1.00	16.7	25.6	17.4	19.9
561	Al (0.200)	Mn (0.200)	Co (0.200)	Ni (0.600)		1.20	17.0	27.7	18.2	22.4
562	Al (0.800)	Co (0.600)				1.40	7.9	16.2	5.8	11.8
563	Sc (0.200)	Co (0.400)	Ni (0.400)			1.00	18.9	29.5	20.4	23.9
564	Mn (0.600)	Nb (0.200)	Pd (0.600)			1.40	8.0	14.3	6.7	10.5
565	Mn (0.200)	Co (0.600)	Ni (0.200)			1.00	16.0	26.6	16.5	21.6
566	Al (0.600)	Sc (0.200)	Fe (0.200)	Co (0.600)		1.60	1.4	1.0	0.0	0.3
567	Al (0.200)	Mn (0.200)	Fe (0.200)	Ni (0.600)	Y (0.200)	1.40	17.7	29.9	19.6	24.9
568	Li (0.200)	Ni (0.600)				0.80	14.9	25.3	15.7	20.2
569	Li (0.400)	Mn (0.200)	Ni (0.600)	Rh (0.200)	W (0.200)	1.60	19.2	31.8	22.1	27.4
570	Li (0.800)	Fe (0.400)	Co (0.200)	Ni (0.200)		1.60	7.7	15.8	5.6	11.6
571	Fe (0.200)	Ni (0.600)	Nb (0.400)			1.20	26.4	32.3	27.7	22.2
572	Mn (0.600)	Co (0.400)	Ni (0.400)	Nb (0.200)		1.60	10.0	18.8	8.7	14.6
573	Al (0.400)	Mn (0.400)	Co (0.200)	Ni (0.400)	Rh (0.200)	1.60	20.0	32.1	22.1	27.4
574	Al (0.400)	Mn (0.200)	Ni (0.400)	Nb (0.200)	Pd (0.200)	1.40	23.7	32.8	25.5	24.0
575	Mn (0.200)	Ni (0.600)				0.80	11.0	20.8	10.2	16.2
576	Al (0.400)	Co (0.200)	Ni (0.600)	Nb (0.200)		1.40	32.8	36.3	32.2	21.6
577	Li (0.200)	Mn (0.600)	Fe (0.200)	Co (0.400)	Ni (0.200)	1.60	9.8	18.4	7.4	13.6
578	Li (0.600)	Ni (0.600)				1.20	30.1	30.9	28.2	19.6
579	Li (0.200)	Al (0.400)	Mn (0.200)	Ni (0.800)		1.60	28.2	30.7	26.5	21.1
580	Li (0.400)	Al (0.200)	Mn (0.200)	Ni (0.800)		1.60	30.1	31.2	28.1	19.7
581	Li (0.400)	Ni (0.600)	Nb (0.400)			1.40	32.6	31.7	30.1	18.4
582	Al (0.600)	Ni (0.600)	Y (0.200)			1.40	19.0	25.8	16.8	20.4
583	Li (0.600)	Ni (0.600)	Nb (0.200)			1.40	30.3	31.0	28.3	19.7
584	Li (0.200)	Al (0.200)	Mn (0.200)	Ni (0.800)	Nb (0.200)	1.60	30.6	31.8	28.3	19.2
585	Li (0.400)	Al (0.200)	Ni (0.400)			1.00	20.8	26.5	18.8	20.2
586	Li (0.400)	Al (0.400)	Ni (0.400)	Rh (0.200)	Ir (0.200)	1.60	19.2	27.3	17.6	22.7

587	Li (0.400)	Al (0.200)	Sc (0.200)	Ni (0.800)		1.60	33.3	34.1	30.0	20.7
588	Li (0.200)	Co (0.400)	Ni (0.400)	Y (0.200)		1.20	30.3	31.2	28.1	18.7
589	Li (0.800)	Ni (0.800)				1.60	34.6	32.7	32.3	18.4
590	Li (0.400)	Al (0.400)	Ni (0.600)			1.40	30.0	31.6	28.2	20.8
591	Al (0.400)	Ni (0.600)	Y (0.200)			1.20	31.1	32.2	29.3	19.8
592	Al (0.200)	Sc (0.200)	Mn (0.200)	Ni (0.800)	Y (0.200)	1.60	31.8	32.8	29.5	19.1
593	Ni (0.800)	Nb (0.200)				1.00	30.8	31.1	28.5	19.7
594	Al (0.200)	Mn (0.400)	Ni (0.800)	Nb (0.200)		1.60	27.3	31.0	26.2	21.8
595	Li (0.600)	Al (0.200)	Ni (0.400)	Rh (0.200)	Ir (0.200)	1.60	19.3	27.2	17.2	22.4
596	Li (0.200)	Al (0.400)	Ni (0.800)	Y (0.200)		1.60	27.3	31.0	25.6	20.5
597	Li (0.400)	Ni (0.600)	Nb (0.200)			1.20	34.9	33.4	32.1	18.3
598	Ni (0.600)	Y (0.200)				0.80	36.5	36.4	33.4	19.1
599	Li (0.200)	Al (0.200)	Sc (0.200)	Ni (0.800)	Nb (0.200)	1.60	36.3	35.8	32.7	18.8
600	Li (0.600)	Co (0.400)	Ni (0.400)	Nb (0.200)		1.60	34.9	37.5	31.3	19.1
601	Li (0.600)	Al (0.200)	Ni (0.200)	Rh (0.200)	Ir (0.400)	1.60	17.5	25.8	16.4	21.7
602	Li (0.400)	Ni (0.800)	Ta (0.200)			1.40	39.8	40.4	35.3	29.6
603	Li (0.200)	Al (0.400)	Sc (0.200)	Ni (0.800)		1.60	30.2	34.8	28.8	20.1
604	Li (0.600)	Ni (0.600)	Ta (0.200)			1.40	36.3	37.5	32.3	18.8
605	Al (0.600)	Ni (0.800)	Nb (0.200)			1.60	34.4	35.8	31.7	18.6
606	Li (0.400)	Sc (0.200)	Co (0.200)	Ni (0.600)	Nb (0.200)	1.60	32.2	34.6	29.9	19.0
607	Li (0.600)	Al (0.200)	Ni (0.800)			1.60	40.3	39.2	34.9	36.3
608	Li (0.800)	Rh (0.200)	Ir (0.600)			1.60	16.5	23.0	17.1	20.3
609	Li (0.400)	Mn (0.200)	Ni (0.800)	Nb (0.200)		1.60	40.8	40.0	35.1	20.2
610	Li (0.200)	Al (0.400)	Ni (0.800)	Nb (0.200)		1.60	39.4	39.3	34.1	17.6
611	Li (0.800)	Ni (0.400)	Rh (0.200)	Ir (0.200)		1.60	17.3	25.6	16.3	21.7
612	Li (0.200)	Al (0.600)	Ni (0.800)			1.60	26.8	31.9	27.0	22.1
613	Li (0.600)	Ni (0.800)	Ta (0.200)			1.60	43.0	40.8	36.8	28.5
614	Li (0.200)	Sc (0.200)	Ni (0.800)			1.20	34.5	36.2	31.6	18.7
615	Li (0.800)	Ni (0.200)	Rh (0.400)	Ir (0.200)		1.60	17.1	24.4	16.1	20.9
616	Li (0.400)	Co (0.200)	Ni (0.600)	Nb (0.400)		1.60	38.1	38.9	33.6	18.4
617	Li (0.400)	Ni (0.800)	Ta (0.400)			1.60	42.8	42.0	35.8	19.8
618	Mn (0.500)	Ni (0.800)				1.30	14.9	27.2	14.9	20.1
619	V (0.100)	Co (0.200)	Ni (0.800)			1.10	0.5	2.7	0.0	0.2
620	V (0.200)	Fe (0.100)	Ni (0.800)	Rh (0.100)		1.20	10.7	22.1	9.7	16.2
621	Co (0.400)	Ni (0.800)				1.20	35.3	37.8	31.9	36.2
622	Fe (0.100)	Co (0.500)	Ni (0.800)			1.40	33.8	35.9	31.3	18.4
623	Fe (0.200)	Co (0.100)	Ni (0.800)	Ba (0.500)		1.60	31.2	33.6	29.5	19.5
624	Mn (0.200)	Ni (0.800)				1.00	22.1	32.2	22.7	23.0
625	Ti (0.200)	Ni (0.800)	Ga (0.100)			1.10	25.8	34.3	25.9	21.9
626	Li (0.100)	Ti (0.100)	Ni (0.800)			1.00	35.1	37.3	31.7	20.0
627	V (0.100)	Ni (0.800)	Pd (0.400)			1.30	1.2	4.6	0.3	1.4
628	Sc (0.400)	Ti (0.100)	Ni (0.800)	Y (0.100)	Pd (0.100)	1.50	25.6	33.6	25.9	23.0
629	Mn (0.800)	Ni (0.800)				1.60	21.4	32.7	22.4	24.6
630	V (0.300)	Ni (0.800)	Pd (0.100)			1.20	8.0	16.2	7.2	11.3
631	Ni (0.800)	Rh (0.200)				1.00	20.2	32.7	21.6	25.9
632	V (0.100)	Ni (0.800)	Zn (0.100)			1.00	0.7	2.6	0.0	0.2

633	V (0.100)	Fe (0.100)	Co (0.500)	Ni (0.800)	Nd (0.100)	1.60	0.5	2.6	0.1	0.3
634	V (0.100)	Ni (0.800)				0.90	0.8	2.5	0.0	0.2
635	Mg (0.100)	Ti (0.100)	Ni (0.800)			1.00	33.2	37.3	30.1	41.5
636	V (0.300)	Co (0.200)	Ni (0.800)			1.30	0.6	3.0	0.0	0.2
637	Ti (0.100)	Ni (0.800)				0.90	32.6	37.1	30.4	19.9
638	Co (0.100)	Ni (0.800)	Cs (0.100)			1.00	35.3	40.7	28.0	21.7
639	Ni (0.800)	Nb (0.100)	Ta (0.200)			1.10	33.0	38.6	26.9	18.5
640	Al (0.100)	Ti (0.300)	Ni (0.800)	Zn (0.300)	Nb (0.100)	1.60	18.7	25.8	15.0	20.8
641	Li (0.200)	Ti (0.300)	Ni (0.800)	Rh (0.100)		1.40	16.1	23.3	12.9	18.7
642	V (0.100)	Ni (0.800)	Rh (0.100)			1.00	34.5	39.6	27.3	20.2
643	Co (0.200)	Ni (0.800)	Hf (0.100)			1.10	36.4	37.5	26.8	15.5
644	Co (0.100)	Ni (0.800)	Rb (0.400)	Nd (0.200)	Hf (0.100)	1.60	30.7	35.1	24.9	19.1
645	Co (0.100)	Ni (0.800)	Sr (0.600)			1.50	32.4	36.9	26.6	18.3
646	Mn (0.100)	Co (0.600)	Ni (0.800)			1.50	30.3	35.7	25.4	18.9
647	Ni (0.800)	Sr (0.400)				1.20	7.9	16.8	5.8	12.0
648	Ni (0.800)	Cs (0.400)	Pr (0.200)	Sm (0.200)		1.60	30.9	41.0	27.1	24.9
649	Ti (0.100)	Ni (0.800)	Pd (0.100)			1.00	32.0	36.5	26.7	18.4
650	Li (0.100)	Co (0.100)	Ni (0.800)			1.00	29.7	35.6	25.3	19.3
651	Mn (0.300)	Ni (0.800)				1.10	33.9	36.5	26.7	17.1
652	Fe (0.300)	Co (0.200)	Ni (0.800)	Rb (0.100)	Nb (0.200)	1.60	13.9	21.6	11.3	17.1
653	V (0.300)	Ni (0.800)	Pt (0.100)			1.20	33.6	40.2	27.7	21.4
654	Co (0.600)	Ni (0.800)				1.40	34.5	40.3	28.1	19.6
655	Ti (0.200)	Co (0.200)	Ni (0.800)			1.20	24.6	31.9	20.9	22.2
656	Al (0.100)	Sc (0.100)	Ni (0.800)			1.00	19.5	26.7	15.6	21.5
657	Ti (0.100)	Ni (0.800)	Rh (0.100)			1.00	33.5	38.2	26.8	17.4
658	Ni (0.800)	Cs (0.700)				1.50	14.3	24.2	12.7	20.0
659	Ni (0.800)	Cs (0.600)				1.40	16.8	26.4	15.7	22.2
660	Fe (0.600)	Ni (0.800)	Rb (0.100)	Cs (0.100)		1.60	5.1	7.8	1.3	5.4
661	Fe (0.100)	Ni (0.800)	Rb (0.700)			1.60	2.3	0.3	0.0	0.1
662	Fe (0.700)	Ni (0.800)	Gd (0.100)			1.60	16.1	25.8	14.6	21.7
663	K (0.500)	Fe (0.100)	Ni (0.800)	Rb (0.100)	Sm (0.100)	1.60	29.5	31.2	26.8	19.0
664	Mn (0.600)	Ni (0.800)	Bi (0.100)			1.50	2.7	0.3	0.0	0.1
665	Ni (0.800)	In (0.100)	Cs (0.600)	Tb (0.100)		1.60	2.9	0.5	0.0	0.1
666	Mn (0.500)	Ni (0.800)	In (0.100)	Nd (0.100)	Bi (0.100)	1.60	2.5	0.3	0.0	0.1
667	Ti (0.200)	Ni (0.800)	Cs (0.600)			1.60	15.2	25.2	13.8	21.0
668	Ni (0.800)	Cs (0.600)	Ce (0.200)			1.60	14.7	24.4	13.1	20.4
669	Fe (0.700)	Ni (0.800)	Rb (0.100)			1.60	13.0	21.9	11.0	18.1
670	Fe (0.700)	Ni (0.800)	Ce (0.100)			1.60	12.5	21.4	10.4	17.6
671	Ni (0.800)	Sr (0.100)	Cs (0.400)			1.30	33.3	33.2	29.8	19.4
672	Ni (0.800)	Rb (0.100)	Cs (0.600)	Nd (0.100)		1.60	14.3	23.8	12.4	19.7
673	Fe (0.100)	Ni (0.800)	Rb (0.600)	Er (0.100)		1.60	19.6	26.6	18.2	21.5
674	Co (0.100)	Ni (0.800)	Rb (0.400)			1.30	38.4	38.0	32.5	29.8
675	Fe (0.600)	Ni (0.800)	Rb (0.100)	Nb (0.100)		1.60	3.0	1.4	0.1	1.0
676	Co (0.100)	Ni (0.800)	Cs (0.300)			1.20	40.7	38.6	32.4	40.2
677	Fe (0.100)	Ni (0.800)	Ba (0.700)			1.60	30.1	33.0	28.5	21.0
678	Ni (0.800)	Cu (0.300)	Bi (0.100)			1.20	2.4	-0.2	0.0	0.1

679	Al (0.600)	Ni (0.800)	In (0.100)	Bi (0.100)		1.60	2.3	-0.3	0.0	0.1
680	Ni (0.800)	Y (0.100)	Cs (0.300)			1.20	36.1	35.6	31.7	18.9
681	Ni (0.800)	Rb (0.400)	Cs (0.300)			1.50	24.9	28.7	22.4	18.0
682	Ni (0.800)	Rb (0.100)	Cs (0.700)			1.60	13.8	22.7	11.9	18.4
683	Mn (0.400)	Ni (0.800)	In (0.300)	Bi (0.100)		1.60	2.3	-0.2	0.0	0.1
684	Ni (0.800)	Cs (0.300)				1.10	35.6	34.9	31.4	19.3
685	K (0.500)	Co (0.100)	Ni (0.800)	Rb (0.100)	Cs (0.100)	1.60	32.1	32.9	28.0	17.2
686	K (0.300)	Co (0.200)	Ni (0.800)	Rb (0.200)	Nb (0.100)	1.60	39.7	40.0	33.2	33.3
687	Ni (0.800)	Ba (0.700)	Nd (0.100)			1.60	27.3	32.3	26.5	32.0
688	Li (0.400)	Al (0.200)	Ni (0.800)	Y (0.100)	Bi (0.100)	1.60	1.9	-0.1	0.0	0.1
689	Ni (0.800)	Zn (0.100)	Bi (0.100)			1.00	2.5	-0.1	0.0	0.1
690	Ni (0.800)	Cs (0.500)				1.30	29.4	30.4	26.9	18.3
691	Sc (0.100)	Fe (0.300)	Ni (0.800)	Nb (0.100)		1.30	27.6	31.2	26.7	21.8
692	Ni (0.800)	Rb (0.300)	Cs (0.500)			1.60	11.6	19.6	9.1	16.2
693	K (0.100)	Ni (0.800)	Cs (0.700)			1.60	12.6	20.8	10.4	17.5
694	Ni (0.800)	In (0.100)				0.90	5.4	7.9	1.5	5.6
695	K (0.300)	Fe (0.300)	Ni (0.800)	Er (0.100)		1.50	17.9	28.0	17.7	24.2
696	K (0.300)	Ni (0.800)	Rb (0.100)			1.20	37.2	35.9	32.2	27.1
697	Al (0.300)	Co (0.200)	Ni (0.800)	Rb (0.200)		1.50	37.4	38.0	32.8	31.1

[a] Individual catalysts are denoted as A–B–C–D–E/γ-Al_2O_3, where the elements A–E are ordered by atomic number, and the values in parentheses correspond to their amounts in mmol/g-support.

[b] M_{total} is the total amount of the supported elements in mmol/g-support.

[c] The conversions and yields were determined as the averages of the time-on-stream data from 15,000 to 20,000 seconds during the DRM reaction at 500 ºC under a CH_4/CO_2/Ar stream of 3/3/4 mL/min/channel (approx. 10000 $mL_{gas}\cdot h^{-1}\cdot g_{cat}^{-1}$ of GHSV) for 6 hours.

[d] Nos. 1–277 were primarily generated through random sampling of the compositional space without relying on any prior knowledge. Catalyst Nos. 278–697 were iteratively selected and evaluated during the active learning process to refine and retrain the machine learning model.

[d] Nos. 1–256 corresponded to the unbiased dataset constructed in Chapter 2 through random sampling. Nos. 1–697 comprise the complete dataset described in Chapter 3, which was employed to comprehensively explore an exceptionally vast catalyst design space.

Table A2. Development of descriptors for DRM catalysts across the active learning loops. The corresponding machine learning scores are also included.[a,b]

Loop	Step	$Score_{train}$	$Score_{LOOCV}$	Descriptors
0	1	0.92	0.93	1. $1/(electron\_negativity\_max)^2$ 2. $1/(num\_valance\_sum)$ 3. $1/exp(lattice\_constant\_min)$ 4. $1/(icsd\_volume\_avg)^{1/2}$ 5. $exp(bulk\_modulus\_min)$ 6. $exp(num\_d\_valence\_max)$ 7. $ln(lattice\_constant\_min)$ 8. $(icsd\_volume\_min)^3$
	2	2.27%	2.50%	1. $(atomic\_number\_ase)^2$ 2. $1/(bulk\_modulus\_sum)$ 3. $exp(fusion\_enthalpy\_ase)$ 4. $(thermal\_conductivity\_ssd)^{1/2}$ 5. $1/ln(density\_gmean)$ 6. $1/exp(hhi\_p\_max)$ 7. $1/(en\_pauling\_max)^3$ 8. $(bulk\_modulus\_max)^2$
1	1	0.95	0.95	1. $1/(covalent\_radius\_pyykko\_triple\_min)^3$ 2. $1/(num\_p\_valence\_max)^{1/2}$ 3. $exp(atomic\_volume\_avg)$ 4. $exp(lattice\_constant\_min)$ 5. $exp(num\_d\_valence\_max)$ 6. $ln(en\_pauling\_ase)$ 7. $1/(bulk\_modulus\_min)^{1/2}$ 8. $exp(covalent\_radius\_pyykko\_triple\_max)$
	2	2.50%	2.67%	1. $(thermal\_conductivity\_max)^2$ 2. $1/(melting\_point\_max)^3$ 3. $1/(num\_d\_unfilled\_avg)$ 4. $1/(sound\_velocity\_sum)$ 5. $exp(vdw\_radius\_mm3\_gmean)$ 6. $gs\_volume\_per\_sum$ 7. $1/(en\_pauling\_max)^2$ 8. $(hhi\_p\_min)^{1/2}$
2	1	0.9	0.93	1. $(covalent\_radius\_pyykko\_triple\_max)^2$ 2. $(gs\_est\_bcc\_latcnt\_min)^3$ 3. $1/exp(atomic\_radius\_sum)$, 4. $1/(lattice\_constant\_min)^{1/2}$ 5. $ln(num\_d\_valence\_max)$ 6. $(gs\_volume\_per\_avg)^{1/2}$ 7. $(melting\_point\_max)^{1/2}$ 8. $1/ln(evaporation\_heat\_max)$
	2	2.63%	2.90%	1. $(covalent\_radius\_pyykko\_min)^2$ 2. $(thermal\_conductivity\_max)^3$ 3. $(hhi\_p\_min)^{1/2}$ 4. $1/(num\_s\_valence\_sum)^3$ 5. $Polarizability\_sum$

				6. (lattice_constant_min)^3 7. exp(sound_velocity_sum) 8. exp(electron_negativity_max)
3	1	0.95	0.93	1. (gs_volume_per_avg)^3 2. 1/(en_pauling_max) 3. 1/(num_p_valence_max)^3 4. 1/exp(en_ghosh_ase) 5. 1/ln(gs_volume_per_min) 6. 1/(atomic_radius_rahm_avg)$^{1/2}$ 7. ln(lattice_constant_min) 8. 1/exp(atomic_radius_rahm_avg)
	2	2.60%	2.75%	1. (density_gmean)^3 2. (thermal_conductivity_max)^3 3. 1/ln(hhi_p_min) 4. vdw_radius_mm3_sum 5. (covalent_radius_pyykko_min)^2 6. 1/exp(atomic_weight_avg) 7. ln(vdw_radius_alvarez_sum) 8. exp(en_pauling_max)
4	1	0.96	0.94	1. 1/(lattice_constant_min)^3 2. 1/(num_p_valence_max)^3 3. 1/exp(bulk_modulus_max) 4. 1/(covalent_radius_pyykko_triple_avg) $^{1/2}$ 5. exp(lattice_constant_min) 6. ln(gs_volume_per_avg) 7. 1/ln(gs_volume_per_ssd) 8. 1/ln(covalent_radius_pyykko_double_ssd)
	2	2.70%	2.88%	1. (density_max)^3 2. (thermal_conductivity_max)^3 3. 1/(bulk_modulus_sum)^3 4. covalent_radius_pyykko_triple_avg 5. ln(lattice_constant_min) 6. ln(num_s_unfilled_sum) 7. (hhi_r_gmean)^3 8. 1/(atomic_number_ase)
5	1	0.95	0.92	1. 1/(gs_est_bcc_latcnt_avg)^2 2. 1/(lattice_constant_min)$^{1/2}$ 3. exp(num_p_valence_ssd) 4. ln(num_d_valence_max) 5. (bulk_modulus_ssd)$^{1/2}$ 6. (lattice_constant_min)$^{1/2}$ 7. 1/ln(c6_gb_ssd) 8. 1/ln(gs_energy_ssd)
	2	2.76%	2.91%	1. (thermal_conductivity_max)^2 2. 1/(bulk_modulus_sum)^3 3. 1/exp(hhi_r_prod) 4. ln(covalent_radius_pyykko_triple_avg) 5. ln(electron_affinity_ssd) 6. (num_s_valence_max)$^{1/2}$ 7. exp(density_max) 8. 1/(num_s_unfilled_ase)^3

6	1	0.93	0.93	1. 1/(gs_volume_per_avg) 2. 1/(num_p_unfilled_avg)^3 3. 1/ln(vdw_radius_mm3_ssd) 4. 1/(num_d_valence_max)$^{1/2}$ 5. (lattice_constant_min)$^{1/2}$ 6. 1/(num_unfilled_min)$^{1/2}$ 7. (en_pauling_ssd)^2 8. (num_d_valence_avg)^3
	2	2.74%	2.91%	1. (thermal_conductivity_max)^3 2. 1/(bulk_modulus_sum)^3 3. (density_max)$^{1/2}$ 4. ln(covalent_radius_slater_avg) 5. (period_max)^3 6. gs_mag_moment_ase 7. (density_prod)^2 8. mendeleev_number_prod
7	1	0.92	0.92	1. (gs_volume_per_avg)^2 2. 1/(en_pauling_ase)^3 3. 1/(num_p_unfilled_max)^2 4. 1/(lattice_constant_min)$^{1/2}$ 5. 1/(num_d_valence_max)$^{1/2}$ 6. 1/exp(atomic_number_min) 7. 1/(melting_point_max)$^{1/2}$ 8. (num_d_valence_avg)^2
	2	2.72%	2.86%	1. (num_s_unfilled_max)^3 2. (thermal_conductivity_max)^3 3. 1/(bulk_modulus_sum)^3 4. 1/(density_max) 5. 1/(num_d_valence_ssd)^2 6. exp(num_s_valence_ssd) 7. ln(covalent_radius_pyykko_double_gmean) 8. num_f_valence_gmean
8	1	0.94	0.94	1. 1/(bulk_modulus_max)^2 2. 1/(gs_est_fcc_latcnt_min)^2 3. 1/(vdw_radius_uff_min)^2 4. exp(gs_volume_per_avg) 5. num_p_valence_max 6. vdw_radius_min 7. 1/ln(icsd_volume_avg) 8. (lattice_constant_min)^3
	2	2.98%	3.15%	1. (hhi_p_max)^2 2. (num_f_valence_gmean)^2 3. 1/(bulk_modulus_max)^3 4. 1/(num_d_valence_max)^2 5. 1/(num_d_valence_max)^3 6. 1/(bulk_modulus_ssd)$^{1/2}$ 7. ln(covalent_radius_cordero_avg) 8. melting_point_ase
9	1	0.95	0.93	1. 1/(en_pauling_max) 2. 1/(lattice_constant_min)^2 3. 1/ln(mendeleev_number_max) 4. (lattice_constant_min)$^{1/2}$ 5. vdw_radius_uff_min 6. 1/ln(molar_volume_avg)

				7. (heat_of_formation_max)^3 8. (atomic_volume_avg)^3
	2	3.07%	3.22%	1. (en_pauling_max)^2 2. (num_d_valence_max)^2 3. (num_f_valence_sum)^2 4. 1/(density_max) 5. 1/ln(num_unfilled_min) 6. 1/(heat_capacity_mass_min)$^{1/2}$ 7. covalent_radius_pyykko_triple_avg 8. num_d_valence_max
10	1	0.93	0.91	1. 1/(en_pauling_max) 2. 1/(lattice_constant_min)^2 3. 1/ln(mendeleev_number_max) 4. (lattice_constant_min)$^{1/2}$ 5. vdw_radius_uff_min 6. 1/ln(molar_volume_avg) 7. (heat_of_formation_max)^3 8. (atomic_volume_avg)^3
	2	2.99%	3.14%	1. (en_pauling_max)^2 2. (num_d_valence_max)^2 3. (num_f_valence_sum)^2 4. 1/(density_max) 5. 1/ln(num_unfilled_min) 6. 1/(heat_capacity_mass_min)$^{1/2}$ 7. covalent_radius_pyykko_triple_avg 8. num_d_valence_max
11	1	0.91	0.9	1. 1/(bulk_modulus_ssd) 2. 1/(molar_volume_avg) 3. 1/exp(num_p_valence_ssd) 4. 1/(lattice_constant_min)$^{1/2}$ 5. lattice_constant_min 6. (en_pauling_max)^3 7. 1/ln(vdw_radius_mm3_ssd) 8. (dipole_polarizability_prod)^2
	2	3.76%	3.94%	1. (atomic_number_ase)^2 2. 1/(bulk_modulus_max) 3. 1/(bulk_modulus_max)^3 4. 1/(period_max)^3 5. 1/(thermal_conductivity_sum) 6. 1/exp(gs_mag_moment_ase) 7. 1/ln(heat_capacity_molar_sum) 8. 1/(en_pauling_ssd)$^{1/2}$ 9. exp(gs_mag_moment_avg) 10. exp(num_d_valence_max) 11. ln(num_d_valence_max) 12. molar_volume_sum
12	1	0.92	0.91	1. (lattice_constant_min)^3 2. 1/(covalent_radius_pyykko_triple_max) 3. 1/exp(lattice_constant_min) 4. 1/ln(num_d_valence_max) 5. 1/(lattice_constant_min)$^{1/2}$ 6. hhi_r_ssd 7. 1/(atomic_radius_rahm_min)

				8. 1/(en_pauling_ase)
	2	3.36%	3.53%	1. $(gs\_mag\_moment\_max)^2$ 2. $(sound\_velocity\_prod)^2$ 3. 1/(c6_gb_gmean) 4. 1/(covalent_radius_slater_gmean) 5. $1/(gs\_est\_bcc\_latcnt\_max)^2$ 6. 1/ln(first_ion_en_avg) 7. 1/ln(heat_of_formation_gmean) 8. $1/(lattice\_constant\_avg)^{1/2}$ 9. density_max 10. ln(vdw_radius_mm3_gmean) 11. $(atomic\_radius\_rahm\_min)^{1/2}$ 12. $(heat\_capacity\_mass\_min)^{1/2}$
13	1	0.94	0.92	1. $(gs\_mag\_moment\_avg)^3$ 2. $1/(atomic\_radius\_min)^2$ 3. 1/(en_pauling_max) 4. $1/(icsd\_volume\_min)^3$ 5. $1/(mendeleev\_number\_max)^3$ 6. $(lattice\_constant\_min)^{1/2}$ 7. $(gs\_volume\_per\_avg)^2$ 8. $(sound\_velocity\_prod)^{1/2}$
	2	3.70%	3.86%	1. $(bulk\_modulus\_max)^2$ 2. $(gs\_mag\_moment\_max)^2$ 3. $(num\_d\_valence\_max)^3$ 4. $1/(bulk\_modulus\_max)^2$ 5. 1/(bulk_modulus_ssd) 6. 1/(lattice_constant_max) 7. $1/(num\_d\_valence\_ssd)^2$ 8. $1/(period\_max)^3$ 9. 1/(sound_velocity_min) 10. 1/exp(atomic_weight_sum) 11. 1/ln(en_allen_max) 12. $(covalent\_radius\_pyykko\_double\_gmean)^{1/2}$

[a] Step denotes the stage in the two-step feature selection process. Step 1 employed random forest classification to extract informative features, while Step 2 applied Huber regression to further refine feature selection. A genetic algorithm was utilized in both steps to determine the optimal number of features, striking a balance between model robustness and computational efficiency.

[b] $Score_{train}$ and $Score_{LOOCV}$ represent the evaluation metrics for the training and cross-validation stages, respectively, corresponding to balanced accuracy in Step 1 and mean absolute error (MAE) in Step 2.

Table A3. Summary of the test set used in active learning exploration process.

Test set	Elemental set	Selection rule	Elemental loading	Total loading limit	Active learning loop
1	Li, Al, Ca, V, Ni, Nb, Rh, Ag, Sn, Cs, Ba, Ce, Sm, Hf, Ir, Au, Bi.	1–5 elements randomly selected	0.5–3.5 mmol/g-support in 0.5 intervals	≤ 3.5 mmol/g-support	Loops0–3
2	Li, Mg, Al, K, Ca, Mn, Ni, Cu, Ga, Zr, Nb, Rh, Pd, Hf, W, Ir, Au	1–5 elements randomly selected	0.5–3.5 mmol/g-support in 0.5 intervals	≤ 3.5 mmol/g-support	Loops4–6
3	Li, Al, Sc, Mn, Fe, Co, Ni, Zn, Y, Nb, Mo, Rh, Pd, Ta, W, Ir, Pt	1–5 elements randomly selected	0.5–3.5 mmol/g-support in 0.5 intervals	≤ 3.5 mmol/g-support	Loops7–9
4	Li, Al, Sc, Mn, Fe, Co, Ni, Zn, Y, Nb, Mo, Rh, Pd, Ta, W, Ir, Pt	1–5 elements randomly selected	Fe, Co, Ni, Rh, Pd, Ir, Pt ≤ 0.8 mmol/g-support; others ≤ 0.8 mmol/g-support	Total ≤ 1.6 mmol/g-support	Loops10–11
5	45-element refined set[a]	1–4 elements randomly selected (excluding Ni)	Ni fixed at 0.8 mmol/g-support; others vary 0.1–0.8 mmol/g-support	Total ≤ 1.6 mmol/g-support	Loops12–13

[a] 16 elements excluded from the original 61 that were too costly and/or risky (Be, Cr, Tc, Ru, Cd, Pm, Dy, Ho, Tm, Yb, Lu, Re, Os, Hg, Tl, and Pb).